Spring 2015

Control of Modular Multilevel Converters for Grid Integration of Full-Scale Wind Energy Conversion Systems

Suman Debnath
Purdue University

Graduate School Form 30
(Updated 11/20/2014)

PURDUE UNIVERSITY
GRADUATE SCHOOL
Thesis/Dissertation Acceptance

This is to certify that the thesis/dissertation prepared

By Suman Debnath

Entitled
Control of Modular Multilevel Converters for Grid Integration of Full-Scale Wind Energy Conversion Systems

For the degree of Doctor of Philosophy

Is approved by the final examining committee:

MARYAM SAEEDIFARD, Co-Chair

STEVEN D. PEKAREK, Co-Chair

JIANGHAI HU

OLEG WASYNCZUK

To the best of my knowledge and as understood by the student in the Thesis/Dissertation Agreement, Publication Delay, and Certification/Disclaimer (Graduate School Form 32), this thesis/dissertation adheres to the provisions of Purdue University's "Policy on Integrity in Research" and the use of copyrighted material.

MARYAM SAEEDIFARD, Co-Chair

Approved by Major Professor(s): _____

_____

Approved by: Michael R. Melloch 03/03/2015

Head of the Department Graduate Program Date

CONTROL OF MODULAR MULTILEVEL CONVERTERS FOR GRID INTEGRATION OF FULL-SCALE WIND ENERGY CONVERSION SYSTEMS

A Dissertation

Submitted to the Faculty

of

Purdue University

by

Suman Debnath

In Partial Fulfillment of the

Requirements for the Degree

of

Doctor of Philosophy

May 2015

Purdue University

West Lafayette, Indiana

This thesis is a dedication to my loving parents.

ACKNOWLEDGMENTS

I would like to thank my advisor, Dr. Maryam Saeedifard, for all the motivation, guidance, and support she provided during my doctoral studies. I am extremely grateful to my co-advisor, Dr. Steve Pekarek, for all his help and timely involvement in this work. I strongly appreciate the support and encouragement provided by Dr. Oleg Wasynczuk. I would also like to thank him and Dr. Jianghai Hu, for serving in my examination committee and for their interest in this research.

Furthermore, I would like to thank Dr. Scott Sudhoff, Dr. Matthew Swabey, Chuck Harrington, David Azpell, and Rob Swanson for assisting with the hardware setup. I would also like to thank my peers at Purdue, including Anandakumar Subbiah, Heng Yang, Jaya Deepti Dasika, James Issac, Jiangchao Qin, Minyu Cai, and Munadir Ahmed for the numerous fascinating discussions I have had with them and for all their help during my doctoral studies.

Finally, I would like to express my sincere gratitude towards my parents and my sister, without whose unwavering support and encouragement, this would not have been possible.

TABLE OF CONTENTS

Page

Page

Page

LIST OF TABLES

LIST OF FIGURES

ABBREVIATIONS

WECS	wind energy conversion system
NPC	neutral-point clamped
MMC	modular multilevel converter
DFIG	doubly-fed induction generator
PMSG	permanent magnet synchronous generator
SCIG	squirrel-cage induction generator
2L-VSC	two-level voltage sourced converter
THD	total harmonic distortion
ANPC	active NPC
HVDC	high voltage direct current
SM	submodule
PWM	pulse width modulation
PD-PWM	phase disposition PWM
PSC-PWM	phase shifted carrier PWM
SLBM	selective loop biasing mapping
EMI	electro-magnetic interference
MPPT	maximum power point tracking
PI	proportional integral
PCC	point of common coupling
DPWM	distributed PWM
ESR	effective series resistance
DSP	digital signal processor
FPGA	field-programmable gate array

ABSTRACT

Debnath, Suman Ph.D., Purdue University, May 2015. Control of Modular Multilevel Converters for Grid Integration of Full-scale Wind Energy Conversion Systems. Major Professors: Maryam Saeedifard and Steve D. Pekarek.

The growing demand for wind power generation has pushed the capacity of wind turbines towards MW power levels. Higher capacity of the wind turbines necessitates operation of the generators and power electronic conversion systems at higher voltage/power levels. The power electronic conversion system of a wind energy conversion system (WECS) needs to meet the stringent requirements in terms of reliability, efficiency, scalability and ease of maintenance, power quality, and dv/dt stress on the generator/transformer. Although the multilevel converters including the neutral point clamped (NPC) converter and the active NPC converter meet most of the requirements, they fall short in reliability and scalability. Motivated by modularity/scalability feature of the modular multilevel converter (MMC), this research is to enable the MMC to meet all of the stringent requirements of the WECS by addressing their unique control challenges. This research presents systematic modeling and control of the MMC to enable it to be a potential converter topology for grid integration of full-scale WECSs. Based on the developed models, appropriate control systems for control of circulating current and capacitor voltages under fixed- and variable-frequency operations are proposed. Using the developed MMC models, a gradient-based cosimulation algorithm to optimize the gains of the developed control systems, is proposed. Performance/effectiveness of the developed models and the proposed control systems for the back-to-back MMC-based WECS are evaluated/verified based on simulations studies in the PSCAD/EMTDC software environment and experimental case studies on a laboratory-scale hardware prototype.

1. INTRODUCTION

Wind energy has been one of the world's fastest growing renewable energy sources [1–4]. While wind generated electricity continues to grow as a premier source of renewable energy, advanced wind energy conversion systems (WECSs) are required to harness this energy more efficiently, reliably and in a cost effective manner. In the following section, an overview of various components of the WECS is provided.

1.1 Overview of WECSs

The basic structure of a typical WECS is shown in Fig. 1.1. The major components of a typical WECS, as shown in Fig. 1.1, include a wind turbine, generator, gear-box (optional), a power electronic conversion system, and the associated control. A wind turbine can be designed for a constant- or variable-speed operation. Variable-speed wind turbines produce up to 10% more annual energy as compared to their constant-speed counterparts [5]. However, they necessitate power electronic converters to provide a required current at a required frequency.

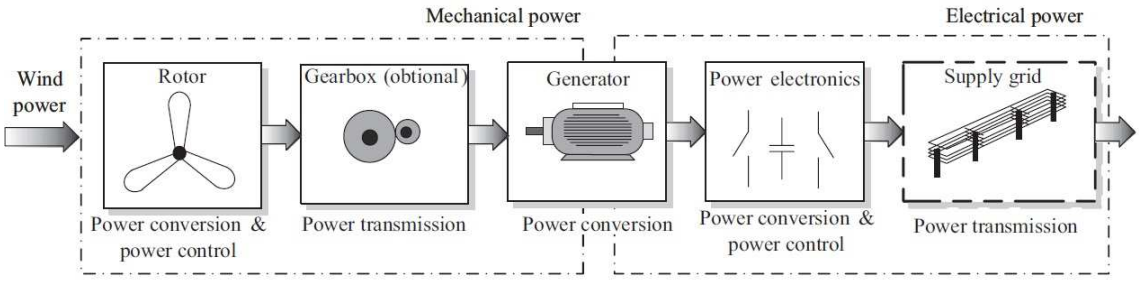

Fig. 1.1. Basic structure of a typical WECS [6].

The roadmap of converting mechanical energy to electrical energy using variable-speed WECSs is shown in Fig. 1.2 [7]. As shown in Fig. 1.2, a variable-speed WECS needs either a partially- or fully-rated back-to-back conversion system.

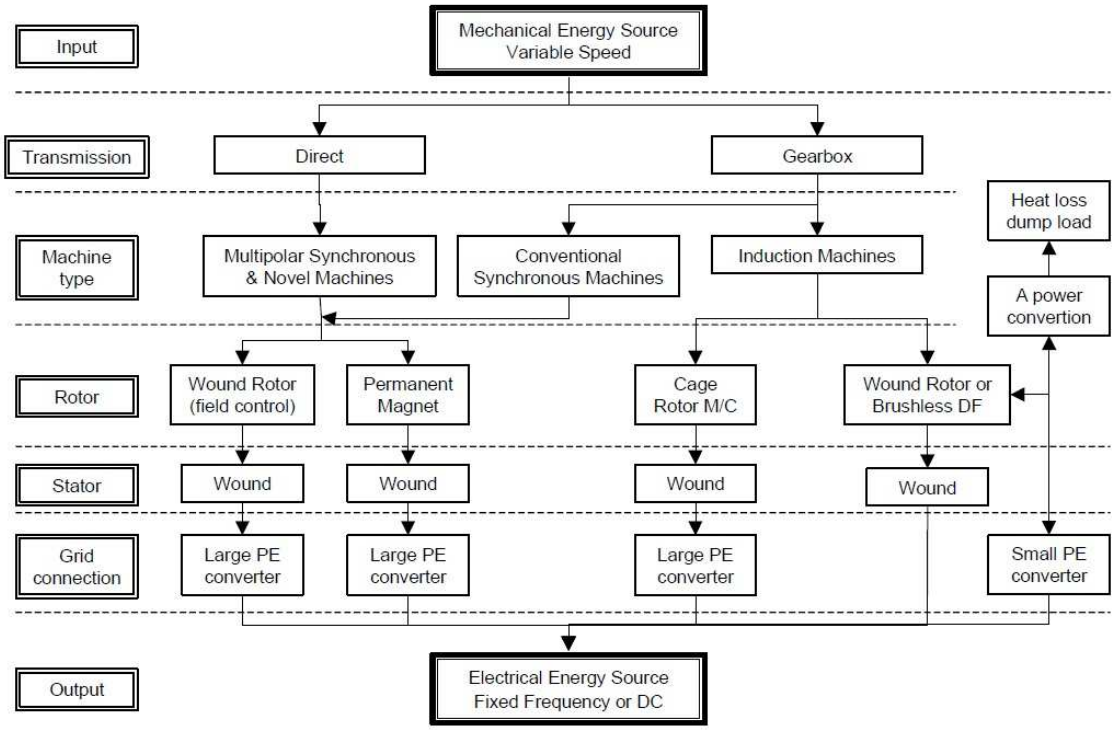

Fig. 1.2. Technology roadmap of variable-speed WECSs [7].

The WECSs with partially-rated back-to-back conversion systems include the wound rotor induction generator with dynamic slip control [8,9], shown in Fig. 1.3(a), and the doubly-fed induction generator (DFIG) [10], shown in Fig. 1.3(b). The main drawback of these configurations is the direct connection of their stator to the grid. Consequently, during a fault in the grid, the system can no longer stay connected to the grid to keep the currents and voltages in the rotor circuit under safe limits [6,11]. Presence of slip rings is another main disadvantage [12]. The partially-rated conversion system based WECSs require a gearbox to couple the wind turbine to the generator.

The WECSs with full-scale back-to-back conversion systems, hereafter referred to as full-scale WECSs, are shown in Figs. 1.4 and 1.5. The generators used in these WECSs include (i) the squirrel-cage induction generator (SCIG) and the wound-rotor synchronous generator with a gearbox as shown in Figs. 1.4(a) and (b), respectively, and (ii) the multi-pole wound-rotor synchronous generator and the multi-pole

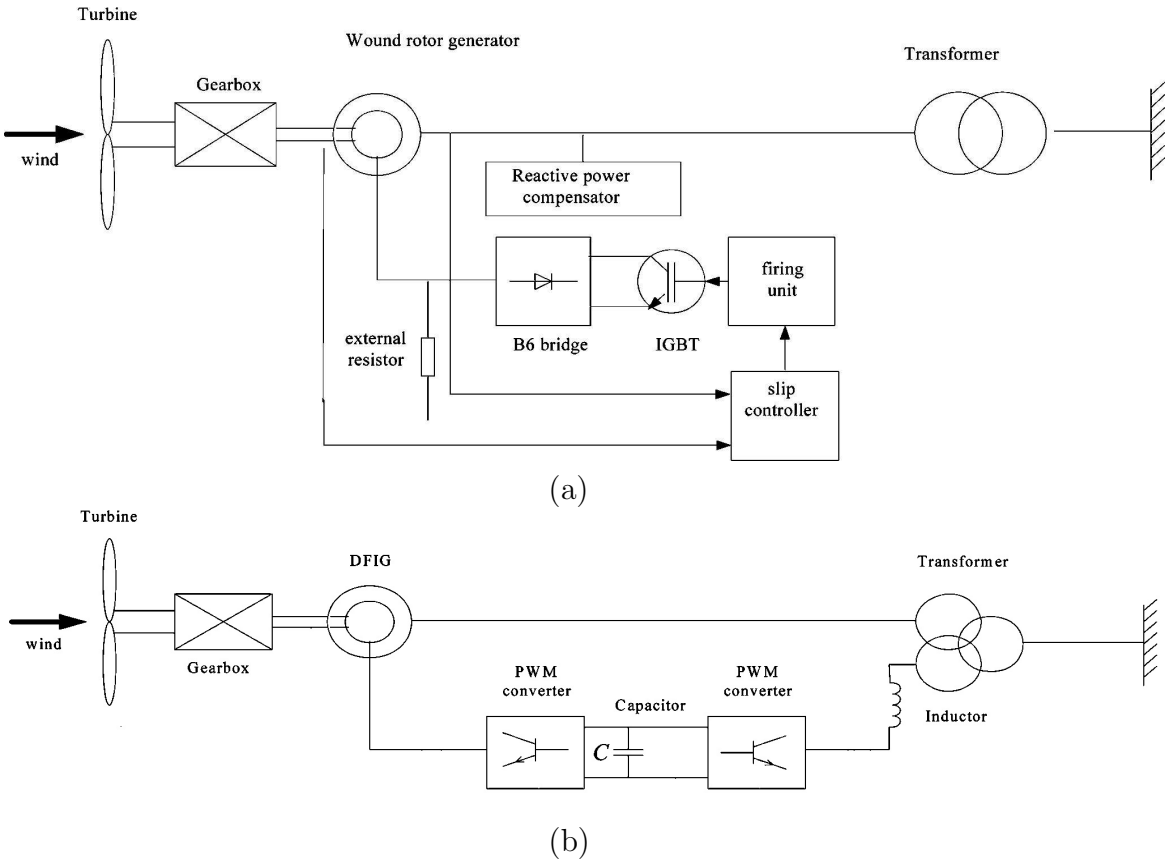

Fig. 1.3. WECSs with partially-rated conversion system: (a) wound rotor induction generator with dynamic slip control, and (b) doubly-fed induction generator (DFIG) [3].

permanent magnet synchronous generator (PMSG) without a gearbox as shown in Figs. 1.5(a) and (b), respectively. Amongst various generators used in a variable-speed full-scale WECS, the direct-drive WECS with a multi-pole PMSG has gained significant interest due to its wind to electrical energy conversion efficiency, reliability and controllability [13]. Furthermore, compared to a SCIG and a wound-rotor synchronous generator system, a direct-drive PMSG-based WECS reduces system failure rate due to the absence of the mechanical gear boxes [14].

The full-scale WECSs are interfaced to the grid through a full-scale power electronic conversion system. The back-to-back connected two-level voltage sourced converter (2L-VSC) is the most prevailing converter configuration for the full-scale

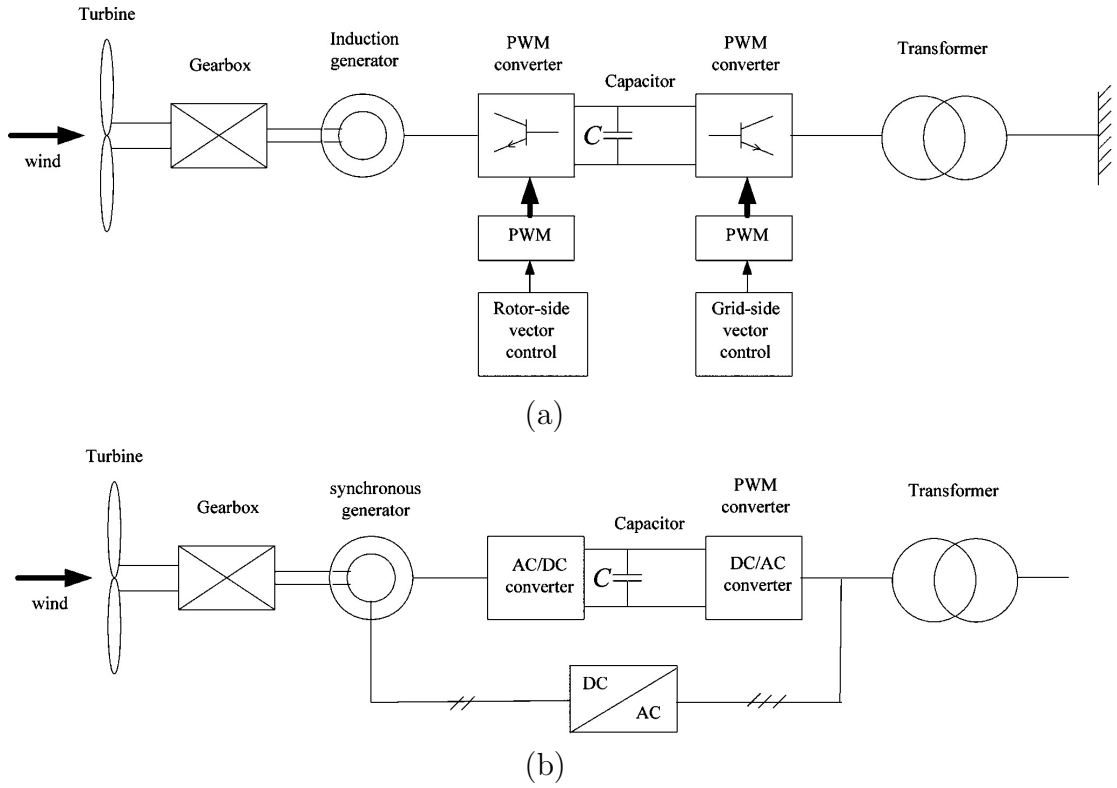

Fig. 1.4. Variable-speed WECSs with full-scale conversion systems: (a) squirrel-cage induction generator, and (b) wound-rotor synchronous generator with gear-box [3].

WECSs [12]. Operation of the 2L-VSC at high voltage levels require switching devices with high voltage ratings. This can be achieved either by using the state-of-the-art switches available at high voltage ratings or cascading switches with lower voltage ratings [15]. Either of the options (i) introduces a relatively high $\frac{\mathrm{d}v}{\mathrm{d}t}$ stress on the generator and transformer, (ii) needs bulky and lossy output filters and/or a high switching frequency to comply with the grid codes in terms of total harmonic distortion (THD) requirements [16], and (iii) does not provide modularity/scalability in the design.

The solution to the aforementioned problems with the 2L-VSC is to use multilevel VSCs. The salient features of multilevel VSCs include: (i) low harmonic distortion of their output voltages/currents with low switching frequency, (ii) capability to handle high power/voltage with low-rating devices [17], and (iii) low $\frac{\mathrm{d}v}{\mathrm{d}t}$ stress on the gen-

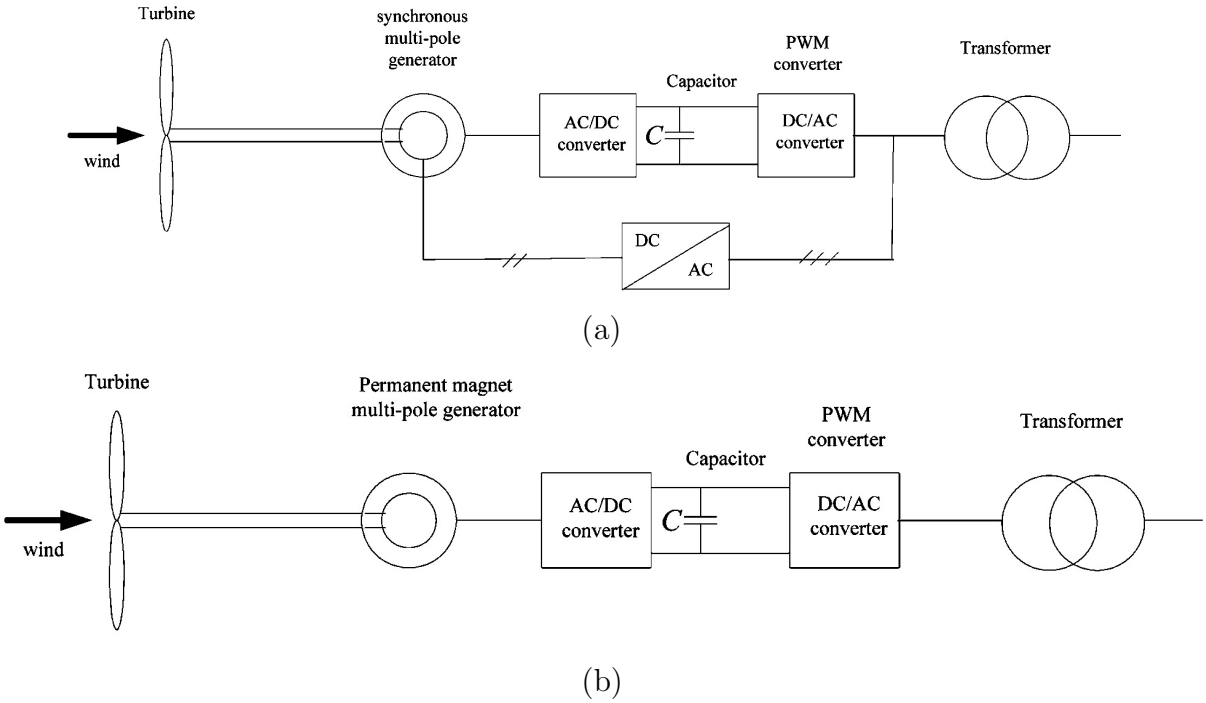

Fig. 1.5. Direct-drive variable-speed WECSs with full-scale conversion systems: (a) multi-pole wound-rotor synchronous generator, and (b) multi-pole permanent magnet synchronous generator [3].

erator/transformer. In the technical literature, various types of multilevel converter topologies have been proposed and investigated for WECSs [15, 16, 18–30]. The most promising topologies include:

- Neutral-point clamped (NPC) converter [24–26]: The application of the NPC converter, due to the complexity in counteracting the dc-capacitor voltage drift phenomenon, has been limited to the three-level NPC converter [31, 32].

- Active NPC (ANPC) converter based topologies [19, 20, 22]: As compared with the conventional multilevel converters in which the capacitor voltage balancing task is challenging and in some cases infeasible [31, 32], the ANPC converter based topologies need a fairly simple capacitor voltage balancing strategy to guarantee proper operation of the converter over all operating conditions. As

compared with the three-level NPC converter, the five- or higher-level ANPC converter improves the THD and can potentially reduce the size of the filters.

Nevertheless, none of the aforementioned multilevel converters address the following features required in the design: (i) equal distribution of losses and/or voltage/current stresses among all the devices, (ii) scalability, (iii) modularity, and/or (iv) fault tolerance. Recently, the emergence of the modular multilevel converter (MMC) has revolutionized high voltage direct current (HVDC) technology because of its modularity and scalability [33–36]. A circuit diagram of the MMC is shown in Fig. 1.6. The MMC addresses all of the above-mentioned features of the design. To date, research on the operation of the MMC has been primarily focused on HVDC transmission systems where the MMC, with a large number of its main building block circuits, i.e., the half-bridge SubModules (SMs), operates with a fixed ac-side frequency. Despite the well-understood technical merits of the MMC with a large number of SMs in HVDC systems, their application to drive systems and WECSs requires further research.

1.2 Motivation and Statement of the Problem

The trend in wind turbine technology has been towards large capacity units to reduce cost per megawatt of capacity [2,17]. This trend is highlighted in the evolution of the wind turbine size and their associated power electronic converters, highlighted with a blue inner circle in Fig. 1.7 [12]. As shown in Fig. 1.7, the market share for full-scale WECSs is growing. This is primarily due to their advantages mentioned in Section 1.1. As a full-scale WECS supplies a significant amount of power and can operate in stand-by/remote locations [37], its full-scale power electronic conversion system needs to meet stringent requirements in terms of reliability, efficiency, scalability and ease of maintenance, power quality, and $\frac{\mathrm{d}v}{\mathrm{d}t}$ stress on the generator/transformer. Although the back-to-back MMC configuration embeds all of these features, for variable-speed WECS applications, many unique challenges are imposed. The main challenges are:

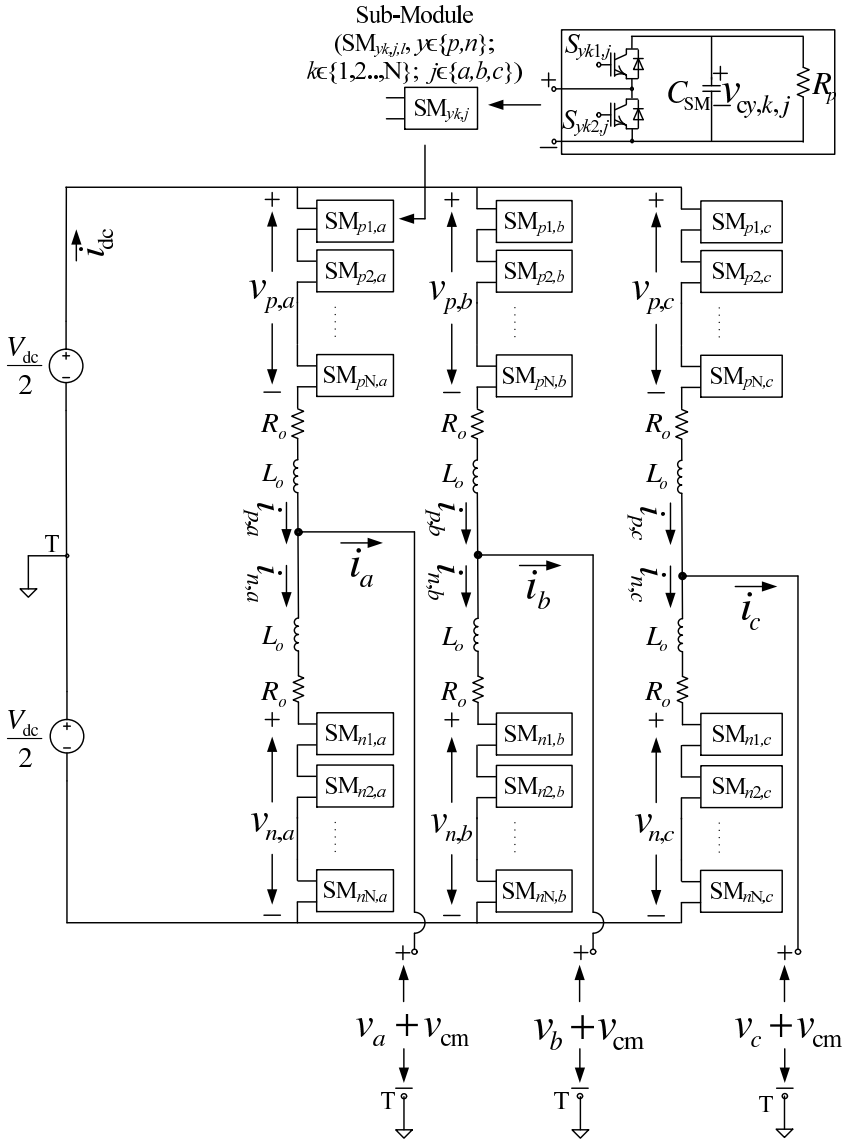

Fig. 1.6. Circuit diagram of an MMC.

- The pulse width modulation (PWM) strategy along with a SM capacitor voltage balancing algorithm is necessary to (i) produce the switching state of each SM switch and (ii) keep the SM capacitor voltages balanced at their nominal values. The existing SM capacitor voltage balancing algorithms are mainly based on a sorting algorithm in which the SM capacitor voltages are measured and sorted within each sampling period. Then, based on the direction of the arm currents and the number of required on-state SMs within each sam-

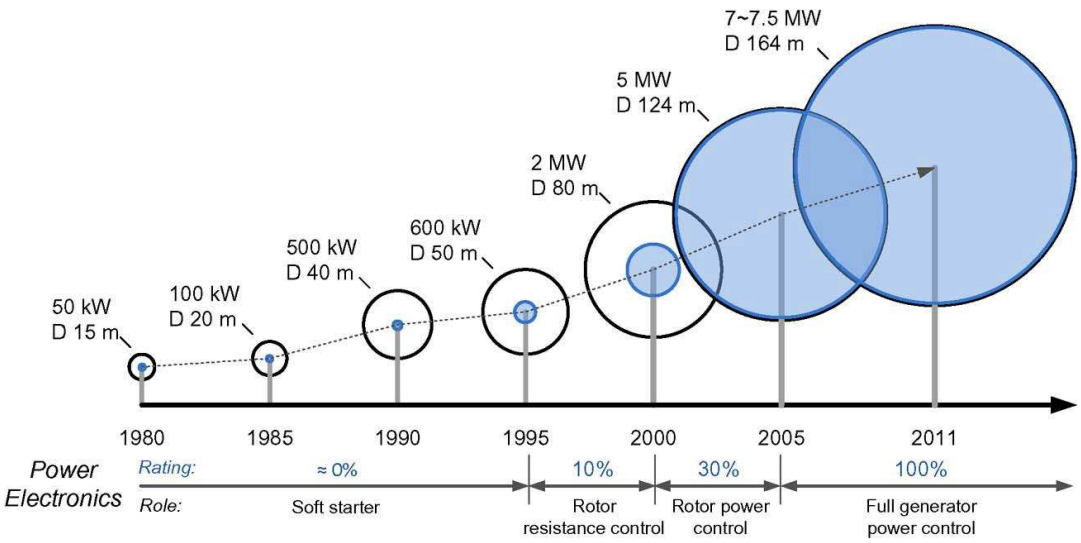

Fig. 1.7. Wind turbine evolution and the main trend of conversion system (blue indicates power level of converters) in the last 30 years [12].

pling period, a number of SMs are inserted/bypassed [38]. Conventionally, the PWM strategies implemented to control the MMC have been primarily based on phase disposition PWM (PD-PWM) and phase shifted carrier PWM (PSC-PWM) [35,38–43]. Each of these PWM strategies have been implemented with different variations. Most notably, a unified PD-PWM strategy with a sorting algorithm to balance the SM capacitor voltages is proposed in [38]. While [39] proposes an improved PD-PWM strategy with indirect modulation and voltage balancing strategy, [40] proposes a PD-PWM strategy with selective loop biasing mapping (SLBM) method. While [41] and [42] propose a PSC-PWM strategy with indirect modulation, [43] proposes a PSC-PWM strategy with a reduced-sensor SM capacitor voltage balancing algorithm and [35] proposes a PSC-PWM strategy with reduced switching frequency. Reference [44] proposes a staircase-PWM strategy with predictive sorting algorithm. A tolerance band modulation method, to balance the SM capacitor voltages, has been investigated in [45]. Reference [46] develops a few SM capacitor voltage balancing strategies in which the SM capacitor voltage balancing algorithm is implemented at a slower rate compared to the sampling period. While the strategies pro-

posed in [38, 40, 43–46] change the state of multiple switches at any instant and thereby increase switching frequency and electro-magnetic interference (EMI), the strategies proposed in [35, 39] reduce the switching frequency by limiting the number of switches changing their state at any instant to the minimum possible value, potentially to only one switch change if the reference waveform shows no sudden change. However, with increase in the carrier frequency and/or the number of SMs, the strategy proposed in [35] suffers from intensive computational burden. The strategies proposed in [39, 41, 42] require special SM capacitor voltage control strategies to stabilize the system [47].

- The magnitude of circulating currents, under fixed-frequency operation, i.e., as the grid-side converter of a WECS, needs to be reduced to improve the efficiency, components' rating and size [35, 48–50]. A control system to reduce the ac components of the circulating currents of the MMC has been studied in [35]. However, it does not operate satisfactorily under unbalanced conditions in the ac side.

- The magnitude of the SM capacitor voltage ripple is inversely proportional to the ac-side frequency. Consequently, when the MMC operates as the generator-side converter of the WECS under low frequency, the magnitude of the SM capacitor voltage ripple becomes very large and, if not properly and actively reduced, may introduce instability and/or increase power losses and components' size of the MMC. In the technical literature, variable-frequency operation of the MMC has been investigated and various remedial measures have been proposed to control the SM capacitor voltage ripple at low frequencies [51–55]. The strategy proposed in [51–54] requires a large circulating current to counteract the SM capacitor voltage ripple, which consequently results in significant power losses. The strategy proposed in [55] has its own practical limitations.

- The controller gains of the MMC control systems have been tuned using either (i) linearized models in [56, 57] and such that the controlled states are

well separated with respect to their corresponding time constants [58, 59], or (ii) approximate linear time-invariant system models [60]. Neither of the aforementioned tuning methods may lead to an optimum performance of the MMC system.

- At the startup of the MMC, all SM capacitors are required to be charged to their nominal voltage values before the converter proceeds to its normal operation. To reduce the surge currents and the startup time, a fast and smooth startup procedure is preferred. Precharging the SM capacitors and startup procedure of the MMC from the de-energized conditions have been explored in [61–67]. Reference [61] proposes a startup procedure in which the SM capacitors are charged from a pre-charged dc-link. An additional resistor, which is inserted/bypassed by its parallel switch, is connected in series with the SMs of each arm to limit the peak current. The main disadvantage of this procedure lies in the long tail-off time noticed in the charging process that increases the time taken to charge the capacitors. Reference [62] presents a startup procedure where the dc link of the MMC is connected to a diode-bridge rectifier. Although this procedure limits the arm currents, it requires a diode-bridge rectifier to charge the dc link which is not feasible for the back-to-back MMCs. Reference [63] proposes a precharging circuit comprised of four thyristors per SM of the MMC. Although, by using an additional circuitry, the SMs can be precharged synchronously and the startup procedure is accelerated, it adds additional complexity and cost to the system. A similar problem is encountered with the charging process described in [64] in which auxiliary voltage sources are required for charging the SM capacitors. Reference [65] develops a charging process for the SM capacitors in a back-to-back MMC-based drive system through the grid. The developed charging process consists of two stages: (i) uncontrolled charging stage, and (ii) controlled charging stage. In the uncontrolled charging stage, all the SMs in both MMCs are blocked and their capacitors charge through the anti-parallel diodes. To limit the peak current from the grid, each phase

of the grid-side MMC is connected to the grid through a resistor. Once the sum of the SM capacitor voltages within each arm of the grid-side MMC reach the peak value of the line-to-line voltage, the controlled charging stage sets in. In the controlled charging stage, the SMs of the grid-side MMC are unblocked and actively controlled using a qd current controller. The qd current controller limits the charging current from the grid and maintains the required power factor. Once the voltages of SM capacitors of the grid-side MMC and the dc link reach their respective rated values, the SM capacitors of the machine-side are unblocked and controlled to reach their respective rated values. The sequential charging process, where the SM capacitors of grid-side are unblocked first and then the SM capacitors of generator-side, results in slowing down the charging process. A similar startup strategy is proposed in [66] for charging the SM capacitors of the MMC through the ac-side. This process considers a closed-loop charging process in the controlled charging stage, where the ac-side currents are controlled at certain fixed values. However, the charging process considers the sequential charging of upper- and lower-arm SM capacitors, which slows down the charging process and limits the ac-side currents to half their rated values due to the constraints imposed by the limits on the arm currents. Reference [67] proposes another similar sequential charging process for the back-to-back MMC that will also not minimize the time taken to charge the SM capacitors.

Having outlined the salient features and limitations of the MMC as a potential full-scale converter in advancing the variable-speed WECSs, this thesis aims at developing control systems to overcome the operational limitations and improve the performance of the MMC.

1.3 Thesis Objectives

The main objectives of this thesis are:

- To develop state-space models that accurately represent the MMC system.

- To improve the PWM strategy used to control the MMC so as to reduce the switching frequency, EMI, and computational burden.
- To enhance the performance of the MMC, in terms of the magnitude of circulating currents, as the grid-side converter of a WECS.
- To improve the stability and performance of the MMC, in terms of the magnitude of circulating currents and SM capacitor voltage ripple, as the generator-side converter of a WECS.
- To optimize the performance of the control systems implemented to control various MMC systems.
- To improve the startup-charging process of the SM capacitors in the back-to-back MMC-based WECS in terms of reduction in the startup time.

Although the developments and studies of this thesis are carried out for a direct-drive PMSG-based WECS, they are equally applicable, with minor modifications, to full-scale WECSs with other generator technologies as well.

1.4 Thesis Outline

There are nine chapters and two appendices in this thesis document. The outline of this thesis is highlighted in Fig. 1.8.

- The basics of operation of a direct-drive full-scale WECS is presented in Chapter 2. In this chapter, the wind turbine characteristics, the PMSG model, a maximum power point tracking (MPPT) strategy, and the grid- and generator-side controllers are described.
- The MMC is introduced in Chapter 3. The structure, modulation strategy, and the state-space models of the MMC are developed and explored in detail in this chapter.

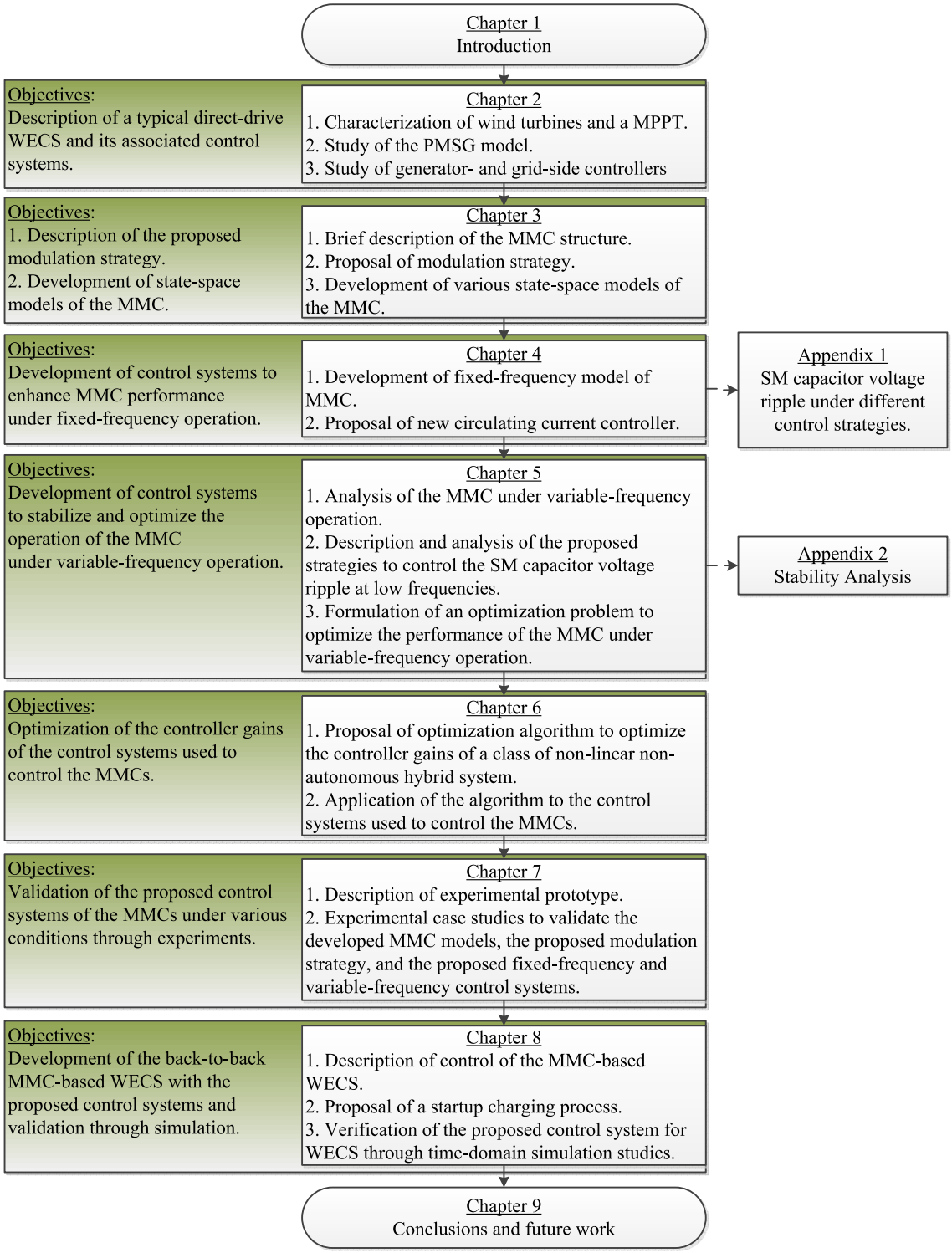

Fig. 1.8. The thesis outline.

- The control system of the MMC under fixed-frequency operation is developed in Chapter 4. In this chapter, the circulating current controller under fixed-frequency operation is proposed.

- A comprehensive analysis of the MMC under variable-frequency operation is provided in Chapter 5. Based on the analysis, two novel strategies are proposed to reduce the large capacitor voltage ripple under low-frequency operation. A detailed analysis of the proposed strategies are provided and an optimization problem is formulated to optimize the performance of the MMC under variable-frequency operation. The corresponding controller and design of the gains of the controller are also explained in this chapter.

- Optimization of the controller gains of a class of non-linear non-autonomous hybrid system is considered in Chapter 6. The application of the developed algorithm to optimize the gains of the control systems proposed in Chapters 4 and 5 is also explored in this chapter.

- Experimental results are provided in Chapter 7 to (i) verify the developed MMC models, (ii) substantiate the performance of the proposed modulation strategy, and (iii) validate the performance of the proposed control systems for fixed- and variable-frequency operations of the MMC.

- The control of an MMC-based WECS is explained and investigated in Chapter 8. The WECS considered in this chapter is a PMSG-based direct-drive system explained in Chapter 2. The WECS consists of a back-to-back MMC, with a grid-side MMC under fixed-frequency operation and a generator-side MMC under variable-frequency operation. That is, the control system developed in this chapter is based on the developments in Chapters 4 and 5. Moreover, the startup charging procedure of the back-to-back MMC capacitors from a de-energized state is considered in this chapter. The performance of the developed control systems of the MMC-based WECS are validated under various operating conditions through time-domain simulation studies.

2. DIRECT-DRIVE WIND ENERGY CONVERSION SYSTEMS

In this chapter, an overview on the direct-drive WECSs is provided. Various components of a direct-drive WECS along with their control structures are presented. In this introductory chapter, the system hub to which the modular multilevel converters and their control systems are accommodated to develop the medium-voltage WECSs is presented.

2.1 Basics of a Direct-Drive WECS

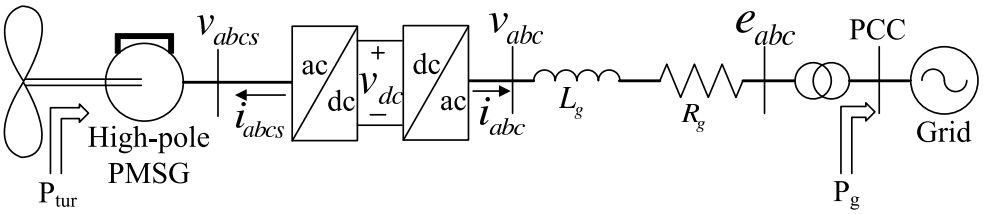

Fig. 2.1. Schematic diagram of a direct-drive WECS.

A single-line schematic representation of a full-scale WECS is shown in Fig. 2.1. The system is comprised of a wind turbine directly coupled to a high-pole PMSG and a back-to-back power conversion system. The PMSG is interfaced to an ac-dc converter which is intended for machine control. Another converter, which is a dc-ac converter, provides an interface to the utility grid and regulates the power transfer. The ac side treminals of the grid-side converter are connected to the utility grid through a series connected R_gL_g branch and a three-phase transformer as shown in Fig. 2.1.

The wind turbine and the PMSG parameters used in this thesis for simulations are presented in Tables 2.1 and 2.2, respectively.

Table 2.1.
Parameters of the study wind turbine [68]

Quantity	Value
Turbine type	three-blade
Rotor radius	58 m
Rated power	5 MW
Rated speed	1.55 rad/s
Rated wind speed	11.8 m/s
Rated torque	3.226×10^6 Nm
Maximum aerodynamic efficiency $C_p(\lambda_{\text{opt}})$	0.48
Optimum tip speed ratio λ_{opt}	7
Cut-in wind speed	3 m/s
Cut-out wind speed	25 m/s
Hub height	138 m
Rotor and turbine inertia J	1.06×10^7 kg.m^2

Table 2.2.
Parameters of the PMSG [68]

Quantity	Value
Rated power	5 MVA
Rated voltage (line-to-line)	4.0 kV
Rated electrical frequency $\omega_{r,\text{rated}}$	224.75 rad/s
Stator winding resistance r_s	72.192 mΩ
Stator leakage inductance L_{ls}	1.549 mH
d-axis inductance L_d	4.33 mH
q-axis inductance L_q	4.33 mH
Number of pole pairs (P/2)	145

2.2 Wind Turbine Characteristics

The wind turbine is often characterized by the relationship among its mechanical power, the environmental conditions like wind speed/kinetic power, and various turbine mechanical parameters.

The kinetic power of wind is

$$P_{\text{wind}} = \frac{1}{2}\left(\rho A V_w\right) V_w^2 = \frac{1}{2}\rho A V_w^3, \tag{2.1}$$

where ρ is the air mass density in kg/m^3, A is the area covered by the rotor blades in m^2, and V_w is the wind speed in m/s. The mechanical power extracted from wind by the wind turbine can be described as a fraction of the wind kinetic power and is given by [69]:

$$P_{\text{tur}} = C_p(\lambda, \beta) P_{\text{wind}} = \frac{1}{2}\rho A V_w^3 C_p(\lambda, \beta), \tag{2.2}$$

where $C_p(\lambda, \beta)$ is the power performance coefficient which is a non-linear function of the pitch angle β in rad, and the blade tip speed ratio λ (dimensionless). λ is defined by

$$\lambda = \frac{r\omega_r}{V_w}, \tag{2.3}$$

where r is the radius of the rotor blades in m and ω_r is the rotor rotational speed in rad/s. The power performance coefficient $C_p(\lambda, \beta)$, based on [69], is described by

$$C_p(\lambda, \beta) = 0.5176\left(116x - 0.4\beta - 5\right) e^{-21x} + 0.007869\lambda, \tag{2.4a}$$

$$x = \left(\frac{1}{1.157\lambda + 0.08\beta} - \frac{0.035}{\beta^3 + 1}\right), \tag{2.4b}$$

and is in the range of zero to 0.59, which is known as the Betz limit [70]. The variation of $C_p(\lambda, \beta)$ with respect to λ and for various β is shown in Fig. 2.2. As shown in Fig. 2.2, the peak value of $C_p(\lambda, \beta)$ is the largest when $\beta = 0$ and it drops as β is increased. This corresponds to the same pattern for the turbine power P_{tur}. In most of WECSs, β is (i) set to zero if the electrical power is below the rated value, (ii) actively controlled to limit the turbine power in case the power exceeds the rated value, and (iii) set to its maximum value , e.g., $\beta = 90°$, to interrupt the power generation under

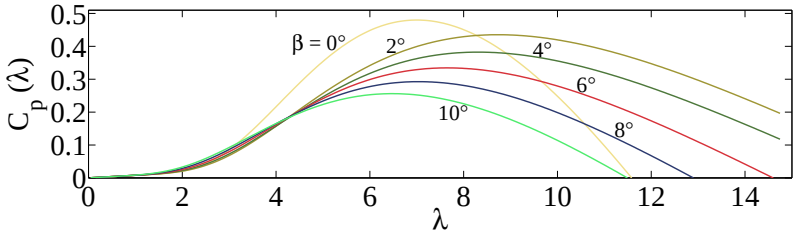

Fig. 2.2. Variation of the power performance coefficient as a function of λ for various β.

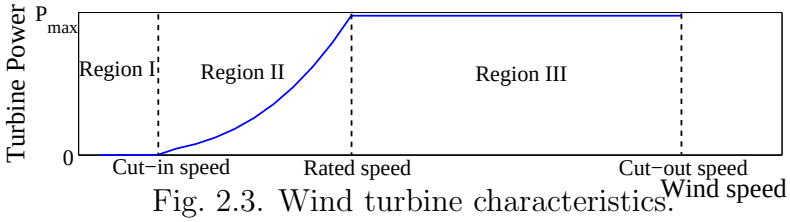

Fig. 2.3. Wind turbine characteristics.

extreme wind conditions. Subsequently, the turbine characteristics, i.e., the turbine power vs. wind speed is divided into three regions as shown in Fig. 2.3 [71]:

1. Region I in which wind speed < cut-in speed: The power generated is too small and largely supplies the losses of the system. Hence, the net generated power is zero.

2. Region II in which cut-in speed < wind speed < rated speed: The power characteristics are described by (2.2) to (2.4). In this case, as shown in Fig. 2.3, the maximum power is generated under the rated conditions.

3. Region III in which rated speed < wind speed < cut-out speed: The power generated by the system is restricted to the power generated under rated conditions. In this case, the pitch angle, β, of the wind turbine is adjusted so that the maximum power that can be extracted at the high wind speeds does not exceed the maximum power generated under rated conditions. Here, the cut-out speed refers to the maximum speed at which the turbine is allowed to deliver energy. This speed is usually limited by the engineering design and safety constraints.

2.3 PMSG Model

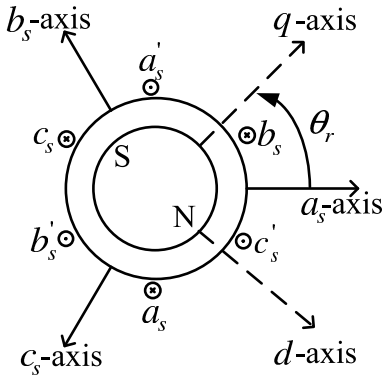

Fig. 2.4. A three-phase PMSG.

Table 2.3.
Glossary of terms

Quantity	Symbol
Stator resistance	r_s
Inductance matrix	$\boldsymbol{L}_s$
Maximum flux produced by the permanent magnet	λ_m^r
Position of rotor as shown in Fig. 2.4	θ_r
Phase voltage vector	$\boldsymbol{v}_{abcs}$
Phase current vector	$\boldsymbol{i}_{abcs}$
Flux linkage vector	$\boldsymbol{\lambda}_{abcs}$
Number of poles	P

The electrical dynamics of a three-phase PMSG shown in Fig. 2.4 is described by [72]

$$\boldsymbol{v}_{abcs} = \boldsymbol{r}_s \boldsymbol{i}_{abcs} + \frac{\mathrm{d}\boldsymbol{\lambda}_{abcs}}{\mathrm{d}t}, \tag{2.5}$$

where

$$\begin{aligned}
\boldsymbol{f}_{abcs}^{T} &= \begin{bmatrix} f_{as} & f_{bs} & f_{cs} \end{bmatrix}, \\
\boldsymbol{r}_s &= \operatorname{diag}\begin{bmatrix} r_s & r_s & r_s \end{bmatrix}, \\
\boldsymbol{\lambda}_{abcs} &= \boldsymbol{L}_s \boldsymbol{i}_{abcs} + \boldsymbol{\lambda}_m^r, \\
\boldsymbol{\lambda}_m^{rT} &= \lambda_m^r \begin{bmatrix} \sin(\theta_r) & \sin\left(\theta_r - \frac{2\pi}{3}\right) & \sin\left(\theta_r + \frac{2\pi}{3}\right) \end{bmatrix},
\end{aligned}$$

and the rest of the terms are introduced in Table 2.3.

Applying a transformation matrix defined by

$$\boldsymbol{T}(\theta) = \frac{2}{3} \begin{bmatrix} \cos(\theta) & \cos\left(\theta - \frac{2\pi}{3}\right) & \cos\left(\theta + \frac{2\pi}{3}\right) \\ \sin(\theta) & \sin\left(\theta - \frac{2\pi}{3}\right) & \sin\left(\theta + \frac{2\pi}{3}\right) \\ \frac{1}{2} & \frac{1}{2} & \frac{1}{2} \end{bmatrix} \tag{2.6}$$

to (2.5), the qd rotor reference frame model of the PMSG is given by

$$L_q \frac{\mathrm{d}i_{qs}^r}{\mathrm{d}t} + r_s i_{qs}^r = v_{qs}^r - \omega_r L_d i_{ds}^r - \omega_r \lambda_m^r, \tag{2.7a}$$

$$L_d \frac{\mathrm{d}i_{ds}^r}{\mathrm{d}t} + r_s i_{ds}^r = v_{ds}^r + \omega_r L_q i_{qs}^r, \tag{2.7b}$$

where $\boldsymbol{i}_{qd0s}^r = \boldsymbol{T}(\theta_r)\boldsymbol{i}_{abcs}$, $\boldsymbol{v}_{qd0s}^r = \boldsymbol{T}(\theta_r)\boldsymbol{v}_{abcs}$, $\omega_r = \dfrac{\mathrm{d}\theta_r}{\mathrm{d}t}$ and the rest of the terms are defined in Table 2.3.

The expression for the electromagnetic torque generated by PMSG is given by [72]

$$T_e = \frac{3}{2}\frac{P}{2}\left[\lambda_m^r i_{qs}^r + (L_d - L_q)\, i_{ds}^r i_{qs}^r\right]. \tag{2.8}$$

The electromagnetic torque in (2.8) is controlled to generate the maximum power from the wind turbine, which is detailed in the following sections.

The mechanical dynamics of the PMSG, whose rotor is connected to the wind turbine, is described by

$$T_e - T_{\text{tur}} = J\frac{2}{P}\frac{\mathrm{d}\omega_r}{\mathrm{d}t} + B_m\frac{2}{P}\omega_r \tag{2.9}$$

where $T_{\text{tur}} = \dfrac{P_{\text{tur}}}{\omega_r}$, and J and B_m are the combined inertia and the damping coefficient of the PMSG rotor and the turbine connected to it, respectively.

The PMSG is described in motor convention by its electrical and mechanical characteristics as represented by (2.7) to (2.9).

2.4 Maximum Power Extraction from a Variable-speed WECS

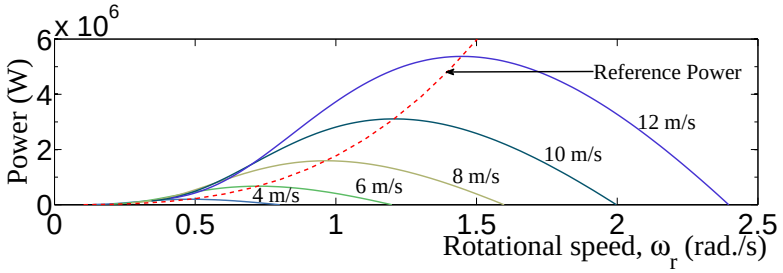

Fig. 2.5. Power-speed characteristics of the wind turbine characterized in Table 2.1 and the reference power calculated by the MPPT algorithm.

The power-speed characteristics of the wind turbine with the parameters listed in Table 2.1, for different speeds and at zero pitch angle is shown in Fig. 2.5. As mentioned before and illustrated in Fig. 2.5, for a given wind speed, P_{tur} is negligible at small rotor speed. Subsequent to an increase in the rotor speed, the power increases till it reaches a peak value corresponding to the peak of $C_p(\lambda)$, which occurs at a rotor speed that corresponds to λ_{opt}. As shown in Fig. 2.5, with the increase in wind speed, the rotor speed corresponding to the maximum power shifts towards a higher speed. Therefore, the rotor, based on (2.3), should run at a proportionally higher speed to keep $\lambda = \lambda_{\text{opt}}$. This, consequently, enables maximum power extraction at any wind speed.

The PMSG electromagnetic torque reference is defined as [2]

$$T_{e,\text{ref}} = -K_{\text{opt}}\omega_r^2, \tag{2.10}$$

where $K_{\text{opt}} = \dfrac{0.5\rho A r^3 C_p(\lambda_{\text{opt}})}{\lambda_{\text{opt}}^3}$ and λ_{opt} is the optimum λ at which the maximum power is extracted from wind. K_{opt} is calculated from the manufacturer's data. There is a negative sign in (2.10) as the PMSG dynamics are considered in motor convention. The solid lines in Fig. 2.5 represent the power extracted from wind by the turbine at various wind speeds and rotor rotational speeds. The dashed line represents the absolute value of the reference power calculated from the reference torque used in (2.10), that is, $P_{\text{ref}} = |T_{e,\text{ref}}|\omega_r = K_{\text{opt}}\omega_r^3$. As shown in Fig. 2.5, by imposing the machine torque based on (2.10), the reference power tracks the maxima in the power vs. rotor rotational speed plot at any wind speed. To verify the stability of the maximum power extraction strategy, the following two conditions are considered:

1. $\omega_r < \omega_{r,\text{opt}}$: Under this condition, based on Fig. 2.5,

$$P_{\text{tur}} > P_{\text{ref}}. \tag{2.11}$$

   This leads to acceleration of the wind turbine, resulting in increase of ω_r and the MPPT controller pushes the system towards the maximum power generation point.

2. $\omega_r > \omega_{r,\text{opt}}$: As an extension of the above description, under this condition

$$P_{\text{tur}} < P_{\text{ref}}. \tag{2.12}$$

   This leads to deceleration of the wind turbine, resulting in a decrease in ω_r and the MPPT controller pushes the system towards the maximum power generation point. In the above two conditions, $\omega_{r,\text{opt}}$ is the optimum rotor rotational speed at the maximum power point.

2.5 Generator-side Converter Control

The task of the generator-side converter is to control the PMSG torque to extract the maximum available power of the wind, except during startup. As discusssed in the previous section, to maximize the turbine power, the PMSG torque T_e should be controlled proportional to the square of the rotor speed, i.e., the control law in (2.10). To achieve this, a current control strategy is implemented to produce the required torque fomulated by (2.10).

The d-axis stator current of the PMSG, $i^r_{ds,\text{ref}}$, is controlled to zero to remove the coupling between q- and d-axis currents in the torque produced by the machine. Subsequently, (2.8) becomes

$$T_e = \frac{3}{2}\frac{P}{2}\lambda^r_m i^r_{qs}. \tag{2.13}$$

As shown in (2.13), under this strategy, the PMSG torque becomes a linear function of i^r_{qs}. Based on (2.10) and (2.13), the q-axis stator current reference, $i^r_{qs,\text{ref}}$, is defined by

$$i^r_{qs,\text{ref}} = -\frac{4}{3P\lambda^r_m} K_{\text{opt}} \omega_r^2, \tag{2.14}$$

which ensures that the maximum available power is extracted from the wind.

During startup or whenever there is a need to build turbine speed, the PMSG operates in motor mode with rated torque. That is, the q-axis stator current reference during startup is given by

$$i^r_{qs,\text{ref}} = \frac{4}{3P\lambda^r_m} T_{e,\text{rated}}, \tag{2.15}$$

where $T_{e,\text{rated}}$ is the rated torque of the PMSG. The aforementioned startup procedure is necessitated due to the dependance of both the turbine torque and the PMSG electromagnetic torque on the speed of the motor.

The model described in (2.7) can be written as

$$L_q \frac{\mathrm{d}i_{qs}^r}{\mathrm{d}t} + r_s i_{qs}^r = u_{qs}^r, \tag{2.16a}$$

$$L_d \frac{\mathrm{d}i_{ds}^r}{\mathrm{d}t} + r_s i_{ds}^r = u_{ds}^r, \tag{2.16b}$$

where,

$$u_{qs}^r = v_{qs}^r - \omega_r L_d i_{ds}^r - \omega_r \lambda_m^r, \tag{2.17a}$$

$$u_{ds}^r = v_{ds}^r + \omega_r L_q i_{qs}^r. \tag{2.17b}$$

Defining the proportional integral (PI) controllers for the q- and d-axis currents, the corresponding currents are regulated at their reference values. The controllers produce u_{qs}^r and u_{ds}^r, which are used to generate the q- and d-axis voltage references v_{qs}^r and v_{ds}^r using (2.17). These voltages are, then, generated at the terminals of the PMSG by the generator-side converter. The block diagram representation of the q- and d-axis current controllers are shown in Fig. 2.6.

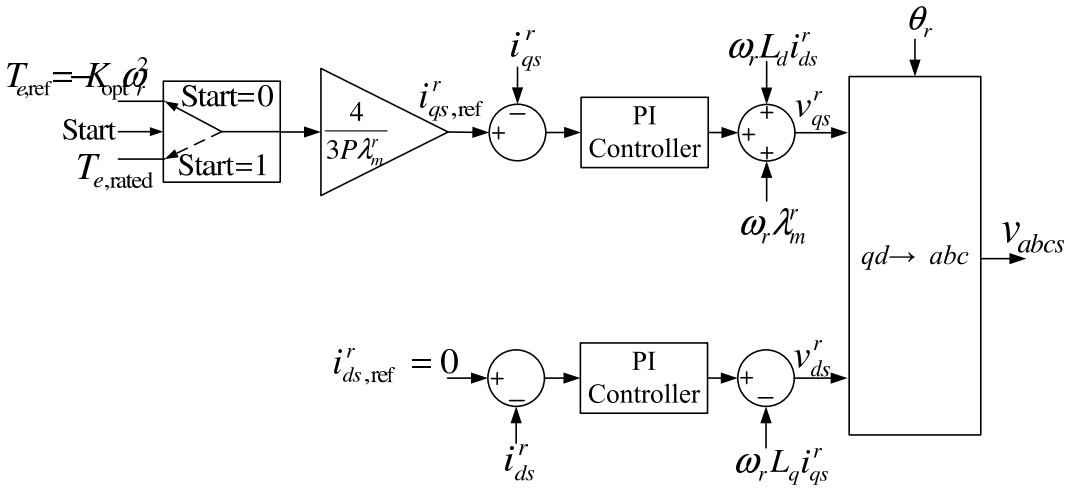

Fig. 2.6. Block diagram of the generator-side current controller

2.6 Grid-side Converter Control

The task of the grid-side converter is to control the power flow at the Point of Common Coupling (PCC).

The grid-side dynamics of the WECS of Fig. 2.1 is governed by

$$e_j = v_j - R_g i_j - L_g \frac{\mathrm{d}i_j}{\mathrm{d}t}. \tag{2.18}$$

Applying qd-transformation given by (2.6) to (2.18) with respect to the grid-reference frame results in

$$L_g \frac{\mathrm{d}i_q^e}{\mathrm{d}t} + R_g i_q^e = v_q^e - e_q^e - \omega_e L_g i_d^e, \tag{2.19a}$$

$$L_g \frac{\mathrm{d}i_d^e}{\mathrm{d}t} + R_g i_d^e = v_d^e - e_d^e + \omega_e L_g i_q^e, \tag{2.19b}$$

where

$$\boldsymbol{e}_{abc}^{\mathrm{T}} = V_s \left[\cos(\theta_e) \quad \cos\left(\theta_e - \frac{2\pi}{3}\right) \quad \cos\left(\theta_e + \frac{2\pi}{3}\right) \right], \tag{2.20}$$

$\boldsymbol{v}_{qd0}^e = \boldsymbol{T}(\theta_e)\boldsymbol{v}_{abc}$, $\boldsymbol{i}_{qd0}^e = \boldsymbol{T}(\theta_e)\boldsymbol{i}_{abc}$, e_q^e is the magnitude of the PCC phase voltages, $e_d^e = 0$, and $\omega_e = \dfrac{\mathrm{d}\theta_e}{\mathrm{d}t}$. Equation (2.19) can be re-written as

$$L_g \frac{\mathrm{d}i_q^e}{\mathrm{d}t} + R_g i_q^e = u_q^e, \tag{2.21a}$$

$$L_g \frac{\mathrm{d}i_d^e}{\mathrm{d}t} + R_g i_d^e = u_d^e, \tag{2.21b}$$

where

$$u_q^e = v_q^e - e_q^e - \omega_e L_g i_d^e, \tag{2.22a}$$

$$u_d^e = v_d^e - e_d^e + \omega_e L_g i_q^e. \tag{2.22b}$$

The active and reactive power at the PCC are given by

$$P_{\rm g} = \frac{3}{2} e_q^e i_q^e, \tag{2.23a}$$

$$Q_{\rm g} = -\frac{3}{2} e_q^e i_d^e. \tag{2.23b}$$

The q- and d-axis grid-side current references $i^e_{q,\rm ref}$ and $i^e_{d,\rm ref}$, respectively, are generated from (2.23). In (2.23), $P_{\rm g}$ is determined by appropriate control of the power electronic conversion system to transfer power generated by the wind turbine to the grid and $Q_{\rm g}$ is determined based on the power factor required at PCC.

The q- and d-axis grid-side currents are controlled at their respective references using PI controllers that are designed using (2.21). Similar to the generator-side control, the controller outputs are used to calculate the q- and d-axis voltages at the output of the grid-side inverter, i.e., v_q^e and v_d^e using (2.22), which are then generated by the inverter. The block diagram representation of the q- and d-axis current controllers are shown in Fig. 2.7.

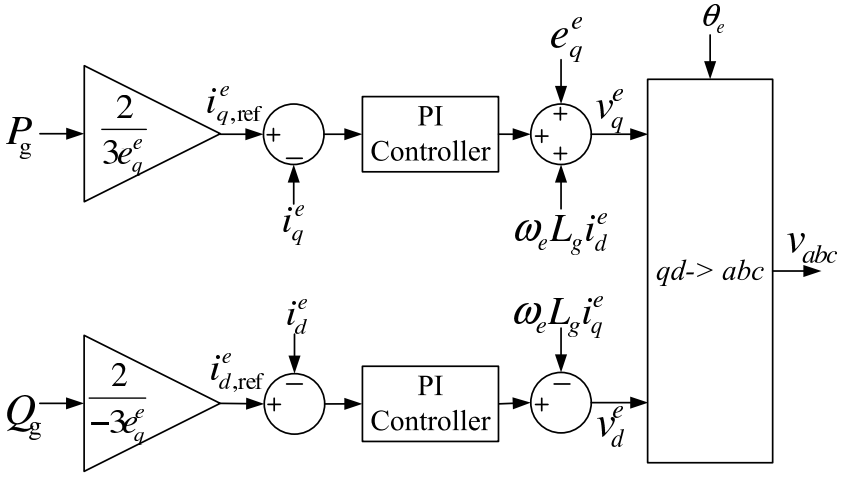

Fig. 2.7. Block diagram of the grid-side current controllers.

3. MODULATION AND MODELING OF MMC

The structure, modulation strategy, and state-space models of an MMC are developed and explored in detail in this chapter.

3.1 Structure and Principles of Operation

The circuit diagram of a three-phase MMC is depicted in Fig. 1.6. Each phase-leg of the MMC is comprised of two arms, i.e., an upper arm (represented by subscript "p") and a lower arm (represented by subscript "n"). Each arm comprises N series connected, nominally identical, half-bridge SMs, a series inductor L_o, and a resistor R_o. Each half-bridge SM consists of two series connected switches, connected in parallel to a capacitor $C_{\rm SM}$ and a resistor R_p. The resistor R_p is used to measure the voltage across the SM capacitor. Each SM of the MMC of Fig. 1.6 can provide two voltage levels at its terminal, i.e., zero or $v_{cy,k,j}, y \in \{p,n\}, k \in \{1,2,..\text{N}\}, j \in \{a,b,c\}$, depending on the state of its two complementary switches $S_{yk1,j}$ and $S_{yk2,j}$. Ideally, the average value of $v_{cy,k,j}$ is maintained at $\dfrac{V_{\rm dc}}{N}$, where $V_{\rm dc}$ is the MMC dc-link voltage. The following pairs of switching conditions represent the different states of the SM-k in arm-y of phase-j:

1. $S_{yk1,j} = 1$ and $S_{yk2,j} = 0$: ON-state or inserted,
2. $S_{yk1,j} = 0$ and $S_{yk2,j} = 1$: OFF-state or bypassed, and
3. $S_{yk1,j} = 0$ and $S_{yk2,j} = 0$: blocked-state.

The inductor L_o limits the short-circuit current of MMC and also removes the high-frequency harmonics from the arm currents. The resistor R_o models the effective series resistance (ESR) of the inductor.

3.2 Modulation Strategy

The proposed modulation strategy to generate the switching states of the SMs in each arm consists of three parts: (i) the SM modulation index generator, (ii) an SM capacitor voltage balancing algorithm, and (iii) a PWM signal generator. The SM modulation index generator generates N temporary modulation indices for each arm, i.e., one for each SM. Based on the SM capacitor voltage balancing algorithm, the temporary modulation indices are assigned to a particular SM in the arm. The PWM signal generator compares the modulation index assigned to each SM in an arm with a triangular carrier, to generate the switching signals for each SM. The SM modulation index generator and the PWM signal generator are together termed as the distributed PWM (DPWM) strategy.

3.2.1 The SM Modulation Index Generator

The modulation reference waveforms of the upper and lower arms, which are used to generate the desired arm voltages, are given by

$$m_{p,j} = \frac{1 - m_j - m_{\text{cm}}}{2} - m_{\text{circ},j}, \tag{3.1a}$$

$$m_{n,j} = \frac{1 + m_j + m_{\text{cm}}}{2} - m_{\text{circ},j}, \tag{3.1b}$$

where m_j represents the fundamental component of the phase reference waveform, m_{cm} represents the common-mode component of the phase reference waveform, and $m_{\text{circ},j}$ is used to control the circulating current that will be explained in detail in the following chapters.

Based on the arm modulation reference waveforms, the proposed strategy keeps a certain number of SMs inserted, one SM under the PWM strategy in each sampling period while the rest of the SMs bypassed, in each arm. That is, the SM modulation index generator consists of the following three components:

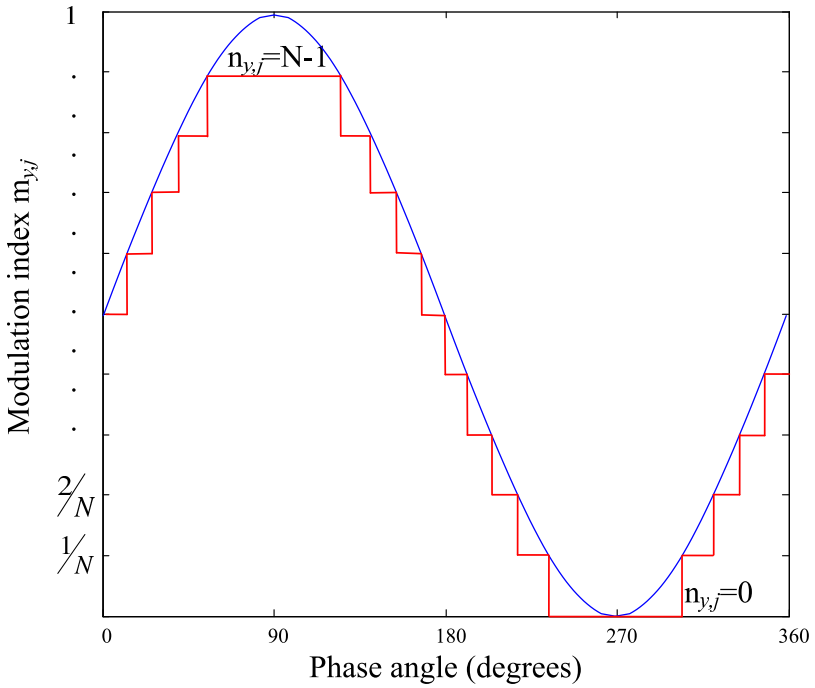

Fig. 3.1. Modulation index and the number of inserted SMs.

1. Number of SMs inserted in arm-y, phase-j is given by

$$n_{y,j} = \lfloor N m_{y,j} \rfloor, \tag{3.2}$$

where $\lfloor . \rfloor$ denotes the floor operation. An illustration of the number of SMs inserted is provided in Fig. 3.1. At any instant, $n_{y,j}$ SMs, determined by (3.2), are inserted in each arm and the corresponding temporary modulation indices are $m_{y,k,j,\text{temp}} = 1$ for $k \in [1, 2, .., n_{y,j}]$.

2. The modulation index of the SM that is under the PWM strategy is

$$m_{\text{PWM},y,j} = N m_{y,j} - n_{y,j}. \tag{3.3}$$

The temporary modulation index described by (3.3), is applied to one of the SMs in the arm-y, phase-j. Let $m_{y,(1+n_{y,j}),j,\text{temp}} = m_{\text{PWM},y,j}$.

3. The rest of the SMs in the arm-y, phase-j are bypassed. That is, $m_{y,k,j,\text{temp}} = 0$ for $k \in [n_{y,j} + 2, ..., N]$.

3.2.2 The SM Capacitor Voltage Balancing Algorithm

Mapping of the N temporary modulation indices to the SMs of each arm is performed based on the proposed SM capacitor voltage balancing algorithm. The proposed algorithm relies on (i) the direction of the arm current, (ii) the difference in the number of inserted SMs in each arm, within the present and the previous sampling period, and (iii) the measured SM capacitor voltages. The direction of the arm current, $i_{y,j}$, determines whether the inserted SMs in each arm are being charged ($i_{y,j} > 0$) or discharged ($i_{y,j} < 0$). The difference in the number of inserted SMs in the present and the previous sampling period is given by

$$\Delta n_{y,j}[k] = n_{y,j}[k] - n_{y,j}[k-1], \tag{3.4}$$

where $n_{y,j}[k]$ and $n_{y,j}[k-1]$ represent the present and previous sample of $n_{y,j}$, respectively. Based on the status of $\Delta n_{y,j}[k]$ from (3.4), the following decision is made:

1. If $\Delta n_{y,j}[k] > 0$, from the bypassed SMs, $\Delta n_{y,j}[k]$ SMs with the highest (lowest) capacitor voltages are inserted, if $i_{y,j} < 0$ ($i_{y,j} \geq 0$).

2. If $\Delta n_{y,j}[k] < 0$, from the inserted SMs and the SM under the PWM strategy, $\Delta n_{y,j}[k]$ SMs with the lowest (highest) capacitor voltages are bypassed, if $i_{y,j} < 0$ ($i_{y,j} \geq 0$). If the SM under the PWM strategy in the previous sampling period is bypassed, then the SM in the inserted state in the previous and present sampling periods and with the next lowest (highest) capacitor voltage is assigned as the PWM module when $i_{y,j} < 0$ ($i_{y,j} \geq 0$).

3. If $\Delta n_{y,j}[k] = 0$ and there is no change in the number of inserted SMs, then, subsequent to every $N_{\text{shift}}/2$ samples, the PWM module is alternatively interchanged with an inserted or a bypassed SM. Defining T_s as the sampling time,

$T_{\text{sc}} = N_{\text{shift}} T_s$, and Δt as the remainder of t divided by T_{sc}. Then, at $\Delta t = T_{\text{sc}}/2$, the PWM module is interchanged with a bypassed SM which has the highest (lowest) capacitor voltage, if $i_{y,j} < 0$ ($i_{y,j} \geq 0$). Similarly, at $\Delta t = T_{\text{sc}}$, the PWM module is interchanged with an inserted SM which has the lowest (highest) capacitor voltage, if $i_{y,j} < 0$ ($i_{y,j} \geq 0$).

The rest of the SMs in arm-y of phase-j continue to operate with their previous states, thereby, the remaining temporary modulation indices are automatically mapped to the SMs in arm-y of phase-j.

One of the key features of the sorting algorithm in the proposed SM capacitor voltage balancing algorithm is the requirement to determine only the inserted and bypassed SMs with the maximum and minimum capacitor voltages, unlike the conventional SM capacitor voltage balancing algorithm in [38] which requires the sorting of all the capacitor voltages. Moreover, unlike the SM capacitor voltage balancing algorithm in [38, 40, 43–46] where unnecessary switching transitions may occur to balance the SM capacitor voltages, the proposed SM capacitor voltage balancing algorithm requires only a minimum number of switches to change their state at any instant, based largely on the modulation reference waveform of the arm. The minimization of the number of switches changing their state at any instant in the proposed SM capacitor voltage balancing algorithm, reduces EMI and the switching frequency. Consequently, the switching losses are reduced. The implementation procedure of the proposed SM capacitor voltage balancing algorithm is summarized in Fig. 3.2, assuming a smooth change in the modulation index, i.e., the absolute maximum value of $\Delta n_{y,j}[k]$, $|\Delta n_{y,j_{\max}}| = 1$. In Fig. 3.2, m(Max On), m(2$^{\text{nd}}$ Max On), m(Max Off), m(Min On), m(2$^{\text{nd}}$ Min On) and m(Min Off) represent the modulation indices assigned to the inserted SM with the maximum capacitor voltage, inserted SM with the second highest capacitor voltage, the bypassed SM with the maximum capacitor voltage, the inserted SM with the minimum capacitor voltage, the inserted SM with the second lowest capacitor voltage, and the bypassed SM with the minimum capacitor voltage, respectively, in the present sample. Similarly, m(earlier PWM) represents

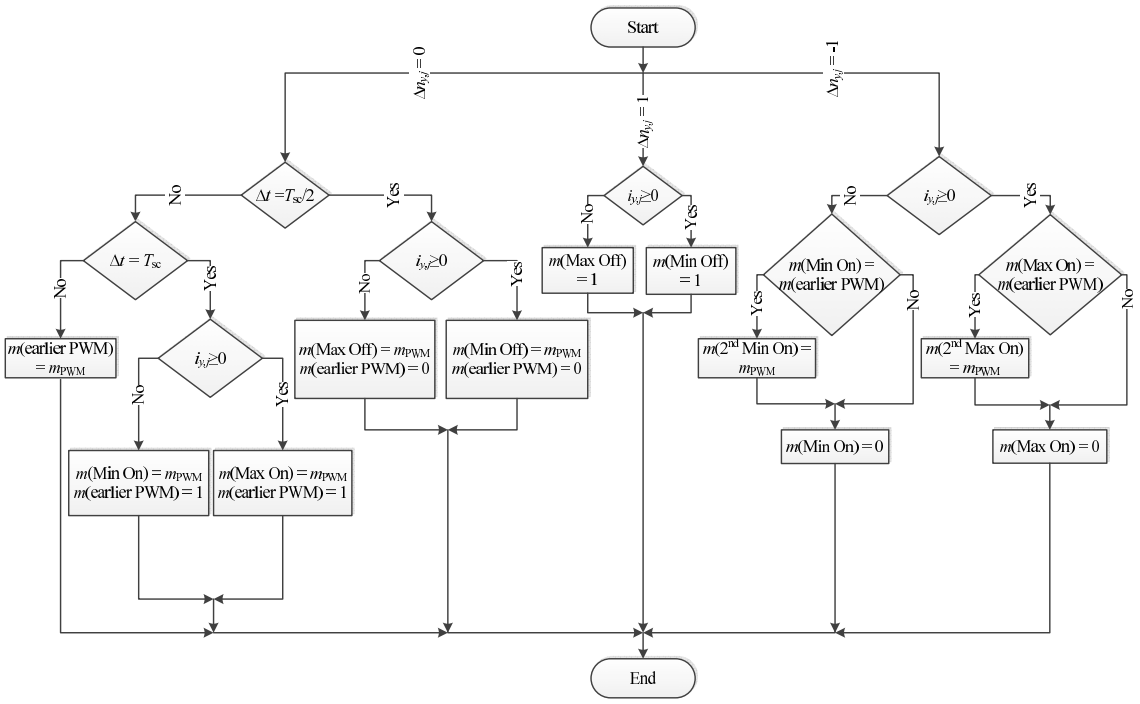

Fig. 3.2. Flowchart of the proposed DPWM strategy.

the modulation index assigned to the SM under the PWM strategy in the previous sample.

3.2.3 The PWM Signal Generator

The PWM signal generator compares the individual modulation indices of the SMs with a triangular carrier of frequency f_c and varying between 0 and 1, to generate the switching signals for each individual SM. The triangular carriers of the upper and lower arms are 180° out of phase to reduce the dc link voltage ripple and the output current harmonics.

The overall implementation process of the DPWM strategy and the SM capacitor voltage balancing algorithm is shown in Fig. 3.3. The proposed SM modulation index generator and the SM capacitor voltage balancing algorithm are implemented in the digital signal processor (DSP) with a sampling time of T_s. The sorting algorithm, which is a part of the SM capacitor voltage balancing algorithm, is implemented with

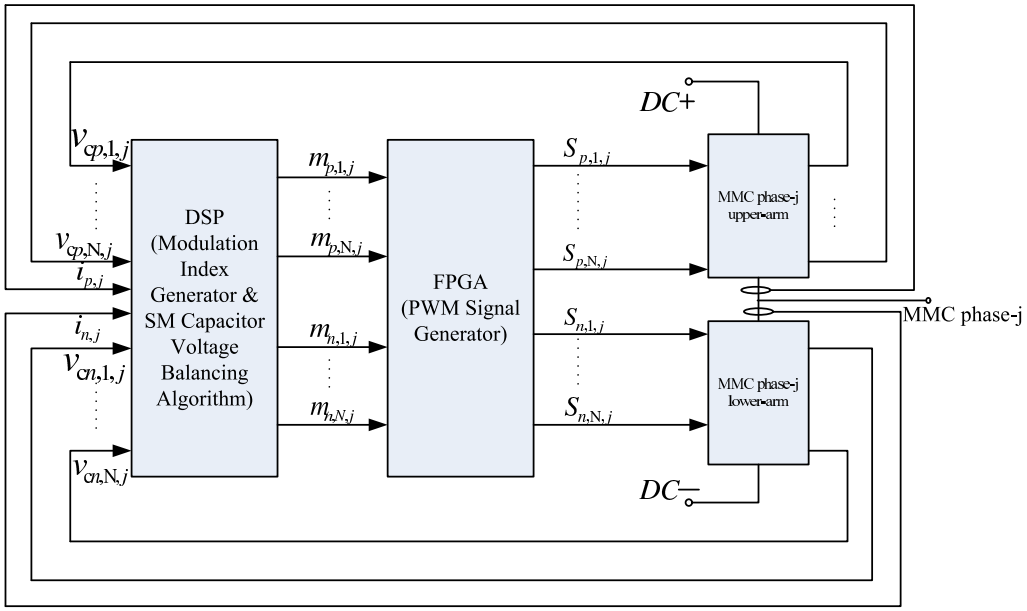

Fig. 3.3. Implementation of the proposed DPWM strategy and SM capacitor voltage balancing algorithm.

a sampling time of $T_{s,\text{cap}}$. The sampling times T_s and $T_{s,\text{cap}}$ may or may not be the same. The choice of $T_{s,\text{cap}}$ depends upon the computational capability of the DSP. The PWM signal generator is implemented in the field-programmable gate array (FPGA), which helps to maintain the sampling times T_s and $T_{s,\text{cap}}$ independent of the carrier frequency f_c. The proposed DPWM strategy and the SM capacitor voltage balancing algorithm are together termed as the proposed modulation strategy, hereafter.

3.2.4 Computational Burden

The claim of reduced computational burden imposed by the proposed SM capacitor voltage balancing algorithm over the existing algorithms in [35, 39], is verified in this section.

The following terms are defined to compare the computational burden between the aforementioned algorithms: (i) $W_{\text{sort},pu}$ is the computational burden imposed by the sorting algorithm to determine the SM with maximum/minimum capacitor voltages,

(ii) $W_{c,pu}$ is the computational burden imposed by a comparator and an assignment operation, and (iii) $T_{s,\text{PWM}}$ is the sampling time used to implement the PWM strategy in FPGA. Typically, $T_{s,\text{cap}} \gg T_{s,\text{PWM}}$ and $T_s \gg T_{s,\text{PWM}}$.

The sorting algorithm in the proposed SM capacitor voltage balancing algorithm imposes $W_{\text{sort},pu}$ computational burden within every $T_{s,\text{cap}}$. The rest of the proposed SM capacitor voltage balancing algorithm imposes $6W_{c,pu}$ computational burden in the worst-case scenario within every T_s. The worst-case scenario occurs in the following conditions:

1. $\Delta n_{y,j}(k) = -1$, $i_{y,j} \geq 0$, and $m(\text{Max On}) = m(\text{earlier PWM})$,

2. $\Delta n_{y,j}(k) = -1$, $i_{y,j} < 0$, and $m(\text{Min On}) = m(\text{earlier PWM})$.

Consequently, the worst-case computational burden imposed by the proposed SM capacitor voltage balancing algorithm is $W_{\text{sort},pu} + 6W_{c,pu}\dfrac{T_{s,\text{cap}}}{T_s}$ within every $T_{s,\text{cap}}$. Applying a similar analysis, the SM capacitor voltage balancing algorithms in [35] and [39] impose $(W_{\text{sort},pu} + 4W_{c,pu})\dfrac{T_{s,\text{cap}}}{T_{s,\text{PWM}}}$ and $W_{\text{con}}+W_{\text{sort},pu}+7W_{c,pu}\dfrac{T_{s,\text{cap}}}{T_{s,\text{PWM}}}$ computational burden within every $T_{s,\text{cap}}$, respectively. The computational burden imposed by the additional voltage controller in the algorithm in [39] is W_{con} within every $T_{s,\text{cap}}$. Therefore, the proposed SM capacitor voltage algorithm imposes much lesser computational burden when compared to the corresponding algorithms in [35, 39] since $T_{s,\text{cap}} \gg T_{s,\text{PWM}}$ and $T_s \gg T_{s,\text{PWM}}$.

3.2.5 SM Capacitor Voltage Ripple

The summation of the SM capacitor voltage ripple in each arm is independent of the SM capacitor voltage balancing algorithm as it depends upon the power processed by each arm. However, the individual SM capacitor voltage ripple in each arm depends upon the SM capacitor voltage balancing algorithm. In the proposed strategy, the individual SM capacitor voltage ripple is a function of $T_{s,\text{cap}}$, T_s, and T_{sc}. As $T_{s,\text{cap}}$, T_s, and T_{sc} are reduced, the individual SM capacitor voltage ripple is reduced, but

the computational burden imposed is increased as shown in Section 3.2.4. Compared to the SM capacitor voltage balancing algorithm in [38], any of the algorithms that impose a reduced switching frequency and computational burden will result in a larger SM capacitor voltage ripple.

3.3 Dynamic Model

In this section, a generalized dynamic model describing the dynamics of the MMC is developed. The developed model is used to derive the advanced state-space model and the approximate per-phase state-space model of the MMC, which are obtained by averaging the states and the inputs over each switching period.

In the MMC of Fig. 1.6, the upper-arm and lower-arm currents of phase-j, i.e., $i_{p,j}$ and $i_{n,j}$ are expressed by [34]:

$$i_{p,j} = i_{\text{circ},j} + \frac{i_j}{2}, \tag{3.5a}$$

$$i_{n,j} = i_{\text{circ},j} - \frac{i_j}{2}, \tag{3.5b}$$

where $i_{\text{circ},j}$ represents the circulating current within phase-leg-j and i_j is the ac-side phase-j current. The circulating current, based on (3.5), is given by

$$i_{\text{circ},j} = \frac{i_{p,j} + i_{n,j}}{2}. \tag{3.6}$$

The mathematical equations that govern the dynamic behavior of the MMC phase-j are

$$\frac{V_{\text{dc}}}{2} - v_{p,j} = L_o \frac{\mathrm{d}i_{p,j}}{\mathrm{d}t} + R_o i_{p,j} + v_j + v_{\text{cm}}, \tag{3.7a}$$

$$\frac{V_{\text{dc}}}{2} - v_{n,j} = L_o \frac{\mathrm{d}i_{n,j}}{\mathrm{d}t} + R_o i_{n,j} - v_j - v_{\text{cm}}, \tag{3.7b}$$

where v_j and v_{cm} represent the fundamental and the common-mode components of the MMC phase-j voltage with respect to the fictitious dc mid-point, and $v_{p,j}$ and $v_{n,j}$

represent the upper-arm and lower-arm voltages of the MMC phase-j, respectively, as shown in Fig. 1.6. Subtracting (3.7b) from (3.7a) and substituting for $i_{p,j}$ and $i_{n,j}$ from (3.5), the dynamics of the phase current is expressed by

$$\frac{L_o}{2}\frac{\mathrm{d}i_j}{\mathrm{d}t} + \frac{R_o}{2}i_j = \frac{v_{n,j} - v_{p,j}}{2} - v_j - v_{\mathrm{cm}}. \tag{3.8}$$

Furthermore, adding (3.7a) with (3.7b) and substituting for $i_{\mathrm{circ},j}$ from (3.6), the internal dynamics of the MMC circulating current is expressed by

$$L_o\frac{\mathrm{d}i_{\mathrm{circ},j}}{\mathrm{d}t} + R_o i_{\mathrm{circ},j} = \frac{V_{\mathrm{dc}}}{2} - \frac{v_{n,j} + v_{p,j}}{2}. \tag{3.9}$$

The upper-arm and lower-arm voltages of the MMC phase-j are also described by

$$v_{p,j} = \sum_{k=1}^{N} S_{pk1,j} v_{cp,k,j} + v_{\mathrm{swd},p,j}, \tag{3.10a}$$

$$v_{n,j} = \sum_{k=1}^{N} S_{nk1,j} v_{cn,k,j} + v_{\mathrm{swd},n,j}, \tag{3.10b}$$

where $v_{\mathrm{swd},p,j}$ and $v_{\mathrm{swd},n,j}$ are the IGBT/diode voltage drops of the upper and lower arms, respectively. Under the assumption of the successful operation of the SM capacitor voltage balancing algorithm, the following approximation is valid:

$$v_{cy,k,j} \approx \frac{1}{N}\sum_{k_1=1}^{N} v_{cy,k_1,j} = v_{cy,j}, \forall y \in \{p,n\}, \forall k \in \{1,2,..,N\}, \forall j \in \{a,b,c\}. \tag{3.11}$$

Substituting for $v_{cp,k,j}$ and $v_{cn,k,j}$ from (3.11) in (3.10), the following expressions are obtained:

$$v_{p,j} \approx n_{p,j} v_{cp,j} + v_{\mathrm{swd},p,j}, \tag{3.12a}$$

$$v_{n,j} \approx n_{n,j} v_{cn,j} + v_{\mathrm{swd},n,j}, \tag{3.12b}$$

Fig. 3.4. IGBT/Diode model.

Table 3.1.
State of IGBT/diode

Switch Status	$i_{y,j}$	ON Device
$S_{yk1,j}=1, S_{yk2,j}=0$	≥ 0	upper diode
	<0	upper IGBT
$S_{yk1,j}=0, S_{yk2,j}=1$	≥ 0	lower IGBT
	<0	lower diode
$S_{yk1,j}=0, S_{yk2,j}=0$	≥ 0	upper diode
	<0	lower diode

where $n_{p,j}$ and $n_{n,j}$ are the number of ON-state SMs in the upper and lower arms, respectively. Furthermore, substituting for $v_{p,j}$ and $v_{n,j}$ from (3.12) in (3.8) and (3.9), the following expressions are obtained:

$$\frac{L_o}{2}\frac{\mathrm{d}i_j}{\mathrm{d}t}+\frac{R_o}{2}i_j=\frac{n_{n,j}v_{cn,j}+v_{\mathrm{swd},n,j}-n_{p,j}v_{cp,j}-v_{\mathrm{swd},p,j}}{2}-v_j-v_{\mathrm{cm}}, \tag{3.13a}$$

$$L_o\frac{\mathrm{d}i_{\mathrm{circ},j}}{\mathrm{d}t}+R_o i_{\mathrm{circ},j}=\frac{V_{\mathrm{dc}}}{2}-\frac{n_{n,j}v_{cn,j}+v_{\mathrm{swd},n,j}+n_{p,j}v_{cp,j}+v_{\mathrm{swd},p,j}}{2}. \tag{3.13b}$$

The IGBT/diode models are shown in Fig. 3.4. The switch status, S, for the diode in Fig. 3.4 is based on the direction of the current. That is, $S=1$ if $i_{\mathrm{d}}\geq 0$ and $S=0$ if $i_{\mathrm{d}}<0$. The ON-state voltage drop across an IGBT/diode is given by

$$v_t=i_tR_t+V_t, \forall t\in\{\mathrm{sw,d}\} \tag{3.14}$$

where i_t is the device current, R_t is the ON-state resistive drop of the device, V_t is the ON-state voltage drop under zero device current, and sw and d in the subscript refer to IGBT and diode, respectively. The OFF-state resistance of IGBT/diode is

assumed to be infinite. When $S_{yk1,j} = 1, i_{y,j} < 0$, the upper IGBT of SM-$k$ conducts. Similarly, the other conditions are summarized in Table 3.1. With the aforesaid description and using (3.14), the arm-y phase-j IGBT/diode voltage drops are given by

$$v_{\mathrm{swd},y,j} = \begin{cases} \sum_{k=1}^{N} \{(V_{\mathrm{d}} + i_{y,j}R_{\mathrm{d}})\, S_{yk1,j} + (V_{\mathrm{sw}} + i_{y,j}R_{\mathrm{sw}})\, S_{yk2,j} \\ \qquad + (V_{\mathrm{d}} + i_{y,j}R_{\mathrm{d}})\,(1 - S_{yk1,j})\,(1 - S_{yk2,j})\}\,, & \text{if } i_{y,j} \geq 0 \\ \sum_{k=1}^{N} \{(-V_{\mathrm{sw}} + i_{y,j}R_{\mathrm{sw}})\, S_{yk1,j} + (-V_{\mathrm{d}} + i_{y,j}R_{\mathrm{d}})\, S_{yk2,j} \\ \qquad + (-V_{\mathrm{d}} + i_{y,j}R_{\mathrm{d}})\,(1 - S_{yk1,j})\,(1 - S_{yk2,j})\}\,, & \text{if } i_{y,j} < 0 \end{cases}. \tag{3.15}$$

The terms with $(1 - S_{yk1,j})\,(1 - S_{yk2,j})$ arise due to the impact of the imposed dead time. The arm-y phase-j IGBT/diode voltage drops in (3.15) can also be rewritten as

$$\begin{aligned} v_{\mathrm{swd},y,j} = \sum_{k=1}^{N} \{(V_{\mathrm{d}} + i_{y,j}R_{\mathrm{d}})\,(S_{yk1,j} + (1 - S_{yk1,j})\,(1 - S_{yk2,j})) + (V_{\mathrm{sw}} + i_{y,j}R_{\mathrm{sw}})\, S_{yk2,j}\} \\ \times \left(\frac{1 + \mathrm{sgn}\,(i_{y,j})}{2}\right) \\ + \sum_{k=1}^{N} \{(i_{y,j}R_{\mathrm{sw}} - V_{\mathrm{sw}})\, S_{yk1,j} + (i_{y,j}R_{\mathrm{d}} - V_{\mathrm{d}})\,(S_{yk2,j} + (1 - S_{yk1,j})\,(1 - S_{yk2,j}))\} \\ \times \left(\frac{1 - \mathrm{sgn}\,(i_{y,j})}{2}\right), \end{aligned} \tag{3.16}$$

where

$$\mathrm{sgn}\,(i_{y,j}) = \begin{cases} 1 & \text{if } i_{y,j} \geq 0 \\ -1 & \text{if } i_{y,j} < 0 \end{cases}. \tag{3.17}$$

Substituting for $n_{y,j}$ as the number SMs turned ON in arm-y phase-j of the MMC in (3.16), the following expressions are obtained:

$$v_{\text{swd},y,j} = \left\{n_{y,j}\left(V_{\text{d}} + R_{\text{d}} i_{y,j}\right) + \left(N - n_{y,j}\right)\left(V_{\text{sw}} + R_{\text{sw}} i_{y,j}\right)\right\}\left(\frac{1+\text{sgn}\left(i_{y,j}\right)}{2}\right) + \left\{\left(N - n_{y,j}\right)\left(-V_{\text{d}} + R_{\text{d}} i_{y,j}\right) + n_{y,j}\left(-V_{\text{sw}} + R_{\text{sw}} i_{y,j}\right)\right\}\left(\frac{1-\text{sgn}\left(i_{y,j}\right)}{2}\right), \quad y \in \{p, n\}. \tag{3.18}$$

The capacitor voltage of each SM in the MMC is modeled by the power processed by the SM capacitors in each arm. The power processed by the SM capacitors in each arm is given by

$$p_{p,j} = \left(v_{p,j} - v_{\text{swd},p,j}\right) i_{p,j} = n_{p,j} v_{cp,j} i_{p,j}, \tag{3.19a}$$

$$p_{n,j} = \left(v_{n,j} - v_{\text{swd},n,j}\right) i_{n,j} = n_{n,j} v_{cn,j} i_{n,j}. \tag{3.19b}$$

The power processed by the SM capacitors in each arm of the MMC can also be expressed as

$$p_{p,j} = \sum_{k=1}^{N}\left(\frac{\text{d}\left(\frac{1}{2}C_{\text{SM}} v_{cp,k,j}^2\right)}{\text{d}t} + \frac{v_{cp,k,j}^2}{R_p}\right) \approx \frac{\text{d}\left(\frac{N}{2}C_{\text{SM}} v_{cp,j}^2\right)}{\text{d}t} + N\frac{v_{cp,j}^2}{R_p} \approx N C_{\text{SM}} v_{cp,j}\frac{\text{d}v_{cp,j}}{\text{d}t} + N\frac{v_{cp,j}^2}{R_p}, \tag{3.20a}$$

$$p_{n,j} = \sum_{k=1}^{N}\left(\frac{\text{d}\left(\frac{1}{2}C_{\text{SM}} v_{cn,k,j}^2\right)}{\text{d}t} + \frac{v_{cn,k,j}^2}{R_p}\right) \approx \frac{\text{d}\left(\frac{N}{2}C_{\text{SM}} v_{cn,j}^2\right)}{\text{d}t} + N\frac{v_{cn,j}^2}{R_p} \approx N C_{\text{SM}} v_{cn,j}\frac{\text{d}v_{cn,j}}{\text{d}t} + N\frac{v_{cn,j}^2}{R_p}. \tag{3.20b}$$

Based on (3.19) and (3.20), the dynamics of the SM capacitor voltages is expressed by

$$NC_{\mathrm{SM}}\frac{\mathrm{d}v_{cp,j}}{\mathrm{d}t}+N\frac{v_{cp,j}}{R_p}=i_{p,j}n_{p,j}, \tag{3.21a}$$

$$NC_{\mathrm{SM}}\frac{\mathrm{d}v_{cn,j}}{\mathrm{d}t}+N\frac{v_{cn,j}}{R_p}=i_{n,j}n_{n,j}. \tag{3.21b}$$

Equations (3.5), (3.13), (3.18), and (3.21) provide the generalized dynamic model of the MMC.

Applying the averaging operator over one switching period to (3.13) and (3.21) results in

$$\frac{L_o}{2}\frac{\mathrm{d}i_j}{\mathrm{d}t}+\frac{R_o}{2}i_j=\frac{\tilde{n}_{n,j}v_{cn,j}+\tilde{v}_{\mathrm{swd},n,j}-\tilde{n}_{p,j}v_{cp,j}-\tilde{v}_{\mathrm{swd},p,j}}{2}-\tilde{v}_j-\tilde{v}_{\mathrm{cm}}, \tag{3.22a}$$

$$L_o\frac{\mathrm{d}i_{\mathrm{circ},j}}{\mathrm{d}t}+R_oi_{\mathrm{circ},j}=\frac{V_{\mathrm{dc}}}{2}-\frac{\tilde{n}_{n,j}v_{cn,j}+\tilde{v}_{\mathrm{swd},n,j}+\tilde{n}_{p,j}v_{cp,j}+\tilde{v}_{\mathrm{swd},p,j}}{2}, \tag{3.22b}$$

$$\frac{\mathrm{d}v_{cp,j}}{\mathrm{d}t}+\frac{v_{cp,j}}{R_pC_{\mathrm{SM}}}=\frac{i_{p,j}}{NC_{\mathrm{SM}}}\tilde{n}_{p,j}, \tag{3.22c}$$

$$\frac{\mathrm{d}v_{cn,j}}{\mathrm{d}t}+\frac{v_{cn,j}}{R_pC_{\mathrm{SM}}}=\frac{i_{n,j}}{NC_{\mathrm{SM}}}\tilde{n}_{n,j}, \tag{3.22d}$$

where $\tilde{x}$ represents the averaged value of variable x over one switching period, and

$$\begin{aligned}\tilde{v}_{\mathrm{swd},y,j}=&\left\{\tilde{n}_{y,j}\left(V_{\mathrm{d}}+R_{\mathrm{d}}i_{y,j}\right)+\left(N-\tilde{n}_{y,j}\right)\left(V_{\mathrm{sw}}+R_{\mathrm{sw}}i_{y,j}\right)\right\}\left(\frac{1+\mathrm{sgn}\left(i_{y,j}\right)}{2}\right)\\&+\left\{\left(N-\tilde{n}_{y,j}\right)\left(-V_{\mathrm{d}}+R_{\mathrm{d}}i_{y,j}\right)+\tilde{n}_{y,j}\left(-V_{\mathrm{sw}}+R_{\mathrm{sw}}i_{y,j}\right)\right\}\left(\frac{1-\mathrm{sgn}\left(i_{y,j}\right)}{2}\right),\\&y\in\{p,n\}.\end{aligned} \tag{3.23}$$

Assuming a well-designed converter with appropriate sizing of the SM capacitors and arm inductors, in (3.22) and (3.23), the following approximations are valid:

$$v_{cp,j}\approx\tilde{v}_{cp,j}, \tag{3.24a}$$

$$v_{cn,j}\approx\tilde{v}_{cn,j}, \tag{3.24b}$$

$$i_{p,j} \approx \tilde{i}_{p,j}, \tag{3.24c}$$

$$i_{n,j} \approx \tilde{i}_{n,j}, \tag{3.24d}$$

$$i_j \approx \tilde{i}_j, \tag{3.24e}$$

$$i_{\text{circ},j} \approx \tilde{i}_{\text{circ},j}. \tag{3.24f}$$

Based on the DPWM strategy,

$$\tilde{n}_{y,j} = N m_{y,j}, y \in \{p, n\}. \tag{3.25}$$

However, the impact of dead time is not considered in (3.25).

The change in state of the switch in SM-k of arm-y phase-j of the MMC, $S_{ykl,j}, l \in \{1, 2\}$, is represented by $S_{ykl,j}$: initial state $\rightarrow$ final state. When $S_{yk1,j} : 0 \rightarrow 1$ and $S_{yk2,j} : 1 \rightarrow 0$, the lower switch is first turned OFF before turning ON the upper switch of SM-k to avoid shoot-through problems. Similarly, when $S_{yk1,j} : 1 \rightarrow 0$ and $S_{yk2,j} : 0 \rightarrow 1$, the upper switch is first turned OFF first before turning ON the lower switch of SM-k. The delay in turning ON the lower (upper) switch after turning OFF the upper (lower) switch is called the dead time and is indicated by t_{d}. When $i_{y,j} > 0$, $S_{yk1,j} : 0 \rightarrow 1$ and $S_{yk2,j} : 1 \rightarrow 0$, then there will be no impact of the dead time on the number of SMs in ON-state as defined by (3.25). The aforesaid is true as there is immediate transfer of current from the lower IGBT to the upper diode of SM-k as soon as the lower switch is turned OFF. Similarly, when $i_{y,j} < 0$, $S_{yk1,j} : 1 \rightarrow 0$ and $S_{yk2,j} : 0 \rightarrow 1$, there is immediate transfer of current from upper IGBT to lower diode of SM-k, resulting in no impact of the dead time on the number of SMs in ON-state. However, when $i_{y,j} > 0$, $S_{yk1,j} : 1 \rightarrow 0$ and $S_{yk2,j} : 0 \rightarrow 1$, and even after the upper switch is turned OFF, the current continues to flow through the upper diode of SM-k until the lower switch is turned ON. Similarly, when $i_{y,j} < 0$, $S_{yk1,j} : 0 \rightarrow 1$ and $S_{yk2,j} : 1 \rightarrow 0$, and even after the lower switch is turned OFF, the current continues to flow through the lower diode of SM-k until the upper switch is turned ON. In the aforementioned two scenarios, there is an impact of dead time on the number of SMs

in ON-state. Under the assumption of only one SM in PWM in each arm in every switching period that is true with the proposed modulation strategy, (3.25) can be modified to

$$\tilde{n}_{y,j} = Nm_{y,j} + \frac{t_{\mathrm{d}}}{T_{\mathrm{sw}}}\mathrm{sgn}\left(i_{y,j}\right). \tag{3.26}$$

Substituting for $\tilde{n}_{y,j}$ from (3.26) in (3.23) and re-arranging the terms, the following expression is obtained:

$$\begin{aligned}\tilde{v}_{\mathrm{swd},y,j} = {} & \frac{N}{2}\left\{\left(V_{\mathrm{d}} + V_{\mathrm{sw}}\right)\mathrm{sgn}\left(i_{y,j}\right) + \left(R_{\mathrm{d}} + R_{\mathrm{sw}}\right)i_{y,j}\right\} \\ & + \frac{N}{2}\left\{\left(V_{\mathrm{sw}} - V_{\mathrm{d}}\right) + \left(R_{\mathrm{sw}} - R_{\mathrm{d}}\right)\left|i_{y,j}\right|\right\}\left(1 - 2m_{y,j}\right) \\ & + \frac{t_{\mathrm{d}}}{T_{\mathrm{sw}}}\left\{\left(V_{\mathrm{d}} - V_{\mathrm{sw}}\right)\mathrm{sgn}\left(i_{y,j}\right) + \left(R_{\mathrm{d}} - R_{\mathrm{sw}}\right)i_{y,j}\right\}, y \in \{p, n\}. \end{aligned} \tag{3.27}$$

Substituting for $\tilde{n}_{p,j}$ and $\tilde{n}_{n,j}$ from (3.26), $i_{p,j}$ and $i_{n,j}$ from (3.5), and $\tilde{v}_{\mathrm{swd},y,j}$ from (3.27) in (3.22), the following state-space model is obtained:

$$\frac{\mathrm{d}}{\mathrm{d}t}\begin{pmatrix} i_j \\ i_{\mathrm{circ},j} \\ v_{cp,j} \\ v_{cn,j} \end{pmatrix} = \begin{pmatrix} -\dfrac{R_o}{L_o}i_j + \dfrac{N\left(m_{n,j}v_{cn,j} - m_{p,j}v_{cp,j}\right)}{L_o} - \dfrac{v_{\mathrm{eff,dm},j}}{L_o} \\ -\dfrac{R_o}{L_o}i_{\mathrm{circ},j} - \dfrac{N\left(m_{p,j}v_{cp,j} + m_{n,j}v_{cn,j}\right)}{2L_o} + \dfrac{v_{\mathrm{eff,cm},j}}{2L_o} \\ -\dfrac{v_{cp,j}}{R_pC_{\mathrm{SM}}} + \dfrac{m_{p,j}}{C_{\mathrm{SM}}}\left(\dfrac{i_j}{2} + i_{\mathrm{circ},j}\right) + \dfrac{t_{\mathrm{d}}}{NC_{\mathrm{SM}}T_{\mathrm{sw}}}\left|\dfrac{i_j}{2} + i_{\mathrm{circ},j}\right| \\ -\dfrac{v_{cn,j}}{R_pC_{\mathrm{SM}}} + \dfrac{m_{n,j}}{C_{\mathrm{SM}}}\left(i_{\mathrm{circ},j} - \dfrac{i_j}{2}\right) + \dfrac{t_{\mathrm{d}}}{NC_{\mathrm{SM}}T_{\mathrm{sw}}}\left|i_{\mathrm{circ},j} - \dfrac{i_j}{2}\right| \end{pmatrix}, \tag{3.28a}$$

$$v_{\mathrm{eff,dm},j} = 2\tilde{v}_j + 2\tilde{v}_{\mathrm{cm}} + \tilde{v}_{\mathrm{sw,dm},j} + v_{\mathrm{td},j}, \tag{3.28b}$$

$$v_{\mathrm{eff,cm},j} = V_{\mathrm{dc}} - \tilde{v}_{\mathrm{sw,cm},j} - v_{\mathrm{td},j}, \tag{3.28c}$$

$$\begin{aligned}\tilde{v}_{\mathrm{sw,dm},j} = {} & \frac{N}{2}\left[\left(V_{\mathrm{sw}} + V_{\mathrm{d}}\right)\left(\mathrm{sgn}\left(i_{p,j}\right) - \mathrm{sgn}\left(i_{n,j}\right)\right)\right. \\ & + \left(R_{\mathrm{sw}} + R_{\mathrm{d}}\right)i_j + 2\left(V_{\mathrm{sw}} - V_{\mathrm{d}}\right)\left(m_{n,j} - m_{p,j}\right) \\ & + \left(R_{\mathrm{sw}} - R_{\mathrm{d}}\right)\left\{\left(1 - 2m_{p,j}\right)\left|i_{p,j}\right| - \left(1 - 2m_{n,j}\right)\left|i_{n,j}\right|\right\}\Big] \\ & + \frac{t_{\mathrm{d}}}{T_{\mathrm{sw}}}\left[\left(V_{\mathrm{d}} - V_{\mathrm{sw}}\right)\left(\mathrm{sgn}\left(i_{p,j}\right) - \mathrm{sgn}\left(i_{n,j}\right)\right) + \left(R_{\mathrm{d}} - R_{\mathrm{sw}}\right)i_j\right], \end{aligned} \tag{3.28d}$$

$$\tilde{v}_{\mathrm{sw,cm},j} = \frac{N}{2}\left[\left(V_{\mathrm{sw}}+V_{\mathrm{d}}\right)\left(\mathrm{sgn}\left(i_{n,j}\right)+\mathrm{sgn}\left(i_{p,j}\right)\right)\right.$$
$$+2\left(R_{\mathrm{sw}}+R_{\mathrm{d}}\right)i_{\mathrm{circ},j}+2\left(V_{\mathrm{sw}}-V_{\mathrm{d}}\right)\left(1-m_{p,j}-m_{n,j}\right)$$
$$\left.+\left(R_{\mathrm{sw}}-R_{\mathrm{d}}\right)\left\{\left(1-2m_{p,j}\right)\left|i_{p,j}\right|+\left(1-2m_{n,j}\right)\left|i_{n,j}\right|\right\}\right]$$
$$+\frac{t_{\mathrm{d}}}{T_{\mathrm{sw}}}\left[\left(V_{\mathrm{d}}-V_{\mathrm{sw}}\right)\left(\mathrm{sgn}\left(i_{p,j}\right)+\mathrm{sgn}\left(i_{n,j}\right)\right)+2\left(R_{\mathrm{d}}-R_{\mathrm{sw}}\right)i_{\mathrm{circ},j}\right], \tag{3.28e}$$

$$v_{\mathrm{td},j} = \frac{t_{\mathrm{d}}}{T_{\mathrm{sw}}}\left(v_{\mathrm{cp},j}\mathrm{sgn}\left(i_{p,j}\right)+v_{\mathrm{cn},j}\mathrm{sgn}\left(i_{n,j}\right)\right). \tag{3.28f}$$

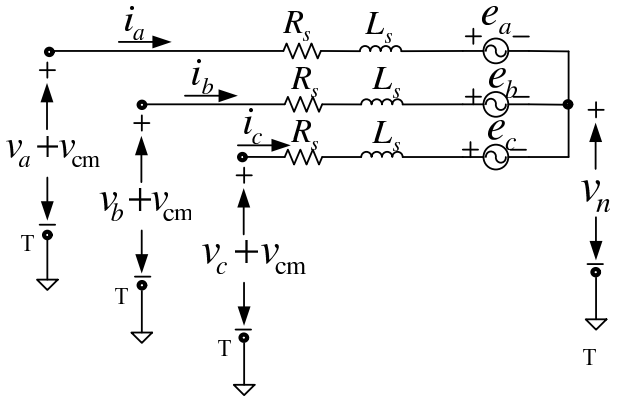

Fig. 3.5. Three-phase start-connected load.

Assume the load connected to the MMC of Fig. 1.6 is the three-phase star-connected load shown in Fig. 3.5. The load may represent a model of a machine or a grid. The phase-j load dynamics is given by

$$v_j + v_{\mathrm{cm}} = L_s\frac{\mathrm{d}i_j}{\mathrm{d}t} + R_s i_j + e_j + v_n. \tag{3.29}$$

Averaging (3.29) over one switching period yields

$$\tilde{v}_j + \tilde{v}_{\mathrm{cm}} = L_s\frac{\mathrm{d}i_j}{\mathrm{d}t} + R_s i_j + e_j + \tilde{v}_n, \tag{3.30}$$

where the load emf e_j is assumed to contain only low-frequency components. Summing (3.30) over the three phases yields

$$\tilde{v}_n = \tilde{v}_{\mathrm{cm}} + \frac{1}{3}\sum_{j=a,b,c} \tilde{v}_j, \tag{3.31}$$

since $\sum_{j=a,b,c} i_j = 0$ and $\sum_{j=a,b,c} e_j = 0$. Similarly, summing the $\dfrac{\mathrm{d}i_j}{\mathrm{d}t}$ in (3.28a) over the three phases yields

$$\tilde{v}_{\mathrm{cm}} + \frac{1}{3}\sum_{j=a,b,c} \tilde{v}_j = \frac{1}{6}\sum_{j=a,b,c} \left[N\left(m_{n,j}v_{\mathrm{cn},j} - m_{p,j}v_{\mathrm{cp},j}\right) - \tilde{v}_{\mathrm{sw,dm},j} - v_{\mathrm{td},j}\right]. \tag{3.32}$$

Equating (3.31) and (3.32), the following is obtained:

$$\tilde{v}_n = \frac{1}{6}\sum_{j=a,b,c} \left[N\left(m_{n,j}v_{\mathrm{cn},j} - m_{p,j}v_{\mathrm{cp},j}\right) - \tilde{v}_{\mathrm{sw,dm},j} - v_{\mathrm{td},j}\right]. \tag{3.33}$$

Substitute $\tilde{v}_n$ from (3.33) in (3.30) results in

$$\tilde{v}_j + \tilde{v}_{\mathrm{cm}} = L_s\frac{\mathrm{d}i_j}{\mathrm{d}t} + R_s i_j + e_j + \frac{1}{6}\sum_{j=a,b,c} \left[N\left(m_{n,j}v_{\mathrm{cn},j} - m_{p,j}v_{\mathrm{cp},j}\right) - \tilde{v}_{\mathrm{sw,dm},j} - v_{\mathrm{td},j}\right]. \tag{3.34}$$

Substituting $\tilde{v}_j + \tilde{v}_{\mathrm{cm}}$ from (3.34) in (3.28) and expanding the resulting equations to all the three phases results in

$$\frac{\mathrm{d}}{\mathrm{d}t}\begin{pmatrix} \boldsymbol{i}_{abc} \\ \boldsymbol{i}_{\mathrm{circ},abc} \\ \boldsymbol{v}_{\mathrm{cp},abc} \\ \boldsymbol{v}_{\mathrm{cn},abc} \end{pmatrix} = \begin{pmatrix} -\dfrac{R_{\mathrm{eq}}}{L_{\mathrm{eq}}}\boldsymbol{i}_{abc} + \dfrac{N\left(\boldsymbol{m}_{n,abc}\odot\boldsymbol{v}_{cn,abc} - \boldsymbol{m}_{p,abc}\odot\boldsymbol{v}_{cp,abc}\right)}{2L_{\mathrm{eq}}} - \dfrac{\boldsymbol{v}_{\mathrm{eff,dm},abc}}{2L_{\mathrm{eq}}} \\ -\dfrac{R_o}{L_o}\boldsymbol{i}_{\mathrm{circ},abc} - \dfrac{N\left(\boldsymbol{m}_{p,abc}\odot\boldsymbol{v}_{cp,abc} + \boldsymbol{m}_{n,abc}\odot\boldsymbol{v}_{\mathrm{cn},abc}\right)}{2L_o} + \dfrac{\boldsymbol{v}_{\mathrm{eff,cm},abc}}{2L_o} \\ \dfrac{\boldsymbol{m}_{p,abc}}{C_{\mathrm{SM}}}\odot\left(\dfrac{\boldsymbol{i}_{abc}}{2} + \boldsymbol{i}_{\mathrm{circ},abc}\right) + \dfrac{t_{\mathrm{d}}}{NC_{\mathrm{SM}}T_{\mathrm{sw}}}\left|\dfrac{\boldsymbol{i}_{abc}}{2} + \boldsymbol{i}_{\mathrm{circ},abc}\right| - \dfrac{\boldsymbol{v}_{cp,abc}}{R_pC_{\mathrm{SM}}} \\ \dfrac{\boldsymbol{m}_{n,abc}}{C_{\mathrm{SM}}}\odot\left(\boldsymbol{i}_{\mathrm{circ},abc} - \dfrac{\boldsymbol{i}_{abc}}{2}\right) + \dfrac{t_{\mathrm{d}}}{NC_{\mathrm{SM}}T_{\mathrm{sw}}}\left|\boldsymbol{i}_{\mathrm{circ},abc} - \dfrac{\boldsymbol{i}_{abc}}{2}\right| - \dfrac{\boldsymbol{v}_{cn,abc}}{R_pC_{\mathrm{SM}}} \end{pmatrix}, \tag{3.35a}$$

$$\boldsymbol{v}_{\mathrm{eff,dm},abc} = \frac{1}{3}\left[N\left(\boldsymbol{m}_{n,abc}^{\mathrm{T}}\boldsymbol{v}_{cn,abc} - \boldsymbol{m}_{p,abc}^{\mathrm{T}}\boldsymbol{v}_{cp,abc}\right) - \left(\tilde{\boldsymbol{v}}_{\mathrm{sw,dm},abc} + \boldsymbol{v}_{\mathrm{td},abc}\right)^{\mathrm{T}}\boldsymbol{1}\right]\boldsymbol{1} + \tilde{\boldsymbol{v}}_{\mathrm{sw,dm},abc} + \boldsymbol{v}_{\mathrm{td},abc} + 2\boldsymbol{e}_{abc}, \tag{3.35b}$$

$$\boldsymbol{v}_{\mathrm{eff,cm},abc} = V_{\mathrm{dc}} - \tilde{\boldsymbol{v}}_{\mathrm{sw,cm},abc} - \boldsymbol{v}_{\mathrm{td},abc}, \tag{3.35c}$$

$$\begin{aligned}\tilde{\boldsymbol{v}}_{\mathrm{sw,dm},abc} = \frac{N}{2}\big[&\left(V_{\mathrm{sw}} + V_{\mathrm{d}}\right)\left(\mathrm{sgn}\left(\boldsymbol{i}_{p,abc}\right) - \mathrm{sgn}\left(\boldsymbol{i}_{n,abc}\right)\right) \\ &+ \left(R_{\mathrm{sw}} + R_{\mathrm{d}}\right)\boldsymbol{i}_{abc} + 2\left(V_{\mathrm{sw}} - V_{\mathrm{d}}\right)\left(\boldsymbol{m}_{n,abc} - \boldsymbol{m}_{p,abc}\right) \\ &+ \left(R_{\mathrm{sw}} - R_{\mathrm{d}}\right)\left\{\left(1 - 2\boldsymbol{m}_{p,abc}\right)\odot\left|\boldsymbol{i}_{p,abc}\right| - \left(1 - 2\boldsymbol{m}_{n,abc}\right)\odot\left|\boldsymbol{i}_{n,abc}\right|\right\}\big] \\ &+ \frac{t_{\mathrm{d}}}{T_{\mathrm{sw}}}\left[\left(V_{\mathrm{d}} - V_{\mathrm{sw}}\right)\left(\mathrm{sgn}\left(\boldsymbol{i}_{p,abc}\right) - \mathrm{sgn}\left(\boldsymbol{i}_{n,abc}\right)\right) + \left(R_{\mathrm{d}} - R_{\mathrm{sw}}\right)\boldsymbol{i}_{abc}\right],\end{aligned} \tag{3.35d}$$

$$\begin{aligned}\tilde{\boldsymbol{v}}_{\mathrm{sw,cm},abc} = \frac{N}{2}\big[&\left(V_{\mathrm{sw}} + V_{\mathrm{d}}\right)\left(\mathrm{sgn}\left(\boldsymbol{i}_{n,abc}\right) + \mathrm{sgn}\left(\boldsymbol{i}_{p,abc}\right)\right) \\ &+ 2\left(R_{\mathrm{sw}} + R_{\mathrm{d}}\right)\boldsymbol{i}_{\mathrm{circ},abc} + 2\left(V_{\mathrm{sw}} - V_{\mathrm{d}}\right)\left(1 - \boldsymbol{m}_{p,abc} - \boldsymbol{m}_{n,abc}\right) \\ &+ \left(R_{\mathrm{sw}} - R_{\mathrm{d}}\right)\left\{\left(1 - 2\boldsymbol{m}_{p,abc}\right)\odot\left|\boldsymbol{i}_{p,abc}\right| + \left(1 - 2\boldsymbol{m}_{n,abc}\right)\odot\left|\boldsymbol{i}_{n,abc}\right|\right\}\big] \\ &+ \frac{t_{\mathrm{d}}}{T_{\mathrm{sw}}}\left[\left(V_{\mathrm{d}} - V_{\mathrm{sw}}\right)\left(\mathrm{sgn}\left(\boldsymbol{i}_{p,abc}\right) + \mathrm{sgn}\left(\boldsymbol{i}_{n,abc}\right)\right) + 2\left(R_{\mathrm{d}} - R_{\mathrm{sw}}\right)\boldsymbol{i}_{\mathrm{circ},abc}\right],\end{aligned} \tag{3.35e}$$

$$\boldsymbol{v}_{\mathrm{td},abc} = \frac{t_{\mathrm{d}}}{T_{\mathrm{sw}}}\left(\boldsymbol{v}_{cp,abc}\odot\mathrm{sgn}\left(\boldsymbol{i}_{p,abc}\right) + \boldsymbol{v}_{cn,abc}\odot\mathrm{sgn}\left(\boldsymbol{i}_{n,abc}\right)\right), \tag{3.35f}$$

$$L_{\mathrm{eq}} = L_s + \frac{L_o}{2}, \tag{3.35g}$$

$$R_{\mathrm{eq}} = R_s + \frac{R_o}{2}, \tag{3.35h}$$

where $\boldsymbol{1} = \begin{pmatrix}1 & 1 & 1\end{pmatrix}^{\mathrm{T}}$. The advanced MMC state-space model is represented by (3.35).

Substituting for $V_{\rm sw} = V_{\rm d} = 0$, $R_{\rm sw} = R_{\rm d} = 0$, and $t_{\rm d} = 0$ in (3.35) yields the following per-phase state-space equation:

$$\frac{\mathrm{d}}{\mathrm{d}t}\begin{pmatrix} i_j \\ i_{\mathrm{circ},j} \\ v_{cp,j} \\ v_{cn,j} \end{pmatrix} = \begin{pmatrix} -\dfrac{R_{\rm eq}}{L_{\rm eq}} & 0 & -\dfrac{Nm_{p,j}}{2L_{\rm eq}} & \dfrac{Nm_{n,j}}{2L_{\rm eq}} \\ 0 & -\dfrac{R_o}{L_o} & -\dfrac{Nm_{p,j}}{2L_o} & -\dfrac{Nm_{n,j}}{2L_o} \\ \dfrac{m_{p,j}}{2C_{\rm SM}} & \dfrac{m_{p,j}}{C_{\rm SM}} & -\dfrac{1}{R_pC_{\rm SM}} & 0 \\ -\dfrac{m_{n,j}}{2C_{\rm SM}} & \dfrac{m_{n,j}}{C_{\rm SM}} & 0 & -\dfrac{1}{R_pC_{\rm SM}} \end{pmatrix} \begin{pmatrix} i_j \\ i_{\mathrm{circ},j} \\ v_{cp,j} \\ v_{cn,j} \end{pmatrix} + \begin{pmatrix} \dfrac{-e_j - \tilde{v}_{n,\rm new}}{L_{\rm eq}} \\ \dfrac{V_{\rm dc}}{2L_o} \\ 0 \\ 0 \end{pmatrix}, \tag{3.36a}$$

$$\tilde{v}_{n,\rm new} = \frac{N}{6}\left(\boldsymbol{m}_{n,abc}^{\rm T}\boldsymbol{v}_{cn,abc} - \boldsymbol{m}_{p,abc}^{\rm T}\boldsymbol{v}_{cp,abc}\right). \tag{3.36b}$$

Substituting for $m_{p,j}$ and $m_{n,j}$ from (3.1) in (3.36), the individual state-space equations become

$$\begin{aligned} L_{\rm eq}\frac{\mathrm{d}i_j}{\mathrm{d}t} + R_{\rm eq}i_j &= -\left(\frac{1}{2} - m_{\mathrm{circ},j}\right)\frac{N}{2}\left(v_{cp,j} - v_{cn,j}\right) \\ &\quad + \frac{(m_j + m_{\rm cm})}{4}N\left(v_{cp,j} + v_{cn,j}\right) - e_j - \tilde{v}_{n,\rm new}, \end{aligned} \tag{3.37a}$$

$$\begin{aligned} L_o\frac{\mathrm{d}i_{\mathrm{circ},j}}{\mathrm{d}t} + R_oi_{\mathrm{circ},j} &= \frac{V_{\rm dc}}{2} - \left(\frac{1}{2} - m_{\mathrm{circ},j}\right)\frac{N}{2}\left(v_{cp,j} + v_{cn,j}\right) \\ &\quad + \frac{(m_j + m_{\rm cm})}{4}N\left(v_{cp,j} - v_{cn,j}\right), \end{aligned} \tag{3.37b}$$

$$\begin{aligned} C_{\rm SM}\frac{\mathrm{d}v_{cp,j}}{\mathrm{d}t} + \frac{v_{cp,j}}{R_p} &= \left(\frac{1}{2} - m_{\mathrm{circ},j}\right)\frac{i_j}{2} - \frac{(m_j + m_{\rm cm})\,i_j}{4} + \left(\frac{1}{2} - m_{\mathrm{circ},j}\right)i_{\mathrm{circ},j} \\ &\quad - \frac{(m_j + m_{\rm cm})}{2}i_{\mathrm{circ},j}, \end{aligned} \tag{3.37c}$$

$$\begin{aligned} C_{\rm SM}\frac{\mathrm{d}v_{cn,j}}{\mathrm{d}t} + \frac{v_{cn,j}}{R_p} &= -\left(\frac{1}{2} - m_{\mathrm{circ},j}\right)\frac{i_j}{2} - \frac{(m_j + m_{\rm cm})\,i_j}{4} + \left(\frac{1}{2} - m_{\mathrm{circ},j}\right)i_{\mathrm{circ},j} \\ &\quad + \frac{(m_j + m_{\rm cm})}{2}i_{\mathrm{circ},j}. \end{aligned} \tag{3.37d}$$

Adding (3.37c) to (3.37d) and subtracting (3.37d) from (3.37c) yield

$$C_{\mathrm{SM}}\frac{\mathrm{d}\left(v_{cp,j}+v_{cn,j}\right)}{\mathrm{d}t}+\frac{\left(v_{cp,j}+v_{cn,j}\right)}{R_p}=-\frac{\left(m_j+m_{\mathrm{cm}}\right)}{2}i_j+2\left(\frac{1}{2}-m_{\mathrm{circ},j}\right)i_{\mathrm{circ},j}, \tag{3.38a}$$

$$C_{\mathrm{SM}}\frac{\mathrm{d}\left(v_{cp,j}-v_{cn,j}\right)}{\mathrm{d}t}+\frac{\left(v_{cp,j}-v_{cn,j}\right)}{R_p}=\left(\frac{1}{2}-m_{\mathrm{circ},j}\right)i_j-\left(m_j+m_{\mathrm{cm}}\right)i_{\mathrm{circ},j}. \tag{3.38b}$$

Defining

$$v_{\mathrm{c},j}^{\Sigma}=\left(v_{cp,j}+v_{cn,j}\right), \tag{3.39a}$$

$$v_{\mathrm{c},j}^{\Delta}=\left(v_{cp,j}-v_{cn,j}\right), \tag{3.39b}$$

and substituting for $(v_{cp,j}+v_{cn,j})$ and $(v_{cp,j}-v_{cn,j})$ from (3.39) in (3.37a), (3.37b), and (3.38) results in

$$L_{\mathrm{eq}}\frac{\mathrm{d}i_j}{\mathrm{d}t}+R_{\mathrm{eq}}i_j=-\frac{N}{2}\left(\frac{1}{2}-m_{\mathrm{circ},j}\right)v_{\mathrm{c},j}^{\Delta}+N\frac{\left(m_j+m_{\mathrm{cm}}\right)}{4}v_{\mathrm{c},j}^{\Sigma}-e_j-\tilde{v}_{n,\mathrm{new}}, \tag{3.40a}$$

$$L_o\frac{\mathrm{d}i_{\mathrm{circ},j}}{\mathrm{d}t}+R_o i_{\mathrm{circ},j}=-\frac{N}{2}\left(\frac{1}{2}-m_{\mathrm{circ},j}\right)v_{\mathrm{c},j}^{\Sigma}+N\frac{\left(m_j+m_{\mathrm{cm}}\right)}{4}v_{\mathrm{c},j}^{\Delta}+\frac{V_{\mathrm{dc}}}{2}, \tag{3.40b}$$

$$C_{\mathrm{SM}}\frac{\mathrm{d}v_{\mathrm{c},j}^{\Sigma}}{\mathrm{d}t}+\frac{v_{\mathrm{c},j}^{\Sigma}}{R_p}=-\frac{\left(m_j+m_{\mathrm{cm}}\right)}{2}i_j+2\left(\frac{1}{2}-m_{\mathrm{circ},j}\right)i_{\mathrm{circ},j}, \tag{3.40c}$$

$$C_{\mathrm{SM}}\frac{\mathrm{d}v_{\mathrm{c},j}^{\Delta}}{\mathrm{d}t}+\frac{v_{\mathrm{c},j}^{\Delta}}{R_p}=\left(\frac{1}{2}-m_{\mathrm{circ},j}\right)i_j-\left(m_j+m_{\mathrm{cm}}\right)i_{\mathrm{circ},j}. \tag{3.40d}$$

The approximate per-phase MMC state-space model that neglects the conduction losses of IGBTs and diodes and the dead time is represented by (3.40).

The developed MMC models in this chapter will be used in the following chapters for designing control strategies of MMCs interfacing grid and driving machines.

4. CONTROL OF THE MMC UNDER FIXED-FREQUENCY OPERATION

In this chapter, control of the MMC as a grid-side converter is explained and investigated. The control problem of the MMC mainly involves reducing the circulating current and the magnitude of the SM capacitor voltage ripple. Based on the dynamic models developed in Chapter 3, a control system to control the MMC is proposed in this chapter.

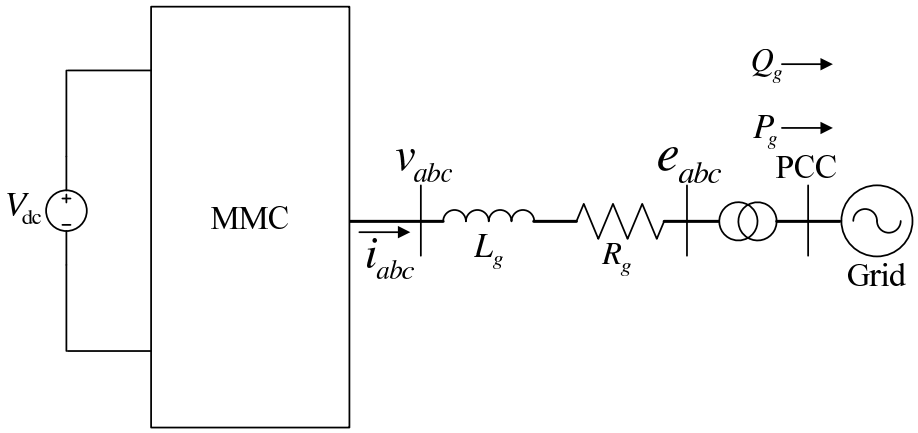

Fig. 4.1. Single-line diagram of a grid-side MMC.

A schematic diagram of the grid-side MMC is shown in Fig. 4.1. Each phase of the converter is interfaced with the utility grid via a series RL branch (R_g and L_g), and a transformer. The converter system of Fig. 4.1 exchanges real and reactive power, $P_g(t)$ and $Q_g(t)$, respectively, with the utility grid at the PCC.

4.1 Dynamic Model

Based on the approximate per-phase MMC state-space model developed in Chapter 3, in this section, the dynamic model of the MMC under fixed-frequency operating conditions, e.g., as the grid-side converter of the WECS, is developed.

In the case of MMC as a grid-side converter, to extend the linear operating region of the PWM strategy and increase the magnitude of the fundamental component of the ac-side phase voltages, the common-mode component of the phase reference waveform $m_{\rm cm}$ in the modulation reference waveforms in (3.1) contains a third-order harmonic with a magnitude of $\frac{1}{6}$th of the magnitude of the fundamental component of the phase reference waveform m_j.

Variable $x = m_{{\rm circ},j},\ i_{{\rm circ},j},\ v^{\Sigma}_{{\rm c},j}$, and $v^{\Delta}_{{\rm c},j}$ in the approximate MMC state-space model in (3.40) can be decomposed to

$$x = \overline{X} + \delta x_{\rm dc} + \tilde{x}_{\rm ac}, \tag{4.1}$$

where $\overline{X}$, $\delta x_{\rm dc}$ and $\tilde{x}_{\rm ac}$ represent the dc operating point, the dc disturbance and the low-frequency ac terms (fundamental and lower-order harmonics) of x, respectively. Furthermore, $i_j = \tilde{i}_{j,{\rm ac}}$, $m_j = \tilde{m}_{j,{\rm ac}}$, and $m_{\rm cm} = \tilde{m}_{{\rm cm,ac}}$ as they are assumed to consist of only the low-frequency components. Decomposing $m_{{\rm circ},j}$, $i_{{\rm circ},j}$, $v^{\Sigma}_{{\rm c},j}$, and $v^{\Delta}_{{\rm c},j}$, based on (4.1), into their corresponding dc and ac components and substituting for them in (3.40), yields

$$\begin{aligned} L_{\rm eq}\frac{{\rm d}i_j}{{\rm d}t} + R_{\rm eq}i_j = &-\frac{N}{2}\left(\frac{1}{2} - \overline{M}_{{\rm circ},j}\right)\tilde{v}^{\Delta}_{{\rm c},j,{\rm ac}} + N\frac{(m_j + m_{\rm cm})}{4}\left(\delta v^{\Sigma}_{{\rm c},j,{\rm dc}}\right) + N\widetilde{\left(\frac{m_j\tilde{v}^{\Sigma}_{{\rm c},j,{\rm ac}}}{4}\right)} \\ &+ N\widetilde{\left(\frac{m_{\rm cm}\tilde{v}^{\Sigma}_{{\rm c},j,{\rm ac}}}{4}\right)} + (m_j + m_{\rm cm})\frac{V_{\rm dc}}{2} - e_j - \tilde{v}_{n,{\rm new}}, \end{aligned} \tag{4.2a}$$

$$L_o\frac{\mathrm{d}\tilde{i}_{\mathrm{circ},j,\mathrm{ac}}}{\mathrm{d}t}+R_o\tilde{i}_{\mathrm{circ},j,\mathrm{ac}}=\tilde{m}_{\mathrm{circ},j,\mathrm{ac}}V_{\mathrm{dc}}-\frac{N}{2}\left(\frac{1}{2}-\overline{M}_{\mathrm{circ},j}\right)\tilde{v}^{\Sigma}_{\mathrm{c},j,\mathrm{ac}}+N\left(\frac{\widetilde{m_j\tilde{v}^{\Delta}_{\mathrm{c},j,\mathrm{ac}}}}{4}\right)$$
$$+N\left(\frac{\widetilde{m_{\mathrm{cm}}\tilde{v}^{\Delta}_{\mathrm{c},j,\mathrm{ac}}}}{4}\right)+N\frac{(m_j+m_{\mathrm{cm}})\,\delta v^{\Delta}_{\mathrm{c},j,\mathrm{dc}}}{4}, \tag{4.2b}$$

$$L_o\frac{\mathrm{d}\left(\delta i_{\mathrm{circ},j,\mathrm{dc}}\right)}{\mathrm{d}t}+R_o\left(\delta i_{\mathrm{circ},j,\mathrm{dc}}\right)=-\frac{N}{2}\left(\frac{1}{2}-\overline{M}_{\mathrm{circ},j}\right)\delta v^{\Sigma}_{\mathrm{c},j,\mathrm{dc}}+\delta m_{\mathrm{circ},j,\mathrm{dc}}V_{\mathrm{dc}}, \tag{4.2c}$$

$$C_{\mathrm{SM}}\frac{\mathrm{d}\tilde{v}^{\Sigma}_{\mathrm{c},j,\mathrm{ac}}}{\mathrm{d}t}+\frac{\tilde{v}^{\Sigma}_{\mathrm{c},j,\mathrm{ac}}}{R_p}=-2\tilde{m}_{\mathrm{circ},j,ac}\frac{i_{\mathrm{dc}}}{3}+2\left(\frac{1}{2}-\overline{M}_{\mathrm{circ},j}\right)\tilde{i}_{\mathrm{circ},j,\mathrm{ac}}-\left(\widetilde{\frac{m_j i_j}{2}}\right)$$
$$-\left(\widetilde{\frac{m_{\mathrm{cm}}i_j}{2}}\right), \tag{4.2d}$$

$$C_{\mathrm{SM}}\frac{\mathrm{d}\left(\delta v^{\Sigma}_{\mathrm{c},j,\mathrm{dc}}\right)}{dt}+\frac{\delta v^{\Sigma}_{\mathrm{c},j,\mathrm{dc}}}{R_p}=-2\delta m_{\mathrm{circ},j,\mathrm{dc}}\frac{i_{\mathrm{dc}}}{3}+2\left(\frac{1}{2}-\overline{M}_{\mathrm{circ},j}\right)\delta i_{\mathrm{circ},j,\mathrm{dc}}, \tag{4.2e}$$

$$C_{\mathrm{SM}}\frac{\mathrm{d}\tilde{v}^{\Delta}_{\mathrm{c},j,\mathrm{ac}}}{\mathrm{d}t}+\frac{\tilde{v}^{\Delta}_{\mathrm{c},j,\mathrm{ac}}}{R_p}=\left(i_j\widetilde{\tilde{m}_{\mathrm{circ},j,\mathrm{ac}}}\right)+i_j\left(\frac{1}{2}-\overline{M}_{\mathrm{circ},j}-\delta m_{\mathrm{circ},j,\mathrm{dc}}\right)$$
$$-m_j\left(\frac{i_{\mathrm{dc}}}{3}+\delta i_{\mathrm{circ},j,\mathrm{dc}}\right)-m_{\mathrm{cm}}\left(\frac{i_{\mathrm{dc}}}{3}+\delta i_{\mathrm{circ},j,\mathrm{dc}}\right)$$
$$-\left(\widetilde{m_j\tilde{i}_{\mathrm{circ},j,\mathrm{ac}}}\right)-\left(\widetilde{m_{\mathrm{cm}}\tilde{i}_{\mathrm{circ},j,\mathrm{ac}}}\right), \tag{4.2f}$$

$$C_{\mathrm{SM}}\frac{\mathrm{d}\left(\delta v^{\Delta}_{\mathrm{c},j,\mathrm{dc}}\right)}{\mathrm{d}t}+\frac{\delta v^{\Delta}_{\mathrm{c},j,\mathrm{dc}}}{R_p}=-\overline{(i_j\tilde{m}_{\mathrm{circ},j,\mathrm{ac}})}-\overline{\left(m_j\tilde{i}_{\mathrm{circ},j,\mathrm{ac}}\right)}, \tag{4.2g}$$

where $\overline{V}^{\Sigma}_{\mathrm{c},j}=2\dfrac{V_{\mathrm{dc}}}{N}$, $\overline{V}^{\Delta}_{\mathrm{c},j}=0$, $\overline{I}_{\mathrm{circ},j}=\dfrac{i_{\mathrm{dc}}}{3}$, i_{dc} is the dc-link current, $L_{\mathrm{eq}}=L_g+\dfrac{L_o}{2}$, and $R_{\mathrm{eq}}=R_g+\dfrac{R_o}{2}$. In deriving (4.2), all the multiplications of the terms with small magnitude are neglected. Using (4.2), the controllers of the MMC as the grid-side converter can be systematically designed.

4.2 Grid-Side Current Controllers

The grid-side current controllers are similar to those explained in Section 2.6 of Chapter 2 and is summarized in Fig. 4.2. In Fig. 4.2, along with *qd* current control, the filters used to remove the high frequency measurement noise from the measured currents, are also shown.

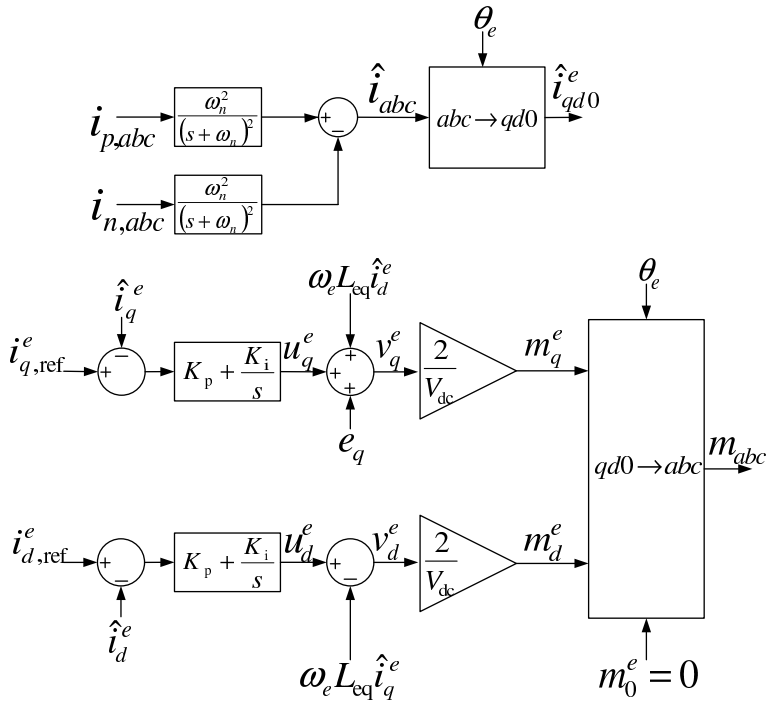

Fig. 4.2. Block diagram of the grid-side qd current controller.

From the controller block diagram in Fig. 4.2, the output of the MMC control system $\boldsymbol{m}_{abc}$, is given by

$$\begin{aligned}\boldsymbol{m}_{abc} &= \boldsymbol{T}(\theta_e)^{-1}\boldsymbol{m}^e_{qd0} \\ &= \frac{2K_\mathrm{p}}{V_\mathrm{dc}}\left(\boldsymbol{i}_{abc,\mathrm{ref}} - \hat{\boldsymbol{i}}_{abc}\right) + \frac{2K_\mathrm{i}}{V_\mathrm{dc}}\boldsymbol{T}^{-1}\int \boldsymbol{T}\left(\boldsymbol{i}_{abc,\mathrm{ref}} - \hat{\boldsymbol{i}}_{abc}\right)\mathrm{d}t + \frac{2\omega_e L_\mathrm{eq}}{\sqrt{3}V_\mathrm{dc}}\boldsymbol{X}\hat{\boldsymbol{i}}_{abc} \\ &\quad + \frac{2}{V_\mathrm{dc}}\boldsymbol{e}_{abc}, \end{aligned} \tag{4.3a}$$

$$\boldsymbol{0} = \frac{\mathrm{d}^2\hat{\boldsymbol{i}}_{abc}}{\mathrm{d}t^2} + 2\omega_n\frac{\mathrm{d}\hat{\boldsymbol{i}}_{abc}}{\mathrm{d}t} + \omega_n^2\left(\hat{\boldsymbol{i}}_{abc} - \boldsymbol{i}_{abc}\right), \tag{4.3b}$$

$$\boldsymbol{X} = \begin{pmatrix} 0 & -1 & 1 \\ 1 & 0 & -1 \\ -1 & 1 & 0 \end{pmatrix}. \tag{4.3c}$$

Applying Laplace transform to (4.3b), the following is obtained:

$$\frac{\hat{\boldsymbol{I}}_{abc}(s)}{\boldsymbol{I}_{abc}(s)} = \frac{\omega_n^2}{s^2 + 2\omega_n s + \omega_n^2}. \tag{4.4}$$

The settling time of the system of (4.4) is $\frac{4}{\omega_n}$. Under the assumption that $\frac{4}{\omega_n}$ is much smaller than the settling time of the qd current control system, the following assumption may be made:

$$\hat{\boldsymbol{I}}_{abc} \approx \boldsymbol{I}_{abc} \Rightarrow \hat{\boldsymbol{i}}_{abc} \approx \boldsymbol{i}_{abc}. \tag{4.5}$$

Applying qd transformation in grid-reference frame to (4.5) results in

$$\hat{\boldsymbol{i}}^e_{qd} \approx \boldsymbol{i}^e_{qd}. \tag{4.6}$$

From the controller block diagram in Fig. 4.2 and using (4.6), the following is deduced:

$$\boldsymbol{m}^e_{qd} \approx \frac{2K_\mathrm{p}}{V_\mathrm{dc}}\left(\boldsymbol{i}^e_{qd,\mathrm{ref}} - \boldsymbol{i}^e_{qd}\right) + \frac{2K_\mathrm{i}}{V_\mathrm{dc}}\int\left(\boldsymbol{i}^e_{qd,\mathrm{ref}} - \boldsymbol{i}^e_{qd}\right)\mathrm{d}t + \frac{2\omega_e L_\mathrm{eq}}{V_\mathrm{dc}}\boldsymbol{X}_1\boldsymbol{i}^e_{qd} + \frac{2}{V_\mathrm{dc}}\boldsymbol{e}_{qd}, \tag{4.7a}$$

$$\boldsymbol{X}_1 = \begin{pmatrix} 0 & 1 \\ -1 & 0 \end{pmatrix}. \tag{4.7b}$$

Multiplying (4.7a) by $\frac{V_\mathrm{dc}}{2}$ results in

$$\boldsymbol{m}^e_{qd}\frac{V_\mathrm{dc}}{2} = K_\mathrm{p}\left(\boldsymbol{i}^e_{qd,\mathrm{ref}} - \boldsymbol{i}^e_{qd}\right) + K_\mathrm{i}\int\left(\boldsymbol{i}^e_{qd,\mathrm{ref}} - \boldsymbol{i}^e_{qd}\right)\mathrm{d}t + \omega_e L_\mathrm{eq}\boldsymbol{X}_1\boldsymbol{i}^e_{qd} + \boldsymbol{e}_{qd}. \tag{4.8}$$

Defining

$$\boldsymbol{u}^e_{qd} = \boldsymbol{m}^e_{qd}\frac{V_\mathrm{dc}}{2} - \boldsymbol{e}_{qd} - \omega_e L_\mathrm{eq}\boldsymbol{X}_1\boldsymbol{i}^e_{qd}, \tag{4.9}$$

and substituting for $\boldsymbol{m}^e_{qd}\frac{V_{\rm dc}}{2} - \boldsymbol{e}_{qd} - \omega_e L_{\rm eq}\boldsymbol{X}_1\boldsymbol{i}^e_{qd}$ from (4.9) in (4.8) results in

$$\boldsymbol{u}^e_{qd} = K_{\rm p}\left(\boldsymbol{i}^e_{qd,\rm ref} - \boldsymbol{i}^e_{qd}\right) + K_{\rm i}\int\left(\boldsymbol{i}^e_{qd,\rm ref} - \boldsymbol{i}^e_{qd}\right)\mathrm{d}t. \tag{4.10}$$

Applying Laplace transform to (4.10) results in

$$\boldsymbol{I}^e_{qd,\rm ref}(s) - \boldsymbol{I}^e_{qd}(s) = \frac{s}{sK_{\rm p} + K_{\rm i}}\boldsymbol{U}^e_{qd}(s). \tag{4.11}$$

Assuming that the terms $\frac{N}{2}\left(\frac{1}{2} - \overline{M}_{{\rm circ},j}\right)\tilde{v}^{\Delta}_{{\rm c},j,\rm ac}$, $N\frac{(m_j + m_{\rm cm})}{4}\delta v^{\Sigma}_{{\rm c},j,\rm dc}$, $N\widetilde{\left(\frac{m_j\tilde{v}^{\Sigma}_{{\rm c},j,\rm ac}}{4}\right)}$, $N\widetilde{\left(\frac{m_{\rm cm}\tilde{v}^{\Sigma}_{{\rm c},j,\rm ac}}{4}\right)}$, and $\left(m_{\rm cm}\frac{V_{\rm dc}}{2} - \tilde{v}_{n,\rm new}\right)$ are small and negligible when compared to $m_j\frac{V_{\rm dc}}{2}$, (4.2a) is approximately given by

$$L_{\rm eq}\frac{\mathrm{d}i_j}{\mathrm{d}t} + R_{\rm eq}i_j \approx m_j\frac{V_{\rm dc}}{2} - e_j, \tag{4.12}$$

Applying qd transformation to (4.12) results in

$$L_{\rm eq}\frac{\mathrm{d}\boldsymbol{i}^e_{qd}}{\mathrm{d}t} + R_{\rm eq}\boldsymbol{i}^e_{qd} = \boldsymbol{u}^e_{qd}. \tag{4.13}$$

Furthermore, applying Laplace transform to (4.13) results in

$$\boldsymbol{U}^e_{qd}(s) = \left(sL_{\rm eq} + R_{\rm eq}\right)\boldsymbol{I}^e_{qd}(s). \tag{4.14}$$

Substituting for $\boldsymbol{U}^e_{qd}(s)$ from (4.14) in (4.11) produces the following transfer function:

$$\frac{\boldsymbol{I}^e_{qd}(s)}{\boldsymbol{I}^e_{qd,\rm ref}(s)} = \frac{sK_{\rm p} + K_{\rm i}}{L_{\rm eq}s^2 + \left(R_{\rm eq} + K_{\rm p}\right)s + K_{\rm i}}. \tag{4.15}$$

The gains of the grid-side qd current controller K_p and K_i are tuned using the characteristic equation $s^2 + \dfrac{(R_\mathrm{eq} + K_\mathrm{p})}{L_\mathrm{eq}} s + \dfrac{K_\mathrm{i}}{L_\mathrm{eq}}$ such that the settling time $\dfrac{8L_\mathrm{eq}}{(R_\mathrm{eq} + K_\mathrm{p})}$ is an order of magnitude greater than the settling time of the current filters.

Besides the grid-side current controllers and the SM capacitor voltage balancing algorithm explained in Section 3.2.2, the MMC needs internal controllers to improve its stability and efficiency and/or to reduce its cost. The internal controllers include the circulating current controller, which is explained in the following section.

4.3 Circulating Current Controller

In this section, a new circulating current controller, consisting of an unbalance controller and an ac-current controller, is proposed.

4.3.1 Unbalance Controller

Under balanced conditions, the circulating current in each phase defined by (3.6) contains one-third the dc-link current. However, under unbalanced ac-side conditions, e.g., a single-phase grid-side fault, the dc component in the circulating currents are unbalanced. To accurately control this dc component, an appropriate circulating current reference should be generated. In this section, a feedforward controller is proposed to generate this reference.

The dc component of the MMC arm current can be estimated from the average power delivered to the corresponding grid-side phase. An estimate of the average power supplied to phase-j is given by

$$P_{j,\mathrm{est}} = \left\langle i_j m_j \frac{V_\mathrm{dc}}{2} \right\rangle, \tag{4.16}$$

where m_j is determined by the grid-side qd current controller, as mentioned in the previous section. The dc component of phase-j arm currents is estimated by

$$i_{\mathrm{dc},j,\mathrm{est}} = \left\langle \frac{m_j i_j}{2} \right\rangle . \tag{4.17}$$

The estimated dc component of the arm current in (4.17) assumes a lossless system. However, to compensate for the losses and inaccuracies in the estimation, an additional dc component is added to the estimated value. The additional component is generated based on the control of the average value of SM capacitor voltages, which controls the dc component of the SM capacitor voltages at their reference value. The proposed controller is shown in Fig. 4.3. The SM capacitor voltage, as explained by (3.37c) and (3.37d), contains predominantly fundamental and second-order harmonic components [73,74]. Equations (3.37c) and (3.37d) also indicate that while the odd-order harmonic components of the SM capacitor voltage ripple in the upper and lower arms have the same magnitude and opposite phase, the even-order harmonic components have the same magnitude and phase, i.e., $v_{\mathrm{c},j}^{\Sigma}$ contains only even-order harmonic components, a predominantly second-order harmonic. Therefore, the dc component of the average SM capacitor voltage is obtained by removing its predominant ac component, i.e., the second-order harmonic component. This is achieved by using a notch filter. Consequently, the reference value for the dc component of the circulating current is given by

$$i_{\mathrm{circ},j,\mathrm{ref}} = i_{\mathrm{dc},j,\mathrm{est}} + K_{\mathrm{pv}} \left(0.5 \left\langle v_{\mathrm{c},j}^{\Sigma} \right\rangle - v_{\mathrm{c,ref}} \right) , \tag{4.18}$$

where K_{pv} is the proportional controller gain and $\langle x \rangle$ is the dc component of x.

4.3.2 Ac Current Controller

As explained in the previous section, the predominant component in $v_{\mathrm{c},j}^{\Sigma}$ is a second-order harmonic component. As an extension of this examination, $v_{\mathrm{c},j}^{\Delta}$ predom-

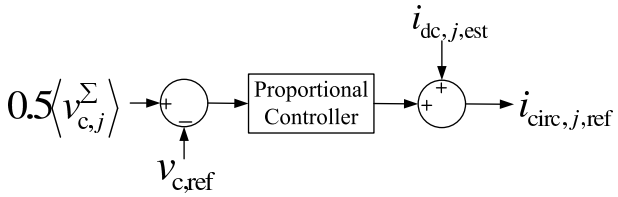

Fig. 4.3. Block diagram of the the proposed unbalance circulating current controller.

inantly contains a fundamental component as the odd-order harmonic components of SM capacitor voltage ripple of the upper and lower arms have the same magnitude with an opposite phase. These results along with (4.2b) indicate the presence of a dominant second-order harmonic in the circulating current. Furthermore, the presence of the third-order harmonic common-mode voltage in each ac-side phase of the MMC and the term $\frac{Nm_{\mathrm{cm}}\tilde{v}^{\Delta}_{\mathrm{c},j,\mathrm{ac}}}{4}$ in the circulating current expression results in the presence of a fourth-order harmonic in the circulating current. Therefore, the ac components of the circulating currents, predominantly second- and fourth-order harmonic components, are non-zero.

The ac components of the circulating currents, if not properly reduced, increase the converter losses and component ratings. In this section, a new controller is proposed to (i) reduce the ac components of the circulating currents, and (ii) control the dc component of the circulating current based on the reference generated from the unbalance control.

The proposed circulating current controller is based on elimination of the dominant components of the circulating current, i.e., the 2^{nd} and 4^{th} order harmonics of the circulating currents. A Proportional Resonant (PR) controller comprising two resonant terms is employed to suppress the 2^{nd} and 4^{th} order harmonic components of the circulating currents. The transfer function of the proposed PR controller is expressed by

$$K_{\mathrm{p1}} + K_{\mathrm{i1}}\frac{s}{s^2 + w_{n3}^2} + K_{\mathrm{p2}} + K_{\mathrm{i2}}\frac{s}{s^2 + w_{n4}^2}, \tag{4.19}$$

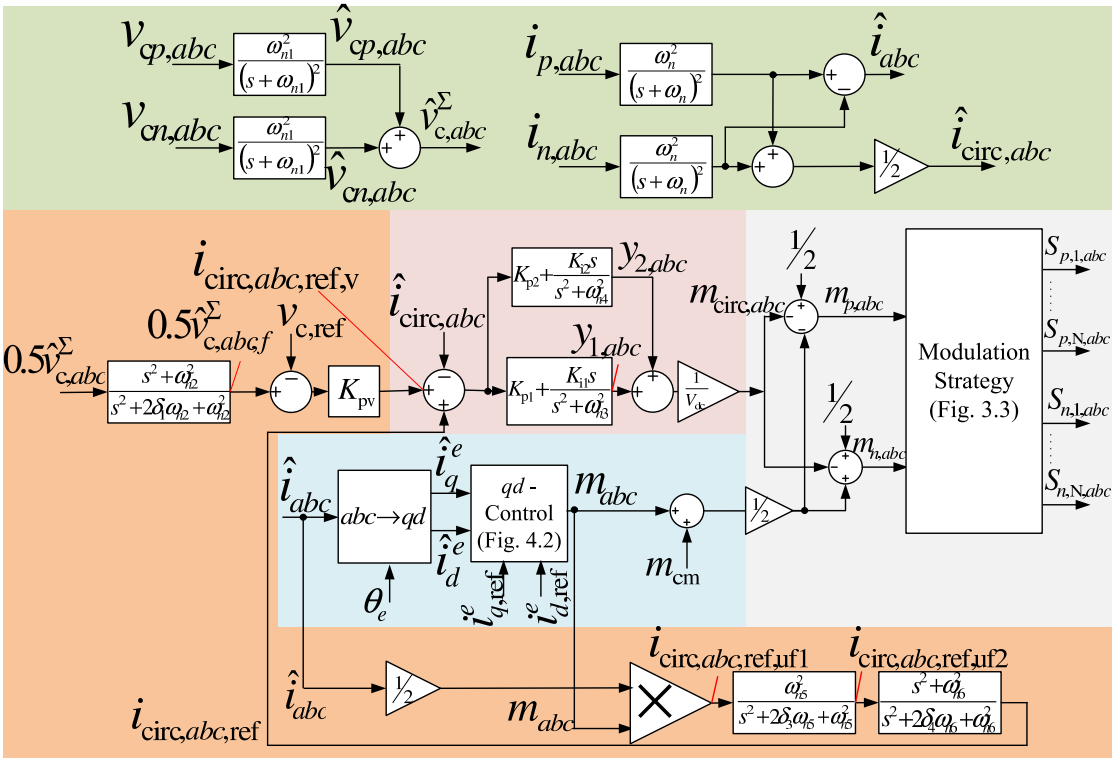

Fig. 4.4. Block diagram of the overall control system of the MMC.

where w_{n3} and w_{n4} are adjusted to the 2nd and 4th harmonic frequencies, respectively.

The implementation procedure of the modulation strategy discussed in Section 3.2, the grid-side current controllers explained in Section 4.2, and the circulating current controller described in this section is summarized in Fig. 4.4. The filters used to remove the high-frequency measurement noise are also shown in Fig. 4.4.

From the controller block diagram in Fig. 4.4, the output of the MMC control system $\boldsymbol{m}_{\mathrm{circ},abc}$, is given by

$$\boldsymbol{0} = \frac{\mathrm{d}^2\hat{\boldsymbol{v}}_{cy,abc}}{\mathrm{d}t^2} + 2\omega_{n1}\frac{\mathrm{d}\hat{\boldsymbol{v}}_{cy,abc}}{\mathrm{d}t} + \omega_{n1}^2\left(\hat{\boldsymbol{v}}_{cy,abc} - \boldsymbol{v}_{cy,abc}\right), y \in \{p, n\}, \tag{4.20a}$$

$$\hat{\boldsymbol{v}}^{\Sigma}_{\mathrm{c},abc} = \hat{\boldsymbol{v}}_{cp,abc} + \hat{\boldsymbol{v}}_{cn,abc}, \tag{4.20b}$$

$$\boldsymbol{0} = \frac{\mathrm{d}^2\hat{\boldsymbol{i}}_{\mathrm{circ},abc}}{\mathrm{d}t^2} + 2\omega_{n}\frac{\mathrm{d}\hat{\boldsymbol{i}}_{\mathrm{circ},abc}}{\mathrm{d}t} + \omega_{n}^2\left(\hat{\boldsymbol{i}}_{\mathrm{circ},abc} - \boldsymbol{i}_{\mathrm{circ},abc}\right), \tag{4.20c}$$

$$\boldsymbol{i}_{\mathrm{circ},abc,\mathrm{ref},\mathrm{uf1}} = 0.5\boldsymbol{m}_{abc} \odot \hat{\boldsymbol{i}}_{abc}, \tag{4.20d}$$

$$\boldsymbol{0} = \frac{\mathrm{d}^2\boldsymbol{i}_{\mathrm{circ},abc,\mathrm{ref},\mathrm{uf2}}}{\mathrm{d}t^2} + 2\omega_{n5}\delta_3\frac{\mathrm{d}\boldsymbol{i}_{\mathrm{circ},abc,\mathrm{ref},\mathrm{uf2}}}{\mathrm{d}t} + \omega_{n5}^2\left(\boldsymbol{i}_{\mathrm{circ},abc,\mathrm{ref},\mathrm{uf2}} - \boldsymbol{i}_{\mathrm{circ},abc,\mathrm{ref},\mathrm{uf1}}\right), \tag{4.20e}$$

$$\boldsymbol{0} = \frac{\mathrm{d}^2\left(\boldsymbol{i}_{\mathrm{circ},abc,\mathrm{ref}} - \boldsymbol{i}_{\mathrm{circ},abc,\mathrm{ref},\mathrm{uf2}}\right)}{\mathrm{d}t^2} + 2\omega_{n6}\delta_4\frac{\mathrm{d}\boldsymbol{i}_{\mathrm{circ},abc,\mathrm{ref}}}{\mathrm{d}t} + \omega_{n6}^2\left(\boldsymbol{i}_{\mathrm{circ},abc,\mathrm{ref}} - \boldsymbol{i}_{\mathrm{circ},abc,\mathrm{ref},\mathrm{uf2}}\right), \tag{4.20f}$$

$$\boldsymbol{0} = \frac{\mathrm{d}^2\left(0.5\hat{\boldsymbol{v}}^{\Sigma}_{\mathrm{c},abc,f} - 0.5\hat{\boldsymbol{v}}^{\Sigma}_{\mathrm{c},abc}\right)}{\mathrm{d}t^2} + 2\delta_1\omega_{n2}\frac{\mathrm{d}\left(0.5\hat{\boldsymbol{v}}^{\Sigma}_{\mathrm{c},abc,f}\right)}{\mathrm{d}t} + \omega_{n2}^2\left(0.5\hat{\boldsymbol{v}}^{\Sigma}_{\mathrm{c},abc,f} - 0.5\hat{\boldsymbol{v}}^{\Sigma}_{\mathrm{c},abc}\right), \tag{4.20g}$$

$$\boldsymbol{i}_{\mathrm{circ},abc,\mathrm{ref},\mathrm{v}} = K_{\mathrm{pv}}\left(0.5\hat{\boldsymbol{v}}^{\Sigma}_{\mathrm{c},abc,f} - v_{\mathrm{c,ref}}\boldsymbol{1}\right), \tag{4.20h}$$

$$\boldsymbol{e}_{i,abc} = \left(\boldsymbol{i}_{\mathrm{circ},abc,\mathrm{ref}} + \boldsymbol{i}_{\mathrm{circ},abc,\mathrm{ref},\mathrm{v}} - \hat{\boldsymbol{i}}_{\mathrm{circ},abc}\right), \tag{4.20i}$$

$$\boldsymbol{0} = \frac{\mathrm{d}^2\left(\boldsymbol{y}_{1,abc} - K_{\mathrm{p1}}\boldsymbol{e}_{i,abc}\right)}{\mathrm{d}t^2} - K_{\mathrm{i1}}\frac{\mathrm{d}\boldsymbol{e}_{i,abc}}{\mathrm{d}t} + \omega_{n3}^2\left(\boldsymbol{y}_{1,abc} - K_{\mathrm{p1}}\boldsymbol{e}_{i,abc}\right), \tag{4.20j}$$

$$\boldsymbol{0} = \frac{\mathrm{d}^2\left(\boldsymbol{y}_{2,abc} - K_{\mathrm{p2}}\boldsymbol{e}_{i,abc}\right)}{\mathrm{d}t^2} - K_{\mathrm{i2}}\frac{\mathrm{d}\boldsymbol{e}_{i,abc}}{\mathrm{d}t} + \omega_{n4}^2\left(\boldsymbol{y}_{2,abc} - K_{\mathrm{p2}}\boldsymbol{e}_{i,abc}\right), \tag{4.20k}$$

$$\boldsymbol{m}_{\mathrm{circ},abc} = \frac{1}{V_{\mathrm{dc}}}\left(\boldsymbol{y}_{1,abc} + \boldsymbol{y}_{2,abc}\right). \tag{4.20l}$$

Considering only the ac components in (4.20j)-(4.20l) results in

$$\boldsymbol{0} = \frac{\mathrm{d}^2\left(\tilde{\boldsymbol{y}}_{1,abc,\mathrm{ac}} - K_{\mathrm{p1}}\tilde{\boldsymbol{e}}_{i,abc,\mathrm{ac}}\right)}{\mathrm{d}t^2} - K_{\mathrm{i1}}\frac{\mathrm{d}\tilde{\boldsymbol{e}}_{i,abc,\mathrm{ac}}}{\mathrm{d}t} + \omega_{n3}^2\left(\tilde{\boldsymbol{y}}_{1,abc,\mathrm{ac}} - K_{\mathrm{p1}}\tilde{\boldsymbol{e}}_{i,abc,\mathrm{ac}}\right), \tag{4.21a}$$

$$\boldsymbol{0} = \frac{\mathrm{d}^2\left(\tilde{\boldsymbol{y}}_{2,abc,\mathrm{ac}} - K_{\mathrm{p2}}\tilde{\boldsymbol{e}}_{i,abc,\mathrm{ac}}\right)}{\mathrm{d}t^2} - K_{\mathrm{i2}}\frac{\mathrm{d}\tilde{\boldsymbol{e}}_{i,abc,\mathrm{ac}}}{\mathrm{d}t} + \omega_{n4}^2\left(\tilde{\boldsymbol{y}}_{2,abc,\mathrm{ac}} - K_{\mathrm{p2}}\tilde{\boldsymbol{e}}_{i,abc,\mathrm{ac}}\right), \tag{4.21b}$$

$$\tilde{\boldsymbol{m}}_{\mathrm{circ},abc,\mathrm{ac}} = \frac{1}{V_{\mathrm{dc}}}\left(\tilde{\boldsymbol{y}}_{1,abc,\mathrm{ac}} + \tilde{\boldsymbol{y}}_{2,abc,\mathrm{ac}}\right). \tag{4.21c}$$

Applying Laplace transform to (4.21) results in

$$\tilde{\boldsymbol{Y}}_{1,abc,\mathrm{ac}}(s) = \frac{K_{\mathrm{p1}}s^2 + K_{\mathrm{i1}}s + K_{\mathrm{p1}}\omega_{n3}^2}{s^2 + \omega_{n3}^2}\tilde{\boldsymbol{E}}_{i,abc,\mathrm{ac}}(s), \tag{4.22a}$$

$$\tilde{\boldsymbol{Y}}_{2,abc,\mathrm{ac}}(s) = \frac{K_{\mathrm{p2}}s^2 + K_{\mathrm{i2}}s + K_{\mathrm{p2}}\omega_{n4}^2}{s^2 + \omega_{n4}^2}\tilde{\boldsymbol{E}}_{i,abc,\mathrm{ac}}(s), \tag{4.22b}$$

$$\tilde{\boldsymbol{M}}_{\mathrm{circ},abc,\mathrm{ac}} = \frac{1}{V_{\mathrm{dc}}} \left(\tilde{\boldsymbol{Y}}_{1,abc,\mathrm{ac}}(s) + \tilde{\boldsymbol{Y}}_{2,abc,\mathrm{ac}}(s) \right). \tag{4.22c}$$

Similar to the approximation used in Section 4.2 on ac-side currents, the approximation

$$\boldsymbol{i}_{\mathrm{circ},abc} \approx \hat{\boldsymbol{i}}_{\mathrm{circ},abc} \tag{4.23}$$

is valid on the basis of the settling time of the circulating current control system being much greater than the settling time of the current filters. Subsequently,

$$\boldsymbol{e}_{i,abc} \approx \left(\boldsymbol{i}_{\mathrm{circ},abc,\mathrm{ref}} + \boldsymbol{i}_{\mathrm{circ},abc,\mathrm{ref,v}} - \boldsymbol{i}_{\mathrm{circ},abc} \right). \tag{4.24}$$

Moreover, considering only the ac components in $\boldsymbol{e}_{i,abc}$ gives rise to

$$\tilde{\boldsymbol{e}}_{i,abc,\mathrm{ac}} = \tilde{\boldsymbol{i}}_{\mathrm{circ},abc,\mathrm{ref,ac}} - \tilde{\boldsymbol{i}}_{\mathrm{circ},abc,\mathrm{ac}}. \tag{4.25}$$

Applying Laplace transform to (4.25) and substituting the result in (4.22a) and (4.22b) results in

$$\tilde{\boldsymbol{Y}}_{1,abc,\mathrm{ac}}(s) = \frac{K_{\mathrm{p1}} s^2 + K_{\mathrm{i1}} s + K_{\mathrm{p1}} \omega_{n3}^2}{s^2 + \omega_{n3}^2} \left(\tilde{\boldsymbol{I}}_{\mathrm{circ},abc,\mathrm{ref,ac}}(s) - \tilde{\boldsymbol{I}}_{\mathrm{circ},abc,\mathrm{ac}}(s) \right), \tag{4.26a}$$

$$\tilde{\boldsymbol{Y}}_{2,abc,\mathrm{ac}}(s) = \frac{K_{\mathrm{p2}} s^2 + K_{\mathrm{i2}} s + K_{\mathrm{p2}} \omega_{n4}^2}{s^2 + \omega_{n4}^2} \left(\tilde{\boldsymbol{I}}_{\mathrm{circ},abc,\mathrm{ref,ac}}(s) - \tilde{\boldsymbol{I}}_{\mathrm{circ},abc,\mathrm{ac}}(s) \right). \tag{4.26b}$$

Separating the ac components of the circulating current into its two major components, namely, the second- and the fourth-harmonic components, and as Laplace transform is a linear operator, (4.26) is rewritten as

$$\begin{aligned} \tilde{\boldsymbol{Y}}_{1,abc,\mathrm{ac}}(s) = {} & \left(K_{\mathrm{p1}} + \frac{K_{\mathrm{i1}} s}{s^2 + \omega_{n3}^2} \right) \left(\tilde{\boldsymbol{I}}_{\mathrm{circ},abc,\mathrm{ref,ac},2}(s) - \tilde{\boldsymbol{I}}_{\mathrm{circ},abc,\mathrm{ac},2}(s) \right) \\ & K_{\mathrm{p1}} \left(\tilde{\boldsymbol{I}}_{\mathrm{circ},abc,\mathrm{ref,ac},4}(s) - \tilde{\boldsymbol{I}}_{\mathrm{circ},abc,\mathrm{ac},4}(s) \right), \end{aligned} \tag{4.27a}$$

$$\tilde{\boldsymbol{Y}}_{2,abc,\mathrm{ac}}(s) = \left(K_{\mathrm{p2}} + \frac{K_{\mathrm{i2}}s}{s^2+\omega_{n4}^2}\right)\left(\tilde{\boldsymbol{I}}_{\mathrm{circ},abc,\mathrm{ref,ac},4}(s) - \tilde{\boldsymbol{I}}_{\mathrm{circ},abc,\mathrm{ac},4}(s)\right) \\ K_{\mathrm{p2}}\left(\tilde{\boldsymbol{I}}_{\mathrm{circ},abc,\mathrm{ref,ac},2}(s) - \tilde{\boldsymbol{I}}_{\mathrm{circ},abc,\mathrm{ac},2}(s)\right), \tag{4.27b}$$

where $\tilde{\boldsymbol{I}}_{\mathrm{circ},abc,\mathrm{ac},k}(s)$ is the Laplace transform of k^{th}-harmonic in $\tilde{\boldsymbol{i}}_{\mathrm{circ},abc,\mathrm{ac}}$. The resonant parts $\frac{K_{\mathrm{i1}}s}{s^2+\omega_{n3}^2}$ and $\frac{K_{\mathrm{i2}}s}{s^2+\omega_{n4}^2}$ in (4.27) have negligible impact on the fourth and second harmonic components, respectively. Substituting for $\tilde{\boldsymbol{Y}}_{1,abc,\mathrm{ac}}(s)$ and $\tilde{\boldsymbol{Y}}_{2,abc,\mathrm{ac}}(s)$ from (4.27) in (4.22c) and splitting $\tilde{\boldsymbol{M}}_{\mathrm{circ},abc,\mathrm{ac}}$ into its corresponding two major components result in

$$\tilde{\boldsymbol{M}}_{\mathrm{circ},abc,\mathrm{ac}} = \tilde{\boldsymbol{M}}_{\mathrm{circ},abc,\mathrm{ac},2} + \tilde{\boldsymbol{M}}_{\mathrm{circ},abc,\mathrm{ac},4}, \tag{4.28a}$$

$$\tilde{\boldsymbol{M}}_{\mathrm{circ},abc,\mathrm{ac},2} = \frac{1}{V_{\mathrm{dc}}}\left(K_{\mathrm{p1}} + K_{\mathrm{p2}} + \frac{K_{\mathrm{i1}}s}{s^2+\omega_{n3}^2}\right)\left(\tilde{\boldsymbol{I}}_{\mathrm{circ},abc,\mathrm{ref,ac},2}(s) - \tilde{\boldsymbol{I}}_{\mathrm{circ},abc,\mathrm{ac},2}(s)\right), \tag{4.28b}$$

$$\tilde{\boldsymbol{M}}_{\mathrm{circ},abc,\mathrm{ac},4} = \frac{1}{V_{\mathrm{dc}}}\left(K_{\mathrm{p1}} + K_{\mathrm{p2}} + \frac{K_{\mathrm{i2}}s}{s^2+\omega_{n4}^2}\right)\left(\tilde{\boldsymbol{I}}_{\mathrm{circ},abc,\mathrm{ref,ac},4}(s) - \tilde{\boldsymbol{I}}_{\mathrm{circ},abc,\mathrm{ac},4}(s)\right). \tag{4.28c}$$

Based on (4.2b), whenever $\delta v_{\mathrm{c},j,\mathrm{dc}}^{\Delta}$ becomes greater than zero, the first harmonic component of $\tilde{i}_{\mathrm{circ},j,\mathrm{ac}}$ increases. However, as shown in (4.2g), this results in the reduction of $\delta v_{\mathrm{c},j,\mathrm{dc}}^{\Delta}$, which in turn reduces the magnitude of $\tilde{i}_{\mathrm{circ},j,\mathrm{ac}}$. Therefore, $v_{\mathrm{c},j,\mathrm{dc}}^{\Delta} = \overline{V}_{c,j,dc}^{\Delta} + \delta v_{c,j,dc}^{\Delta}$ is always zero or close to zero. Therefore, $\delta v_{\mathrm{c},j,\mathrm{dc}}^{\Delta}$ can be neglected hereafter. Consequently, (4.2b) becomes

$$L_o\frac{\mathrm{d}\tilde{i}_{\mathrm{circ},j,\mathrm{ac}}}{\mathrm{d}t} + R_o\tilde{i}_{\mathrm{circ},j,\mathrm{ac}} = \tilde{m}_{\mathrm{circ},j,\mathrm{ac}}V_{\mathrm{dc}} + \tilde{v}_{\mathrm{circ,source},j}, \tag{4.29}$$

where

$$v_{\mathrm{circ,source},j} = -\frac{N}{2}\left(\frac{1}{2} - \overline{M}_{\mathrm{circ},j}\right)\tilde{v}_{\mathrm{c},j,\mathrm{ac}}^{\Sigma} + N\widetilde{\left(\frac{m_j\tilde{v}_{\mathrm{c},j,\mathrm{ac}}^{\Delta}}{4}\right)} + N\widetilde{\left(\frac{m_{\mathrm{cm}}\tilde{v}_{\mathrm{c},j,\mathrm{ac}}^{\Delta}}{4}\right)}.$$

The transfer function relating $\tilde{I}_{\mathrm{circ},j,\mathrm{ac}}(s)$ to $\tilde{M}_{\mathrm{circ},j,\mathrm{ac}}(s)$ is given by

$$\tilde{I}_{\mathrm{circ},j,\mathrm{ac}}(s) = \frac{V_{\mathrm{dc}}}{sL_o + R_o}\tilde{M}_{\mathrm{circ},j,\mathrm{ac}}(s). \tag{4.30}$$

Separating the ac components of the circulating current into the second and fourth harmonic components, (4.30) is rewritten as

$$\tilde{I}_{\mathrm{circ},j,\mathrm{ac},2}(s) = \frac{V_{\mathrm{dc}}}{sL_o + R_o}\tilde{M}_{\mathrm{circ},j,\mathrm{ac},2}(s), \tag{4.31a}$$

$$\tilde{I}_{\mathrm{circ},j,\mathrm{ac},4}(s) = \frac{V_{\mathrm{dc}}}{sL_o + R_o}\tilde{M}_{\mathrm{circ},j,\mathrm{ac},4}(s). \tag{4.31b}$$

Substituting for $\tilde{M}_{\mathrm{circ},j,\mathrm{ac},2}(s)$ and $\tilde{M}_{\mathrm{circ},j,\mathrm{ac},4}(s)$ from (4.28) in (4.31) results in

$$\frac{\tilde{I}_{\mathrm{circ},j,\mathrm{ac},2}(s)}{\tilde{I}_{\mathrm{circ},j,\mathrm{ref,ac},2}(s)} = \frac{K_{\mathrm{pt}}s^2 + K_{\mathrm{i1}}s + K_{\mathrm{pt}}\omega_{n3}^2}{L_o s^3 + (K_{\mathrm{pt}} + R_o)\,s^2 + (K_{\mathrm{i1}} + L_o\omega_{n3}^2)\,s + (K_{\mathrm{pt}} + R_o)\,\omega_{n3}^2}, \tag{4.32a}$$

$$\frac{\tilde{I}_{\mathrm{circ},j,\mathrm{ac},4}(s)}{\tilde{I}_{\mathrm{circ},j,\mathrm{ref,ac},4}(s)} = \frac{K_{\mathrm{pt}}s^2 + K_{\mathrm{i2}}s + K_{\mathrm{pt}}\omega_{n4}^2}{L_o s^3 + (K_{\mathrm{pt}} + R_o)\,s^2 + (K_{\mathrm{i2}} + L_o\omega_{n4}^2)\,s + (K_{\mathrm{pt}} + R_o)\,\omega_{n4}^2}, \tag{4.32b}$$

where $K_{\mathrm{pt}} = K_{\mathrm{p1}} + K_{\mathrm{p2}}$. The gains of the circulating current controller K_{pt} and K_{i1} are tuned using the characteristic equation $s^3 + \dfrac{(K_{\mathrm{pt}} + R_o)}{L_o}s^2 + \dfrac{(K_{\mathrm{i1}} + L_o\omega_{n3}^2)}{L_o}s + \dfrac{(K_{\mathrm{pt}} + R_o)\,\omega_{n3}^2}{L_o}$, and K_{i2} is tuned using the characteristic equation $s^3 + \dfrac{(K_{\mathrm{pt}} + R_o)}{L_o}s^2 + \dfrac{(K_{\mathrm{i2}} + L_o\omega_{n4}^2)}{L_o}s + \dfrac{(K_{\mathrm{pt}} + R_o)\,\omega_{n4}^2}{L_o}$ such that the corresponding settling times are an order of magnitude greater than the settling time of the grid-side qd current controllers.

Considering only the dc components in (4.20i)-(4.20l) and using $\hat{\boldsymbol{i}}_{\mathrm{circ},abc,\mathrm{dc}} \approx \boldsymbol{i}_{\mathrm{circ},abc,\mathrm{dc}}$ results in

$$\boldsymbol{e}_{i,abc,\mathrm{dc}} = \left(\boldsymbol{i}_{\mathrm{circ},abc,\mathrm{ref,dc}} + \boldsymbol{i}_{\mathrm{circ},abc,\mathrm{ref,v,dc}} - \boldsymbol{i}_{\mathrm{circ},abc,\mathrm{dc}}\right), \tag{4.33a}$$

$$\boldsymbol{0} = \frac{\mathrm{d}^2\left(\boldsymbol{y}_{1,abc,\mathrm{dc}} - K_{\mathrm{p1}}\boldsymbol{e}_{i,abc,\mathrm{dc}}\right)}{\mathrm{d}t^2} - K_{\mathrm{i1}}\frac{\mathrm{d}\boldsymbol{e}_{i,abc,\mathrm{dc}}}{\mathrm{d}t} + \omega_{n3}^2\left(\boldsymbol{y}_{1,abc,\mathrm{dc}} - K_{\mathrm{p1}}\boldsymbol{e}_{i,abc,\mathrm{dc}}\right), \tag{4.33b}$$

$$\boldsymbol{0} = \frac{\mathrm{d}^2\left(\boldsymbol{y}_{2,abc,\mathrm{dc}} - K_{\mathrm{p}2}\boldsymbol{e}_{i,abc,\mathrm{dc}}\right)}{\mathrm{d}t^2} - K_{\mathrm{i}2}\frac{\mathrm{d}\boldsymbol{e}_{i,abc,\mathrm{dc}}}{\mathrm{d}t} + \omega_{n4}^2\left(\boldsymbol{y}_{2,abc,\mathrm{dc}} - K_{\mathrm{p}2}\boldsymbol{e}_{i,abc,\mathrm{dc}}\right), \tag{4.33c}$$

$$\boldsymbol{m}_{\mathrm{circ},abc,\mathrm{dc}} = \frac{1}{V_{\mathrm{dc}}}\left(\boldsymbol{y}_{1,abc,\mathrm{dc}} + \boldsymbol{y}_{2,abc,\mathrm{dc}}\right). \tag{4.33d}$$

Substituting for $x_{\mathrm{dc}} = \overline{X} + \delta x_{\mathrm{dc}}$ with $x = \boldsymbol{e}_{i,abc,\mathrm{dc}}, \boldsymbol{i}_{\mathrm{circ},abc,\mathrm{ref,v,dc}}, \boldsymbol{i}_{\mathrm{circ},abc,\mathrm{dc}}, \boldsymbol{y}_{1,abc,\mathrm{dc}}$, and $\boldsymbol{y}_{2,abc,\mathrm{dc}}$ in (4.33) results in

$$\delta\boldsymbol{e}_{i,abc,\mathrm{dc}} = \left(\delta\boldsymbol{i}_{\mathrm{circ},abc,\mathrm{ref,v,dc}} - \delta\boldsymbol{i}_{\mathrm{circ},abc,\mathrm{dc}}\right), \tag{4.34a}$$

$$\boldsymbol{0} = \omega_{n3}^2\left(\delta\boldsymbol{y}_{1,abc,\mathrm{dc}} - K_{\mathrm{p}1}\delta\boldsymbol{e}_{i,abc,\mathrm{dc}}\right), \tag{4.34b}$$

$$\boldsymbol{0} = \omega_{n4}^2\left(\delta\boldsymbol{y}_{2,abc,\mathrm{dc}} - K_{\mathrm{p}2}\delta\boldsymbol{e}_{i,abc,\mathrm{dc}}\right), \tag{4.34c}$$

$$\delta\boldsymbol{m}_{\mathrm{circ},abc,\mathrm{dc}} = \frac{1}{V_{\mathrm{dc}}}\left(\delta\boldsymbol{y}_{1,abc,\mathrm{dc}} + \delta\boldsymbol{y}_{2,abc,\mathrm{dc}}\right), \tag{4.34d}$$

where $\overline{\boldsymbol{E}}_{i,abc,\mathrm{dc}} = 0$, $\overline{\boldsymbol{I}}_{\mathrm{circ},abc,\mathrm{ref,v,dc}} = 0$, and $\overline{\boldsymbol{I}}_{\mathrm{circ},abc,\mathrm{dc}} = \boldsymbol{i}_{\mathrm{circ},abc,\mathrm{ref,dc}}$. Substituting for $\delta\boldsymbol{e}_{i,abc,\mathrm{dc}}$ from (4.34a) in (4.34b) and (4.34c) results in

$$\delta\boldsymbol{y}_{1,abc,\mathrm{dc}} = K_{\mathrm{p}1}\left(\delta\boldsymbol{i}_{\mathrm{circ},abc,\mathrm{ref,v,dc}} - \delta\boldsymbol{i}_{\mathrm{circ},abc,\mathrm{dc}}\right), \tag{4.35a}$$

$$\delta\boldsymbol{y}_{2,abc,\mathrm{dc}} = K_{\mathrm{p}2}\left(\delta\boldsymbol{i}_{\mathrm{circ},abc,\mathrm{ref,v,dc}} - \delta\boldsymbol{i}_{\mathrm{circ},abc,\mathrm{dc}}\right). \tag{4.35b}$$

Substituting for $\delta\boldsymbol{y}_{1,abc,\mathrm{dc}}$ and $\delta\boldsymbol{y}_{2,abc,\mathrm{dc}}$ from (4.35) in (4.34d) results in

$$\delta\boldsymbol{m}_{\mathrm{circ},abc,\mathrm{dc}} = \frac{1}{V_{\mathrm{dc}}}\left(K_{\mathrm{p}1} + K_{\mathrm{p}2}\right)\left(\delta\boldsymbol{i}_{\mathrm{circ},abc,\mathrm{ref,v,dc}} - \delta\boldsymbol{i}_{\mathrm{circ},abc,\mathrm{dc}}\right). \tag{4.36}$$

Based on $\hat{\boldsymbol{v}}_{cy,abc,\mathrm{dc}} \approx \boldsymbol{v}_{cy,abc,\mathrm{dc}} \forall y \in \{p, n\}$, $\hat{\boldsymbol{v}}^{\Sigma}_{\mathrm{c},abc,f,\mathrm{dc}} \approx \hat{\boldsymbol{v}}^{\Sigma}_{\mathrm{c},abc,\mathrm{dc}}$, (4.20h) is modified to

$$\delta\boldsymbol{i}_{\mathrm{circ},abc,\mathrm{ref,v,dc}} = 0.5K_{\mathrm{pv}}\delta\boldsymbol{v}^{\Sigma}_{\mathrm{c},abc,\mathrm{dc}}, \tag{4.37}$$

with $\overline{\boldsymbol{V}}^{\Sigma}_{\mathrm{c},abc,\mathrm{dc}} = 2v_{\mathrm{c,ref}}\boldsymbol{1}$. Substituting for $\delta\boldsymbol{i}_{\mathrm{circ},abc,\mathrm{ref,v,dc}}$ from (4.37) in (4.36) results in

$$\delta\boldsymbol{m}_{\mathrm{circ},abc,\mathrm{dc}} = \frac{1}{V_{\mathrm{dc}}}\left(K_{\mathrm{p1}} + K_{\mathrm{p2}}\right)\left(0.5K_{\mathrm{pv}}\delta\boldsymbol{v}^{\Sigma}_{\mathrm{c},abc,\mathrm{dc}} - \delta\boldsymbol{i}_{\mathrm{circ},abc,\mathrm{dc}}\right). \tag{4.38}$$

Based on (4.2c), (4.2e), and (4.38), the following per-phase state-space representation is derived:

$$\frac{\mathrm{d}}{\mathrm{d}t}\begin{pmatrix}\delta i_{\mathrm{circ},j,\mathrm{dc}}\\ \delta v^{\Sigma}_{\mathrm{c},j,\mathrm{dc}}\end{pmatrix} = A\begin{pmatrix}\delta i_{\mathrm{circ},j,\mathrm{dc}}\\ \delta v^{\Sigma}_{\mathrm{c},j,\mathrm{dc}}\end{pmatrix}, \tag{4.39}$$

where

$$A = \begin{pmatrix} -\dfrac{R_o + N\left(K_{\mathrm{p1}} + K_{\mathrm{p2}}\right)}{L_o} & -\dfrac{N}{2}\dfrac{\dfrac{1}{2} - \overline{M}_{\mathrm{circ},j} - \dfrac{\left(K_{\mathrm{p1}} + K_{\mathrm{p2}}\right)K_{\mathrm{pv}}}{N}}{L_o} \\ \dfrac{V_{\mathrm{dc}} + 2\dfrac{i_{\mathrm{dc}}}{3}\left(K_{\mathrm{p1}} + K_{\mathrm{p2}}\right) - 2\overline{M}_{\mathrm{circ},j}V_{\mathrm{dc}}}{C_{\mathrm{SM}}V_{\mathrm{dc}}} & -\dfrac{1}{R_pC_{\mathrm{SM}}} - \dfrac{i_{\mathrm{dc}}\left(K_{\mathrm{p1}} + K_{\mathrm{p2}}\right)K_{\mathrm{pv}}}{3C_{\mathrm{SM}}V_{\mathrm{dc}}} \end{pmatrix}.$$

Based on (4.39), the proportional controller gain K_{pv} is chosen such that the settling time of the system of (4.39) is an order of magnitude greater than the settling time of the current/voltage filters. The aforementioned constraints have been implicitly used in the derivation of (4.39).

The mathematical procedure to prove that mitigation of the second-order harmonic component of the circulating current results in the reduction of the voltage ripple, is explained in detail in Appendix A.

5. CONTROL OF THE MMC UNDER VARIABLE-FREQUENCY OPERATION

As compared with the fixed-frequency operation, control of the MMC under variable-frequency constant-current operation has its unique challenges. The main challenges are the magnitude of the SM capacitor voltage ripple that is inversely proportional to the frequency and, if not properly and actively mitigated, introduces instability and increases power losses and component sizes of the MMC. Based on the developments of Chapter 3, in this chapter, the MMC system subject to variable-frequency operation is modeled and analyzed, and two new strategies to control its operation are proposed. A comprehensive analysis of the two proposed strategies is provided and an optimization problem to establish the Pareto-optimal front, given the circuit parameters, is formulated in this chapter.

5.1 Statement of the Problem under Low-Frequency Operation

Neglecting R_p in (3.40c) and (3.40d), the derivative of the SM capacitor voltages of the upper and lower arms of phase-j is given by

$$\frac{\mathrm{d}v_{cp,j}}{\mathrm{d}t} = \frac{\left(i_{\mathrm{circ},j} + \frac{i_j}{2}\right)}{C_{\mathrm{SM}}} \left(\frac{1 - m_j - m_{\mathrm{cm}}}{2} - m_{\mathrm{circ},j}\right), \tag{5.1a}$$

$$\frac{\mathrm{d}v_{cn,j}}{\mathrm{d}t} = \frac{\left(i_{\mathrm{circ},j} - \frac{i_j}{2}\right)}{C_{\mathrm{SM}}} \left(\frac{1 + m_j + m_{\mathrm{cm}}}{2} - m_{\mathrm{circ},j}\right). \tag{5.1b}$$

Assuming $m_{\text{cm}} = 0$ and $m_{\text{circ},j} = 0$ in (5.1), the following expressions are obtained:

$$\begin{aligned}\frac{\mathrm{d}v_{cp,j}}{\mathrm{d}t} &= \frac{\left(i_{\text{circ},j} + \frac{i_j}{2}\right)}{C_{\text{SM}}}\left(\frac{1-m_j}{2}\right) \\ &= \frac{i_j}{4C_{\text{SM}}} - \frac{m_j i_{\text{circ},j}}{2C_{\text{SM}}} - \frac{m_j i_j}{4C_{\text{SM}}} + \frac{i_{\text{circ},j}}{2C_{\text{SM}}}, \end{aligned} \tag{5.2a}$$

$$\begin{aligned}\frac{\mathrm{d}v_{cn,j}}{\mathrm{d}t} &= \frac{\left(i_{\text{circ},j} - \frac{i_j}{2}\right)}{C_{\text{SM}}}\left(\frac{1+m_j}{2}\right) \\ &= -\frac{i_j}{4C_{\text{SM}}} + \frac{m_j i_{\text{circ},j}}{2C_{\text{SM}}} - \frac{m_j i_j}{4C_{\text{SM}}} + \frac{i_{\text{circ},j}}{2C_{\text{SM}}}. \end{aligned} \tag{5.2b}$$

Furthermore, assuming

$$i_j = I_o \cos\left(\omega_r t + \phi\right), \tag{5.3a}$$

$$m_j = m \cos\left(\omega_r t\right), \tag{5.3b}$$

$$i_{\text{circ},j} \approx \frac{i_{\text{dc}}}{3} = \frac{P_{\text{dc}}}{3V_{\text{dc}}} \approx \frac{P_{\text{ac}}}{3V_{\text{dc}}} \approx \frac{mI_o \cos\phi}{4}, \tag{5.3c}$$

in (5.2) and upon the subsequent integration of the modified equation, the peak-to-peak value of the SM capacitor voltage ripple is given by [75]

$$\delta v_{\text{c,pp}} = \frac{I_o}{2C_{\text{SM}}\omega_r}\left(1 - \left(\frac{m\cos\phi}{2}\right)^2\right)^{\frac{3}{2}}. \tag{5.4}$$

As shown in (5.4), the magnitude of the SM capacitor voltage ripple has inverse dependance on the ac-side frequency and direct dependance on the magnitude of the ac-side phase current. Consequently, in constant-torque applications, at low speeds, the magnitude of the voltage ripple becomes pronounced. This issue is less pronounced in quadrature-torque applications since the current magnitude is proportional to the frequency. Therefore, there is a need to actively mitigate the low-frequency components of the SM capacitor voltage ripple when the MMC is used in variable-speed constant-

torque applications, e.g., as the generator-side converter of the WECS during startup or whenever there is a need to build the turbine speed.

5.2 The Existing Capacitor Voltage Ripple Reduction Strategies and Their Limitations

In the technical literature, a few control strategies have been proposed/investigated to resolve the aforementioned issue [51–55]. Considering the common-mode voltage and the circulating current as two degrees of freedom, all of those solutions are based on injecting a common-mode voltage at the ac-side phase voltage and a circulating current in the phase-legs of the MMC to cancel the low-frequency components of the SM capacitor voltage ripple. In this chapter, the low-frequency components refer to the components whose frequencies are significantly smaller than the rated frequency of the machine.

5.2.1 Sine-Wave Strategy

A sinusoidal common-mode phase voltage and circulating current injection strategy is proposed in [51, 52, 54]. In this strategy, the common-mode phase voltage reference waveform and the reference for the circulating current are given by

$$m_{\mathrm{cm}} = M_{\mathrm{cm}} \sin\left(\omega_{\mathrm{cm}} t\right), \tag{5.5a}$$

$$i_{\mathrm{circ},j,\mathrm{ref}} = i_j \left(\frac{1 - m_j^2}{M_{\mathrm{cm}}}\right) \sin\left(\omega_{\mathrm{cm}} t\right) + \frac{m_j i_j}{2}, \tag{5.5b}$$

where M_{cm} and ω_{cm} are the magnitude and the angular frequency of the common-mode voltage, respectively. The reference waveforms used to control the voltages in

the upper and lower arms of phase-j to generate the common-mode voltage and the required circulating current are given by (3.1) and is repeated here for convenience:

$$m_{p,j} = \frac{1 - m_j - m_{\text{cm}}}{2} - m_{\text{circ},j}, \tag{5.6a}$$

$$m_{n,j} = \frac{1 + m_j + m_{\text{cm}}}{2} - m_{\text{circ},j}. \tag{5.6b}$$

Substituting for m_{cm} from (5.5a), $i_{\text{circ},j} \approx i_{\text{circ},j,\text{ref}}$ from (5.5b), and $m_{p,j}$ from (5.6a) in (5.1a), the derivative of the upper-arm phase-j SM capacitor voltages is deduced as

$$\begin{aligned}\frac{\mathrm{d}v_{cp,j}}{\mathrm{d}t} &= \frac{\left(i_{\text{circ},j} + \frac{i_j}{2}\right)}{C_{\text{SM}}}\left(\frac{1 - m_j - m_{\text{cm}}}{2} - m_{\text{circ},j}\right) \\ &= \frac{1}{C_{\text{SM}}}\left[\left(-\frac{m_j M_{\text{cm}}}{4} - \frac{M_{\text{cm}}}{4} + \frac{\left(1 - m_j - m_j^2 + m_j^3\right)}{2M_{\text{cm}}}\right) i_j \sin\left(\omega_{\text{cm}} t\right)\right. \\ &\quad \left. + \frac{\left(1 - m_j^2\right)}{4} i_j \cos\left(2\omega_{\text{cm}} t\right) - m_{\text{circ},j}\left(i_{\text{circ},j} + \frac{i_j}{2}\right)\right].\end{aligned} \tag{5.7}$$

The validity of $i_{\text{circ},j} \approx i_{\text{circ},j,\text{ref}}$ is under the assumption of a sufficiently fast closed-loop circulating current controller. Typically, $m_{\text{circ},j}$ in (5.7) is extremely small and is neglected. Considering appropriate phase shifts, similar expressions can be concluded for the derivative of the lower-arm phase-j SM capacitor voltages. As may be noticed from (5.7), the derivative of the upper-arm SM capacitor voltages does not contain low-frequency components. Upon integration of (5.7), the capacitor voltage ripple of the upper-arm SMs can be obtained, which will have an inverse dependance on the frequency of the components present in the derivative of the SM capacitor voltages. Thus, the absence of the low-frequency components in the derivative of the SM capacitor voltages reduces the magnitude of the capacitor voltage ripple. A similar deduction can also be extended to the lower-arm SM capacitor voltages.

Although by the sine-wave strategy, the magnitude of the SM capacitor voltage ripple is reduced, the large magnitude of the circulating current increases the converter

power losses as well as the rating values of the components. To resolve this problem, a square-wave strategy has been proposed in [55] that is explained in the following section.

5.2.2 Square-Wave Strategy

As opposed to the sinusoidal common-mode voltage and circulating current injection, to reduce the peak and rms values of the circulating current, a square-wave common-mode voltage and circulating current injection strategy is proposed in [55]. The main drawback of the square-wave strategy lies in the control of the circulating currents. The circulating current in phase-j, $i_{\text{circ},j}$, of the MMC is controlled by the voltage across the arm inductor that is given by $v_{\text{circ},j} = L_o \dfrac{\mathrm{d}i_{\text{circ},j}}{\mathrm{d}t}$. To inject a square-wave circulating current, at certain instants $v_{\text{circ},j} \to \infty$, which is impossible to attain. In reality, the maximum attainable $v_{\text{circ},j}$ is limited and depends on the MMC circuit parameters. This limitation, consequently, impacts the control of the circulating current and the magnitude of the SM capacitor voltage ripple. Furthermore, because of the finite rise/fall time of the square-wave circulating current, additional harmonic components are introduced into the circulating current that would further impact the results. To resolve the above-mentioned issues associated with the sine-wave and square-wave strategies, in the following section, two new strategies are proposed.

5.3 The Proposed Strategies

The proposed strategies are based on injecting a square-wave common-mode phase voltage whose corresponding reference waveform is expressed by

$$m_{\text{cm}} = \begin{cases} M_{\text{cm}} & \text{if } 0 < t' \leq \dfrac{1}{2f_{\text{cm}}} \\ -M_{\text{cm}} & \text{if } \dfrac{1}{2f_{\text{cm}}} < t' \leq \dfrac{1}{f_{\text{cm}}} \end{cases}, \tag{5.8}$$

where f_{cm} is the common-mode frequency and t' is the remainder of time, t, divided by $\frac{1}{f_{\text{cm}}}$. The distinction between the two new proposed strategies lies in the circulating current that is used to mitigate the low-frequency components of the SM capacitor voltage ripple, as explained in the following sections.

5.3.1 Strategy I

In this strategy, the reference for the sinusoidal circulating current with components in the vicinity of the common-mode frequency, is given by

$$i_{\text{circ},j,\text{ref}} = i_j \left(\frac{1 - m_j^2}{\frac{4}{\pi} M_{\text{cm}}} \right) \sin\left(\omega_{\text{cm}} t\right) + \frac{m_j i_j}{2}. \tag{5.9}$$

The square-wave common-mode reference waveform in (5.8) can be expressed by its Fourier series expansion as

$$m_{\text{cm}} = \sum_{k=0}^{\infty} \frac{4 M_{\text{cm}}}{\pi \left(2k+1\right)} \sin\left\{\left(2k+1\right) \omega_{\text{cm}} t\right\}. \tag{5.10}$$

Substituting for m_{cm} from (5.10) in (5.6) results in

$$m_{p,j} = \frac{1 - m_j - \sum_{k=0}^{\infty} \frac{4 M_{\text{cm}}}{\pi \left(2k+1\right)} \sin\left\{\left(2k+1\right) \omega_{\text{cm}} t\right\}}{2} - m_{\text{circ},j}, \tag{5.11a}$$

$$m_{n,j} = \frac{1 + m_j + \sum_{k=0}^{\infty} \frac{4 M_{\text{cm}}}{\pi \left(2k+1\right)} \sin\left\{\left(2k+1\right) \omega_{\text{cm}} t\right\}}{2} - m_{\text{circ},j}. \tag{5.11b}$$

Substituting for $m_{p,j}$ from (5.11a), and for $i_{\text{circ},j} \approx i_{\text{circ},j,\text{ref}}$ from (5.9) in (5.1a) results in

$$\begin{aligned}\frac{\mathrm{d}v_{cp,j}}{\mathrm{d}t} = \frac{1}{C_{\text{SM}}}\Bigg[&-m_{\text{circ},j}\left(i_{\text{circ},j}+\frac{i_j}{2}\right)+\frac{\pi}{8M_{\text{cm}}}i_j\left(1-m_j\right)\left(1-m_j^2\right)\sin\left(\omega_{\text{cm}}t\right)\\&+\frac{i_j}{4}\left(1-m_j^2\right)\cos\left(2\omega_{\text{cm}}t\right)-\frac{1}{2}\sum_{k=1}^{\infty}\frac{i_j\sin\left(\omega_{\text{cm}}t\right)}{2k+1}\sin\left\{\left(2k+1\right)\omega_{\text{cm}}t\right\}\left(1-m_j^2\right)\\&-\frac{i_j}{4}\left(1+m_j\right)\sum_{k=0}^{\infty}\frac{4M_{\text{cm}}}{\pi\left(2k+1\right)}\sin\left\{\left(2k+1\right)\omega_{\text{cm}}t\right\}\Bigg].\end{aligned} \tag{5.12}$$

As shown by (5.12), the frequency spectrum of the derivative of the upper-arm SM capacitor voltages is shifted to the vicinity of f_{cm}, which assists in reducing the magnitude of the upper-arm SM capacitor voltage ripple. A similar deduction can also be extended to the lower-arm SM capacitor voltage ripple.

5.3.2 Strategy II

In this strategy, the reference for the sinusoidal circulating current with components in the vicinity of the common-mode frequency and a third harmonic of the common-mode frequency, is given by

$$i_{\text{circ},j,\text{ref}} = i_j\left(m_1\sin\left(\omega_{\text{cm}}t\right)+m_3\sin\left(3\omega_{\text{cm}}t\right)\right)\left(\frac{1-m_j^2}{\frac{4}{\pi}M_{\text{cm}}}\right)+\frac{m_j i_j}{2}. \tag{5.13}$$

m_1 and m_3 in (5.13) are determined to minimize the rms value of circulating current and to mitigate the low-frequency components of the SM capacitor voltage ripple.

Substituting for $m_{p,j}$ from (5.11a), and for $i_{\text{circ},j} \approx i_{\text{circ},j,\text{ref}}$ from (5.13) in (5.1a) results in

$$\begin{aligned}\frac{\mathrm{d}v_{cp,j}}{\mathrm{d}t} = -\frac{1}{C_{\text{SM}}}\Bigg[& m_{\text{circ},j}\left(i_{\text{circ},j}+\frac{i_j}{2}\right) - \frac{i_j}{4}\left(1+m_j\right)\sum_{k=0}^{\infty}\frac{4M_{\text{cm}}}{\pi\left(2k+1\right)}\sin\left\{\left(2k+1\right)\omega_{\text{cm}}t\right\} \\ & + \left(1-m_j\right)\frac{\pi i_j\left(1-m_j^2\right)}{8M_{\text{cm}}}\left(m_1\sin\left(\omega_{\text{cm}}t\right)+m_3\sin\left(3\omega_{\text{cm}}t\right)\right) \\ & + \frac{i_j\left(1-m_j^2\right)}{2}\left(\left(\frac{m_1}{3}-\frac{m_3}{2}\right)\cos\left(2\omega_{\text{cm}}t\right)+\left(\frac{m_1}{6}+\frac{m_3}{2}\right)\cos\left(4\omega_{\text{cm}}t\right)\right) \\ & - \frac{i_j\left(1-m_j^2\right)}{2}\left(m_1\sin\left(\omega_{\text{cm}}t\right)+m_3\sin\left(3\omega_{\text{cm}}t\right)\right)\sum_{k=2}^{\infty}\frac{1}{\left(2k+1\right)}\sin\left\{\left(2k+1\right)\omega_{\text{cm}}t\right\} \\ & + \frac{i_j\left(1-m_j^2\right)}{2}\frac{m_3}{6}\cos\left(6\omega_{\text{cm}}t\right) + \frac{i_j\left(1-m_j^2\right)}{4}\left(1-m_1-\frac{m_3}{3}\right)\Bigg]. \end{aligned} \tag{5.14}$$

To mitigate the low-frequency components of the SM capacitor voltage ripple, the last term in (5.14) should be enforced to zero, i.e.,

$$1 - m_1 - \frac{m_3}{3} = 0. \tag{5.15}$$

Also, as shown by (5.13), to minimize the rms value of the circulating currents, $m_1^2+m_3^2$ needs to be minimized. Therefore, the coefficients, m_1 and m_3, are determined by

$$\begin{aligned} &\text{Minimize } m_1^2 + m_3^2 \\ &\text{subject to } m_1 + \frac{m_3}{3} = 1 \end{aligned} \tag{5.16}$$

Solving (5.16) gives $m_1 = 0.9$ and $m_3 = 0.3$. Substituting for m_1 and m_3 in (5.14), the derivative of the upper-arm SM capacitor voltages is given by

$$\begin{aligned}\frac{\mathrm{d}v_{cp,j}}{\mathrm{d}t} = &-m_{\mathrm{circ},j}\left(i_{\mathrm{circ},j} + \frac{i_j}{2}\right) - \frac{i_j}{4}\left(1 + m_j\right)\sum_{k=0}^{\infty}\frac{4M_{\mathrm{cm}}}{\pi\left(2k+1\right)}\sin\left\{\left(2k+1\right)\omega_{\mathrm{cm}}t\right\} \\ &+ \left(1 - m_j\right)\frac{\pi i_j\left(1 - m_j^2\right)}{8M_{\mathrm{cm}}}\left(0.9\sin\left(\omega_{\mathrm{cm}}t\right) + 0.3\sin\left(3\omega_{\mathrm{cm}}t\right)\right) \\ &+ \frac{i_j\left(1 - m_j^2\right)}{2}\left(0.15\cos\left(2\omega_{\mathrm{cm}}t\right) + 0.3\cos\left(4\omega_{\mathrm{cm}}t\right) + 0.05\cos\left(6\omega_{\mathrm{cm}}t\right)\right) \\ &- \frac{i_j\left(1 - m_j^2\right)}{2}\left(0.9\sin\left(\omega_{\mathrm{cm}}t\right) + 0.3\sin\left(3\omega_{\mathrm{cm}}t\right)\right)\sum_{k=2}^{\infty}\frac{1}{\left(2k+1\right)}\sin\left\{\left(2k+1\right)\omega_{\mathrm{cm}}t\right\}.\end{aligned} \tag{5.17}$$

As indicated by (5.17), under low-frequency operation, the frequency spectrum of the derivative of the upper-arm SM capacitor voltages is shifted to the vicinity of f_{cm}, thereby, reducing the magnitude of the upper-arm SM capacitor voltage ripple. A similar deduction can also be extended to the lower-arm SM capacitor voltage ripple.

5.3.3 Comparison of the Proposed Strategies with the Existing Strategy and Formulation of an Optimization Problem

As discussed in Section 5.2, the square-wave strategy in [55] does not provide the expected results. So the performance of the proposed strategies are compared against the sine-wave strategy in [51]. Assuming the same peak value for the common-mode voltage reference waveforms of the two proposed strategies and the sine-wave strategy, i.e., the same M_{cm}, the resultant reduction in the peak value of the circulating current is 21.5 % and 33.8 %, respectively. The squared rms value of the circulating current, which is proportional to the conduction losses of the converter, is reduced by 38% and 44.2%, respectively. However, as compared to Strategy I, Strategy II requires a higher $m_{\mathrm{circ},j}$, which, subsequently, limits the peak value of the common-mode voltage reference M_{cm}. To determine the peak value of the common-mode voltage for each of

the proposed strategies, the following constraint that represents the viable range of the upper-arm reference waveform, should be satisfied:

$$\begin{aligned} & 0 \leq m_{p,j} \leq 1 \\ \Longrightarrow & 0 \leq \frac{1 - m_j - m_{\mathrm{cm}}}{2} - m_{\mathrm{circ},j} \leq 1. \end{aligned} \tag{5.18}$$

Based on (5.18), the limits of the common-mode voltage reference waveform and, subsequently, the peak and squared rms values of the circulating currents of the three strategies are shown in Table 5.1. The variable x in Table 5.1 is defined as $x = \dfrac{4 I_o L_o \omega_{\mathrm{cm}}}{V_{\mathrm{dc}} (1-m)^2}$.

Table 5.1.
Comparison of the two proposed strategies with the sine-wave strategy

Strategy	M_{cm}	$i_{\mathrm{circ},j,\mathrm{peak}}$	$i^2_{\mathrm{circ},j,\mathrm{rms}}$
Strategy I	$\frac{(1-m)}{2}\left(1+\sqrt{1-0.5\pi x}\right)$	$I_{\mathrm{cm1,NM1}} = \frac{2I_{\mathrm{cm1,NM1}},}{\frac{\pi I_o}{4(1-m)\left(1+\sqrt{1-0.5\pi x}\right)}}$	$I^2_{\mathrm{cm1,NM1}}$
Strategy II	$\frac{(1-m)}{2}\left(1+\sqrt{1-0.9\pi x}\right)$	$I_{\mathrm{cm1,NM2}} = \frac{1.874\ I_{\mathrm{cm1,NM2}},}{\frac{0.9\pi I_o}{4(1-m)\left(1+\sqrt{1-0.9\pi x}\right)}}$	$\frac{10}{9} I^2_{\mathrm{cm1,NM2}}$
Sine-Wave Strategy in [51]	$\frac{(1-m)}{2}\left(1+\sqrt{1-2x}\right)$	$I_{\mathrm{cm1,sine}} = \frac{2I_{\mathrm{cm1,sine}},}{\frac{I_o}{(1-m)\left(1+\sqrt{1-2x}\right)}}$	$I^2_{\mathrm{cm1,sine}}$

As shown in Table 5.1, the value of M_{cm}, and the peak and squared rms values of the circulating current depend on the strategy and the common-mode frequency. Therefore, for variable-frequency operation of the MMC, a multi-objective optimization procedure is required to make a tradeoff among the various strategies and common-mode frequencies using the performance indices such as the magnitude

of SM capacitor voltage ripple and the peak/rms values of the circulating currents. That is,

$$\boldsymbol{x} = \begin{pmatrix} \text{strategy} \\ f_{\text{cm}} \end{pmatrix}$$

$$\underset{\boldsymbol{x}}{\text{minimize}}\ \boldsymbol{F}(\boldsymbol{x}) = \begin{pmatrix} \delta v_{\text{c,pp}}(\boldsymbol{x}) \\ i_{\text{circ},j,\text{rms}}(\boldsymbol{x})^2 \\ i_{\text{circ},j,\text{peak}}(\boldsymbol{x}) \end{pmatrix} \tag{5.19}$$

$$\text{subject to } 0 \leq m_{p,j}(\boldsymbol{x}) \leq 1 \ \text{ and}$$

$$0 \leq m_{n,j}(\boldsymbol{x}) \leq 1$$

These performance indices are calculated from (5.5b), (5.7), (5.9), (5.12), (5.13), and (5.17) for the three different strategies. This multi-objective optimization leads to a Pareto-optimal front.

For a variable-speed constant-torque drive application, an offline optimization can be run at various operating ac-side low frequencies and for a given set of MMC parameters to generate the Pareto-optimal front at each operating frequency. From this Pareto front, the best strategy and the common-mode frequency at each operating ac-side frequency can be chosen depending upon the application requirements and saved in a look-up table. While the system runs, based on the operating ac-side frequency, the appropriate strategy and common-mode frequency can be selected from the look-up table. The block diagram of the MMC control system is shown in Fig. 5.1. The optimal circulating current and common-mode voltage reference generator and the control of circulating current and common-mode voltage are shown in Fig. 5.1. The block diagram of the machine *qd* current controller is shown in Fig. 5.2.

In the wind energy conversion system of Fig. 2.1 with the MMC as the generator-side converter, the aforementioned control system is required only during startup or whenever the turbine speed needs to be built up. Otherwise, the quadrature torque

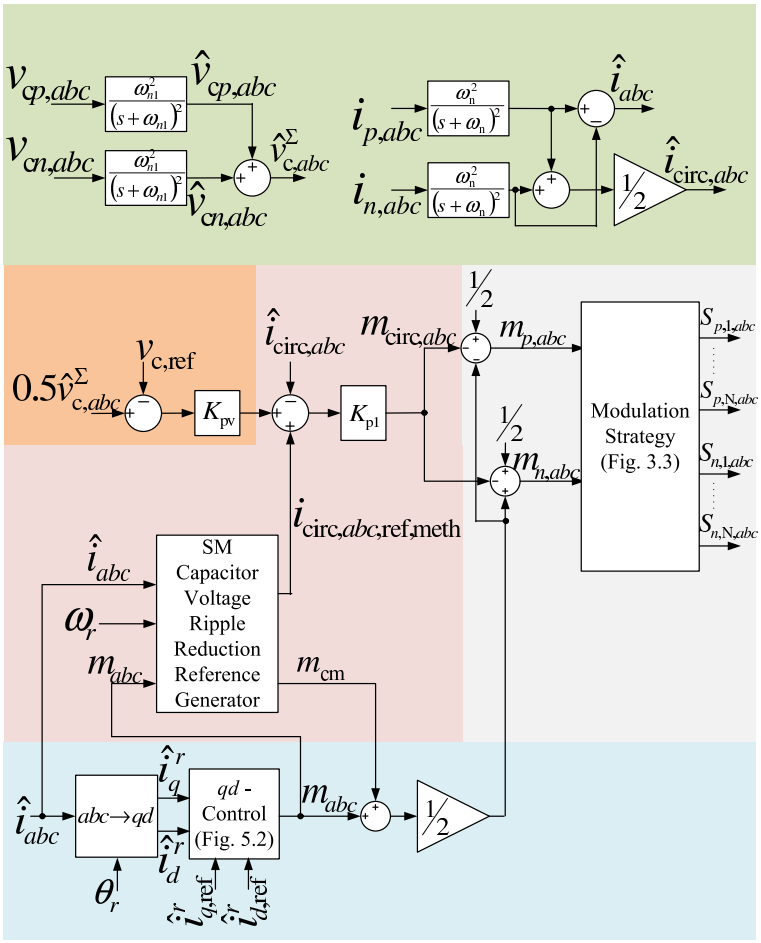

Fig. 5.1. Block diagram of the MMC control system.

helps keep the magnitude of SM capacitor voltage ripple under required constraints and the control system employed may resemble that described in Chapter 4.

5.4 Controller Design Methodology

The summary of the MMC control system to drive a machine during constant-torque low-speed operation is shown in Fig. 5.1. The block diagram of the machine *qd* current controller is shown in Fig. 5.2.

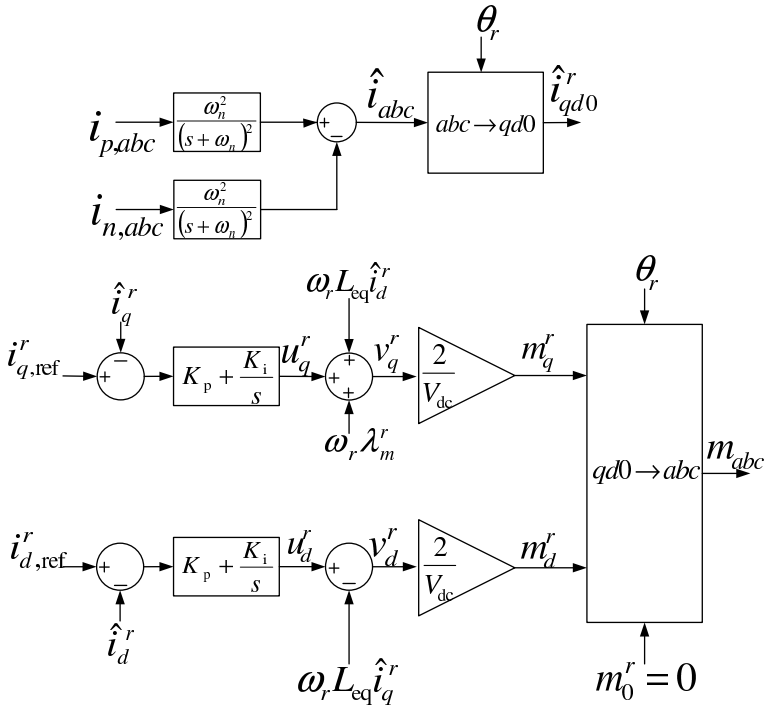

Fig. 5.2. Block diagram of the machine qd current controllers.

5.4.1 Machine Current Controller

Similar to (4.9) and (4.13) that describe the ac-side current dynamics in qd grid-reference frame, the dynamics of the ac-side currents of the MMC with machine load in qd rotor-reference frame, is given by

$$L_{\text{eq}} \frac{\mathrm{d}\boldsymbol{i}^r_{qd}}{\mathrm{d}t} + R_{\text{eq}} \boldsymbol{i}^r_{qd} = \boldsymbol{u}^r_{qd}, \tag{5.20}$$

where

$$\boldsymbol{u}^r_{qd} = \boldsymbol{m}^e_{qd} \frac{V_{\text{dc}}}{2} - \boldsymbol{e}^r_{qd} - \omega_r L_{\text{eq}} \boldsymbol{X}_1 \boldsymbol{i}^r_{qd}, \tag{5.21a}$$

$$L_{\text{eq}} = \left(L_{\text{load}} + \frac{L_o}{2} \right), \tag{5.21b}$$

$$R_{\text{eq}} = \left(R_{\text{load}} + \frac{R_o}{2} \right). \tag{5.21c}$$

With a balanced three-phase ac-side load,

$$i_0^r = m_0^r = e_0^r = 0. \tag{5.22}$$

The back-emf $\boldsymbol{e}_{abc}$ is given by

$$\boldsymbol{e}_{abc} = \begin{pmatrix} \omega_r \lambda_m^r \cos(\theta_r) \\ \omega_r \lambda_m^r \cos\left(\theta_r - \dfrac{2\pi}{3}\right) \\ \omega_r \lambda_m^r \cos\left(\theta_r + \dfrac{2\pi}{3}\right) \end{pmatrix}. \tag{5.23}$$

That is,

$$\boldsymbol{e}_{qd}^r = \begin{pmatrix} \omega_r \lambda_m^r \\ 0 \end{pmatrix}. \tag{5.24}$$

A standard PI controller given by

$$K_\mathrm{p} + \frac{K_\mathrm{i}}{s}, \tag{5.25}$$

is used to control the machine qd currents, as summarized in Fig. 5.2. The machine qd current controller is similar to the grid-side qd current controller. That is, the closed-loop machine qd current control system may be derived on the lines similar to the derivation in Section 4.2 of Chapter 4. The closed-loop machine qd current control system is shown in Fig. 5.3. The characteristic equation of the system in Fig. 5.3 is given by

$$s^2 + \left(\frac{R_\mathrm{eq} + K_\mathrm{p}}{L_\mathrm{eq}}\right) s + \left(\frac{K_\mathrm{i}}{L_\mathrm{eq}}\right). \tag{5.26}$$

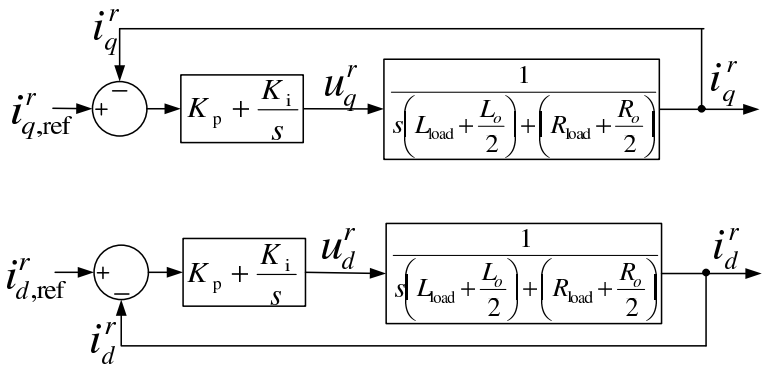

Fig. 5.3. Block diagram of the closed-loop machine qd current control system.

The settling time t_s and damping constant δ of the system, whose characteristic function is defined by (5.26), are then given by

$$t_\mathrm{s} = 8\left(\frac{L_\mathrm{eq}}{K_\mathrm{p} + R_\mathrm{eq}}\right), \tag{5.27a}$$

$$\delta = \frac{R_\mathrm{eq} + K_\mathrm{p}}{2\sqrt{K_\mathrm{i} L_\mathrm{eq}}}. \tag{5.27b}$$

Substituting a given settling time $t_\mathrm{s,out}$ and damping constant δ_out in (5.27), the PI controller parameters in the machine qd current controller are given by

$$K_\mathrm{p} = 8\left(\frac{L_\mathrm{eq}}{t_\mathrm{s,out}}\right) - R_\mathrm{eq}, \tag{5.28a}$$

$$K_\mathrm{i} = \frac{(R_\mathrm{eq} + K_\mathrm{p})^2}{4\delta_\mathrm{out}^2 L_\mathrm{eq}}. \tag{5.28b}$$

5.4.2 Circulating Current Controller

Based on the circulating current controller shown in Fig. 5.1, the output of the controller $\boldsymbol{m}_{\mathrm{circ},abc}$ is given by

$$\boldsymbol{m}_{\mathrm{circ},abc} = \frac{K_\mathrm{p1}}{V_\mathrm{dc}}\left(\boldsymbol{i}_{\mathrm{circ},abc,\mathrm{ref}} - \hat{\boldsymbol{i}}_{\mathrm{circ},abc}\right), \tag{5.29a}$$

$$\boldsymbol{0} = \frac{\mathrm{d}^2\hat{\boldsymbol{i}}_{\mathrm{circ},abc}}{\mathrm{d}t^2} + 2\omega_n\frac{\mathrm{d}\hat{\boldsymbol{i}}_{\mathrm{circ},abc}}{\mathrm{d}t} + \omega_n^2\left(\hat{\boldsymbol{i}}_{\mathrm{circ},abc} - \boldsymbol{i}_{\mathrm{circ},abc}\right), \tag{5.29b}$$

$$\boldsymbol{0} = \frac{\mathrm{d}^2\hat{\boldsymbol{v}}_{cy,abc}}{\mathrm{d}t^2} + 2\omega_{n1}\frac{\mathrm{d}\hat{\boldsymbol{v}}_{cy,abc}}{\mathrm{d}t} + \omega_{n1}^2\left(\hat{\boldsymbol{v}}_{cy,abc} - \boldsymbol{v}_{cy,abc}\right), y \in \{p,n\}, \tag{5.29c}$$

$$\hat{\boldsymbol{v}}^{\Sigma}_{\mathrm{c},abc} = \hat{\boldsymbol{v}}_{cp,abc} + \hat{\boldsymbol{v}}_{\mathrm{c}n,abc}, \tag{5.29d}$$

$$\boldsymbol{i}_{\mathrm{circ},abc,\mathrm{ref}} = K_{\mathrm{pv}}\left(0.5\hat{\boldsymbol{v}}^{\Sigma}_{\mathrm{c},abc} - v_{\mathrm{c,ref}}\boldsymbol{1}\right) + \boldsymbol{i}_{\mathrm{circ},abc,\mathrm{ref,meth}}, \tag{5.29e}$$

where $\boldsymbol{i}_{\mathrm{circ},abc,\mathrm{ref,meth}}$ depends upon the strategy chosen from Section 5.3 in constant torque low-speed operation. Approximating the impact of the filters, that is, assuming

$$\hat{\boldsymbol{i}}_{\mathrm{circ},abc} \approx \boldsymbol{i}_{\mathrm{circ},abc}, \tag{5.30a}$$

$$\hat{\boldsymbol{v}}_{cy,abc} \approx \boldsymbol{v}_{cy,abc}, y \in \{p,n\} \tag{5.30b}$$

in (5.29) results in

$$\boldsymbol{m}_{\mathrm{circ},abc} = \frac{K_{\mathrm{p1}}}{V_{\mathrm{dc}}}\left(K_{\mathrm{pv}}\left(0.5\boldsymbol{v}^{\Sigma}_{\mathrm{c},abc} - v_{\mathrm{c,ref}}\boldsymbol{1}\right) + \boldsymbol{i}_{\mathrm{circ},abc,\mathrm{ref,meth}} - \boldsymbol{i}_{\mathrm{circ},abc}\right). \tag{5.31}$$

Substituting for $x = \overline{X} + \delta x_{\mathrm{dc}} + \tilde{x}_{\mathrm{ac}}$ with $x = \boldsymbol{m}_{\mathrm{circ},abc}$, $\boldsymbol{i}_{\mathrm{circ},abc}$, $\boldsymbol{i}_{\mathrm{circ},abc,\mathrm{ref,meth}}$, and $\boldsymbol{v}^{\Sigma}_{\mathrm{c},abc}$ in (5.31) results in

$$\delta\boldsymbol{m}_{\mathrm{circ},abc,\mathrm{dc}} = \frac{K_{\mathrm{p1}}}{V_{\mathrm{dc}}}\left(0.5K_{\mathrm{pv}}\delta\boldsymbol{v}^{\Sigma}_{\mathrm{c},abc,\mathrm{dc}} - \delta\boldsymbol{i}_{\mathrm{circ},abc,\mathrm{dc}}\right), \tag{5.32a}$$

$$\tilde{\boldsymbol{m}}_{\mathrm{circ},abc,\mathrm{ac}} = \frac{K_{\mathrm{p1}}}{V_{\mathrm{dc}}}\left(0.5K_{\mathrm{pv}}\tilde{\boldsymbol{v}}^{\Sigma}_{\mathrm{c},abc,\mathrm{ac}} + \tilde{\boldsymbol{i}}_{\mathrm{circ},abc,\mathrm{ref,meth,ac}} - \tilde{\boldsymbol{i}}_{\mathrm{circ},abc,\mathrm{ac}}\right), \tag{5.32b}$$

with $\overline{M}_{\mathrm{circ},abc} = 0$, $\overline{\boldsymbol{I}}_{\mathrm{circ},abc} = \overline{\boldsymbol{I}}_{\mathrm{circ},abc,\mathrm{ref,meth}}$, and $\overline{\boldsymbol{V}}^{\Sigma}_{\mathrm{c},abc} = 2v_{\mathrm{c,ref}}\boldsymbol{1}$. Under the assumption that $\tilde{\boldsymbol{v}}^{\Sigma}_{\mathrm{c},abc,\mathrm{ac}}$ is small, (5.32b) can be rewritten as

$$\tilde{\boldsymbol{m}}_{\mathrm{circ},abc,\mathrm{ac}} \approx \frac{K_{\mathrm{p1}}}{V_{\mathrm{dc}}}\left(\tilde{\boldsymbol{i}}_{\mathrm{circ},abc,\mathrm{ref,meth,ac}} - \tilde{\boldsymbol{i}}_{\mathrm{circ},abc,\mathrm{ac}}\right). \tag{5.33}$$

Applying Laplace transform to (5.33) results in

$$\tilde{\boldsymbol{M}}_{\mathrm{circ},abc,\mathrm{ac}}(s) = \frac{K_{\mathrm{p1}}}{V_{\mathrm{dc}}}\left(\tilde{\boldsymbol{I}}_{\mathrm{circ},abc,\mathrm{ref,meth,ac}}(s) - \tilde{\boldsymbol{I}}_{\mathrm{circ},abc,\mathrm{ac}}(s)\right). \tag{5.34}$$

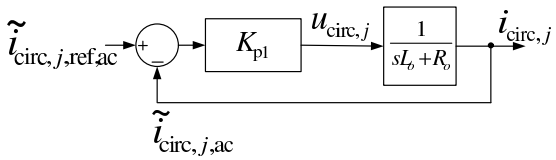

Fig. 5.4. Block diagram of the closed-loop control system of the ac components of the circulating currents.

The dynamics of the ac components of the circulating current is obtained from Section 4.3 in Chapter 4. The closed-loop control system of the ac components of the circulating currents, which is described by (5.34) and (4.30), is summarized in Fig. 5.4.

The transfer function of the closed-loop control system shown in Fig. 5.4, is given by

$$\frac{K_{\text{p1}}}{sL_o + R_o + K_{\text{p1}}}. \tag{5.35}$$

The settling time and time constant of the closed-loop circulating current control system described by (5.35) are given by

$$t_{\text{s,int}} = \frac{5L_o}{R_o + K_{\text{p1}}}, \text{ and} \tag{5.36a}$$

$$T_{\text{con}} = \frac{L_o}{R_o + K_{\text{p1}}}, \tag{5.36b}$$

respectively. The design of the proportional controller gain K_{p1} depends upon the desired characteristics of the closed-loop circulating current control system that include:

1. The settling time of the closed-loop circulating current control system should satisfy

$$t_{\text{s,filter}} \ll t_{\text{s,int}} \ll t_{\text{s,out}}, \tag{5.37}$$

where $t_{\text{s,filter}}$ represents the settling time of the current/voltage filters used to remove high-frequency measurement noise in the arm currents and/or SM capacitor voltages. The condition given by (5.37) ensures that the closed-loop control system of (5.35) settles much faster than the closed-loop machine qd current control system and much slower than the current/voltage filter.

2. The closed-loop control system should not attenuate the common-mode frequency components in the circulating currents. That is, the inverse of the time constant of the closed-loop circulating current control system is

$$\frac{1}{T_{\text{con}}} = \frac{K_{\text{p1}} + R_o}{L_o} \gg 2\pi f_{\text{cm}}. \tag{5.38}$$

Based on (5.37), the minimum and maximum settling times, $t_{\text{s,int,max}}$ and $t_{\text{s,int,min}}$ are defined as

$$t_{\text{s,int,max}} = \frac{t_{\text{s,out}}}{5}, \tag{5.39a}$$

$$t_{\text{s,int,min}} = 5t_{\text{s,filter}}. \tag{5.39b}$$

Let $K_{\text{p1,min}_1}$ and $K_{\text{p1,max}}$ be the proportional controller gains corresponding to $t_{\text{s,int}} = t_{\text{s,int,min}}$ and $t_{\text{s,int}} = t_{\text{s,int,max}}$, respectively. Then, based on (5.39) and (5.36a),

$$K_{\text{p1,min}_1} = 5\frac{L_o}{\frac{t_{\text{s,out}}}{5}} - R_o, \tag{5.40a}$$

$$K_{\text{p1,max}} = 5\frac{L_o}{5t_{\text{s,filter}}} - R_o. \tag{5.40b}$$

Based on (5.38), the maximum time constant of the closed-loop circulating current control system is defined as

$$T_{\text{con,max}} = \frac{1}{10 \times 2\pi f_{\text{cm}}}. \tag{5.41}$$

The corresponding proportional controller gain, $K_{\mathrm{p1,min_2}}$, based on (5.41) and (5.36b), is

$$K_{\mathrm{p1,min_2}} = 10 \times 2\pi f_{\mathrm{cm}} L_o - R_o. \tag{5.42}$$

The constraints on K_{p1} are given by

$$\max\left\{K_{\mathrm{p1,min_1}}, K_{\mathrm{p1,min_2}}\right\} < K_{\mathrm{p1}} < K_{\mathrm{p1,max}} \tag{5.43}$$

The control of the dc components of the circulating current and SM capacitor voltages is similar to the one described in Section 4.3 of Chapter 4, as may be noticed by comparing (5.32a) to (4.38). That is, if $K_{\mathrm{p1}} + K_{\mathrm{p2}}$ is replaced with K_{p1} in (4.39), then the modified expression represents the closed-loop control system of the dc components of the circulating current and SM capacitor voltages. The aforementioned system may be used to choose K_{pv} as was explained in Section 4.3 of Chapter 4.

The stability analysis of the MMC control system to drive a machine during constant-torque low-speed operation is performed in Appendix B.

6. OPTIMAL CONTROL

The controller gains of the MMC control system in Chapters 4 and 5 are designed such that the MMC system is stable. The design procedure utilizes the approximate per-phase MMC state-space model. Furthermore, it neglects (i) the higher-order terms in the Taylor series expansion of the aforementioned MMC state-space model, and (ii) the small terms in the Fourier series expansion of the linearized model. This controller design procedure may not generate the controller gains that lead to the optimal performance of the MMC system.

The optimization of the controller gains of a class of non-linear non-autonomous hybrid system is considered in this chapter. The system of MMC described by the advanced MMC state-space model and its controllers described in Chapters 4 and 5, are examples of the aforementioned class of the hybrid system.

Glossary of terms

States of the system	$\boldsymbol{x} \in \mathbb{R}^n$
States of the controller	$\boldsymbol{x}_{\mathrm{c}} \in \mathbb{R}^c$
Outputs of the controller	$\boldsymbol{u}_1 \in \Omega^{u_1} = [-1,1]^{u_1} \subset \mathbb{R}^{u_1}$
	$\boldsymbol{u}_2 \in \Omega^{u_2} = [-1,1]^{u_2} \subset \mathbb{R}^{u_2}$
	$\boldsymbol{u} \in \Omega^{u} = [-1,1]^{u} \subset \mathbb{R}^{u}$
Decision variables	$\boldsymbol{K} \in \Omega^K \subset \mathbb{R}^K$
Cost function	$L : \mathbb{R}^n \to \mathbb{R}$
Total cost function	$J : \Omega^K \to \Omega \subset \mathbb{R}$
Tangent to state trajectory	$\boldsymbol{f} : \mathbb{R}^n \times \Omega^u \times \mathbb{R} \to \mathbb{R}^n$
Controller state function	$\boldsymbol{g} : \mathbb{R}^c \times \mathbb{R}^n \times \Omega^K \times \mathbb{Z} \to \mathbb{R}^c$

Controller output functions	$\boldsymbol{h}_1 : \mathbb{R}^c \times \Omega^K \times \mathbb{Z} \to \Omega^{u_1}$
	$\boldsymbol{h}_2 : \Omega^{u_1} \times \mathbb{R}^c \times \Omega^K \times \mathbb{Z} \to \Omega^{u_2}$
	$\boldsymbol{h} : \Omega^{u_1} \times \Omega^{u_2} \to \Omega^u$
Control period	T_{sc}

6.1 Hybrid System and Cosimulation

In this chapter, a class of non-linear non-autonomous hybrid system with continuous-time system states and discrete-time control states is considered. The motivation to use discrete-time control states lies in the digital implementation of the controllers of many practical systems. Instead of a continuous-time system and control state-space model, the use of a hybrid system state-space model allows for parallel computation of the system and control states, which can increase the speed of simulation. The hybrid system state-space model also improves the accuracy of the calculated states as it represents a model closer to the real model.

To optimize the gains of the controller of the aforementioned class of hybrid system, the following variational quadratic regulator problem is considered:

$$\underset{\boldsymbol{K}}{\text{minimize}}\ J\left(\boldsymbol{K}\right) = \sum_{k=0}^{N_{\text{t}}} L\left(\boldsymbol{x}_c[k]\right) T_{\text{sc}} \tag{6.1a}$$

$$\text{subject to}\ \frac{\mathrm{d}\boldsymbol{x}(t)}{\mathrm{d}t} = \boldsymbol{f}\left(\boldsymbol{x}(t), \boldsymbol{u}[k], t\right),\ kT_{\text{sc}} \leq t < (k+1)T_{\text{sc}}, \tag{6.1b}$$

$$\boldsymbol{x}_{\text{c}}[k] = \boldsymbol{g}\left(\boldsymbol{x}_{\text{c}}[k-1], \boldsymbol{x}[k-1], \boldsymbol{K}, k\right), \tag{6.1c}$$

$$\boldsymbol{u}_1[k] = \boldsymbol{h}_1\left(\boldsymbol{x}_{\text{c}}[k], \boldsymbol{K}, k\right), \tag{6.1d}$$

$$\boldsymbol{u}_2[k] = \boldsymbol{h}_2\left(\boldsymbol{u}_1[k], \boldsymbol{x}_{\text{c}}[k], \boldsymbol{K}, k\right), \tag{6.1e}$$

$$\boldsymbol{u}[k] = \boldsymbol{h}\left(\boldsymbol{u}_1[k], \boldsymbol{u}_2[k]\right). \tag{6.1f}$$

The constraints in the optimization problem in (6.1), that is (6.1b)-(6.1f), define the dynamics of the hybrid system. The optimization problem in (6.1) is solved using gradient-based optimization algorithms that require determination of the gradient of the cost function defined in (6.1). The gradient-based optimization algorithms also require an initial guess for the gains of the controller (the decision variable) that al-

lows stable operation of the system. Assuming a continuous-time system and control state-space model, the initial guess may be determined based on the application of Lyapunov analysis of singularly perturbed systems to the continuous-time state-space model. Typically, the discrete-time control states are obtained based on discretization of continuous-time control states, which may be used in the aforementioned continuous-time state-space model to determine the initial guess. The aforementioned method to determine the initial guess provides local exponential stability [76].

6.1.1 Gradient of Cost Function

Assumptions 1 *The optimization problem in* (6.1) *assumes the following:*

1. *L is twice continuously differentiable.*
2. *$\boldsymbol{f}$ is continuously differentiable in $\mathbb{R}^n \times \Omega^u$ at any time t.*
3. *$\boldsymbol{g}$ is continuously differentiable in $\mathbb{R}^c \times \mathbb{R}^n \times \Omega^K$ for any k.*
4. *$\boldsymbol{h}_1$, $\boldsymbol{h}_2$, and $\boldsymbol{h}$ are continuously differentiable in $\mathbb{R}^c \times \Omega^K$, $\Omega^{u_1} \times \mathbb{R}^c \times \Omega^K$, and $\Omega^{u_1} \times \Omega^{u_2}$, respectively, for any k.*

Lemma 1 *Let $\boldsymbol{K}_1$ and $\boldsymbol{K}_2$ be two decision variables for the optimization problem in* (6.1)*. Let the corresponding states of the system be $\boldsymbol{x}_{\boldsymbol{K}_1}(t)$ and $\boldsymbol{x}_{\boldsymbol{K}_2}(t)$, states of the controller be $\boldsymbol{x}_{\mathrm{c},\boldsymbol{K}_1}[k]$ and $\boldsymbol{x}_{\mathrm{c},\boldsymbol{K}_2}[k]$, and outputs of the controller be $\boldsymbol{u}_{\boldsymbol{K}_1}[k] = \boldsymbol{h}(\boldsymbol{u}_{1,\boldsymbol{K}_1}[k], \boldsymbol{u}_{2,\boldsymbol{K}_1}[k])$ and $\boldsymbol{u}_{\boldsymbol{K}_2}[k] = \boldsymbol{h}(\boldsymbol{u}_{1,\boldsymbol{K}_2}[k], \boldsymbol{u}_{2,\boldsymbol{K}_2}[k])$. Moreover, let*

$$\delta \boldsymbol{K} = \boldsymbol{K}_1 - \boldsymbol{K}_2, \tag{6.2a}$$

$$\Delta \boldsymbol{x}_{\delta \boldsymbol{K}}(t) = \boldsymbol{x}_{\boldsymbol{K}_1}(t) - \boldsymbol{x}_{\boldsymbol{K}_2}(t), \tag{6.2b}$$

$$\Delta \boldsymbol{x}_{\mathrm{c},\delta \boldsymbol{K}}[k] = \boldsymbol{x}_{\mathrm{c},\boldsymbol{K}_1}[k] - \boldsymbol{x}_{\mathrm{c},\boldsymbol{K}_2}[k], \tag{6.2c}$$

$$\Delta \boldsymbol{u}_{1,\delta \boldsymbol{K}}[k] = \boldsymbol{u}_{1,\boldsymbol{K}_1}[k] - \boldsymbol{u}_{1,\boldsymbol{K}_2}[k], \tag{6.2d}$$

$$\Delta \boldsymbol{u}_{2,\delta \boldsymbol{K}}[k] = \boldsymbol{u}_{2,\boldsymbol{K}_1}[k] - \boldsymbol{u}_{2,\boldsymbol{K}_2}[k], \tag{6.2e}$$

$$\Delta \boldsymbol{u}_{\delta \boldsymbol{K}}[k] = \boldsymbol{u}_{\boldsymbol{K}_1}[k] - \boldsymbol{u}_{\boldsymbol{K}_2}[k]. \tag{6.2f}$$

Under the conditions that $\Delta \boldsymbol{x}_{\delta \boldsymbol{K}}(0) = \Delta \boldsymbol{x}_{\mathrm{c},\delta \boldsymbol{K}}[0] = \Delta \boldsymbol{u}_{1,\delta \boldsymbol{K}}[0] = \Delta \boldsymbol{u}_{2,\delta \boldsymbol{K}}[0] = \Delta \boldsymbol{u}_{\delta \boldsymbol{K}}[0] = 0$ *and based on Assumptions 1, the following are true:*

$$\Delta \boldsymbol{x}_{\delta \boldsymbol{K}}(t) = O\left(\|\delta \boldsymbol{K}\|\right) \ \forall t, \tag{6.3a}$$

$$\Delta \boldsymbol{x}_{\mathrm{c},\delta \boldsymbol{K}}[k] = O\left(\|\delta \boldsymbol{K}\|\right) \ \forall k, \tag{6.3b}$$

$$\Delta \boldsymbol{u}_{1,\delta \boldsymbol{K}}[k] = O\left(\|\delta \boldsymbol{K}\|\right) \ \forall k, \tag{6.3c}$$

$$\Delta \boldsymbol{u}_{2,\delta \boldsymbol{K}}[k] = O\left(\|\delta \boldsymbol{K}\|\right) \ \forall k, \tag{6.3d}$$

$$\Delta \boldsymbol{u}_{\delta \boldsymbol{K}}[k] = O\left(\|\delta \boldsymbol{K}\|\right) \ \forall k, \tag{6.3e}$$

where O *is defined by [77]*

$$\boldsymbol{l}(\boldsymbol{x}) = O\left(g\left(\boldsymbol{x}\right)\right) \iff \exists K > 0, \delta > 0 : \ \textit{if} \ \|\boldsymbol{x}\| < \delta, \frac{\|\boldsymbol{l}(\boldsymbol{x})\|}{|g\left(\boldsymbol{x}\right)|} \leq K. \tag{6.4}$$

Proof Proof by induction. Given that $\Delta \boldsymbol{x}_{\delta \boldsymbol{K}}(0) = \Delta \boldsymbol{x}_{\mathrm{c},\delta \boldsymbol{K}}[0] = \Delta \boldsymbol{u}_{1,\delta \boldsymbol{K}}[0] = \Delta \boldsymbol{u}_{2,\delta \boldsymbol{K}}[0] = \Delta \boldsymbol{u}_{\delta \boldsymbol{K}}[0] = 0$ and Assumptions 1 is valid, then

$$\Delta \boldsymbol{x}_{\delta \boldsymbol{K}}(t) = 0 \ \forall t \in [0, T_{\mathrm{sc}}], \tag{6.5a}$$

$$\Delta \boldsymbol{x}_{\mathrm{c},\delta \boldsymbol{K}}[1] = \boldsymbol{J}_{\boldsymbol{g}}\left(\boldsymbol{K}\right)|_{\boldsymbol{K}_2} . \delta \boldsymbol{K} + o\left(\|\delta \boldsymbol{K}\|\right) = O\left(\|\delta \boldsymbol{K}\|\right), \tag{6.5b}$$

$$\begin{aligned} \Delta \boldsymbol{u}_{1,\delta \boldsymbol{K}}[1] = {} & \boldsymbol{J}_{\boldsymbol{h}_1}\left(\boldsymbol{x}_{\mathrm{c}}[k]\right)|_{\boldsymbol{x}_{\mathrm{c},\boldsymbol{K}_2}[1]} . \Delta \boldsymbol{x}_{\mathrm{c},\delta \boldsymbol{K}}[1] + \boldsymbol{J}_{\boldsymbol{h}_1}\left(\boldsymbol{K}\right)|_{\boldsymbol{K}_2} . \delta \boldsymbol{K} \\ & + o\left(\|\Delta \boldsymbol{x}_{\mathrm{c},\delta \boldsymbol{K}}[1]\|\right) + o\left(\|\delta \boldsymbol{K}\|\right) \\ = {} & O\left(\|\delta \boldsymbol{K}\|\right), \end{aligned} \tag{6.5c}$$

$$\begin{aligned}\Delta\boldsymbol{u}_{2,\delta\boldsymbol{K}}[1] &= \boldsymbol{J}_{\boldsymbol{h}_2}\left(\boldsymbol{u}_1[k]\right)\big|_{\boldsymbol{u}_{1,\boldsymbol{K}_2}[1]}.\Delta\boldsymbol{u}_{1,\delta\boldsymbol{K}}[1] + \boldsymbol{J}_{\boldsymbol{h}_2}\left(\boldsymbol{x}_{\mathrm{c}}[k]\right)\big|_{\boldsymbol{x}_{\mathrm{c},\boldsymbol{K}_2}[1]}.\Delta\boldsymbol{x}_{\mathrm{c},\delta\boldsymbol{K}}[1] \\ &\quad + \boldsymbol{J}_{\boldsymbol{h}_2}\left(\boldsymbol{K}\right)\big|_{\boldsymbol{K}_2}.\delta\boldsymbol{K} + o\left(\|\Delta\boldsymbol{x}_{\mathrm{c},\delta\boldsymbol{K}}[1]\|\right) + o\left(\|\Delta\boldsymbol{u}_{1,\delta\boldsymbol{K}}[1]\|\right) + o\left(\|\delta\boldsymbol{K}\|\right) \\ &= O\left(\|\delta\boldsymbol{K}\|\right), \qquad (6.5\mathrm{d}) \\ \Delta\boldsymbol{u}_{\delta\boldsymbol{K}}[1] &= \boldsymbol{J}_{\boldsymbol{h}}\left(\boldsymbol{u}_1[k]\right)\big|_{\boldsymbol{u}_{1,\boldsymbol{K}_2}[1]}.\Delta\boldsymbol{u}_{1,\delta\boldsymbol{K}}[1] + \boldsymbol{J}_{\boldsymbol{h}}\left(\boldsymbol{u}_2[k]\right)\big|_{\boldsymbol{u}_{2,\boldsymbol{K}_2}[1]}.\Delta\boldsymbol{u}_{2,\delta\boldsymbol{K}}[1] \\ &\quad + o\left(\|\Delta\boldsymbol{u}_{1,\delta\boldsymbol{K}}[1]\|\right) + o\left(\|\Delta\boldsymbol{u}_{2,\delta\boldsymbol{K}}[1]\|\right) \\ &= O\left(\|\delta\boldsymbol{K}\|\right), \qquad (6.5\mathrm{e})\end{aligned}$$

where o is defined by [77]

$$\boldsymbol{l}\left(\boldsymbol{x}\right) = o\left(g\left(\boldsymbol{x}\right)\right) \iff \lim_{\boldsymbol{x}\to\boldsymbol{0}} \frac{\|\boldsymbol{l}\left(\boldsymbol{x}\right)\|}{|g\left(\boldsymbol{x}\right)|} = 0, \qquad (6.6)$$

and $\boldsymbol{J}_{\boldsymbol{g}}\left(\boldsymbol{K}\right)$ is defined as the Jacobian of $\boldsymbol{g}$ with respect to $\boldsymbol{K}$. That is, the validity of the lemma for $0 \leq t \leq T_{\mathrm{sc}}$ is shown in (6.5).

Next, assuming the lemma to be true for $(k-1)T_{\mathrm{sc}} \leq t \leq kT_{\mathrm{sc}}$, the following are true:

$$\begin{aligned}\Delta\boldsymbol{x}_{\delta\boldsymbol{K}}(t) &= O\left(\|\delta\boldsymbol{K}\|\right)\ \forall t \in \left[(k-1)T_{\mathrm{sc}}, kT_{\mathrm{sc}}\right], \qquad (6.7\mathrm{a}) \\ \Delta\boldsymbol{x}_{\mathrm{c},\delta\boldsymbol{K}}[k] &= O\left(\|\delta\boldsymbol{K}\|\right), \qquad (6.7\mathrm{b}) \\ \Delta\boldsymbol{u}_{1,\delta\boldsymbol{K}}[k] &= O\left(\|\delta\boldsymbol{K}\|\right), \qquad (6.7\mathrm{c}) \\ \Delta\boldsymbol{u}_{2,\delta\boldsymbol{K}}[k] &= O\left(\|\delta\boldsymbol{K}\|\right), \qquad (6.7\mathrm{d}) \\ \Delta\boldsymbol{u}_{\delta\boldsymbol{K}}[k] &= O\left(\|\delta\boldsymbol{K}\|\right). \qquad (6.7\mathrm{e})\end{aligned}$$

In the following few lines, the lemma is proved for $kT_{\mathrm{sc}} \leq t < (k+1)T_{\mathrm{sc}}$. Since $\boldsymbol{f}$ is continuously differentiable on $\mathbb{R}^n \times \Omega^u$, by Taylor's theorem

$$\begin{aligned}\frac{\mathrm{d}\Delta\boldsymbol{x}_{\delta\boldsymbol{K}}}{\mathrm{d}t} &= \boldsymbol{f}\left(\boldsymbol{x}_{\boldsymbol{K}_1}, \boldsymbol{u}_{\boldsymbol{K}_1}[k], t\right) - \boldsymbol{f}\left(\boldsymbol{x}_{\boldsymbol{K}_2}, \boldsymbol{u}_{\boldsymbol{K}_2}[k], t\right) \\ &= \boldsymbol{J}_{\boldsymbol{f}}\left(\boldsymbol{x}\right)\big|_{\boldsymbol{x}_{\boldsymbol{K}_2}} \Delta\boldsymbol{x}_{\delta\boldsymbol{K}} + \boldsymbol{J}_{\boldsymbol{f}}\left(\boldsymbol{u}[k]\right)\big|_{\boldsymbol{u}_{\boldsymbol{K}_2}[k]} \Delta\boldsymbol{u}_{\delta\boldsymbol{K}}[k] \\ &\quad + o\left(\|\Delta\boldsymbol{x}_{\delta\boldsymbol{K}}\|\right) + o\left(\|\Delta\boldsymbol{u}_{\delta\boldsymbol{K}}[k]\|\right). \qquad (6.8)\end{aligned}$$

Using

$$o\left(\|\Delta \boldsymbol{x}_{\delta \boldsymbol{K}}\|\right) \subset O\left(\|\Delta \boldsymbol{x}_{\delta \boldsymbol{K}}\|\right) \Leftrightarrow o\left(\|\Delta \boldsymbol{x}_{\delta \boldsymbol{K}}\|\right) \leq L\left\|\Delta \boldsymbol{x}_{\delta \boldsymbol{K}}\right\|, L \in \mathbb{R}, L>0 \tag{6.9}$$

in (6.8), the following is obtained:

$$\begin{aligned} \frac{\mathrm{d} \Delta \boldsymbol{x}_{\delta \boldsymbol{K}}}{\mathrm{d} t} \leq & \left(\boldsymbol{J}_{\boldsymbol{f}}\left(\boldsymbol{x}\right)\big|_{\boldsymbol{x}_{\boldsymbol{K}_2}}+L\right) \Delta \boldsymbol{x}_{\delta \boldsymbol{K}}+\boldsymbol{J}_{\boldsymbol{f}}\left(\boldsymbol{u}[k]\right)\big|_{\boldsymbol{u}_{\boldsymbol{K}_2}[k]} \Delta \boldsymbol{u}_{\delta \boldsymbol{K}}[k] \\ & +o\left(\|\Delta \boldsymbol{u}_{\delta \boldsymbol{K}}[k]\|\right. \end{aligned} \tag{6.10}$$

Integrating (6.10) results in

$$\Delta \boldsymbol{x}_{\delta \boldsymbol{K}}(t) \leq \Delta \boldsymbol{x}_{\delta \boldsymbol{K}}(k T_{sc})+\int_{k T_{sc}}^{t} \Phi\left(t, \tau\right) B d \tau, \tag{6.11a}$$

$$B=\left(\boldsymbol{J}_{\boldsymbol{f}}\left(\boldsymbol{u}[k]\right)\big|_{\boldsymbol{u}_{\boldsymbol{K}_2}[k]} \Delta \boldsymbol{u}_{\delta \boldsymbol{K}}[k]+o\left(\|\Delta \boldsymbol{u}_{\delta \boldsymbol{K}}[k]\|\right)\right), \tag{6.11b}$$

where $\Phi\left(t, \tau\right)$ is the state transition matrix corresponding to the matrix $\boldsymbol{J}_{\boldsymbol{f}}\left(\boldsymbol{x}\right)\big|_{\boldsymbol{x}_{\boldsymbol{K}_2}}+L$. Based on (6.7) and (6.11), the following is deduced:

$$\Delta \boldsymbol{x}_{\delta \boldsymbol{K}}(t)=O\left(\|\delta \boldsymbol{K}\|\right), \ \forall t \in\left[k T_{\mathrm{sc}},(k+1) T_{sc}\right]. \tag{6.12}$$

Since $\boldsymbol{g}$ is continuously differentiable on $\mathbb{R}^c \times \Omega^K$, by Taylor's theorem

$$\begin{aligned} \Delta \boldsymbol{x}_{\mathrm{c}, \delta \boldsymbol{K}}[k+1]= & \boldsymbol{J}_{\boldsymbol{g}}\left(\boldsymbol{x}_{\mathrm{c}}[k]\right)\big|_{\boldsymbol{x}_{\mathrm{c}, \boldsymbol{K}_2}[k]} . \Delta \boldsymbol{x}_{\mathrm{c}, \delta \boldsymbol{K}}[k] \\ & +\boldsymbol{J}_{\boldsymbol{g}}\left(\boldsymbol{x}[k]\right)\big|_{\boldsymbol{x}_{\boldsymbol{K}_2}[k]} . \Delta \boldsymbol{x}_{\delta \boldsymbol{K}}[k]+\boldsymbol{J}_{\boldsymbol{g}}\left(\boldsymbol{K}\right)\big|_{\boldsymbol{K}_2} . \delta \boldsymbol{K} \\ & +o\left(\|\Delta \boldsymbol{x}_{\mathrm{c}, \delta \boldsymbol{K}}[k]\|\right)+o\left(\|\Delta \boldsymbol{x}_{\delta \boldsymbol{K}}[k]\|\right)+o\left(\|\delta \boldsymbol{K}\|\right). \end{aligned} \tag{6.13}$$

Using $o(y) \subset O(y), y \in \mathbb{R}, y>0$ in (6.13), and based on (6.7), the following is deduced:

$$\Delta \boldsymbol{x}_{\mathrm{c}, \delta \boldsymbol{K}}[k+1]=O\left(\|\delta \boldsymbol{K}\|\right). \tag{6.14}$$

Using similar arguments on $\Delta \boldsymbol{u}_{1,\delta \boldsymbol{K}}[k+1]$, $\Delta \boldsymbol{u}_{2,\delta \boldsymbol{K}}[k+1]$, and $\Delta \boldsymbol{u}_{\delta \boldsymbol{K}}[k+1]$, the following results are obtained:

$$\Delta \boldsymbol{u}_{1,\delta \boldsymbol{K}}[k+1] = O\left(\|\delta \boldsymbol{K}\|\right), \tag{6.15a}$$

$$\Delta \boldsymbol{u}_{2,\delta \boldsymbol{K}}[k+1] = O\left(\|\delta \boldsymbol{K}\|\right), \tag{6.15b}$$

$$\Delta \boldsymbol{u}_{\delta \boldsymbol{K}}[k+1] = O\left(\|\delta \boldsymbol{K}\|\right). \tag{6.15c}$$

Equations (6.12), (6.14), and (6.15) prove the lemma for $kT_{\mathrm{sc}} \leq t \leq (k+1)T_{\mathrm{sc}}$. This completes the proof of Lemma 1 by induction. ■

Theorem 6.1.1 *Based on Assumption 1 and Lemma 1, the gradient of the total cost of the optimization problem in* (6.1)*, may be defined as*

$$\nabla_{\boldsymbol{K}} J = \sum_{k=0}^{N_t} \left(\frac{d\boldsymbol{x}_{\mathrm{c}}[k]}{d\boldsymbol{K}} \right)^{T} \left(\nabla_{\boldsymbol{x}_{\mathrm{c}}[k]} L \right) T_{sc}, \tag{6.16}$$

where

$$\frac{\mathrm{d}}{\mathrm{d}t}\left(\frac{\mathrm{d}\boldsymbol{x}(t)}{\mathrm{d}\boldsymbol{K}} \right) = \boldsymbol{J}_{\boldsymbol{f}}(\boldsymbol{x}) \frac{\mathrm{d}\boldsymbol{x}(t)}{\mathrm{d}\boldsymbol{K}} + \boldsymbol{J}_{\boldsymbol{f}}(\boldsymbol{u}[k]) \frac{\mathrm{d}\boldsymbol{u}[k]}{\mathrm{d}\boldsymbol{K}}, \; kT_{sc} \leq t < (k+1)T_{sc}, \tag{6.17a}$$

$$\frac{\mathrm{d}\boldsymbol{x}_c[k]}{\mathrm{d}\boldsymbol{K}} = \boldsymbol{J}_{\boldsymbol{g}}\left(\boldsymbol{x}_c[k-1]\right) \frac{\mathrm{d}\boldsymbol{x}_c[k-1]}{\mathrm{d}\boldsymbol{K}} + \boldsymbol{J}_{\boldsymbol{g}}\left(\boldsymbol{x}[k-1]\right) \frac{\mathrm{d}\boldsymbol{x}[k-1]}{\mathrm{d}\boldsymbol{K}} + \boldsymbol{J}_{\boldsymbol{g}}\left(\boldsymbol{K}\right), \tag{6.17b}$$

$$\frac{\mathrm{d}\boldsymbol{u}_1[k]}{\mathrm{d}\boldsymbol{K}} = \boldsymbol{J}_{\boldsymbol{h}_1}\left(\boldsymbol{x}_c[k]\right) \frac{\mathrm{d}\boldsymbol{x}_c[k]}{\mathrm{d}\boldsymbol{K}} + \boldsymbol{J}_{\boldsymbol{h}_1}\left(\boldsymbol{K}\right), \tag{6.17c}$$

$$\frac{\mathrm{d}\boldsymbol{u}_2[k]}{\mathrm{d}\boldsymbol{K}} = \boldsymbol{J}_{\boldsymbol{h}_2}\left(\boldsymbol{u}_1[k]\right) \frac{\mathrm{d}\boldsymbol{u}_1[k]}{\mathrm{d}\boldsymbol{K}} + \boldsymbol{J}_{\boldsymbol{h}_2}\left(\boldsymbol{x}_c[k]\right) \frac{\mathrm{d}\boldsymbol{x}_c[k]}{\mathrm{d}\boldsymbol{K}} + \boldsymbol{J}_{\boldsymbol{h}_2}\left(\boldsymbol{K}\right), \tag{6.17d}$$

$$\frac{\mathrm{d}\boldsymbol{u}[k]}{\mathrm{d}\boldsymbol{K}} = \boldsymbol{J}_{\boldsymbol{h}}\left(\boldsymbol{u}_1[k]\right) \frac{\mathrm{d}\boldsymbol{u}_1[k]}{\mathrm{d}\boldsymbol{K}} + \boldsymbol{J}_{\boldsymbol{h}}\left(\boldsymbol{u}_2[k]\right) \frac{\mathrm{d}\boldsymbol{u}_2[k]}{\mathrm{d}\boldsymbol{K}}, \tag{6.17e}$$

and $\boldsymbol{J}$ *is the Jacobian matrix.*

Proof The gradient of the total cost function of (6.1) is given by

$$\nabla_{\boldsymbol{K}} J = \begin{pmatrix} \dfrac{\partial J}{\partial K_1} & \dfrac{\partial J}{\partial K_2} & .... & \dfrac{\partial J}{\partial K_K} \end{pmatrix}^{\mathrm{T}}, \tag{6.18a}$$

$$\boldsymbol{K} = \begin{pmatrix} K_1 & K_2 & .... & K_K \end{pmatrix}^{\mathrm{T}}, \tag{6.18b}$$

The derivation of $\frac{\partial J}{\partial K_1}$ is shown here and it can be easily extended to any $\frac{\partial J}{\partial K_i}, i \in \{2, 3, .., K\}$.

Let

$$\begin{aligned}\Delta J_{\delta K_1} &= J(\boldsymbol{K}_1) - J(\boldsymbol{K}_2) \\ &= \sum_{k=0}^{N_\mathrm{t}} \left(L\left(\boldsymbol{x}_{\mathrm{c},K_1+\delta K_1}[k]\right) - L\left(\boldsymbol{x}_{\mathrm{c},K_1}[k]\right)\right) T_\mathrm{sc},\end{aligned} \tag{6.19}$$

where $\boldsymbol{K}_1 = \begin{pmatrix} K_1 + \delta K_1 & K_2 & .... & K_K \end{pmatrix}^\mathrm{T}$, $\boldsymbol{K}_2 = \begin{pmatrix} K_1 & K_2 & .... & K_K \end{pmatrix}^\mathrm{T}$, $\delta K_1 > 0$, and $\boldsymbol{x}_{\mathrm{c},K_1+\delta K_1}$ and $\boldsymbol{x}_{\mathrm{c},K_1}$ are the corresponding states of the control system. Then, by mean value theorem, (6.19) is modified to

$$\Delta J_{\delta K_1} = \sum_{k=0}^{N_\mathrm{t}} \frac{\partial L}{\partial \boldsymbol{x}_\mathrm{c}} \left(\boldsymbol{x}_{\mathrm{c},K_1}[k] + s[k]\Delta \boldsymbol{x}_{\mathrm{c},\delta K_1}[k]\right) \Delta \boldsymbol{x}_{\mathrm{c},\delta K_1}[k] T_\mathrm{sc}, \tag{6.20a}$$

$$\Delta \boldsymbol{x}_{\mathrm{c},\delta K_1}[k] = \boldsymbol{x}_{\mathrm{c},K_1+\delta K_1}[k] - \boldsymbol{x}_{\mathrm{c},K_1}[k], \tag{6.20b}$$

where $s[k] \in (0, 1)$. Since L is twice continuous differentiable,

$$\left\| \frac{\partial L}{\partial \boldsymbol{x}_\mathrm{c}} (\boldsymbol{x}_{\mathrm{c},K_1}[k] + s[k]\Delta \boldsymbol{x}_{\mathrm{c},\delta K_1}[k]) - \frac{\partial L}{\partial \boldsymbol{x}_\mathrm{c}} \left(\boldsymbol{x}_{\mathrm{c},K_1}[k]\right) \right\| \leq K^{'} \left\| \Delta \boldsymbol{x}_{\mathrm{c},\delta K_1}[k] \right\|, K^{'} > 0. \tag{6.21}$$

Using Lemma 1 in (6.21), the following is obtained:

$$\begin{aligned}&\left\| \left(\frac{\partial L}{\partial \boldsymbol{x}_\mathrm{c}} (\boldsymbol{x}_{\mathrm{c},K_1}[k] + s[k]\Delta \boldsymbol{x}_{\mathrm{c},\delta K_1}[k]) - \frac{\partial L}{\partial \boldsymbol{x}_\mathrm{c}} \left(\boldsymbol{x}_{\mathrm{c},K_1}[k]\right) \right) \Delta \boldsymbol{x}_{\mathrm{c},\delta K_1}[k] \right\| \\ &\quad \leq K^{'} \left\| \Delta \boldsymbol{x}_{\mathrm{c},\delta K_1}[k] \right\|^2 \leq K^{''} \delta K_1^2, K^{''} > 0.\end{aligned} \tag{6.22}$$

Based on (6.20a) and (6.22), the following is obtained:

$$\Delta J_{\delta K_1} = \sum_{k=0}^{N_\mathrm{t}} \frac{\partial L}{\partial \boldsymbol{x}_\mathrm{c}} \left(\boldsymbol{x}_{\mathrm{c},K_1}[k]\right) \Delta \boldsymbol{x}_{\mathrm{c},\delta K_1}[k] T_\mathrm{sc} + o\left(\delta K_1\right). \tag{6.23}$$

Therefore,

$$\begin{aligned}\lim_{\delta K_1 \to 0} \frac{\Delta J_{\delta K_1}}{\delta K_1} &= \frac{\partial J}{\partial K_1} \\ &= \sum_{k=0}^{N_\mathrm{t}} \frac{\partial L}{\partial \boldsymbol{x}_\mathrm{c}[k]} \frac{\mathrm{d}\boldsymbol{x}_\mathrm{c}[k]}{\mathrm{d}K_1} T_\mathrm{sc}. \end{aligned} \tag{6.24}$$

Based on (6.1) and (6.20b), the following is deduced:

$$\begin{aligned}\frac{\mathrm{d}\Delta\boldsymbol{x}_{\delta K_1}(t)}{\mathrm{d}t} &= \frac{\mathrm{d}\left(\boldsymbol{x}_{K_1+\delta K_1}(t) - \boldsymbol{x}_{K_1}(t)\right)}{\mathrm{d}t} \\ &= \boldsymbol{f}\left(\boldsymbol{x}_{K_1+\delta K_1}, \boldsymbol{u}_{K_1+\delta K_1}[k], t\right) - \boldsymbol{f}\left(\boldsymbol{x}_{K_1}, \boldsymbol{u}_{K_1}[k], t\right), \ kT_\mathrm{sc} \le t < (k+1)T_\mathrm{sc}, \end{aligned} \tag{6.25a}$$

$$\begin{aligned}\Delta\boldsymbol{x}_{\mathrm{c},\delta K_1}[k] &= \boldsymbol{g}\left(\boldsymbol{x}_{\mathrm{c},K_1+\delta K_1}[k-1], \boldsymbol{x}_{K_1+\delta K_1}[k-1], \boldsymbol{K}_1, k\right) \\ &\quad - \boldsymbol{g}\left(\boldsymbol{x}_{\mathrm{c},K_1}[k-1], \boldsymbol{x}_{K_1}[k-1], \boldsymbol{K}_2, k\right), \end{aligned} \tag{6.25b}$$

$$\begin{aligned}\Delta\boldsymbol{u}_{1,\delta K_1}[k] &= \boldsymbol{u}_{1,K_1+\delta K_1}[k] - \boldsymbol{u}_{1,K_1}[k] \\ &= \boldsymbol{h}_1\left(\boldsymbol{x}_{\mathrm{c},K_1+\delta K_1}[k], \boldsymbol{K}_1, k\right) - \boldsymbol{h}_1\left(\boldsymbol{x}_{\mathrm{c},K_1}[k], \boldsymbol{K}_2, k\right), \end{aligned} \tag{6.25c}$$

$$\begin{aligned}\Delta\boldsymbol{u}_{2,\delta K_1}[k] &= \boldsymbol{u}_{2,K_1+\delta K_1}[k] - \boldsymbol{u}_{2,K_1}[k] \\ &= \boldsymbol{h}_2\left(\boldsymbol{u}_{1,K_1+\delta K_1}[k], \boldsymbol{x}_{\mathrm{c},K_1+\delta K_1}[k], \boldsymbol{K}_1, k\right) - \boldsymbol{h}_2\left(\boldsymbol{u}_{1,K_1}[k], \boldsymbol{x}_{\mathrm{c},K_1}[k], \boldsymbol{K}_2, k\right), \end{aligned} \tag{6.25d}$$

$$\begin{aligned}\Delta\boldsymbol{u}_{\delta K_1}[k] &= \boldsymbol{u}_{K_1+\delta K_1}[k] - \boldsymbol{u}_{K_1}[k] \\ &= \boldsymbol{h}\left(\boldsymbol{u}_{1,K_1+\delta K_1}[k], \boldsymbol{u}_{2,K_1+\delta K_1}[k]\right) - \boldsymbol{h}\left(\boldsymbol{u}_{1,K_1}[k], \boldsymbol{u}_{2,K_1}[k]\right). \end{aligned} \tag{6.25e}$$

Since $\boldsymbol{f}$, $\boldsymbol{g}$, $\boldsymbol{h}_1$, $\boldsymbol{h}_2$, and $\boldsymbol{h}$ are continuously differentiable in $\mathbb{R}^n \times \Omega^u$, $\mathbb{R}^c \times \mathbb{R}^n \times \Omega^K$, $\mathbb{R}^c \times \Omega^K$, $\Omega^{u_1} \times \mathbb{R}^c \times \Omega^K$, and $\Omega^{u_1} \times \Omega^{u_2}$, respectively, by Taylor's theorem,

$$\begin{aligned}\frac{\mathrm{d}\Delta\boldsymbol{x}_{\delta K_1}(t)}{\mathrm{d}t} &= \boldsymbol{J}_{\boldsymbol{f}}(\boldsymbol{x})\,|_{\boldsymbol{x}_{K_1}(t)}\,\Delta\boldsymbol{x}_{\delta K_1}(t) + \boldsymbol{J}_{\boldsymbol{f}}(\boldsymbol{u}[k])\,|_{\boldsymbol{u}_{K_1}[k]}\,\Delta\boldsymbol{u}_{\delta K_1}[k] \\ &\quad + o\left(\|\Delta\boldsymbol{x}_{\delta K_1}\|\right) + o\left(\|\Delta\boldsymbol{u}_{\delta K_1}[k]\|\right), \ kT_\mathrm{sc} \le t < (k+1)T_\mathrm{sc}, \end{aligned} \tag{6.26a}$$

$$\Delta \boldsymbol{x}_{\mathrm{c},\delta K_1}[k] = \boldsymbol{J_g}\left(\boldsymbol{x}_{\mathrm{c}}[k-1]\right)|_{\boldsymbol{x}_{\mathrm{c},K_1}[k-1]} \Delta \boldsymbol{x}_{\mathrm{c},\delta K_1}[k-1] + \boldsymbol{J_g}\left(\boldsymbol{x}[k-1]\right)|_{\boldsymbol{x}_{K_1}[k-1]} \Delta \boldsymbol{x}_{\delta K_1}[k-1] + \boldsymbol{J_g}\left(K_1\right)\delta K_1 + o\left(\|\Delta \boldsymbol{x}_{\mathrm{c},\delta K_1}[k-1]\|\right) + o\left(\|\Delta \boldsymbol{x}_{\delta K_1}[k-1]\|\right) + o\left(\delta K_1\right), \tag{6.26b}$$

$$\Delta \boldsymbol{u}_{1,\delta K_1}[k] = \boldsymbol{J_{h_1}}\left(\boldsymbol{x}_{\mathrm{c}}[k]\right)|_{\boldsymbol{x}_{\mathrm{c},K_1}[k]} \Delta \boldsymbol{x}_{\mathrm{c},\delta K_1}[k] + \boldsymbol{J_{h_1}}\left(K_1\right)\delta K_1 + o\left(\|\Delta \boldsymbol{x}_{\mathrm{c},\delta K_1}[k]\|\right) + o\left(\delta K_1\right), \tag{6.26c}$$

$$\Delta \boldsymbol{u}_{2,\delta K_1}[k] = \boldsymbol{J_{h_2}}\left(\boldsymbol{u}_1[k]\right)|_{\boldsymbol{u}_{1,K_1}[k]} \Delta \boldsymbol{u}_{1,\delta K_1}[k] + \boldsymbol{J_{h_2}}\left(\boldsymbol{x}_{\mathrm{c}}[k]\right)|_{\boldsymbol{x}_{\mathrm{c},K_1}[k]} \Delta \boldsymbol{x}_{\mathrm{c},\delta K_1}[k] + \boldsymbol{J_{h_2}}\left(K_1\right)\delta K_1 + o\left(\|\Delta \boldsymbol{x}_{\mathrm{c},\delta K_1}[k]\|\right) + o\left(\|\Delta \boldsymbol{u}_{1,\delta K_1}[k]\|\right) + o\left(\delta K_1\right), \tag{6.26d}$$

$$\Delta \boldsymbol{u}_{\delta K_1}[k] = \boldsymbol{J_h}\left(\boldsymbol{u}_1[k]\right)|_{\boldsymbol{u}_{1,K_1}[k]} \Delta \boldsymbol{u}_{1,\delta K_1}[k] + \boldsymbol{J_h}\left(\boldsymbol{u}_2[k]\right)|_{\boldsymbol{u}_{2,K_1}[k]} \Delta \boldsymbol{u}_{2,\delta K_1}[k] + o\left(\|\Delta \boldsymbol{u}_{1,\delta K_1}[k]\|\right) + o\left(\|\Delta \boldsymbol{u}_{2,\delta K_1}[k]\|\right). \tag{6.26e}$$

With $\Delta \boldsymbol{x}_{\delta K_1}(0) = \Delta \boldsymbol{x}_{\mathrm{c},\delta K_1}[0] = \Delta \boldsymbol{u}_{1,\delta K_1}[0] = \Delta \boldsymbol{u}_{2,\delta K_1}[0] = \Delta \boldsymbol{u}_{\delta K_1}[0] = 0$ and using Lemma 1, the following results are obtained:

$$\|\Delta \boldsymbol{x}_{\delta K_1}(t)\| \leq K^{'''}\delta K_1, \forall t \in [(k-1)T_{\mathrm{sc}}, kT_{\mathrm{sc}}], \forall k, K^{'''} > 0, \tag{6.27a}$$

$$\|\Delta \boldsymbol{x}_{\mathrm{c},\delta K_1}[k]\| \leq K^{''''}\delta K_1, \forall k, K^{''''} > 0, \tag{6.27b}$$

$$\|\Delta \boldsymbol{u}_{1,\delta K_1}[k]\| \leq K^{'''''}\delta K_1, \forall k, K^{'''''} > 0, \tag{6.27c}$$

$$\|\Delta \boldsymbol{u}_{2,\delta K_1}[k]\| \leq K^{''''''}\delta K_1, \forall k, K^{''''''} > 0, \tag{6.27d}$$

$$\|\Delta \boldsymbol{u}_{\delta K_1}[k]\| \leq K^{'''''''}\delta K_1, \forall k, K^{'''''''} > 0. \tag{6.27e}$$

Based on (6.26) and (6.27), the following are obtained:

$$\frac{\mathrm{d}\Delta \boldsymbol{x}_{\delta K_1}(t)}{\mathrm{d}t} = \boldsymbol{J_f}\left(\boldsymbol{x}\right)|_{\boldsymbol{x}_{K_1}(t)} \Delta \boldsymbol{x}_{\delta K_1}(t) + \boldsymbol{J_f}\left(\boldsymbol{u}[k]\right)|_{\boldsymbol{u}_{K_1}[k]} \Delta \boldsymbol{u}_{\delta K_1}[k] + o\left(\delta K_1\right), \quad kT_{\mathrm{sc}} \leq t < (k+1)T_{\mathrm{sc}}, \tag{6.28a}$$

$$\Delta \boldsymbol{x}_{\mathrm{c},\delta K_1}[k] = \boldsymbol{J_g}\left(\boldsymbol{x}_{\mathrm{c}}[k-1]\right)|_{\boldsymbol{x}_{\mathrm{c},K_1}[k-1]} \Delta \boldsymbol{x}_{\mathrm{c},\delta K_1}[k-1] + \boldsymbol{J_g}\left(\boldsymbol{x}[k-1]\right)|_{\boldsymbol{x}_{K_1}[k-1]} \Delta \boldsymbol{x}_{\delta K_1}[k-1] + \boldsymbol{J_g}\left(K_1\right)\delta K_1 + o\left(\delta K_1\right), \tag{6.28b}$$

$$\Delta \boldsymbol{u}_{1,\delta K_1}[k] = \boldsymbol{J}_{\boldsymbol{h}_1}\left(\boldsymbol{x}_{\mathrm{c}}[k]\right)|_{\boldsymbol{x}_{\mathrm{c},K_1}[k]} \Delta \boldsymbol{x}_{\mathrm{c},\delta K_1}[k] + \boldsymbol{J}_{\boldsymbol{h}_1}\left(K_1\right)\delta K_1 + o\left(\delta K_1\right), \tag{6.28c}$$

$$\Delta \boldsymbol{u}_{2,\delta K_1}[k] = \boldsymbol{J}_{\boldsymbol{h}_2}\left(\boldsymbol{u}_1[k]\right)|_{\boldsymbol{u}_{1,K_1}[k]} \Delta \boldsymbol{u}_{1,\delta K_1}[k] + \boldsymbol{J}_{\boldsymbol{h}_2}\left(\boldsymbol{x}_{\mathrm{c}}[k]\right)|_{\boldsymbol{x}_{\mathrm{c},K_1}[k]} \Delta \boldsymbol{x}_{\mathrm{c},\delta K_1}[k] + \boldsymbol{J}_{\boldsymbol{h}_2}\left(K_1\right)\delta K_1 + o\left(\delta K_1\right), \tag{6.28d}$$

$$\Delta \boldsymbol{u}_{\delta K_1}[k] = \boldsymbol{J}_{\boldsymbol{h}}\left(\boldsymbol{u}_1[k]\right)|_{\boldsymbol{u}_{1,K_1}[k]} \Delta \boldsymbol{u}_{1,\delta K_1}[k] + \boldsymbol{J}_{\boldsymbol{h}}\left(\boldsymbol{u}_2[k]\right)|_{\boldsymbol{u}_{2,K_1}[k]} \Delta \boldsymbol{u}_{2,\delta K_1}[k] + o\left(\delta K_1\right). \tag{6.28e}$$

Dividing (6.28) by δK_1 and applying the limiting case of $\delta K_1 \to 0$ in (6.28) results in

$$\frac{\mathrm{d}}{\mathrm{d}t}\left(\frac{\mathrm{d}\boldsymbol{x}(t)}{\mathrm{d}K_1}\right) = \boldsymbol{J}_{\boldsymbol{f}}\left(\boldsymbol{x}\right)\frac{\mathrm{d}\boldsymbol{x}}{\mathrm{d}K_1} + \boldsymbol{J}_{\boldsymbol{f}}\left(\boldsymbol{u}[k]\right)\frac{\mathrm{d}\boldsymbol{u}[k]}{\mathrm{d}K_1},\ kT_{\mathrm{sc}} \le t < (k+1)T_{\mathrm{sc}}, \tag{6.29a}$$

$$\frac{\mathrm{d}\boldsymbol{x}_{\mathrm{c}}[k]}{\mathrm{d}K_1} = \boldsymbol{J}_{\boldsymbol{g}}\left(\boldsymbol{x}_{\mathrm{c}}[k-1]\right)\frac{\mathrm{d}\boldsymbol{x}_{\mathrm{c}}[k-1]}{\mathrm{d}K_1} + \boldsymbol{J}_{\boldsymbol{g}}\left(\boldsymbol{x}[k-1]\right)\frac{\mathrm{d}\boldsymbol{x}[k-1]}{\mathrm{d}K_1} + \boldsymbol{J}_{\boldsymbol{g}}\left(K_1\right) \tag{6.29b}$$

$$\frac{\mathrm{d}\boldsymbol{u}_1[k]}{\mathrm{d}K_1} = \boldsymbol{J}_{\boldsymbol{h}_1}\left(\boldsymbol{x}_{\mathrm{c}}[k]\right)\frac{\mathrm{d}\boldsymbol{x}_{\mathrm{c}}[k]}{\mathrm{d}K_1} + \boldsymbol{J}_{\boldsymbol{h}_1}\left(K_1\right), \tag{6.29c}$$

$$\frac{\mathrm{d}\boldsymbol{u}_2[k]}{\mathrm{d}K_1} = \boldsymbol{J}_{\boldsymbol{h}_2}\left(\boldsymbol{u}_1[k]\right)\frac{\mathrm{d}\boldsymbol{u}_1[k]}{\mathrm{d}K_1} + \boldsymbol{J}_{\boldsymbol{h}_2}\left(\boldsymbol{x}_{\mathrm{c}}[k]\right)\frac{\mathrm{d}\boldsymbol{x}_{\mathrm{c}}[k]}{\mathrm{d}K_1} + \boldsymbol{J}_{\boldsymbol{h}_2}\left(K_1\right), \tag{6.29d}$$

$$\frac{\mathrm{d}\boldsymbol{u}[k]}{\mathrm{d}K_1} = \boldsymbol{J}_{\boldsymbol{h}}\left(\boldsymbol{u}_1[k]\right)\frac{\mathrm{d}\boldsymbol{u}_1[k]}{\mathrm{d}K_1} + \boldsymbol{J}_{\boldsymbol{h}}\left(\boldsymbol{u}_2[k]\right)\frac{\mathrm{d}\boldsymbol{u}_2[k]}{\mathrm{d}K_1}. \tag{6.29e}$$

For the sake of generalization, the subscript K_1 has been dropped in all the variables in (6.29). Expressions similar to (6.24) and (6.29) may be obtained for any $K_i, i \in \{2, 3, ..., K\}$. Combination of aforementioned expressions for any K_i leads to (6.16) and (6.17). ■

6.1.2 Gradient-based Cosimulation

The algorithm used to solve the optimization problem of (6.1) is based on the gradient-descent algorithm, summarized as:

Step-1 Initialize the decision variable $\boldsymbol{K}^1$ based on the Lyapunov analysis of singularly perturbed systems, as discussed earlier. Set a counter $i = 1$.

Step-2 Set the initial values of the states of the system $\boldsymbol{x}(0)$, states of the controller $\boldsymbol{x}_{\mathrm{c}}[0]$, and outputs of the controller $\boldsymbol{u}_1[0]$ and $\boldsymbol{u}_2[0]$. Set the initial values of $\dfrac{\mathrm{d}\boldsymbol{x}(t)}{\mathrm{d}\boldsymbol{K}}$, $\dfrac{\mathrm{d}\boldsymbol{x}_{\mathrm{c}}[k]}{\mathrm{d}\boldsymbol{K}}$, and $\dfrac{\mathrm{d}\boldsymbol{u}[k]}{\mathrm{d}\boldsymbol{K}}$. Set a counter $k = 0$. Set $J^i = 0$ and $\nabla_{\boldsymbol{K}} J^i = 0$.

Step-3 Using the decision variable $\boldsymbol{K}^i$, perform the following tasks:

Step-3a Simulate the states of the system $\boldsymbol{x}(t)$ given by (6.1b) for $kT_{\mathrm{sc}} \leq t < (k+1)T_{\mathrm{sc}}$. Simultaneously, simulate $\dfrac{\mathrm{d}\boldsymbol{x}(t)}{\mathrm{d}\boldsymbol{K}}$ during the control period based on (6.17a).

Step-3b In parallel, evaluate the states of the controller $\boldsymbol{x}_{\mathrm{c}}[k]$ and outputs of the controller $\boldsymbol{u}_1[k]$, $\boldsymbol{u}_2[k]$, and $\boldsymbol{u}[k]$ given by (6.1c)-(6.1f), respectively, in the present control period. Moreover, evaluate $\dfrac{\mathrm{d}\boldsymbol{x}_{\mathrm{c}}[k]}{\mathrm{d}\boldsymbol{K}}$, $\dfrac{\mathrm{d}\boldsymbol{u}_1[k]}{\mathrm{d}\boldsymbol{K}}$, $\dfrac{\mathrm{d}\boldsymbol{u}_2[k]}{\mathrm{d}\boldsymbol{K}}$, and $\dfrac{\mathrm{d}\boldsymbol{u}[k]}{\mathrm{d}\boldsymbol{K}}$ given by (6.17b)-(6.17e), respectively, in the present control period.

Step-4 Evaluate the cost function L and gradient of the cost function $\nabla_{\boldsymbol{x}_{\mathrm{c}}[k]} L$ in the present control period. Using the cost function, increment the existing total cost J^i based on (6.1a). Similarly, utilizing the gradient of the cost function, increment the gradient of the total cost $\nabla_{\boldsymbol{K}} J^i$ based on (6.16).

Step-5 Increment k by one and repeats steps 3-5 until $t = N_t T_{\mathrm{sc}}$.

Step-6 If $\nabla_{\boldsymbol{K}} J^i < \epsilon_0$, stop. Otherwise, reinitialize $\boldsymbol{K}^{i+1} = \boldsymbol{K}^i - \alpha \nabla_{\boldsymbol{K}} J^i$, increment i by one, and repeat steps 2-6.

In the aforementioned algorithm, α and ϵ_0 are the gradient-descent algorithm parameters that are chosen based on the accuracy and convergence rate required in the algorithm [77].

6.2 Application to The MMC System

Application of the aforementioned gradient-based cosimulation algorithm to optimize the controller gains of an MMC system requires a continuous-time state-space

model to describe the dynamics of the states of the MMC and a discrete-time state-space model of the control system. The continuous-time state-space model to accurately predict the dynamics of the states of the MMC is given by the advanced MMC state-space model in (3.35). However, the tangent to the state trajectory function in (3.35) is not continuously differentiable in $\mathbb{R}^n \times \Omega^u$ due to the presence of sgn and absolute value functions. Thus, it does not satisfy the properties described in Assumptions 1. To satisfy the Assumptions 1, the following approximations are made to the tangent to the state trajectory function in (3.35):

$$\operatorname{sgn}(b) \approx \tan^{-1}\left(\frac{b}{\epsilon}\right), \tag{6.30a}$$

$$|b| = b.\operatorname{sgn}(b) \approx b.\tan^{-1}\left(\frac{b}{\epsilon}\right), \tag{6.30b}$$

where b is the variable and ϵ is chosen so as to enhance the simulation accuracy while avoiding simulation jitters.

The control system to control the MMC in variable-frequency operations is described by (4.3) and (5.29). The aforementioned control system is implemented through the standard Runge-Kutta order-4 discretization that yields (6.1c)-(6.1f) with

$$\boldsymbol{u}_1 = \boldsymbol{m}_{abc}, \tag{6.31a}$$

$$\boldsymbol{u}_2 = \boldsymbol{m}_{\mathrm{circ},abc}, \tag{6.31b}$$

$$\boldsymbol{u} = \begin{pmatrix} \boldsymbol{m}_{p,abc} & \boldsymbol{m}_{n,abc} \end{pmatrix}^{\mathrm{T}}, \tag{6.31c}$$

$$\boldsymbol{x}_{\mathrm{c}} = \begin{pmatrix} \boldsymbol{x}_{\mathrm{c1}} & \dfrac{\mathrm{d}\left(0.5\hat{\boldsymbol{v}}^{\Sigma}_{\mathrm{c},abc}\right)}{\mathrm{d}t} & \hat{\boldsymbol{i}}_{\mathrm{circ},abc} & \dfrac{\mathrm{d}\hat{\boldsymbol{i}}_{\mathrm{circ},abc}}{\mathrm{d}t} \end{pmatrix}^{\mathrm{T}}, \tag{6.31d}$$

$$\boldsymbol{x}_{\mathrm{c1}} = \begin{pmatrix} \int \boldsymbol{T}\left(\boldsymbol{i}_{abc,\mathrm{ref}} - \hat{\boldsymbol{i}}_{abc}\right) & \hat{\boldsymbol{i}}_{abc} & \dfrac{\mathrm{d}\hat{\boldsymbol{i}}_{abc}}{\mathrm{d}t} & 0.5\hat{\boldsymbol{v}}^{\Sigma}_{\mathrm{c},abc} \end{pmatrix}^{\mathrm{T}}. \tag{6.31e}$$

and the forms of $\boldsymbol{g}$, $\boldsymbol{h}_1$, and $\boldsymbol{h}_2$ are based on the Runge-Kutta discretization of (4.3) and (5.29). The form of $\boldsymbol{h}$ is given by (3.1). The decision variable $\boldsymbol{K}$ in the variable-frequency operation of MMC is given by

$$\boldsymbol{K} = \begin{pmatrix} K_{\mathrm{p}} & K_{\mathrm{i}} & K_{\mathrm{p1}} & K_{\mathrm{pv}} \end{pmatrix}^{\mathrm{T}}. \tag{6.32}$$

The control system used to control the MMC in fixed-frequency operations is described by (4.3) and (4.20). The aforementioned control system is implemented through the standard Runge-Kutta order-4 discretization that yields (6.1c)-(6.1f) with

$$\boldsymbol{u}_1 = \boldsymbol{m}_{abc}, \tag{6.33a}$$

$$\boldsymbol{u}_2 = \boldsymbol{m}_{\mathrm{circ},abc}, \tag{6.33b}$$

$$\boldsymbol{u} = \begin{pmatrix} \boldsymbol{m}_{p,abc} & \boldsymbol{m}_{n,abc} \end{pmatrix}^{\mathrm{T}}, \tag{6.33c}$$

$$\boldsymbol{x}_{\mathrm{c}} = \begin{pmatrix} \boldsymbol{x}_{\mathrm{c1}} & \dfrac{\mathrm{d}\left(0.5\hat{\boldsymbol{v}}^{\Sigma}_{\mathrm{c},abc}\right)}{\mathrm{d}t} & \boldsymbol{x}_{\mathrm{c2}} & \boldsymbol{x}_{\mathrm{c3}} & \boldsymbol{x}_{\mathrm{c4}} \end{pmatrix}^{\mathrm{T}}, \tag{6.33d}$$

$$\boldsymbol{x}_{\mathrm{c1}} = \begin{pmatrix} \int \boldsymbol{T}\left(\boldsymbol{i}_{abc,\mathrm{ref}} - \hat{\boldsymbol{i}}_{abc}\right) & \hat{\boldsymbol{i}}_{abc} & \dfrac{\mathrm{d}\hat{\boldsymbol{i}}_{abc}}{\mathrm{d}t} & 0.5\hat{\boldsymbol{v}}^{\Sigma}_{\mathrm{c},abc} \end{pmatrix}^{\mathrm{T}}, \tag{6.33e}$$

$$\boldsymbol{x}_{\mathrm{c2}} = \begin{pmatrix} 0.5\hat{\boldsymbol{v}}^{\Sigma}_{\mathrm{c},abc,f} & \dfrac{\mathrm{d}\left(0.5\hat{\boldsymbol{v}}^{\Sigma}_{\mathrm{c},abc,f}\right)}{\mathrm{d}t} & \hat{\boldsymbol{i}}_{\mathrm{circ},abc} & \dfrac{\mathrm{d}\hat{\boldsymbol{i}}_{\mathrm{circ},abc}}{\mathrm{d}t} \end{pmatrix}^{\mathrm{T}}, \tag{6.33f}$$

$$\boldsymbol{x}_{\mathrm{c3}} = \begin{pmatrix} \boldsymbol{y}_{1,abc} & \dfrac{\mathrm{d}\boldsymbol{y}_{1,abc}}{\mathrm{d}t} & \boldsymbol{y}_{2,abc} & \dfrac{\mathrm{d}\boldsymbol{y}_{2,abc}}{\mathrm{d}t} & \boldsymbol{i}_{\mathrm{circ},abc,\mathrm{ref,uf2}} \end{pmatrix}^{\mathrm{T}}, \tag{6.33g}$$

$$\boldsymbol{x}_{\mathrm{c4}} = \begin{pmatrix} \dfrac{\mathrm{d}\boldsymbol{i}_{\mathrm{circ},abc,\mathrm{ref,uf2}}}{\mathrm{d}t} & \boldsymbol{i}_{\mathrm{circ},abc,\mathrm{ref}} & \dfrac{\mathrm{d}\boldsymbol{i}_{\mathrm{circ},abc,\mathrm{ref}}}{\mathrm{d}t} \end{pmatrix}^{\mathrm{T}}. \tag{6.33h}$$

and the forms of $\boldsymbol{g}$, $\boldsymbol{h}_1$, and $\boldsymbol{h}_2$ are based on the Runge-Kutta discretization of (4.3) and (4.20). The form of $\boldsymbol{h}$ is given by (3.1). The decision variable $\boldsymbol{K}$ in the fixed-frequency operation of MMC is given by

$$\boldsymbol{K} = \begin{pmatrix} K_{\mathrm{p}} & K_{\mathrm{i}} & K_{\mathrm{p1}} & K_{\mathrm{i1}} & K_{\mathrm{p2}} & K_{\mathrm{i2}} & K_{\mathrm{pv}} \end{pmatrix}^{\mathrm{T}}. \tag{6.34}$$

The initial value of the decision variables in the fixed-frequency and variable-frequency operation of the MMC are determined based on the design procedure described in Chapters 4 and 5, respectively.

7. EXPERIMENTAL RESULTS

In this chapter, experimental results are provided to (i) verify the developed MMC models, (ii) substantiate the performance of the proposed modulation strategy, and (iii) validate the performance of the proposed control systems for fixed-frequency and variable-frequency operations of the MMC.

7.1 Hardware Prototype

An overview of the hardware prototype is provided in this section that includes details on the design and development of a 2 kVA laboratory-scale prototype of MMC and the implementation of the control system in OP5600 system of Opal-RT.

7.1.1 Design of the MMC Prototype

The design of the MMC involves the determination of the number of SMs in each arm, size of the SM capacitor, size of the inductor, and the voltage/current rating of the IGBTs/diodes used in the half-bridge. The number of SMs in each arm is determined based on the ac-side current/voltage total harmonic distortion (THD) requirements. In the prototype developed, the number of SMs in each arm is set to 4. The size of the SM capacitor is determined based on the constraints on its voltage ripple. The voltage ripple on the SM capacitor is given by (5.4). Substituting for

$$I_o = \frac{4P_n}{3mV_{\rm dc}\cos(\phi)} \tag{7.1}$$

Table 7.1.
MMC Design

Quantity	Value
Nominal power	2 kVA
Nominal net dc voltage V_{dc}	200 V
L_{o}	2.2 mH
SM capacitance C_{SM}	1.41 mF
Number of SMs per arm N	4

in (5.4) and given a voltage ripple $\delta v_{\mathrm{c,pp,op}}$ under the rated operating conditions of the MMC, the size of the SM capacitor is given by

$$C_{\mathrm{SM}} = \frac{2P_n}{3mV_{\mathrm{dc}}\omega\cos(\phi)\,\delta v_{\mathrm{c,pp,op}}}\left(1-\left(\frac{m\cos(\phi)}{2}\right)^2\right)^{\frac{3}{2}}, \tag{7.2}$$

where P_n is the nominal power. With a 10% voltage ripple, 200 V dc link voltage, $m = 0.9$ at rated operating conditions, and $\cos(\phi) = 0.95$ results in $C_{\mathrm{SM}} = 1.53$ mF. Based on the electrolytic capacitors available in the market, $C_{\mathrm{SM}} = 1.41$ mF is chosen. The inductor is sized based on the limits imposed on the high-frequency ripple of the arm currents [78]. The inductor is sized as $L_o = 2.2$ mH. The voltage across the inductor may contain switching frequency harmonics due to the circulating current control strategies. Therefore, to minimize the stray inductances at high frequencies, an air-core inductor is used. The half-bridge circuit in the SMs are implemented using IXYS FII40-06D that allow sufficiently high device current and blocking voltage to allow the operation of a 10 kVA MMC prototype. The design of the MMC is summarized in Table 7.1.

7.1.2 Sensing Circuits

Each arm of the MMC has a current sensor and each SM has a voltage sensor to measure its capacitor voltage. Hall effect-based LEM voltage/current sensors that

provide isolation and have a bandwidth of 50 kHz, are used. A resistor $R_p = 20$ kΩ is used as the measuring resistance in the primary side of the voltage sensor. The measured signals from the sensors are filtered using simple RC networks to remove the high-frequency noise in the range of 1 MHz or higher that were noticed during the experiments.

7.1.3 Development of the MMC Prototype

Based on the designed MMC and the required sensing circuits, PCBs are designed for each SM and for each inductor. The SM board consists of the half-bridge, capacitor(s), gate-drive circuit, and the capacitor-voltage sensor circuit. The inputs to the gate-drive circuit include two digital signals: (i) status of the upper switch, and (ii) shutdown signal. The shutdown signal is implemented for emergency shutdown using the software that will be explained in detail in Section 7.1.5. Upon inversion of the status of the upper switch, the status of the lower switch is obtained. The gate-drive circuit introduces a dead-time delay in the gating signals of the upper and lower switches using an RC network. It also optically isolates the gating signals. Isolation is necessary due to the cascaded structure of the topology that require floating local references. The floating local references are produced with the help of isolated dc-dc converters. The implementation of the gate-drive circuit is summarized in Fig. 7.1. The inductor board consists of the arm inductor and the current sensor circuit. The SM board and the MMC prototype are shown in Fig. 7.2.

7.1.4 Three-phase Load

The load considered in the experimental case studies include a resistor-inductor (RL) load and a permanent magnet synchronous machine (PMSM).

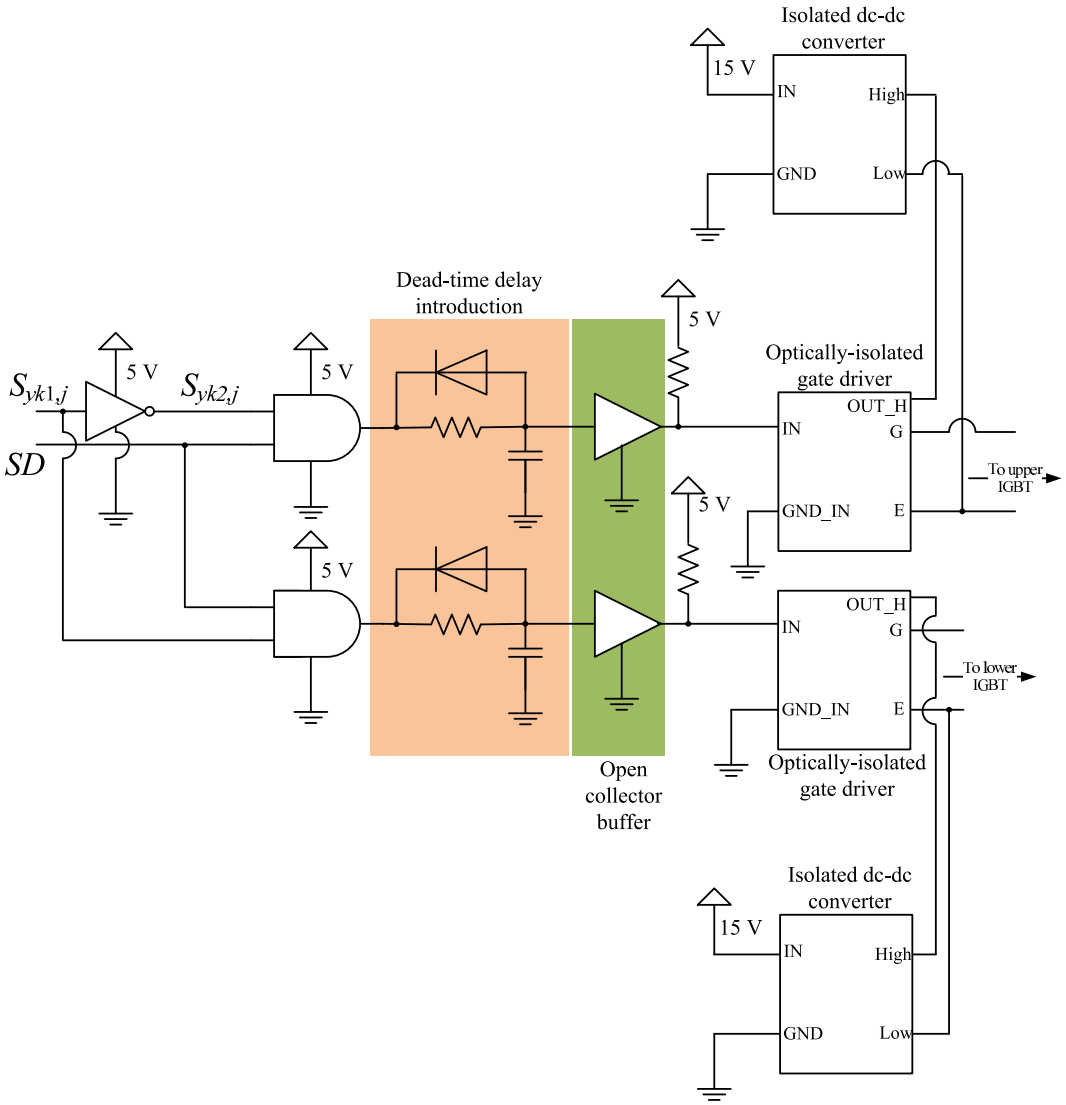

Fig. 7.1. Gate-drive circuit.

7.1.5 Control Implementation

The control system of the MMC is implemented in one of the cores of OP5600 of Opal-RT. The implementation also uses the Spartan 3 FPGA present in OP5600. The main processing unit, consisting of one of the cores of OP5600, implements the current and voltage controllers, SM modulation index generator, and SM capacitor voltage balancing algorithm. The inputs to the main processing unit are the processed voltage and current signals from the FPGA and the user input signals from the host

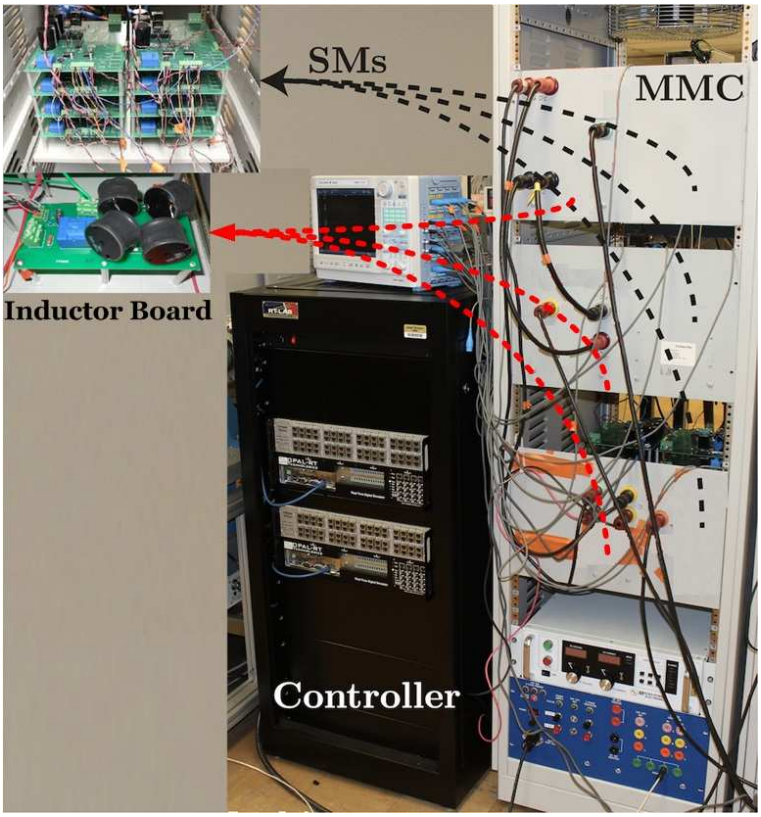

Fig. 7.2. MMC prototype.

computer. The outputs of the main processing unit are the individual SM modulation indices that are fed as input to the FPGA.

The inputs to the control system of the MMC include the measured SM capacitor voltages and arm currents that are interfaced to the main processing unit through the analog-to-digital converters (A/Ds) and the FPGA. The outputs of the control system include the status of the upper switch of each SM and the shutdown signal that are produced in the FPGA. The status of the upper switch of each SM is produced in the FPGA based on the corresponding individual SM modulation index. The shutdown signal is activated when either the measured voltage or current exceeds a pre-set value. The pre-set value is based on the rating of the half-bridges, the capacitors, and the inductors. The structure of the controller architecture is summarized in Fig. 7.3.

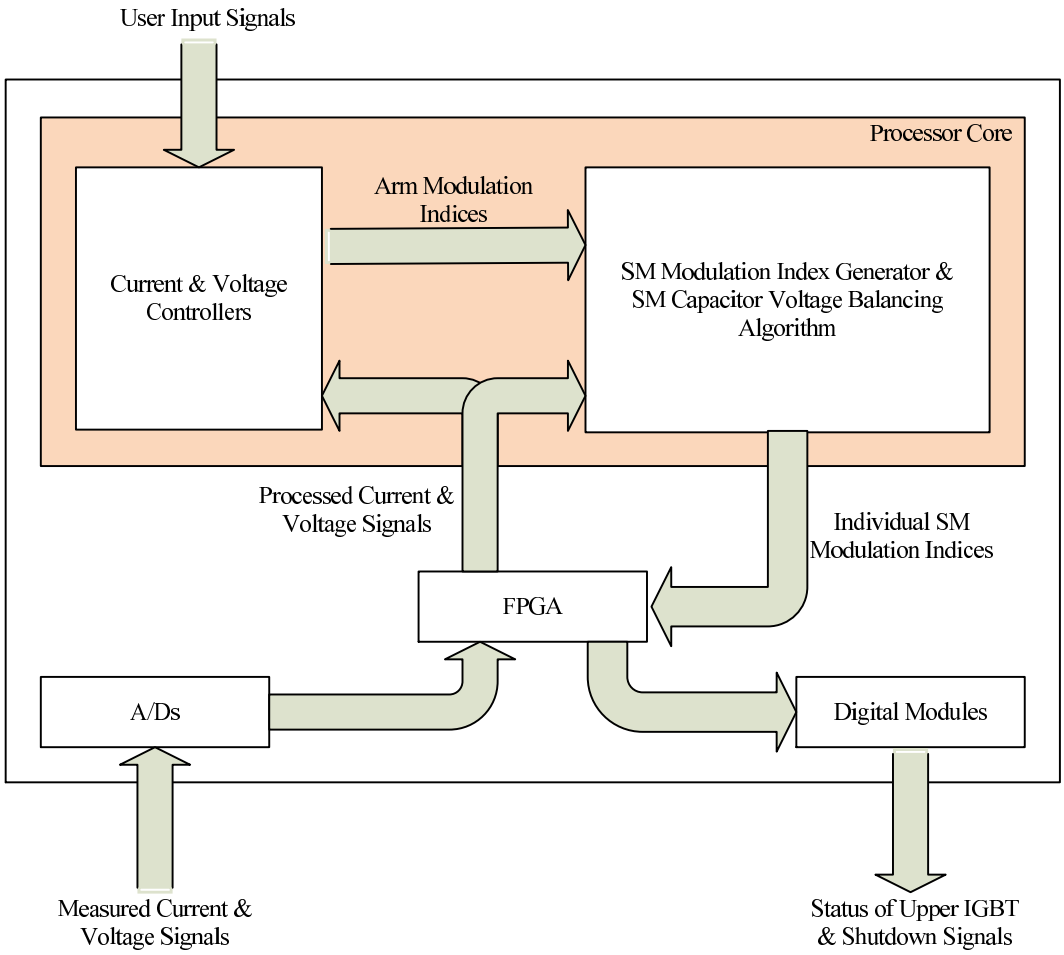

Fig. 7.3. Structure of the controller architecture.

7.2 MMC Model Validation

The MMC models developed in Chapter 3 are validated with experimental results on the developed MMC system, which feeds (i) an RL load with resistance $R_{\text{load}} = 8\ \Omega$ and inductance $L_{\text{load}} = 1.1$ mH, and (ii) PMSM load. The parameters of the MMC system and PMSM load are listed in Tables 7.2 and 7.3, respectively. The resistor R_o is determined by measuring the ESR of the inductor. The capacitor C_{SM} is estimated from the datasheet based on the frequency of its current ripple. The IGBT/diode voltage drop and resistance are obtained from their respective datasheets. The dead-

Table 7.2.
MMC Parameters

Quantity	Value
R_o	800 mΩ
Estimated SM capacitance C_{SM}	1.24 mF
IGBT voltage drop	1.05 V
IGBT resistance	33.33 mΩ
Diode voltage drop	0.95 V
Diode resistance	20 mΩ
Dead-time t_{d}	1 us
Carrier frequency f_{c}	9 kHz
Sampling time $f_{\text{s}} = \dfrac{1}{T_{\text{s}}}$	9 kHz

time is calculated based on the RC network used to introduce dead-time in the SM board.

Table 7.3.
Load Parameters

Quantity	Value
Rated power	2 kVA
Rated voltage (line-to-line)	109 V
Rated electrical frequency f_r	120 Hz
R_{load}	0.22 Ω
L_{load}	1.63 mH
Number of poles pairs (P/2)	2

7.2.1 Case Study-I

The simulation results (based on the advanced MMC state-space model) and the experimental results for the aforementioned MMC system with $i_{q,\text{ref}} = 9.5$ A, $i_{d,\text{ref}} = 0$ A, and $f = 60$ Hz is shown in Fig. 7.4. The phase-a ac-side current, circulating current, and upper- and lower-arm SM capacitor voltages are shown in Figs. 7.4(a)-

(d), respectively. As shown in the figures, the simulation results closely follow the experimental results for all the MMC states.

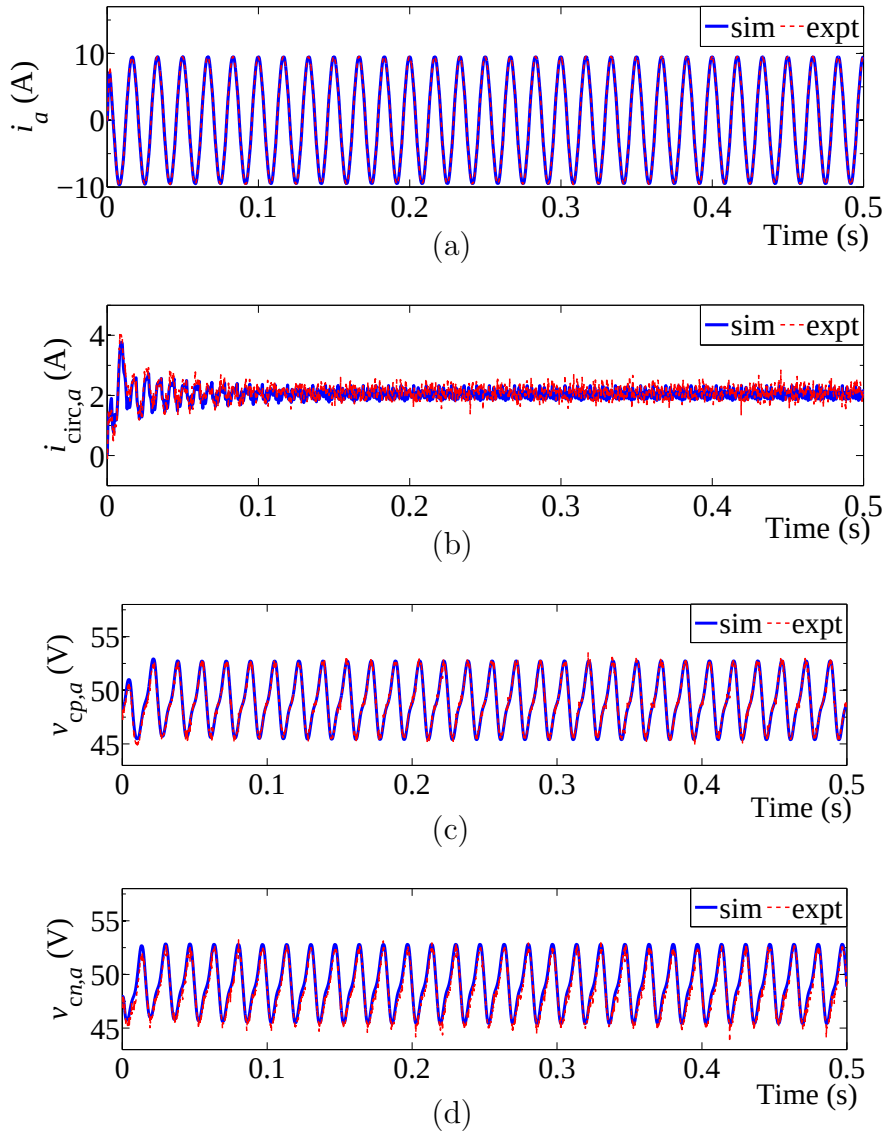

Fig. 7.4. MMC experimental and simulation waveforms: (a) phase-a ac-side current, (b) phase-a circulating current, (c) phase-a upper-arm SM capacitor voltage, and (d) phase-a lower-arm SM capacitor voltage.

To quantify the corresponding differences, the normed errors between the simulation and experimental results are listed in Table 7.4. Two different MMC models are

Table 7.4.
Accuracy Comparison

Model	Errors (%)			
	i_a	$i_{\text{circ},a}$	$v_{\text{cp},a}$	$v_{\text{cn},a}$
Advanced MMC state-space model	0.7762	7.6341	0.2953	0.8492
Approximate MMC state-space model	1.0687	12.4417	1.0111	1.7585

Table 7.5.
PWM & Capacitor Voltage Balancing Algorithm Parameters

Quantity	Value
Carrier frequency f_c	9 kHz
Sampling time $f_s = \dfrac{1}{T_s}$	9 kHz
N_{shift}	6
Capacitor voltage & arm current sampling time $f_{s,\text{cap}} = \dfrac{1}{T_{s,\text{cap}}}$	1.8 kHz

considered: (i) advanced MMC state-space model, and (ii) approximate MMC state-space model. As may be noticed from the table, compared with the approximate model, the advanced MMC state-space model improves the accuracy of the simulated states of the MMC system.

While the time taken to simulate 5 s of the aforementioned MMC system using the advanced MMC state-space model is 268 s, the time taken to simulate the same duration of the aforementioned MMC system using a detailed MMC model in PSCAD/EMTDC is 1181 s. That is, the advanced MMC state-space model is around 4 times faster than the detailed model, while capturing the essential details.

For a step change in the ac-side q-axis current reference from $i_{q,\text{ref}} = 9.5$ A to $i_{q,\text{ref}} = 4$ A, the simulation and experimental results are shown in Fig. 7.5. The simulation is performed using the advanced MMC state-space model. The step change happens at $t = 5.238$ s. The remarkable qualitative similarity for all the states of the MMC system between the simulation and experimental results is noticed in Fig. 7.5.

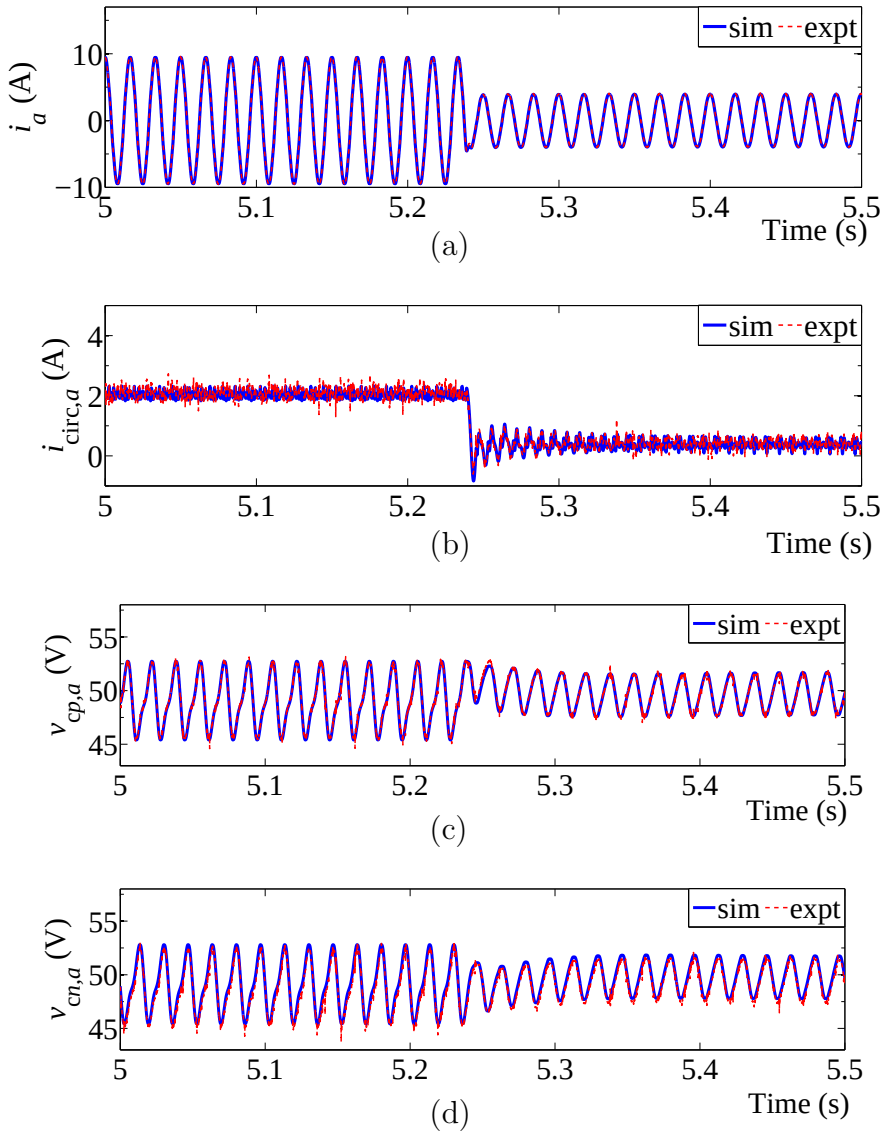

Fig. 7.5. MMC experimental and simulation waveforms for a step change in ac-side q-axis current reference: (a) phase-a ac-side current, (b) phase-a circulating current, (c) phase-a upper-arm SM capacitor voltage, and (d) phase-a lower-arm SM capacitor voltage.

7.2.2 Case Study-II

The simulation and experimental results of the MMC-based PMSM-drive with a change in torque from $T_{e,\text{ref}} = -2$ Nm to $T_{e,\text{ref}} = -1$ Nm at $\omega_{\text{rm}} = -480$ rpm

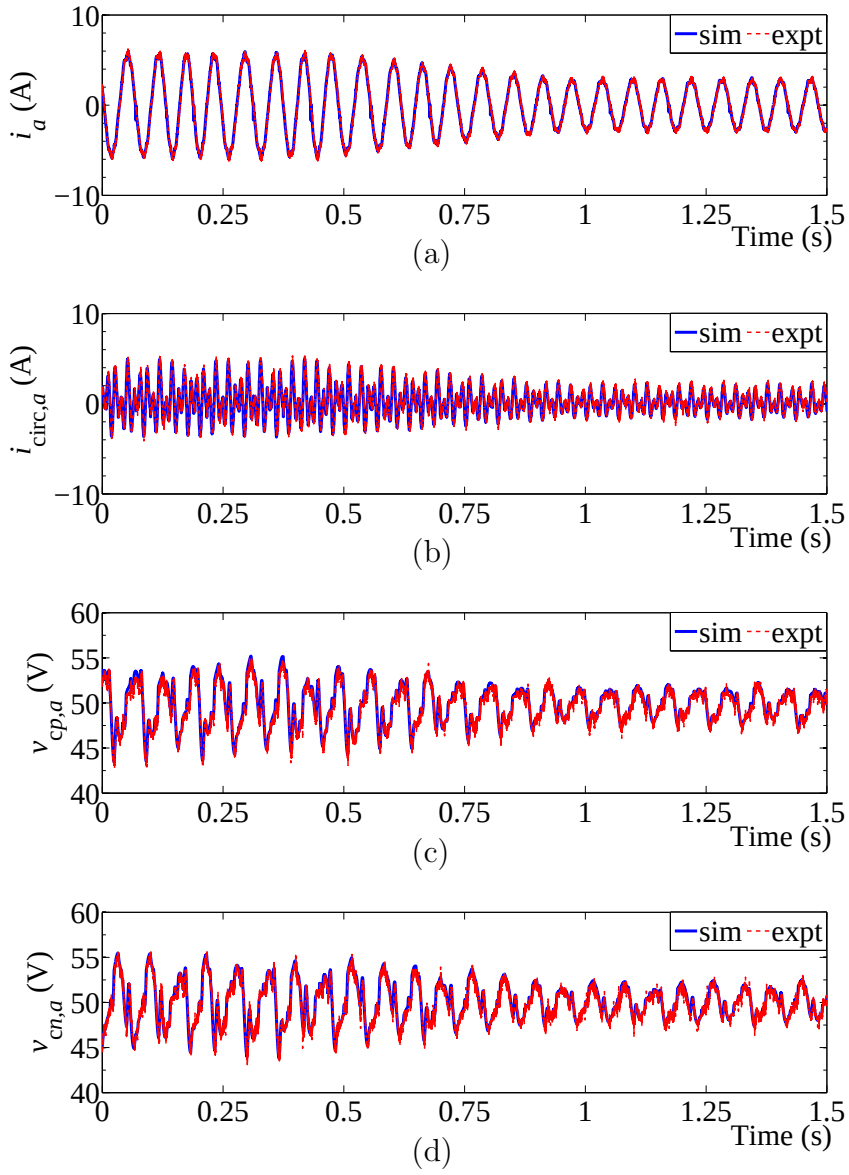

Fig. 7.6. MMC experimental and simulation waveforms for a step change in ac-side q-axis current reference: (a) phase-a ac-side current, (b) phase-a circulating current, (c) phase-a upper-arm SM capacitor voltage, and (d) phase-a lower-arm SM capacitor voltage.

are shown in Fig. 7.6. The simulation is performed using the advanced MMC state-space model and the mechanical dynamics of the PMSM obtained from experimental results. The phase-a ac-side current, circulating current, and upper- and lower-arm

SM capacitor voltages are shown in Figs. 7.6(a)-(d), respectively. As shown in the figures, the simulation results closely follow the experimental results for all the MMC states.

7.3 Proposed Modulation Strategy

This section validates the performance of the proposed modulation strategy through experimental results of a study MMC system. The study MMC system comprises a three-phase RL load with $R_{\text{load}} = 25\ \Omega$ and $L_{\text{load}} = 40$ mH connected to the developed MMC. The parameters of the DPWM strategy are listed in Table 7.5.

The experimental results of the study MMC system with peak phase current of 2 A and ac-side frequency of 60 Hz are shown in Fig. 7.7. The phase currents of the MMC are shown in Fig. 7.7(a). The line-to-line voltage v_{ab} of the MMC is shown in Fig. 7.7(b). As expected, the line-to-line voltage exhibits a seven-level voltage waveform. The phase-a SM capacitor voltages of the MMC are shown in Fig. 7.7(c). The average and peak-to-peak values of the SM capacitor voltages are 50 V and 4 V, respectively. The phase-a arm currents are shown in Fig. 7.7(d). The experimental results show the successful operation of the proposed modulation strategy.

The state of the SMs in an MMC can be determined by the state of the switches $S_{yk1,j},\ y \in \{p,n\},\ k \in \{1,2,..,N\},\ j \in \{a,b,c\}$. The switching signals, $S_{pk1,a}$ and $S_{nk1,a}$, are shown in Fig. 7.8. The switching signals show that the simultaneous switching of the devices is largely limited and only one switching transition occurs at any instant, except for two instances within a fundamental cycle when two switches change their states. The advantage of this type of switching strategy over the conventional strategies is the reduced EMI and reduced number of unnecessary switching transitions due to the SM capacitor voltage balancing algorithm, thereby reducing the switching losses.

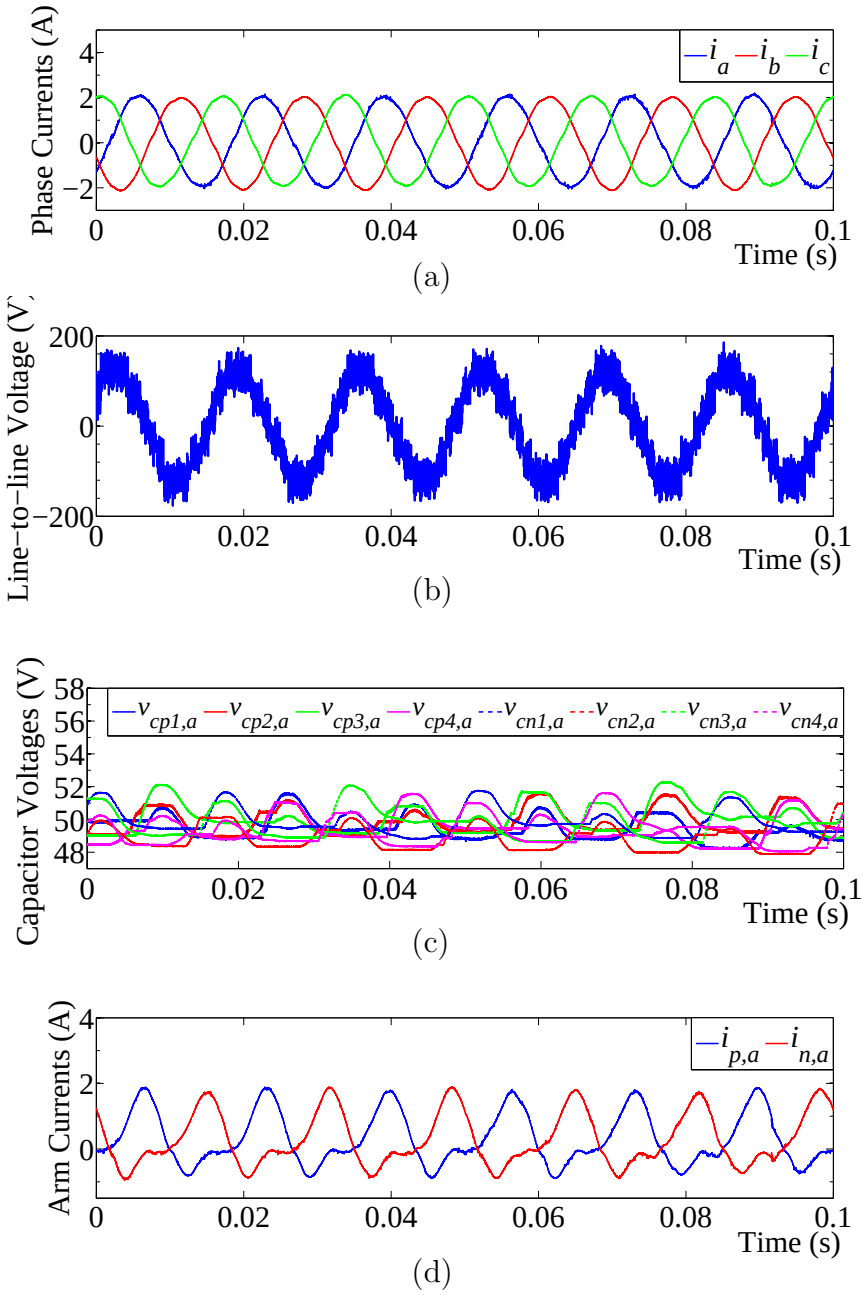

Fig. 7.7. MMC experimental waveforms with the proposed modulation strategy for a peak ac-side current of 2 A and $f = 60$ Hz: (a) phase currents, (b) line-to-line voltage v_{ab}, (c) phase-a SM capacitor voltages of MMC, and (d) phase-a arm currents of MMC.

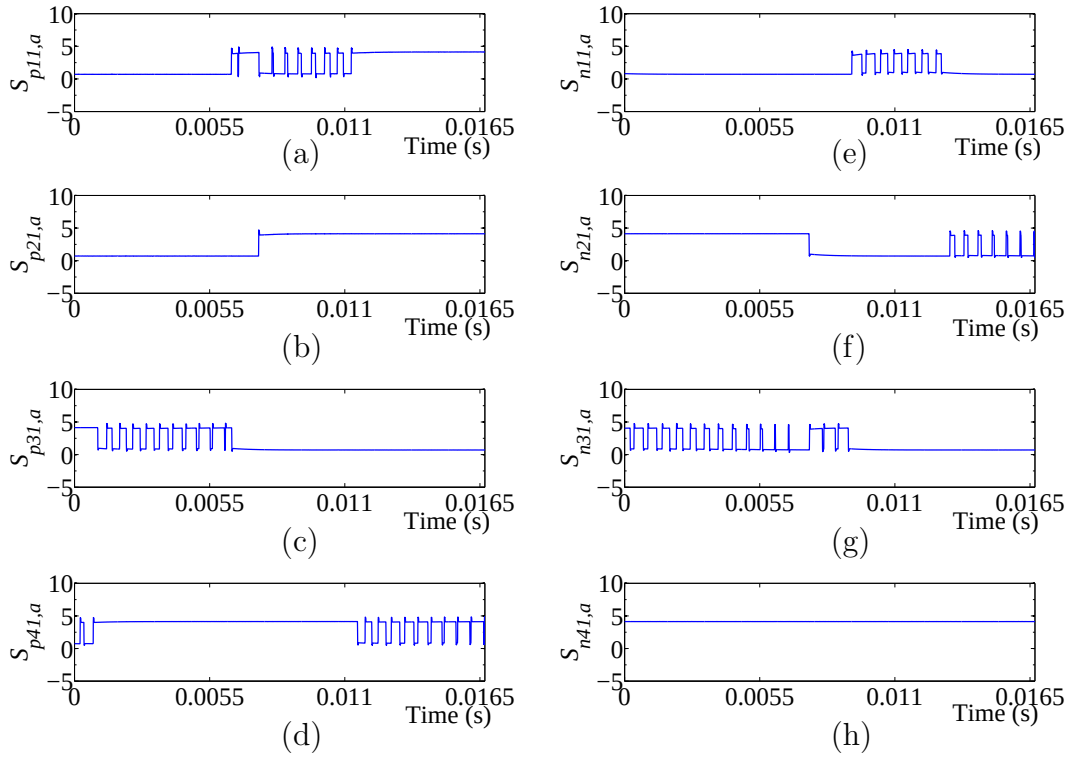

Fig. 7.8. The experimental switching signals to phase-a SMs for a peak ac-side current of 2 A and $f = 60$ Hz: (a) $S_{p11,a}$, (b) $S_{p21,a}$, (c) $S_{p31,a}$, (d) $S_{p41,a}$, (e) $S_{n11,a}$, (f) $S_{n21,a}$, (g) $S_{n31,a}$, and (h) $S_{n41,a}$.

7.4 Comparison of the Proposed Strategies for Low-Frequency Operation of the MMCs

The performance of the proposed strategies for low-frequency operation of the MMCs is verified through experiments on the developed MMC prototype with a PMSM and inductor load. The parameters of the PMSM and inductor load and the DPWM strategy are listed in Tables 7.6 and 7.7, respectively. Three case studies are presented in this section: (a) steady-state performance to validate the superiority of the proposed strategies over the existing sine strategy, (b) startup of the PMSM, and (c) step change in torque reference. The final two case studies validate the stability of

the proposed strategies and the controller design methodology studied in Chapter 5.

Table 7.6.
Load Parameters

Quantity	Value
Rated power	2 kVA
Rated voltage (line-to-line)	109 V
Rated electrical frequency f_r	120 Hz
R_{load}	0.22 Ω
L_{load}	6.03 mH
Number of poles pairs (P/2)	2

Table 7.7.
PWM & Capacitor Voltage Balancing Algorithm Parameters

Quantity	Value
Carrier frequency f_c	3.6 kHz
Sampling time $f_s = \dfrac{1}{T_s}$	18 kHz
N_{shift}	6
Capacitor voltage & arm current sampling time $f_{s,\text{cap}} = \dfrac{1}{T_{s,\text{cap}}}$	1.8 kHz

7.4.1 Steady-state

The experimental results of the MMC system driving the PMSM at 240 rpm speed with the motor qd current references of $i_{q,\text{ref}} = 4.24$ A and $i_{d,\text{ref}} = 0$ A using the sine-wave strategy and the proposed Strategies I and II are shown in Figs. 7.9 to 7.11, respectively. The common-mode frequency used in all the strategies is $f_{\text{cm}} =$ 30 Hz. One phase-a upper-arm SM capacitor voltage and one phase-a lower-arm SM capacitor voltage for the three strategies are shown in Figs. 7.9(a) to 7.11(a). As shown in Figs. 7.9(a) to 7.11(a), the peak-to-peak ripple of the SM capacitor voltages for the sine-wave strategy, Strategy I, and Strategy II is maintained within 22 V,

19 V, and 16 V, respectively. The phase-a arm currents for the three strategies are shown in Figs. 7.9(b) to 7.11(b). As shown in Figs. 7.9(b) to 7.11(b), the peak value of the circulating current for the sine-wave strategy, Strategy I, and Strategy II are 10 A, 7.5 A, and 6 A, respectively. The ac-side currents for the three strategies are shown in Figs. 7.9(c) to 7.11(c). The line-to-line voltage v_{ab} is shown in Figs. 7.9(d) to 7.11(d). The experimental results show the superior performance of the proposed strategies over the sine-wave strategy, in terms of the peak-to-peak ripple of the SM capacitor voltage and the peak value of the circulating current.

7.4.2 Startup

The startup of the PMSM involves the acceleration of the PMSM from zero to 240 rpm with motor qd current references of $i_{q,\text{ref}} = 2.12$ A and $i_{d,\text{ref}} = 0$ A. The startup process is performed by both of the proposed strategies using $f_{\text{cm}} = 90$ Hz.

The experimental results of the MMC system during startup of the PMSM using Strategies I and II are shown in Figs. 7.12 and 7.13. Startup of the PMSM with Strategies I and II is initiated at $t = 0.15$ s. One phase-a upper-arm SM capacitor voltage and one phase-a lower-arm SM capacitor voltage are shown in Figs. 7.12(a) and 7.13(a). As shown in Figs. 7.12(a) and 7.13(a), the peak-to-peak ripple of the SM capacitor voltages during startup process using Strategies I and II is maintained within 10 V and 13 V, respectively. The phase-a arm currents during the startup process using Strategies I and II are shown in Figs. 7.12(b) and 7.13(b). In addition to the low-frequency ac-side motor current, a high-frequency circulating current is observed in the arm currents during the stratup process using Strategies I and II. The ac-side motor currents during the startup process are shown in Figs. 7.12(c) and 7.13(c). The line-to-line voltage v_{ab} during the startup process using Strategies I and II are shown in Figs. 7.12(d)-7.13(d).

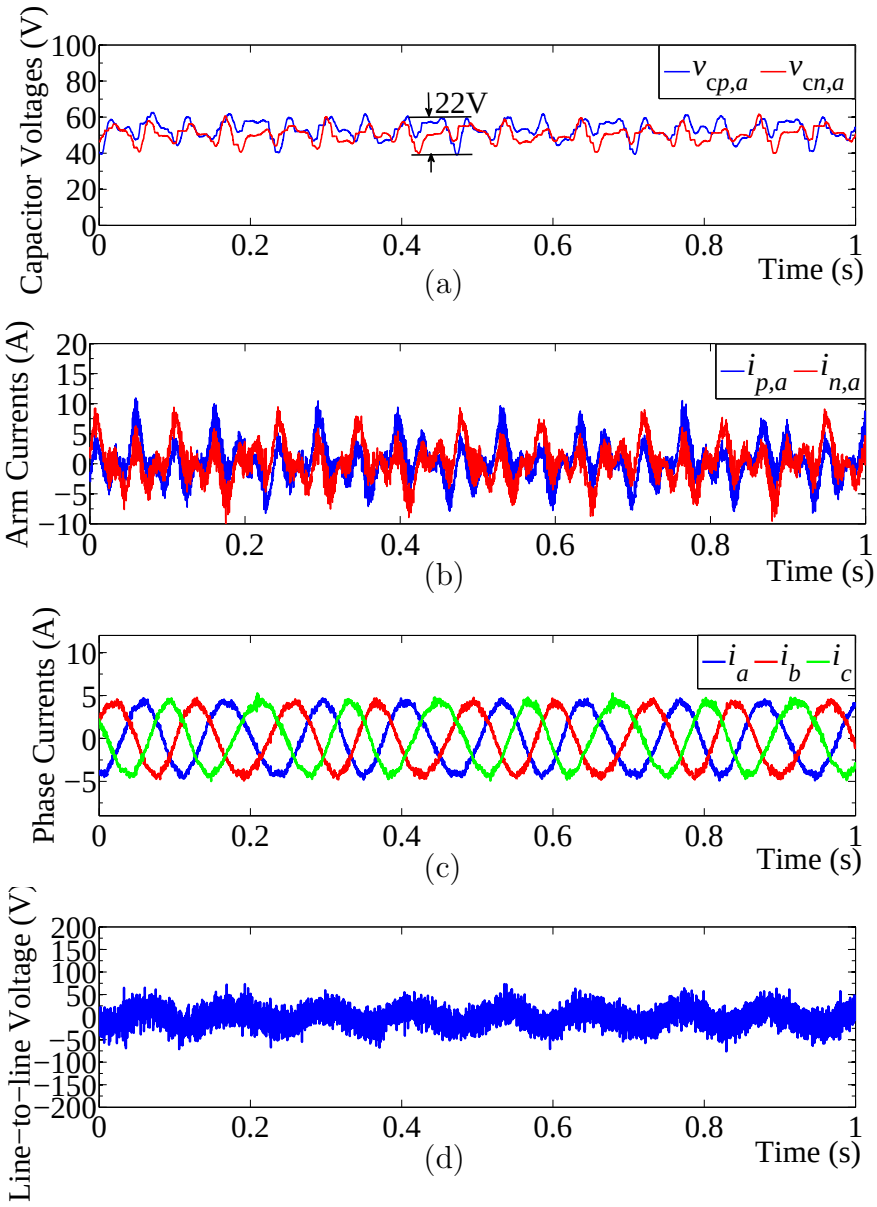

Fig. 7.9. MMC experimental waveforms for the sine-wave strategy in steady-state: (a) phase-a SM capacitor voltages, (b) phase-a arm currents, (c) ac-side currents, and (d) line-to-line voltage.

7.4.3 Step Change in Torque

A step change in the torque reference is equivalent to a step change in $i_{q,\text{ref}}$ [72]. For a change in $i_{q,\text{ref}}$ from 2.82 A to 1.41 A and with $i_{d,\text{ref}} = 0$ A, the experimental

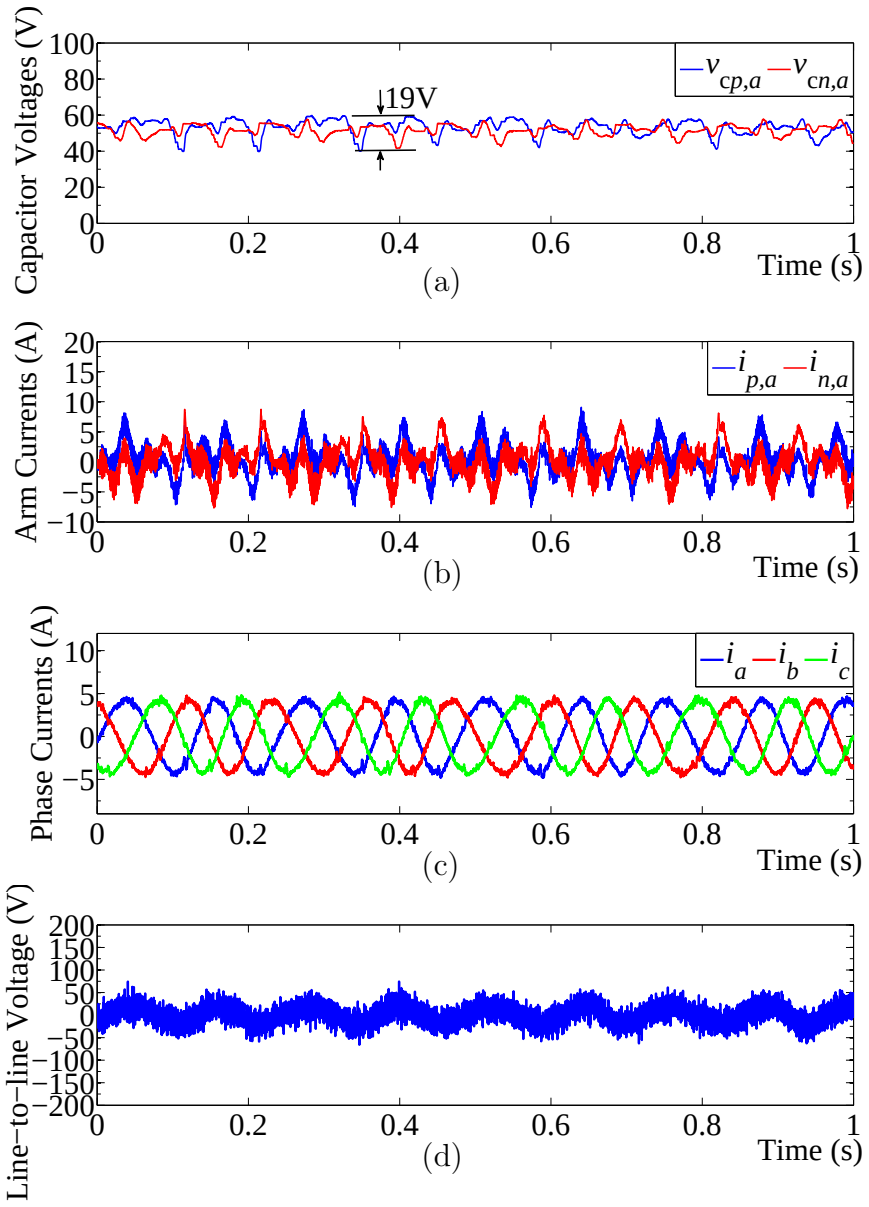

Fig. 7.10. MMC experimental waveforms for Strategy I in steady-state: (a) phase-a SM capacitor voltages, (b) phase-a arm currents, (c) ac-side currents, and (d) line-to-line voltage.

results of the MMC system operating with both of the proposed strategies and using $f_{\text{cm}} = 90$ Hz are shown and explained in this section.

The experimental results of the MMC system with a step change in the torque reference of the PMSM using the Strategies I and II are shown in Figs. 7.14 and 7.15.

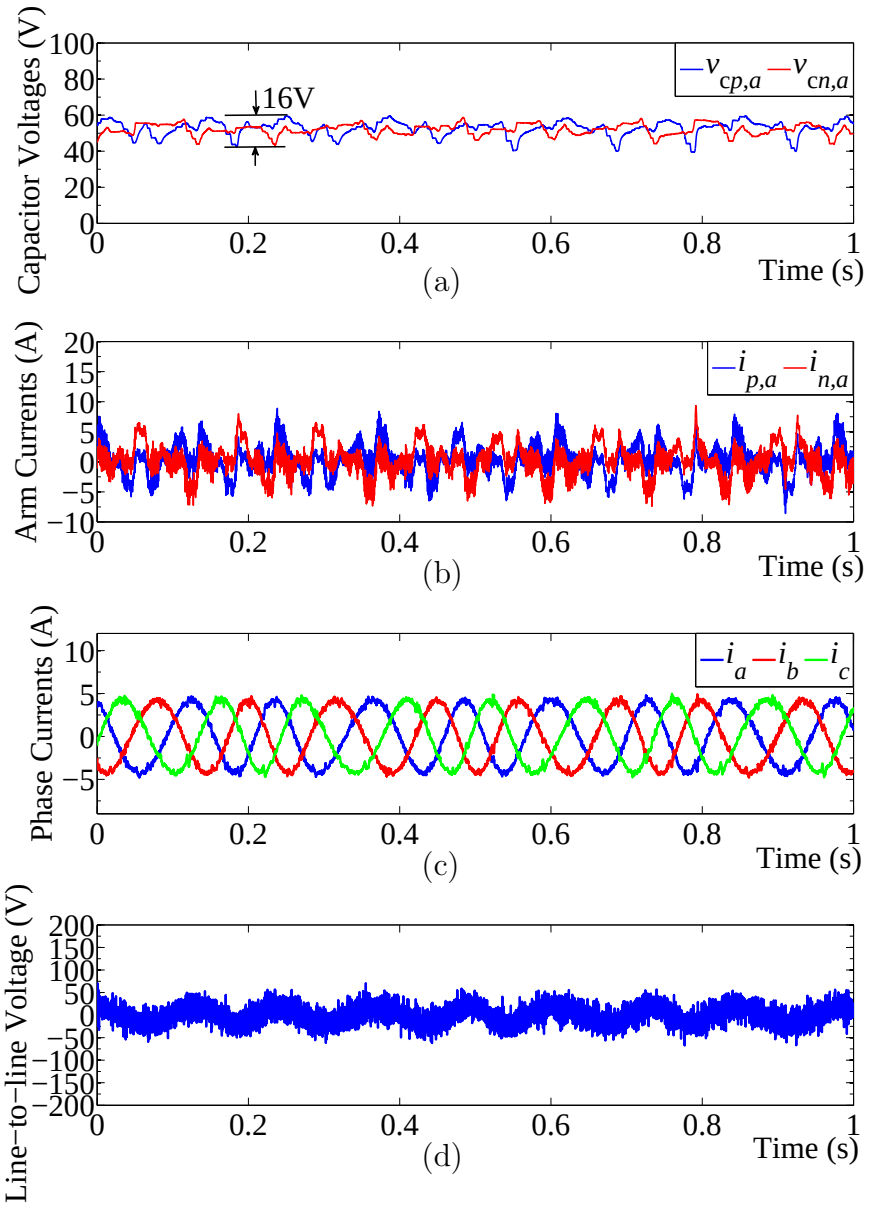

Fig. 7.11. MMC experimental waveforms for Strategy II in steady-state: (a) phase-a SM capacitor voltages, (b) phase-a arm currents, (c) ac-side currents, and (d) line-to-line voltage.

The step change in the torque occurs at $t = 0.35$ s. One phase-a upper-arm SM capacitor voltage and one phase-a lower-arm SM capacitor voltage subsequent to the step change in the torque using Strategies I and II are shown in Figs. 7.14(a) and 7.15(a). As shown in Figs. 7.14(a) and 7.15(a), the peak-to-peak ripple of the SM

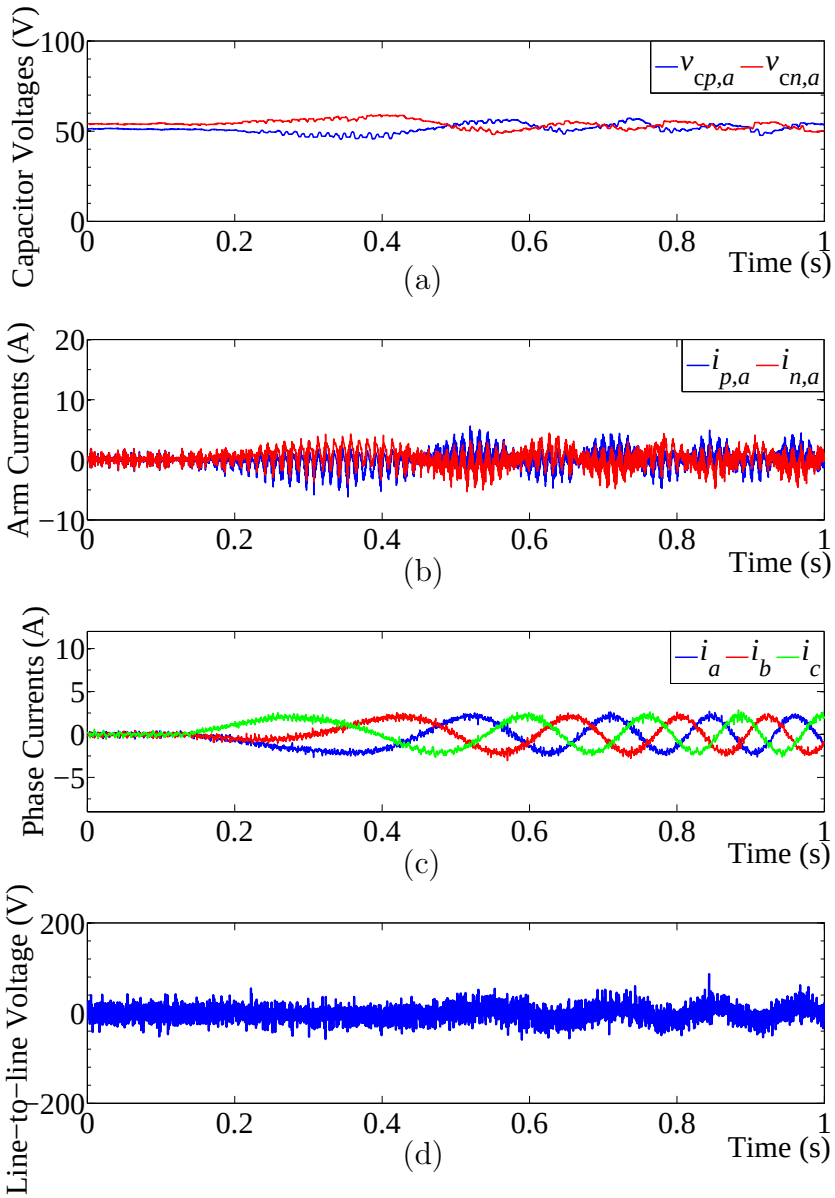

Fig. 7.12. MMC experimental waveforms for Strategy I during startup: (a) phase-a SM capacitor voltages, (b) phase-a arm currents, (c) ac-side currents, and (d) line-to-line voltage.

capacitor voltages is well maintained during the transience associated with the step change in the torque. The phase-a arm currents during the step change in the torque using Strategies I and II are shown in Figs. 7.14(b) and 7.15(b). The ac-side motor currents subsequent to the step change in the torque using Strategies I and II are

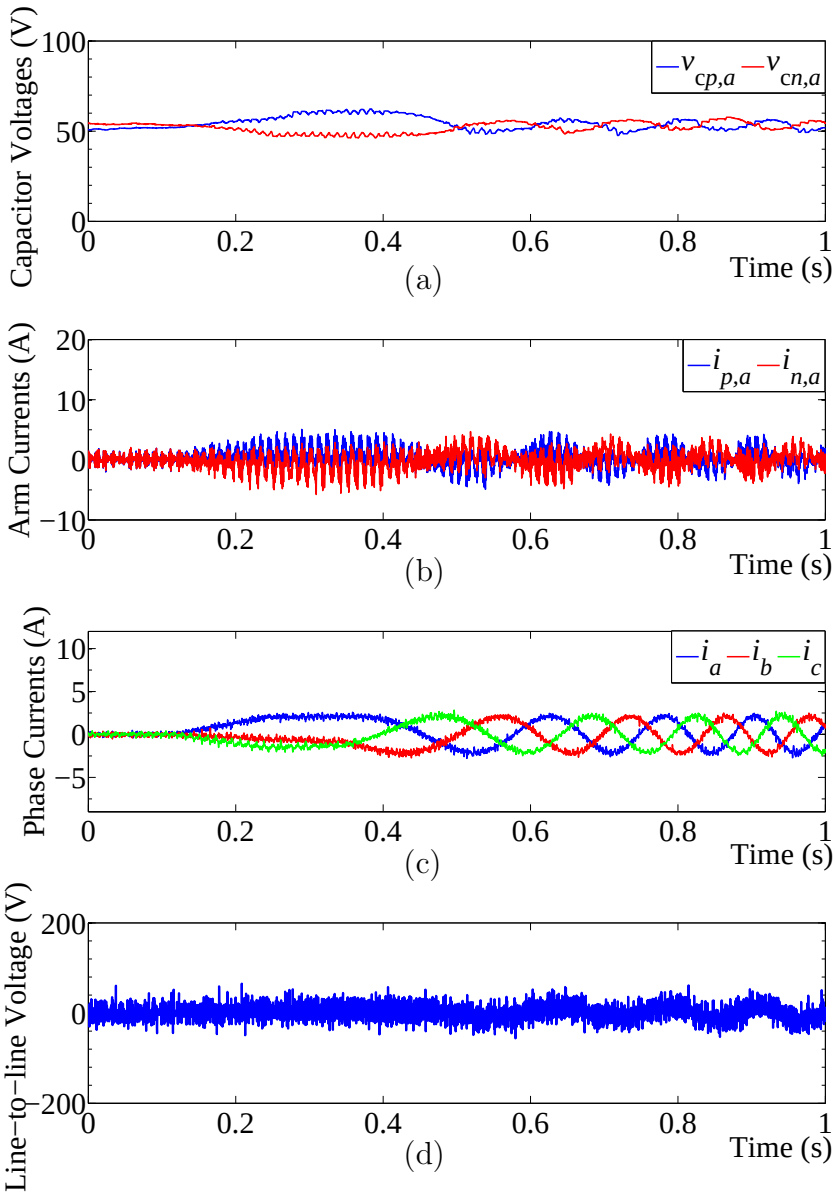

Fig. 7.13. MMC experimental waveforms for Strategy II during startup: (a) phase-a SM capacitor voltages, (b) phase-a arm currents, (c) ac-side currents, and (d) line-to-line voltage.

shown in Figs. 7.14(c) and 7.15(c). The line-to-line voltage v_{ab} during step change in torque using Strategies I and II are shown in Figs. 7.14(d)-7.15(d).

In both the startup and the step change in torque case studies, the SM capacitor voltages have a low-frequency component which has not been completely suppressed

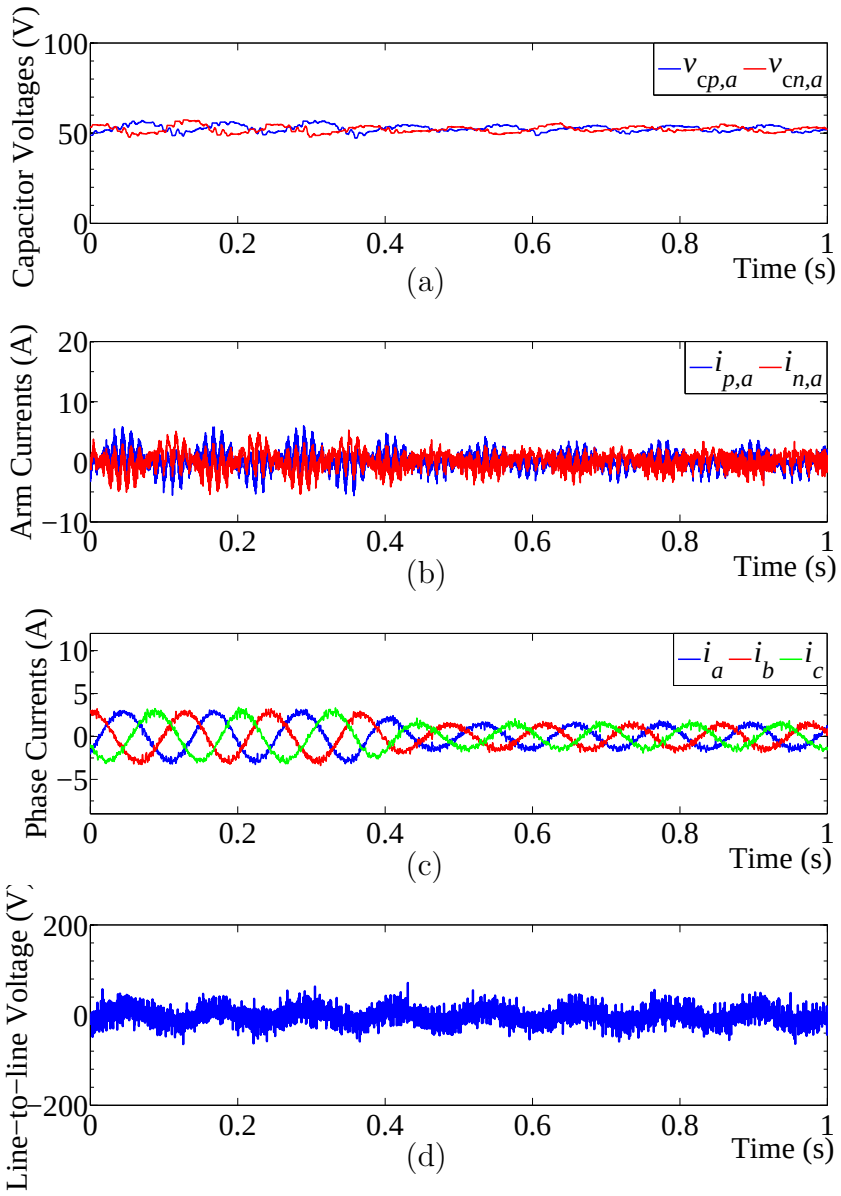

Fig. 7.14. MMC experimental waveforms for Strategy I during step change in the torque: (a) phase-a SM capacitor voltages, (b) phase-a arm currents, (c) ac-side currents, and (d) line-to-line voltage.

as shown in Figs. 7.12(a) to 7.15(a). The reason behind the incomplete suppression of the low-frequency components of the SM capacitor voltage ripple is the inadequate circulating current controller gain for $f_{\text{cm}} = 90$ Hz, which results in a steady-state error in the circulating current. Due to the limits on the circulating current controller

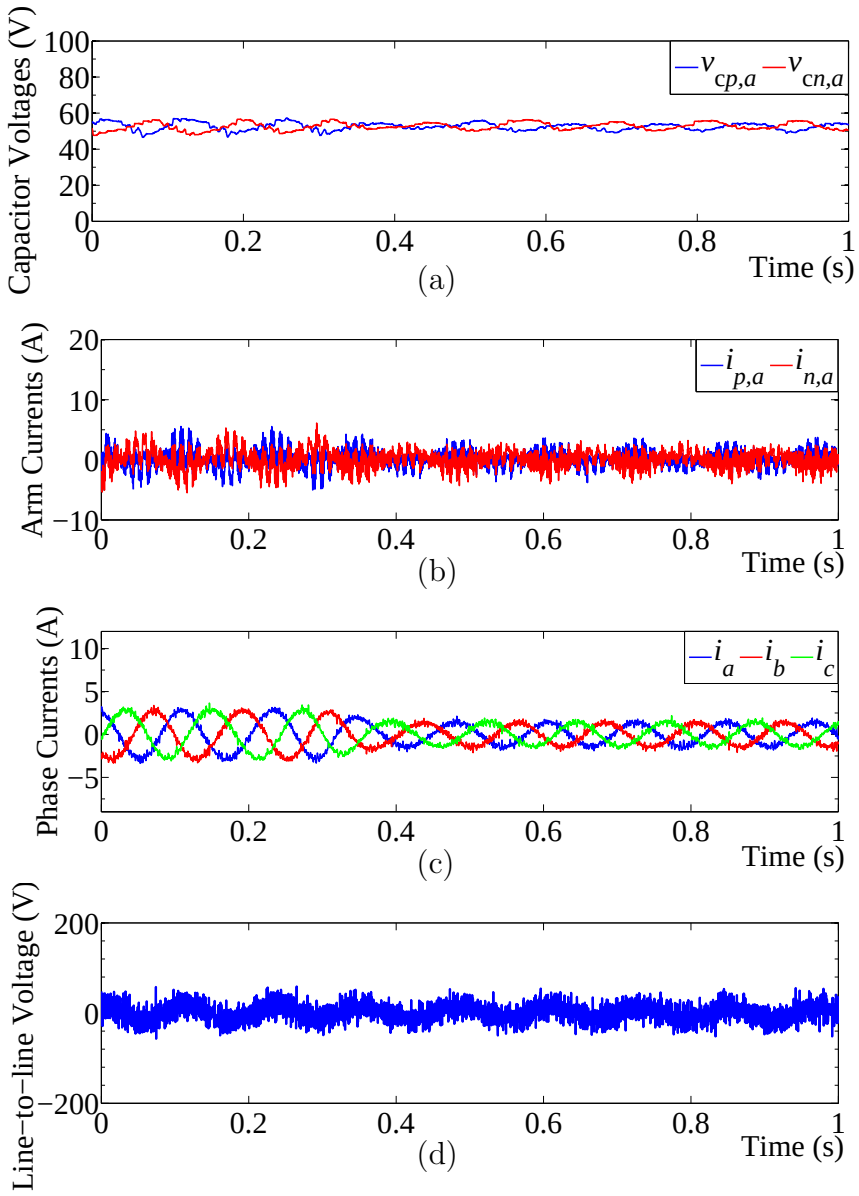

Fig. 7.15. MMC experimental waveforms for Strategy II during step change in the torque: (a) phase-a SM capacitor voltages, (b) phase-a arm currents, (c) ac-side currents, and (d) line-to-line voltage.

gain given by (5.40) and (5.43), the gain can not be increased further. Nonetheless, as Figs. 7.12(a) to 7.15(a) show, the SM capacitor voltage ripple is adequately controlled.

7.5 MMC-based Drives

The optimization of the controller gains of the control system of the MMC-based drive based on the algorithm described in Chapter 6 and the corresponding experimental results on the developed MMC system with a PMSM load, are demonstrated in this section. The parameters of the DPWM strategy and the PMSM load are listed in Tables 7.8 and 7.3, respectively.

Table 7.8.
PWM & Capacitor Voltage Balancing Algorithm Parameters

Quantity	Value
Carrier frequency f_{c}	9 kHz
Sampling time $f_{\mathrm{s}} = \dfrac{1}{T_{\mathrm{s}}}$	9 kHz
N_{shift}	6
Capacitor voltage & arm current sampling time $f_{s,\mathrm{cap}} = \dfrac{1}{T_{s,\mathrm{cap}}}$	9 kHz

7.5.1 Low-frequency Operation

The solution of the optimization problem of (6.1) for the MMC-based drive system during low-frequency operation at $T_{e,\mathrm{ref}} = -2$ Nm ($i_{q,\mathrm{ref}} = -5.65$ A) and $\omega_{\mathrm{rm}} = -480$ rpm, is

$$\boldsymbol{K} = \begin{pmatrix} 14.78 & 2656.63 & 10.05 & -0.792 \end{pmatrix}^{\mathrm{T}}, \tag{7.3}$$

with

$$L\left(\boldsymbol{x}_{\mathrm{c}}\right)=\left(\boldsymbol{x}_{\mathrm{c,ref}}-\boldsymbol{x}_{\mathrm{c}}\right)^{\mathrm{T}}\boldsymbol{Q}\left(\boldsymbol{x}_{\mathrm{c,ref}}-\boldsymbol{x}_{\mathrm{c}}\right), \tag{7.4a}$$

$$\boldsymbol{Q}=\mathrm{diag}\begin{pmatrix}\boldsymbol{v}_3 & 50\boldsymbol{v}_3 & \boldsymbol{0}_3 & 0.1\boldsymbol{v}_3 & \boldsymbol{0}_3 & 2\boldsymbol{v}_3 & \boldsymbol{0}_3\end{pmatrix}^{\mathrm{T}}, \tag{7.4b}$$

$$\boldsymbol{v}_{\mathrm{n}}=\mathrm{ones}(1,\mathrm{n}), \tag{7.4c}$$

$$\boldsymbol{0}_{\mathrm{n}}=\mathrm{zeros}(1,\mathrm{n}). \tag{7.4d}$$

The choice of the cost function in (7.3) not only ensures minimum steady-state error in the MMC states but also ensures minimum rise time of the ac-side current. The minimum rise time of the ac-side current is indirectly obtained through minimization of the integral of the ac-side $qd0$ current error. The rest of the controller parameters are listed in Table 7.9. The controller gains obtained from the optimization algorithm, results in 10 times reduction in the total cost function when compared to the initial guess of the controller gains.

Table 7.9.
MMC Controller Parameters

Quantity	Value	Quantity	Value
ω_{n}	10×10^3	f_{cm}	60 Hz
ω_{n1}	10×10^3	Strategy	I
f_{s}	18 kHz		

The experimental results of the MMC-based drive during startup of the PMSM with $T_{e,\mathrm{ref}}=-2$ Nm are shown in Fig. 7.16. During startup, the reference torque slowly changes from 0 Nm to -2 Nm to avoid high ripple in the SM capacitor voltages. The maximum speed it reaches is $\omega_{\mathrm{rm}}=-480$ rpm. The phase-a ac-side current, circulating current, and SM capacitor voltages are shown in Figs. 7.16(a)-(c), respectively. The states of the MMC show a stable startup and steady-state operation of the MMC-based drive.

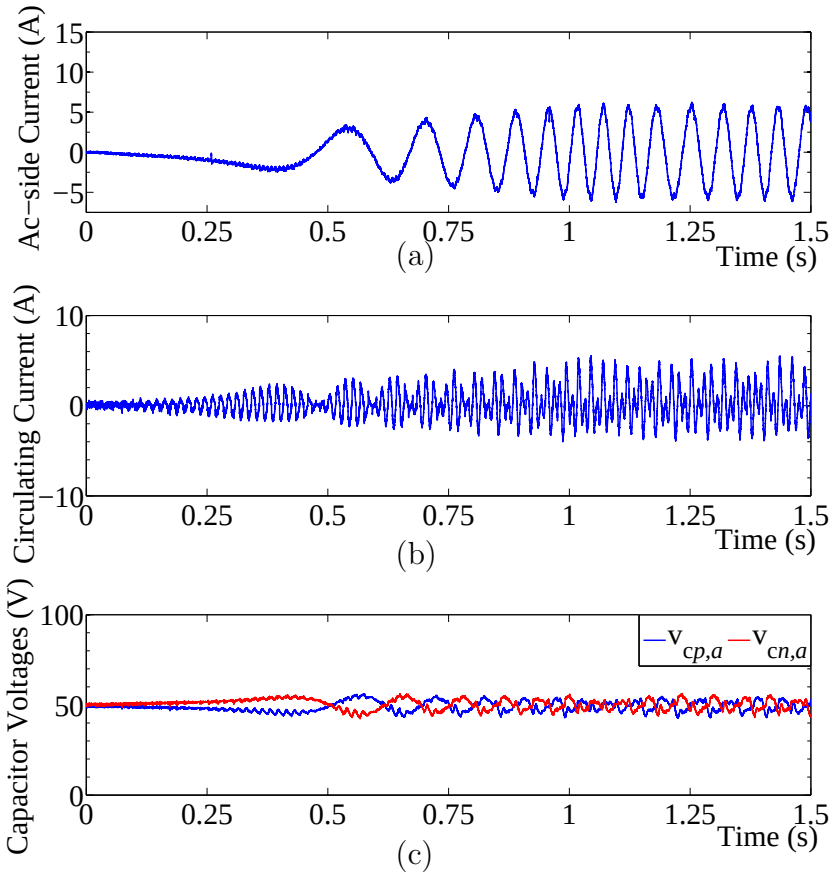

Fig. 7.16. MMC experimental waveforms during startup of PMSM: (a) phase-a ac-side current, (b) phase-a circulating current, and (c) phase-a SM capacitor voltages.

7.5.2 High-frequency Operation

The MMC-based drive system under high-frequency operation implements the circulating current controller described in Section 4.3 of Chapter 4. The solution of the optimization problem of (6.1) for the MMC-based drive system under high-frequency operation at $T_{e,\text{ref}} = -2$ Nm and $\omega_{\text{rm}} = -1800$ rpm, is given in Table 7.10.

The other controller parameters are also shown in Table 7.10. The cost function used in the optimization algorithm is given by

$$L\left(\boldsymbol{x}_{\mathrm{c}}\right)=\left(\boldsymbol{x}_{\mathrm{c,ref}}-\boldsymbol{x}_{\mathrm{c}}\right)^{\mathrm{T}}\boldsymbol{Q}\left(\boldsymbol{x}_{\mathrm{c,ref}}-\boldsymbol{x}_{\mathrm{c}}\right), \tag{7.5a}$$

$$\boldsymbol{Q}=\mathrm{diag}\begin{pmatrix}\boldsymbol{v}_3 & 10\boldsymbol{v}_3 & \boldsymbol{0}_9 & \boldsymbol{v}_3 & \boldsymbol{0}_3 & 10\boldsymbol{v}_3 & \boldsymbol{0}_{27}\end{pmatrix}^{\mathrm{T}}. \tag{7.5b}$$

The choice of the cost function is similar to the low-frequency operation case.

Table 7.10.
MMC Controller Parameters

Quantity	Value	Ouantity	Value
K_{p}	3.75	ω_{n}	10×10^3
K_{i}	2730	ω_{n}	10×10^3
K_{p1}	1	ω_{n1}	10×10^3
K_{i1}	500	ω_{n2}	$2\omega_{\mathrm{rm}}$
K_{p2}	1	ω_{n3}	$2\omega_{\mathrm{rm}}$
K_{i2}	1000	ω_{n4}	$4\omega_{\mathrm{rm}}$
K_{pv}	-0.25	ω_{n5}	$2\pi40$ rad/s
		ω_{n6}	$2\omega_{\mathrm{rm}}$

The experimental results of the MMC-based drive with $T_{e,\mathrm{ref}}=-2$ Nm and $\omega_{\mathrm{rm}}=-1800$ rpm is shown in Fig. 7.17. The phase-a ac-side current, circulating current, and SM capacitor voltages, are shown in Figs. 7.17(a)-(c), respectively. The ac-side current is tracked well and the ac components in the circulating current are reduced, as shown in Fig. 7.17. This case study shows both the high-frequency operation of an MMC-based drive as well as emulates a grid-connected MMC.

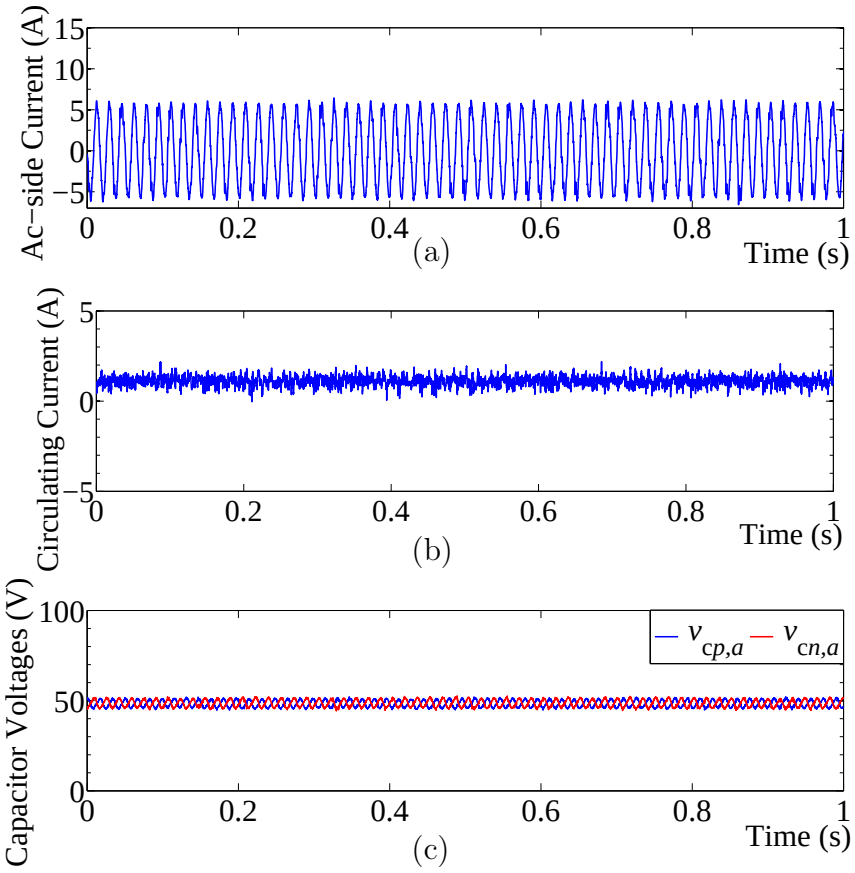

Fig. 7.17. MMC experimental waveforms driving a PMSM at $\omega_{\mathrm{rm}} = -1800$ rpm and $T_{e,\mathrm{ref}} = -2$ Nm: (a) phase-a ac-side current, (b) phase-a circulating current, and (c) phase-a SM capacitor voltages.

8. CONTROL OF MMC-BASED WIND ENERGY CONVERSION SYSTEM

The control of an MMC-based WECS is explained and investigated in this chapter. The WECS considered in this chapter is a PMSG-based direct-drive WECS explained in Chapter 2. The WECS consists of a back-to-back MMC, with a grid-side MMC under fixed-frequency operation and a generator-side MMC under variable-frequency operation. The control system developed in this chapter is based on the developments in Chapters 4 and 5. Moreover, the startup charging procedure of the back-to-back MMC capacitors from a de-energized state is described in this chapter. The performance of the developed control systems of the MMC-based WECS are validated under various operating conditions through simulation studies in the PSCAD/EMTDC software environment.

8.1 Back-to-back MMC-based WECS

8.1.1 Structure

The single-line schematic diagram of an MMC-based WECS is shown in Fig. 8.1. MMC-1 refers to the generator-side MMC and MMC-2 refers to the grid-side MMC.

8.1.2 Modes of Operation

There are three modes of operation of the back-to-back MMC-based WECS, namely

1. MMC capacitor startup charging: In this operating mode, the capacitors in the back-to-back MMC are charged from de-energized state such that the generator

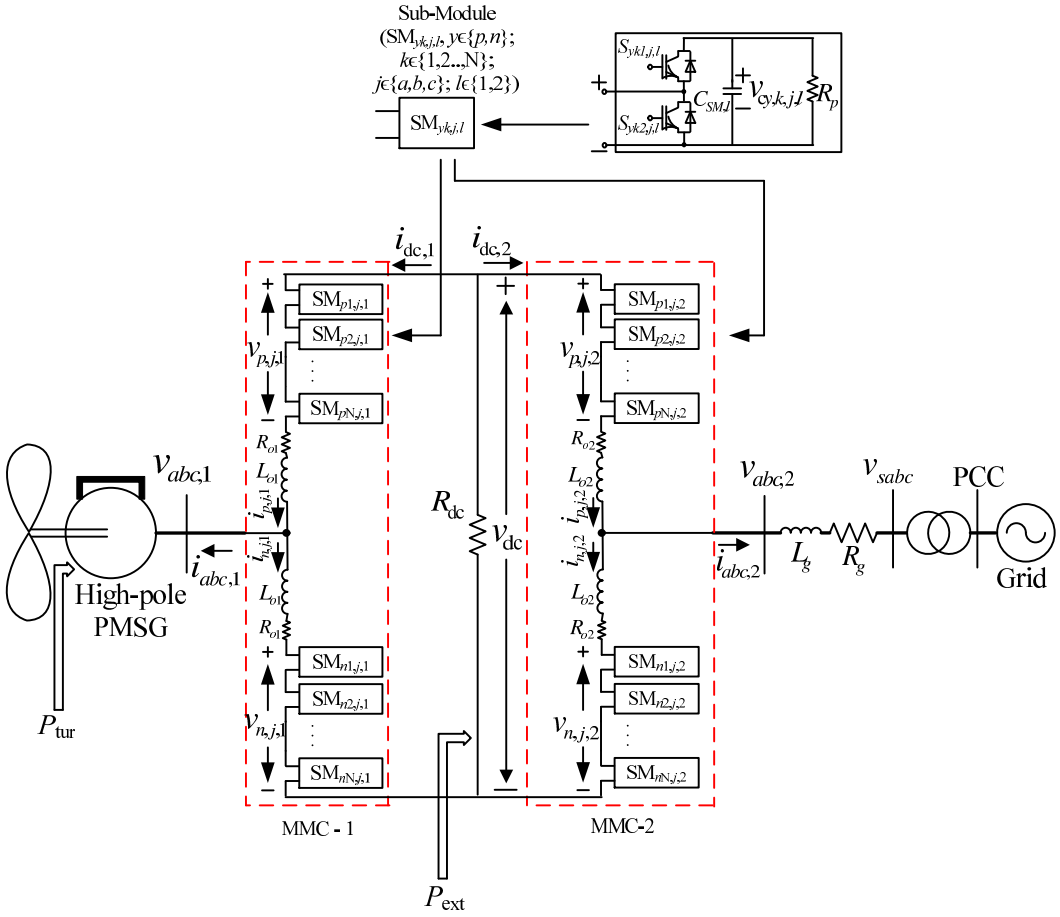

Fig. 8.1. Single-line schematic diagram of an MMC-based WECS.

is blocked and the currents in the arms and ac side are within their respective constraints.

2. WECS startup: In the WECS startup operating mode, the PMSG is operated in motor mode with constant torque to build up the turbine speed. As explained in Section 2.5 of Chapter 2, this mode is required during the startup of wind turbine or whenever there is a need to build the turbine speed.

3. Normal WECS operation: The normal WECS operation is the mode in which the WECS extracts maximum available power from the wind and transfers it to the grid.

In the following sections, the control system used in the aforementioned modes of operation is explained in detail.

8.2 MMC Capacitor Startup Charging

The objective of the MMC capacitor startup charging mode is to charge the SM capacitors in the back-to-back MMC, while limiting the inrush arm currents of the MMCs and blocking the PMSG. To achieve this goal, the proposed procedure performs the charging of the SM capacitors of the back-to-back MMC in the following five regions:

1. Uncontrolled region: The voltage required to operate the gate-drive circuit is provided by the SM capacitors. As long as the SM capacitors do not reach an initial voltage V_1, which is typically 15 V, the gate-drive circuits do not operate. Therefore, in the uncontrolled region, all the SM capacitors are in the blocked state. Additionally, there is a resistor connected in series with each ac-side phase of the grid-side MMC. The resistor is required to limit the initial inrush current.

2. Resistor control region: Once the SM capacitor voltages reach the initial voltage V_1, the gate drive circuits begin to operate. The SMs of the back-to-back MMCs are controlled such that the difference between the SM capacitor voltages and their corresponding references is minimized with constraints placed on the arm currents. The constraints on the arm currents are based on the rating of the devices and capacitors of the MMC. In this region, the resistors connected in series to the phases of the grid-side MMC, are still in the circuit.

3. Resistor-less control region: Once the SM capacitor voltages of the grid-side MMC reach a voltage of $V_2 = \frac{V}{N}\sqrt{\frac{2}{3}}$, where V is the rms value of the line-to-line grid-side voltage, the series resistors are bypassed. The series resistors are bypassed as the arm currents can be controlled and constrained within their

limits once the SM capacitor voltages of the grid-side MMC reach V_2. The SMs of the back-to-back MMCs are still controlled such that the difference between the SM capacitor voltages and their corresponding references is minimized with constraints placed on the arm currents.

4. Dc current region: Once the SM capacitor voltages of the grid-side MMC reach a voltage of V_3, SMs of the back-to-back MMCs are controlled such that the difference between the SM capacitor voltages and their corresponding references is minimized with constraints on the arm, dc-link, and grid-side currents, and the change in the state of the SMs in the generator-side MMC. A lower limit is placed on the dc-link current based on the constraints on the arm currents. The additional constraint of a lower limit on the dc-link current is placed to accelerate the charging of the SM capacitors in the generator-side MMC. A lower limit is placed on the grid-side q-axis current such that, in addition to charging the SM capacitors of the generator-side MMC, there is enough power to charge the SM capacitors of grid-side MMC. The d-axis current is imposed to zero to ensure that power is transferred from the grid at unity power factor. The change in the state of the SMs in the generator-side MMC is limited such that only one SM may change its state at any instant. The constraint on the change in the state of the SMs in the generator-side MMC helps reduce the switching frequency and hence, the switching losses.

5. Tail-end region: Once the SM capacitor voltages of the generator-side MMC reach a voltage of V_4, the lower limit of the dc-link current is exponentially reduced to zero. The SMs of the back-to-back MMC are controlled such that the difference between the SM capacitor voltages and their references is minimized, power is transferred from the grid at unity power factor, the state of only one SM is changed in the generator-side MMC, and the arm currents are constrained. As the name of the region suggests, the difference between the SM capacitor voltages and their references is expected to tail off.

In the aforementioned procedure, the voltages V_3 and V_4 are chosen such that the SM capacitors are charged in minimum time without violating the constraints imposed on the arm currents.

In each of the regions of the proposed procedure, $n_{c,1}$ ($n_{c,1} \in \{0, 1, 2, .., N\}$) SMs are inserted in each arm of the MMC-1 to avoid any impact of the startup procedure on the PMSG. By maintaining the same number of inserted SMs in the upper and lower arms of MMC-1, the generator-side voltage is maintained at zero, thereby, insulating the PMSG from any impact of the startup procedure. Assuming, that the MMC-2 has $n_{y,j,2}$ SMs inserted in arm-y phase-j and using the generalized dynamic model of the MMC described in Section 3.3 of Chapter 3, the following state-space equation is developed to describe the dynamics of the back-to-back MMCs under the proposed startup procedure

$$\frac{\mathrm{d}\boldsymbol{x}}{\mathrm{d}t} = \boldsymbol{f}(\boldsymbol{x}, \boldsymbol{u}), \tag{8.1}$$

where

$$\boldsymbol{x}^{\mathrm{T}} = \begin{pmatrix} \boldsymbol{v}_{\mathrm{c},2}^{\mathrm{T}} & v_{\mathrm{c},1} & i_{p,a,2} & i_{n,a,2} & i_{p,b,2} & i_{n,b,2} & i_{\mathrm{dc}} \end{pmatrix}, \tag{8.2a}$$

$$\boldsymbol{v}_{\mathrm{c},2}^{\mathrm{T}} = \begin{pmatrix} v_{\mathrm{c}p,a,2} & v_{\mathrm{c}n,a,2} & v_{\mathrm{c}p,b,2} & v_{\mathrm{c}n,b,2} & v_{\mathrm{c}p,c,2} & v_{\mathrm{c}n,c,2} \end{pmatrix}, \tag{8.2b}$$

$$\boldsymbol{u}^{\mathrm{T}} = \begin{pmatrix} \boldsymbol{n}_{c,2}^{\mathrm{T}} & n_{c,1} \end{pmatrix}, \tag{8.2c}$$

$$\boldsymbol{n}_{c,2}^{\mathrm{T}} = \begin{pmatrix} n_{p,a,2} & n_{n,a,2} & n_{p,b,2} & n_{n,b,2} & n_{p,c,2} & n_{n,c,2} \end{pmatrix}, \tag{8.2d}$$

$$\boldsymbol{f}(\boldsymbol{x}, \boldsymbol{u})^{\mathrm{T}} = \begin{pmatrix} \dfrac{1}{NC_{\mathrm{SM},2}} \left(\boldsymbol{n}_{c,2} \odot \boldsymbol{i}_2\right)^{\mathrm{T}} & \dfrac{n_{c,1} i_{\mathrm{dc}}}{3NC_{\mathrm{SM},1}} & \left(\boldsymbol{A}^{-1}\boldsymbol{b}\right)^{\mathrm{T}} \end{pmatrix}, \tag{8.2e}$$

$$i_{\mathrm{dc},1} = -i_{\mathrm{dc},2} = i_{\mathrm{dc}} = -\sum_{j\in\{a,b,c\}} i_{p,j,2} = -\sum_{j\in\{a,b,c\}} i_{n,j,2}, \tag{8.2f}$$

$$\boldsymbol{i}_2^{\mathrm{T}} = \begin{pmatrix} i_{p,a,2} & i_{n,a,2} & i_{p,b,2} & i_{n,b,2} & i_{p,c,2} & i_{n,c,2} \end{pmatrix}, \tag{8.2g}$$

$$v_{\mathrm{c}p,a,1} = v_{\mathrm{c}n,a,1} = v_{\mathrm{c}p,b,1} = v_{\mathrm{c}n,b,1} = v_{\mathrm{c}p,c,1} = v_{\mathrm{c}n,c,1} = v_{\mathrm{c},1}, \tag{8.2h}$$

$$\boldsymbol{A} = \begin{pmatrix} -L_g & L_{o2}+L_g & L_g & -L_{o2}-L_g & 0 \\ -L_{o2}-L_g & L_g & L_{o2}+L_g & -L_g & 0 \\ -L_g & L_{o2}+L_g & -2L_g & 2L_{o2}+2L_g & L_{o2} \\ -L_{o2}-L_g & L_g & -2L_{o2}-2L_g & 2L_g & -L_{o2} \\ 0 & 0 & 0 & 0 & \frac{2}{3}\left(L_{o1}+L_{o2}\right) \end{pmatrix}, \tag{8.2i}$$

$$\boldsymbol{b} = \begin{pmatrix} v_{ab} + n_{n,b,2}v_{cn,b,2} - n_{n,a,2}v_{cn,a,2} + v_{rg1} - R_{o2}\left(i_{n,a,2} - i_{n,b,2}\right) \\ v_{ab} + n_{p,a,2}v_{cp,a,2} - n_{p,b,2}v_{cp,b,2} + v_{rg1} + R_{o2}\left(i_{p,a,2} - i_{p,b,2}\right) \\ v_{bc} + n_{n,c,2}v_{cn,c,2} - n_{n,b,2}v_{cn,b,2} + v_{rg2} - R_{o2}\left(i_{n,a,2} + 2i_{n,b,2} + i_{\mathrm{dc}}\right) \\ v_{bc} + n_{p,b,2}v_{cp,b,2} - n_{p,c,2}v_{cp,c,2} + v_{rg2} + R_{o2}\left(i_{p,a,2} + 2i_{p,b,2} + i_{\mathrm{dc}}\right) \\ \frac{1}{3}\boldsymbol{n}_{c,2}^{\mathrm{T}}\boldsymbol{v}_{\mathrm{c},2} - 2n_{c,1}v_{\mathrm{c},1} - \frac{2}{3}\left(R_{o1}+R_{o2}\right)i_{\mathrm{dc}} \end{pmatrix}, \tag{8.2j}$$

$$v_{rg1} = R_g\left(i_{p,a,2} - i_{n,a,2} - i_{p,b,2} + i_{n,b,2}\right), \tag{8.2k}$$

$$v_{rg2} = R_g\left(i_{p,a,2} - i_{n,a,2} + 2i_{p,b,2} - 2i_{n,b,2}\right). \tag{8.2l}$$

where the subscripts 1 and 2 indicate the variables associated with the MMC-1 and 2, respectively. The IGBT/diode losses and the resistor R_p have been neglected in (8.1) and (8.2). In resistor control and resistor-less control regions, the input, $\boldsymbol{u}$, in (8.1) and (8.2) is determined to

$$\begin{aligned} &\underset{\boldsymbol{u}\in G}{\text{Minimize}}\ F(\boldsymbol{u}) = \left(\boldsymbol{v}_{c,\mathrm{ref}} - \boldsymbol{D}\boldsymbol{x}\left(\boldsymbol{u}\right)\right)^{\mathrm{T}}\left(\boldsymbol{v}_{\mathrm{c,ref}} - \boldsymbol{D}\boldsymbol{x}\left(\boldsymbol{u}\right)\right) \\ &\text{subject to } \boldsymbol{C}\boldsymbol{x}\left(\boldsymbol{u}\right) \leq \boldsymbol{x}_{\mathrm{lim}} \end{aligned} \tag{8.3}$$

where

$$\boldsymbol{D} = \begin{pmatrix} \boldsymbol{I}_{7\times 7} & \boldsymbol{0}_{7\times 5} \\ \boldsymbol{0}_{5\times 7} & \boldsymbol{0}_{5\times 5} \end{pmatrix}, \tag{8.4a}$$

$$\boldsymbol{C} = \begin{pmatrix} \boldsymbol{E} \\ \boldsymbol{I}_{12\times 12} \\ \boldsymbol{H} \end{pmatrix}, \tag{8.4b}$$

$$\boldsymbol{E} = \begin{pmatrix} -\boldsymbol{I}_{7\times 7} & \boldsymbol{0}_{7\times 5} \end{pmatrix}, \tag{8.4c}$$

$$\boldsymbol{H} = \begin{pmatrix} \boldsymbol{0}_{1\times 7} & -1 & 0 & -1 & 0 & -1 \\ \boldsymbol{0}_{1\times 7} & 0 & -1 & 0 & -1 & -1 \end{pmatrix}, \tag{8.4d}$$

$$\boldsymbol{x}_{\text{lim}} = \begin{pmatrix} \boldsymbol{0}_{7\times 1}^{\text{T}} & \boldsymbol{v}_{\text{c,lim}}^{\text{T}} & \boldsymbol{i}_{\text{lim}}^{\text{T}} \end{pmatrix}^{\text{T}}, \tag{8.4e}$$

$$\boldsymbol{v}_{\text{c,ref}} = V_{\text{c,ref}} \boldsymbol{1}_7, \tag{8.4f}$$

$$\boldsymbol{v}_{c,\text{lim}} = V_{\text{c,lim}} \boldsymbol{1}_7, \tag{8.4g}$$

$$\boldsymbol{i}_{\text{lim}} = \begin{pmatrix} I_{\text{lim}} \boldsymbol{1}_4^{\text{T}} & 2I_{\text{lim}} & I_{\text{lim}} \boldsymbol{1}_2^{\text{T}} \end{pmatrix}^{\text{T}}, \tag{8.4h}$$

$$G = \{0, 1, 2..., N\}, \tag{8.4i}$$

$$\boldsymbol{1}_n = \text{Ones}\,(n, 1), \tag{8.4j}$$

$V_{\text{c,ref}}$, $V_{\text{c,lim}}$ and I_{lim} are the reference value of the capacitor voltages, the upper limit of the capacitor voltages, and the upper limit of the arm currents, respectively. The goal of the optimization problem in (8.3) is to minimize the capacitor voltage error function while placing upper limits on the capacitor voltages, arm currents, and dc-link current. In the dc current and tail-end regions, the constraints defined in (8.3) and (8.4) are modified to

$$\boldsymbol{C}' \begin{pmatrix} \boldsymbol{x}\,(\boldsymbol{u})^{\text{T}} & \Delta \boldsymbol{u}^{\text{T}} \end{pmatrix}^{\text{T}} \leq \begin{pmatrix} \boldsymbol{x}_{\text{lim}}'^{T} \boldsymbol{u}_{\text{lim}}'^{T} \end{pmatrix}^{\text{T}} \tag{8.5a}$$

$$\boldsymbol{C}' = \begin{pmatrix} \boldsymbol{C} & \boldsymbol{0}_{21\times 7} \\ \boldsymbol{H}' & \boldsymbol{0}_{1\times 7} \\ \boldsymbol{E}' & \boldsymbol{0}_{3\times 7} \\ \boldsymbol{0}_{2\times 12} & \boldsymbol{K}' \end{pmatrix}, \tag{8.5b}$$

$$\boldsymbol{H}' = \begin{pmatrix} \boldsymbol{0}_{1\times 11} & -1 \end{pmatrix}, \tag{8.5c}$$

$$\boldsymbol{E}' = \boldsymbol{T}_2 \boldsymbol{E}'', \tag{8.5d}$$

$$\boldsymbol{K}' = \begin{pmatrix} \boldsymbol{0}_{1\times 6} & 1 \\ \boldsymbol{0}_{1\times 6} & -1 \end{pmatrix}, \tag{8.5e}$$

$$\boldsymbol{T}_2 = \begin{pmatrix} \cos(\theta_e) & \cos\left(\theta_e - \frac{2\pi}{3}\right) & \cos\left(\theta_e + \frac{2\pi}{3}\right) \\ \sin(\theta_e) & \sin\left(\theta_e - \frac{2\pi}{3}\right) & \sin\left(\theta_e + \frac{2\pi}{3}\right) \\ -\sin(\theta_e) & -\sin\left(\theta_e - \frac{2\pi}{3}\right) & -\sin\left(\theta_e + \frac{2\pi}{3}\right) \end{pmatrix}, \tag{8.5f}$$

$$\boldsymbol{E}'' = \begin{pmatrix} \boldsymbol{0}_{1\times 7} & 1 & -1 & 0 & 0 & 0 \\ \boldsymbol{0}_{1\times 7} & 0 & 0 & 1 & -1 & 0 \\ \boldsymbol{0}_{1\times 7} & -1 & 1 & -1 & 1 & 0 \end{pmatrix}, \tag{8.5g}$$

$$\boldsymbol{x}'_{\text{lim}} = \begin{pmatrix} \boldsymbol{x}_{\text{lim}}^{\text{T}} & -i_{\text{dc,lim}} & -2k_1 \dfrac{P_{\text{c,loss}} + P_{\text{c,1}}}{3v_{sq}} & 0 & 0 \end{pmatrix}^{\text{T}}, \tag{8.5h}$$

$$\boldsymbol{u}'_{\text{lim}} = \begin{pmatrix} 1 & 1 \end{pmatrix}^{\text{T}}, \tag{8.5i}$$

$$\Delta\boldsymbol{u} = \boldsymbol{u}[k]^{\text{T}} - \boldsymbol{u}[k-1]^{\text{T}}, \tag{8.5j}$$

where $i_{\text{dc,lim}} = I_{\text{lim}}$ in the dc current region and $i_{\text{dc,lim}} = I_{\text{lim}}e^{-N_1 t}$ in the tail-end region, $P_{\text{c,loss}}$ is the loss in the MMCs, and $P_{\text{c,1}}$ is the power required to charge the SM capacitors of MMC-1. The values k_1 and N_1 are chosen such that the SM capacitor voltages charge in minimum time without violating the constraints on the arm currents. The objective function to be minimized in the dc current and tail-end region remains the same as in (8.3) and (8.4).

The optimization problem in each of the aforementioned regions is an integer quadratic optimization problem, which is a non-deterministic polynomial-time (NP) problem. Therefore, it is solved offline using the genetic algorithm (GA) in the MATLAB to generate the input $\boldsymbol{u}$, which is stored in a lookup table and used during the MMC capacitor startup charging process.

8.3 WECS Startup

The WECS startup involves control of the generator-side MMC as explained in Section 5.4 of Chapter 5 and of the grid-side MMC similar to as explained in Sections 4.2 and 4.3 of Chapter 4. In addition to the aforementioned control systems

for the generator-side and grid-side MMCs, an energy controller that generates the grid-side q-axis current reference is also presented.

8.3.1 Energy Controller

The energy controller generates the grid-side q-axis current reference through control of the energy of the SM capacitors in the generator- and grid-side MMCs.

Based on (3.19a) and (3.7a), the power processed by the upper-arm SM capacitors of MMC-2, can be expressed as

$$p_{p,j,2} = \left(\frac{V_{\mathrm{dc}}}{2} - L_{o2} \frac{\mathrm{d}i_{p,j,2}}{\mathrm{d}t} - R_{o2} i_{p,j,2} - v_{j,2} - v_{\mathrm{cm},2} \right) i_{p,j,2}. \tag{8.6}$$

Substituting for $i_{p,j,2}$ from (3.5) in (8.6) results in

$$p_{p,j,2} = \left(\frac{V_{\mathrm{dc}}}{2} - L_{o2} \frac{\mathrm{d}\left(\frac{i_{j,2}}{2} + i_{\mathrm{circ},j,2} \right)}{\mathrm{d}t} - R_{o2} \left(\frac{i_{j,2}}{2} + i_{\mathrm{circ},j,2} \right) - v_{j,2} - v_{\mathrm{cm},2} \right) \times \left(\frac{i_{j,2}}{2} + i_{\mathrm{circ},j,2} \right). \tag{8.7}$$

Substituting for

$$v_{j,2}^{'} = v_{j,2} + \frac{L_{o2}}{2} \frac{\mathrm{d}i_{j,2}}{\mathrm{d}t} + \frac{R_{o2}}{2} i_{j,2}, \tag{8.8a}$$

$$v_{\mathrm{circ},j,2} = L_{o2} \frac{\mathrm{d}i_{\mathrm{circ},j,2}}{\mathrm{d}t} + R_{o2} i_{\mathrm{circ},j,2}, \tag{8.8b}$$

in (8.7) results in

$$\begin{aligned} p_{p,j,2} &= \left(\frac{V_{\mathrm{dc}}}{2} - v_{j,2}^{'} - v_{\mathrm{cm},2} - v_{\mathrm{circ},j,2} \right) \left(\frac{i_{j,2}}{2} + i_{\mathrm{circ},j,2} \right) \\ &= \frac{V_{\mathrm{dc}} i_{j,2}}{4} + \frac{V_{\mathrm{dc}}}{2} i_{\mathrm{circ},j,2} - \frac{v_{j,2}^{'} i_{j,2}}{2} - v_{j,2}^{'} i_{\mathrm{circ},j,2} - (v_{\mathrm{cm},2} + v_{\mathrm{circ},j,2}) \left(\frac{i_{j,2}}{2} + i_{\mathrm{circ},j,2} \right). \end{aligned} \tag{8.9}$$

Substituting for $p_{p,j,2}$ from (3.20a) in (8.9) results in

$$\sum_{k=1}^{N}\left(\frac{C_{\mathrm{SM},2}}{2}\frac{\mathrm{d}\left(v_{cp,k,j,2}^{2}\right)}{\mathrm{d}t}+\frac{v_{cp,k,j,2}^{2}}{R_{p,2}}\right)=\frac{V_{\mathrm{dc}}i_{j,2}}{4}+\frac{V_{\mathrm{dc}}}{2}i_{\mathrm{circ},j,2}-\frac{v_{j,2}^{'}i_{j,2}}{2}-v_{j,2}^{'}i_{\mathrm{circ},j,2}$$
$$-\left(v_{\mathrm{cm},2}+v_{\mathrm{circ},j,2}\right)\left(\frac{i_{j,2}}{2}+i_{\mathrm{circ},j,2}\right). \quad (8.10)$$

With a similar procedure, the dynamics of energy in the SM capacitors of the lower arms of MMC-2 is expressed by:

$$\sum_{k=1}^{N}\left(\frac{C_{\mathrm{SM},2}}{2}\frac{\mathrm{d}\left(v_{cn,k,j,2}^{2}\right)}{\mathrm{d}t}+\frac{v_{cn,k,j,2}^{2}}{R_{p,2}}\right)=-\frac{V_{\mathrm{dc}}i_{j,2}}{4}+\frac{V_{\mathrm{dc}}}{2}i_{\mathrm{circ},j,2}-\frac{v_{j,2}^{'}i_{j,2}}{2}+v_{j,2}^{'}i_{\mathrm{circ},j,2}$$
$$+\left(v_{\mathrm{cm},2}-v_{\mathrm{circ},j,2}\right)\left(-\frac{i_{j,2}}{2}+i_{\mathrm{circ},j,2}\right). \quad (8.11)$$

Adding (8.10) to (8.11) results in

$$\sum_{y\in\{p,n\}}\sum_{k=1}^{N}\left(\frac{C_{\mathrm{SM},2}}{2}\frac{\mathrm{d}\left(v_{cy,k,j,2}^{2}\right)}{\mathrm{d}t}+\frac{v_{cy,k,j,2}^{2}}{R_{p,2}}\right)=V_{\mathrm{dc}}i_{\mathrm{circ},j,2}-v_{j,2}^{'}i_{j,2}-v_{\mathrm{cm},2}i_{j,2}$$
$$-2v_{\mathrm{circ},j,2}i_{\mathrm{circ},j,2}. \quad (8.12)$$

Summing (8.12) over all the phases results in

$$\sum_{j\in\{a,b,c\}}\sum_{y\in\{p,n\}}\sum_{k=1}^{N}\left(\frac{C_{\mathrm{SM},2}}{2}\frac{\mathrm{d}\left(v_{cy,k,j,2}^{2}\right)}{\mathrm{d}t}+\frac{v_{cy,k,j,2}^{2}}{R_{p,2}}\right)=P_{\mathrm{dc}}-P_{\mathrm{ac},2}$$
$$-2\sum_{j\in\{a,b,c\}}v_{\mathrm{circ},j,2}i_{\mathrm{circ},j,2}, \quad (8.13)$$

where P_{dc} is the dc-link power and $P_{\mathrm{ac},2}$ is the power sent to grid. Based on (8.8b), the last term in the right hand side of (8.13) may also be written as

$$2\sum_{j\in\{a,b,c\}}v_{\mathrm{circ},j,2}i_{\mathrm{circ},j,2}=2R_{o2}\sum_{j\in\{a,b,c\}}i_{\mathrm{circ},j}^{2}=P_{\mathrm{loss},2}, \quad (8.14)$$

where $P_{\text{loss},2}$ represents the conduction losses in MMC-2. Substituting for $2\sum_{j\in\{a,b,c\}} v_{\text{circ},j,2}\dot{i}_{\text{circ},j,2}$ from (8.14) in (8.13) results in

$$\sum_{j\in\{a,b,c\}}\sum_{y\in\{p,n\}}\sum_{k=1}^{N}\left(\frac{C_{\text{SM},2}}{2}\frac{\mathrm{d}\left(v_{cy,k,j,2}^2\right)}{\mathrm{d}t}+\frac{v_{cy,k,j,2}^2}{R_{p,2}}\right)=P_{\text{dc}}-P_{\text{ac},2}-P_{\text{loss},2}. \tag{8.15}$$

Similar derivation of the dynamics of the energy in the SM capacitors of MMC-1 leads to

$$\sum_{j\in\{a,b,c\}}\sum_{y\in\{p,n\}}\sum_{k=1}^{N}\left(\frac{C_{\text{SM},1}}{2}\frac{\mathrm{d}\left(v_{cy,k,j,1}^2\right)}{\mathrm{d}t}+\frac{v_{cy,k,j,1}^2}{R_{p,1}}\right)=-P_{\text{dc}}+P_{\text{ac},1}-P_{\text{loss},1}, \tag{8.16}$$

where $P_{\text{ac},1}$ and $P_{\text{loss},1}$ represent the power generated by the generator and the conduction losses in MMC-1, respectively. Adding (8.15) to (8.16) results in

$$\sum_{l=1}^{2}\sum_{j\in\{a,b,c\}}\sum_{y\in\{p,n\}}\sum_{k=1}^{N}\left(\frac{C_{\text{SM},l}}{2}\frac{\mathrm{d}\left(v_{cy,k,j,l}^2\right)}{\mathrm{d}t}+\frac{v_{cy,k,j,l}^2}{R_{p,l}}\right)=-P_{\text{ac},2}+P_{\text{ac},1}-P_{\text{loss},1}-P_{\text{loss},2}. \tag{8.17}$$

Defining

$$z_l=\sum_{j\in\{a,b,c\}}\sum_{y\in\{p,n\}}\sum_{k=1}^{N}\left(v_{cy,k,j,l}^2\right), \tag{8.18}$$

(8.17) is rewritten as

$$\frac{C_{\text{SM},1}}{2}\frac{\mathrm{d}z_1}{\mathrm{d}t}+\frac{z_1}{R_{p,1}}+\frac{C_{\text{SM},2}}{2}\frac{\mathrm{d}z_2}{\mathrm{d}t}+\frac{z_2}{R_{p,2}}=-P_{\text{ac},2}+P_{\text{ac},1}-P_{\text{loss},1}-P_{\text{loss},2}. \tag{8.19}$$

Assuming that the grid-side qd current controller is faster than the energy controller, the grid-side power is given by

$$P_{\text{ac},2}\approx\frac{3}{2}v_{sq}i_{q,\text{ref},2}^{e}. \tag{8.20}$$

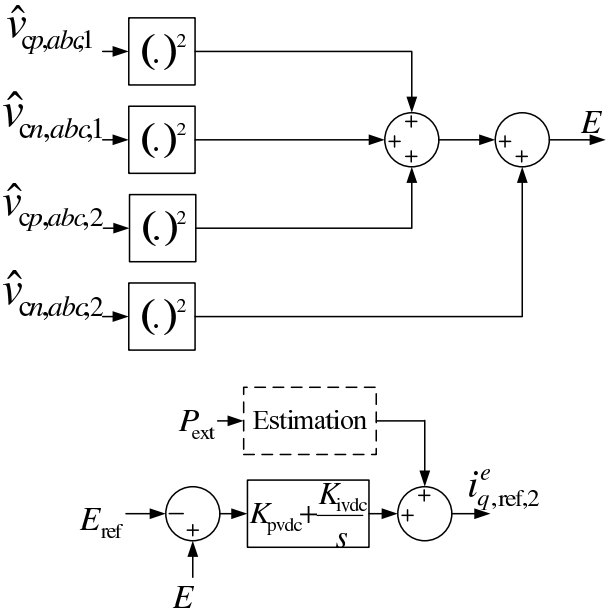

Fig. 8.2. Block diagram of the energy controllers.

Substituting $P_{\mathrm{ac},2}$ from (8.20) in (8.19) results in

$$\frac{C_{\mathrm{SM},1}}{2}\frac{\mathrm{d}z_1}{\mathrm{d}t}+\frac{z_1}{R_{p,1}}+\frac{C_{\mathrm{SM},2}}{2}\frac{\mathrm{d}z_2}{\mathrm{d}t}+\frac{z_2}{R_{p,2}}=-\frac{3}{2}v_{sq}i^e_{q,\mathrm{ref},2}+P_{\mathrm{ac},1}-P_{\mathrm{loss},1}-P_{\mathrm{loss},2}. \quad (8.21)$$

Applying Laplace transform to (8.21), the following transfer functions are obtained:

$$Z_1(s)=-\frac{3v_{sq}}{C_{\mathrm{SM},1}}\left(\frac{1}{s+\dfrac{2}{R_{\mathrm{p},1}C_{\mathrm{SM},1}}}\right)I^e_{q,\mathrm{ref},2,1}(s), \quad (8.22a)$$

$$Z_2(s)=-\frac{3v_{sq}}{C_{\mathrm{SM},2}}\left(\frac{1}{s+\dfrac{2}{R_{\mathrm{p},2}C_{\mathrm{SM},2}}}\right)I^e_{q,\mathrm{ref},2,2}(s), \quad (8.22b)$$

$$I^e_{q,\mathrm{ref},2}(s)=I^e_{q,\mathrm{ref},2,1}(s)+I^e_{q,\mathrm{ref},2,2}(s). \quad (8.22c)$$

Using (8.22), a PI controller is designed to control the SM capacitor energy such that the settling time of the energy control system is much higher than the settling time of the grid-side qd current control system. The output of the aforementioned

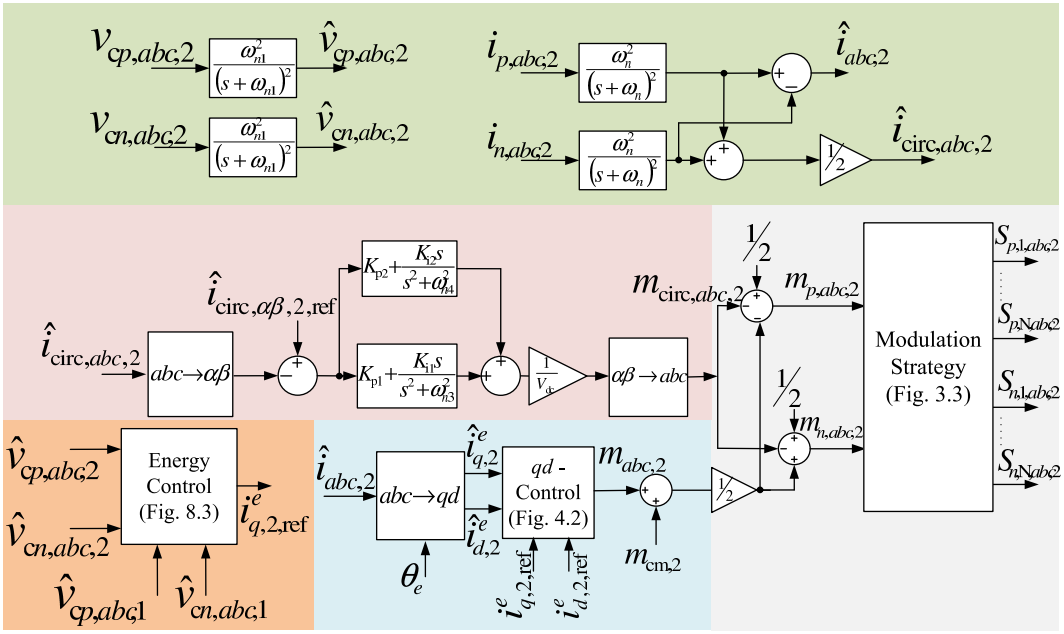

Fig. 8.3. Block diagram of the overall control of the grid-side MMC during WECS startup.

controller is the q-axis grid-side current reference $i^e_{q,\mathrm{ref},2}$. The block diagram of the energy controller is shown in Fig. 8.2. A feed-forward term, as shown in Fig. 8.2, is introduced to improve the loop dynamics.

8.3.2 Overview of the Control System

The control of the generator-side MMC is explained in Section 5.4 of Chapter 5. The control of the grid-side MMC is similar to the one explained in Section 4.2 and 4.3 of Chapter 4, except for the control of the circulating currents in $\alpha\beta$ reference frame and the additional energy controller mentioned in the previous section. Since the circulating currents of all the phases in the generator-side MMC are controlled,

all the circulating currents in the grid-side MMC are not independent variable. The aforementioned may be noticed in

$$\sum_{j\in\{a,b,c\}} i_{\text{circ},j,1} = i_{\text{dc},1} = -i_{\text{dc},2} = -\sum_{j\in\{a,b,c\}} i_{\text{circ},j,2}, \tag{8.23}$$

which is derived based on the back-to-back MMC shown in Fig. 8.1. The dynamics of the circulating currents of the grid-side MMC in $\alpha\beta$ reference frame is similar to the dynamics in *abc* domain that was explained in Chapter 4 and is not repeated here. The block diagram of the overall control of the grid-side MMC is shown in Fig. 8.3. The overview of the control system of the MMC-based WECS during WECS startup is summarized in Fig. 8.4.

8.4 Normal WECS Operation

Under normal WECS operation, the control system of both the generator- and grid-side MMCs is based on the control systems described in Sections 4.2 and 4.3 of Chapter 4, except for the control of the generator-side circulating currents in $\alpha\beta$ reference frame. The generator-side circulating currents are controlled in the $\alpha\beta$ reference frame due to similar reasons as the ones mentioned in the previous section for the control of grid-side circulating currents in $\alpha\beta$ reference frame during WECS startup. The block diagram of the overall control of the generator-side MMC is shown in Fig. 8.5. Similar to the previous section, the grid-side q-axis current reference for the grid-side MMC control system is generated by the energy controller. The overview of the control system of the MMC-based WECS during normal WECS operation is shown in Fig. 8.6.

8.5 Simulation Results

The WECS described in Fig. 8.1, based on the system parameters in Table 8.1, wind turbine parameters in Table 2.1, PMSG parameters in Table 2.2, and the pro-

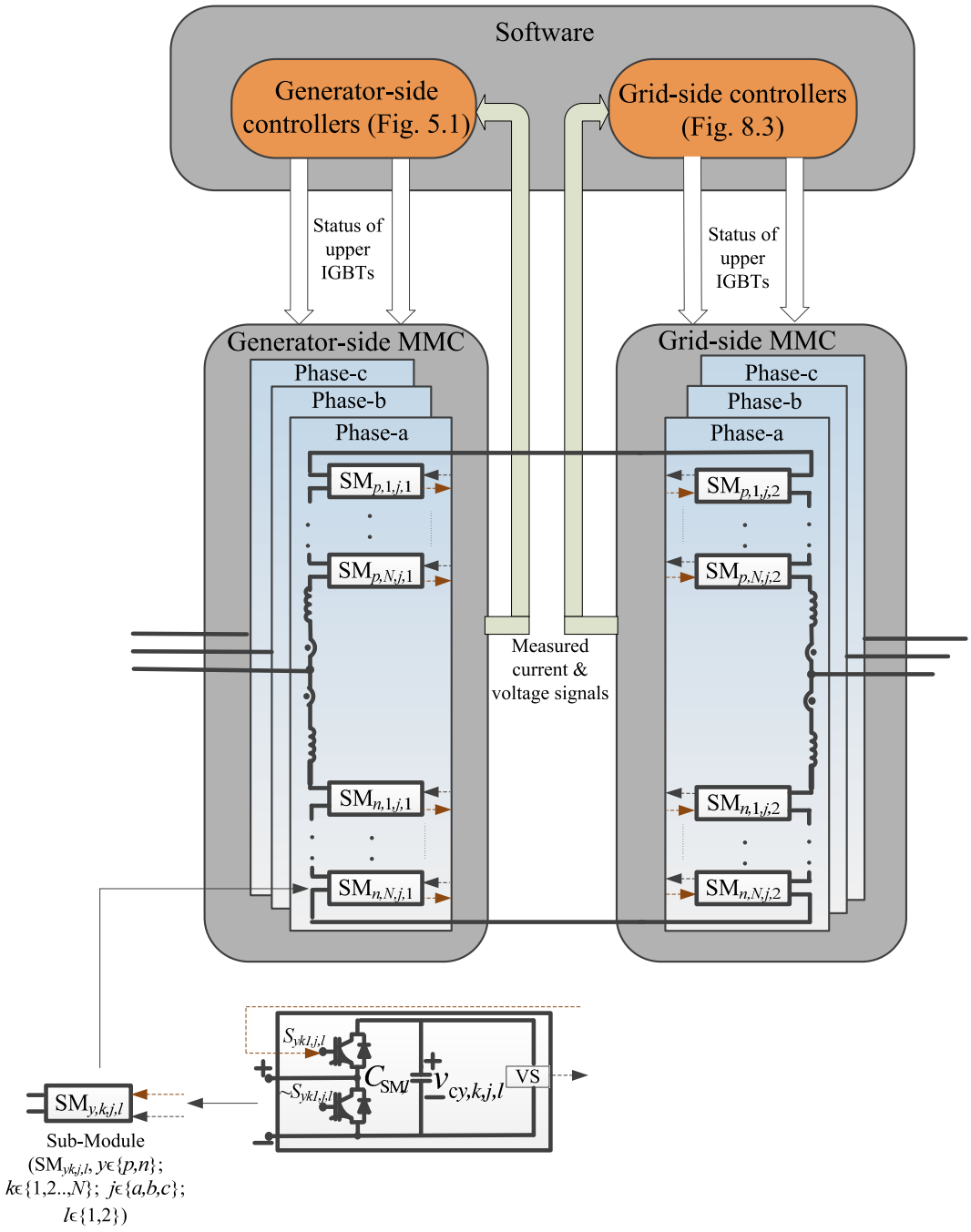

Fig. 8.4. Overview of the control system of the MMC-based WECS during WECS startup.

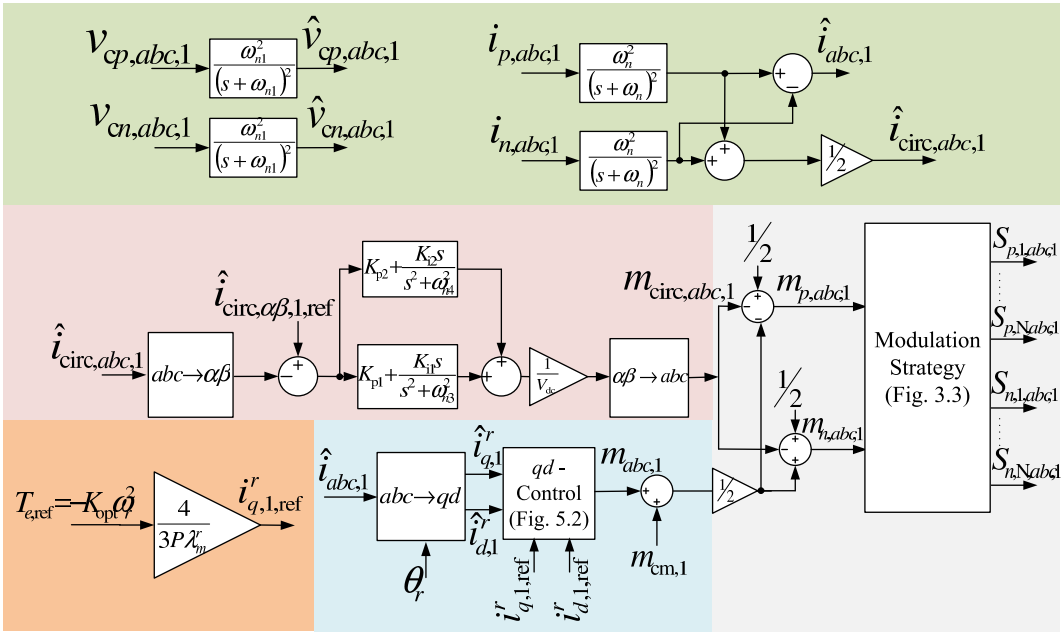

Fig. 8.5. Block diagram of the overall control of the generator-side MMC during normal WECS operation.

posed control systems, is simulated in the PSCAD/EMTDC software environment. A variable wind profile, similar to [2], is chosen to simulate the real wind conditions. The wind profile is shown in Fig. 8.7. The simulation is run for 27 s in which the following test scenarios are demonstrated: (i) MMC capacitor startup charging from $t = 0$ s to $t = 0.188$ s where the MMC capacitors are charged; (ii) WECS startup from $t = 0.188$ s to $t = 4$ s where the PMSG rotor speed is built; (iii) normal WECS operation under constant average wind speed from $t = 4$ s to $t = 10$ s; (iv) normal WECS operation under step changes in wind speed at $t = 10$ s and $t = 18$ s; and (v) normal WECS operation with single phase-to-ground fault on the grid side at $t = 25$ s.

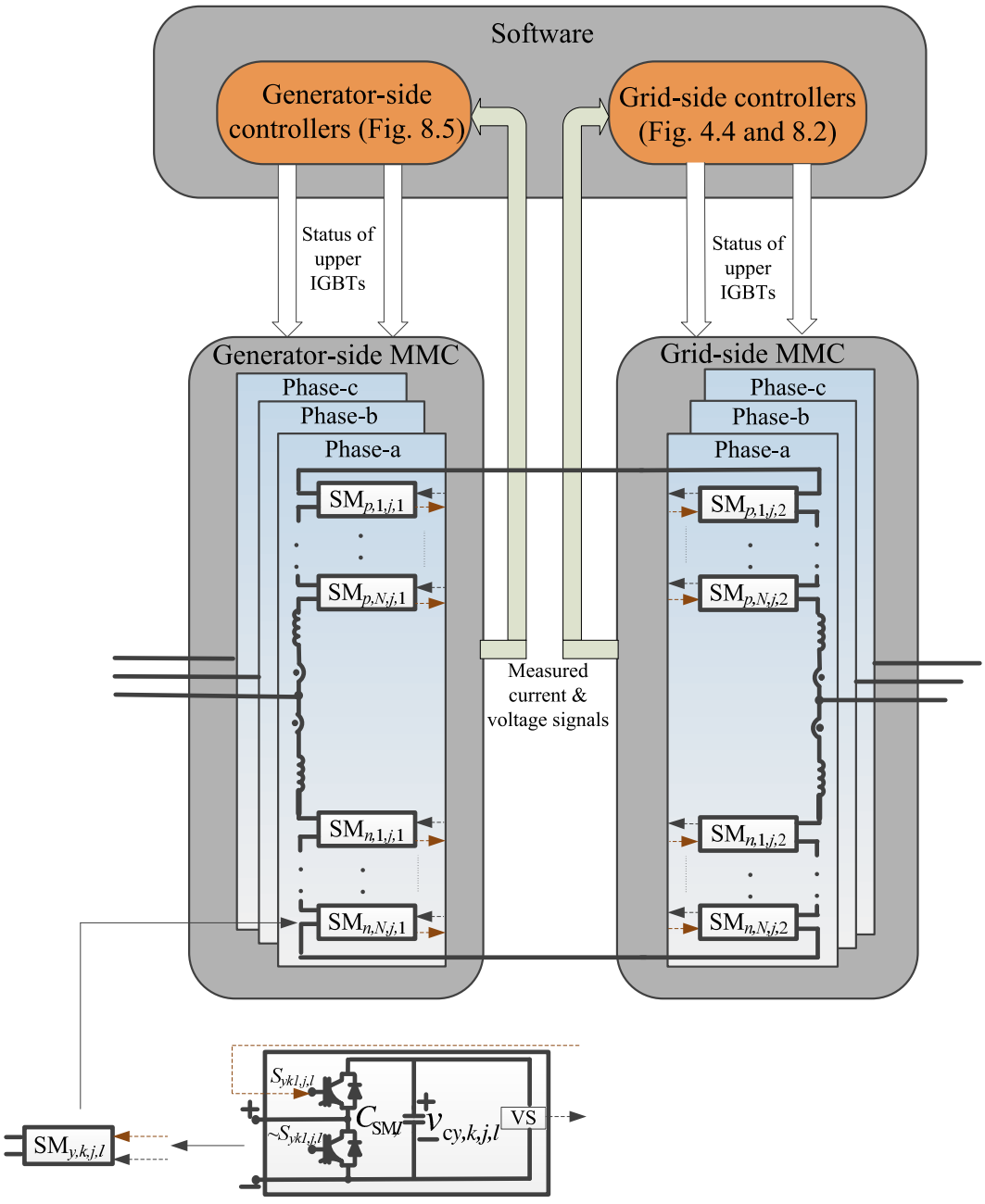

Fig. 8.6. Overview of control system of the MMC-based WECS during normal WECS operation.

8.5.1 Simulation: MMC Capacitor Startup Charging

For the wind energy system described by Tables 8.1, 2.1, and 2.2, the MMC startup optimization problem described in Section 8.2 is solved using the GA in the

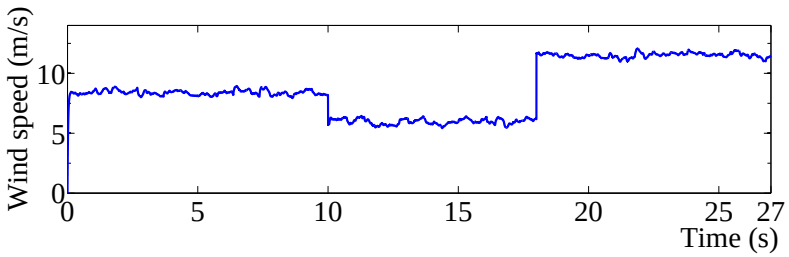

Fig. 8.7. Wind speed.

Table 8.1.
System Parameters

Quantity	Value	Quantity	Value
MMC nominal power	6 MVA	Nominal net dc voltage V_{dc}	6.4 kV
Grid voltage (line-to-line)	3.8 kV	PWM Carrier frequency f_s	1.8 kHz
Nominal frequency f	60 Hz	MMC-1 Submodule capacitance $C_{SM,1}$	8 mF
SCR at PCC	19	MMC-2 Submodule capacitance $C_{SM,2}$	5 mF
AC System industance L_s	1 mH	Switch voltage drop	1.5 V
AC System resistance R_s	30 mΩ	Switch resistance	1.0 mΩ
L_{o1}	2 mH	Diode voltage drop	1.4 V
R_{o1}	800 mΩ	Diode resistance	0.5 mΩ
L_{o2}	4 mH	No. of SMs in MMC-k, $k \in \{1, 2\}$, N	4
R_{o2}	800 mΩ		

MATLAB with $V_{\text{c,ref}} = 1600$, $V_{\text{c,lim}} = 1600$, and $I_{\text{lim}} = 1200$. The corresponding results, i.e., number of inserted SMs in each arm of the MMC-1 and phase-a,b, and c of the MMC-2 are shown in Fig. 8.8. The regions 2, 3, 4, and 5, marked in Fig. 8.8, represent the resistor control, resistor-less control, dc current, and tail-end regions, respectively. The state of the back-to-back MMCs during the startup procedure is theoretically solved by substituting the input $\boldsymbol{u}$ from Fig. 8.8 in (8.1) and (8.2). The theoretical results of the state variables are shown in Fig. 8.9. The SM capacitor voltages, as shown in Figs. 8.9(a)-(b), are built smoothly during the startup procedure to reach their reference value, i.e., 1600 V. The dc-link and arm currents, as shown in Figs. 8.9(c) and (d), respectively, are within their limits of 1200 A and 2400 A in all the regions of operation. As shown in Fig. 8.9(d), in the dc current region or region-4, the dc-link current rises and maintains an average value of 1200 A. The corresponding region in Fig. 8.9(a) shows that the charging of the SM capacitors in the MMC-1 accelerate due to the rise in the dc-link current. The corresponding region in

Fig. 8.9(b) shows that the SM capacitor voltages of the MMC-2 also rise, albeit slower. The aforementioned may be attributed to the constraint placed on the grid-side q-axis currents such that the SM capacitors of the MMC-2 also charge in the dc current region. The exponential decrease in the dc-link current in region-5, or the tail-end region, is noticed in Fig. 8.9(d). This may be attributed to the exponential decrease in the lower limit of the dc-link current. The corresponding region in Figs. 8.9(a) and (b) shows that the SM capacitor voltages of the back-to-back MMC tail off to reach their reference voltage of 1600 V.

The startup results obtained from the theoretical model of the back-to-back MMC system are verified by simulation studies in the PSCAD/EMTDC environment for the system of Fig. 8.1. The optimization results of Fig. 8.8 are stored in a lookup table and are used to control the MMCs during the MMC capacitor startup charging process. The simulation results of the SM capacitor voltages and the arm currents during the startup procedure for both the MMCs are shown in Fig. 8.10. A comparison of the theoretical results for the arm currents of MMC-2 and the dc-link current into MMC-1 shown in Figs. 8.9(c)-(d) with the simulation results from PSCAD shown in Figs. 8.10(c) and (e) shows a small difference, which is due to the absence of the real switch characteristics in the theoretical model. A similar comparison of the SM capacitor voltages between the theoretical results in Figs. 8.9(a)-(b) with the simulations results in Figs. 8.10(a)-(b) shows remarkable similarities. The results shown in Figs. 8.9-8.10 validate the performance of the proposed MMC capacitor startup charging procedure for the WECS of Fig. 8.1.

8.5.2 Simulation: WECS Startup

Once the SM capacitors are charged to their reference values, the PMSG is controlled as a motor with constant electromagnetic torque to build the turbine torque and speed. To avoid high voltage ripple in the SM capacitors during the WECS startup, Strategy I proposed in Section 5.3.1 of Chapter 5 is implemented. The re-

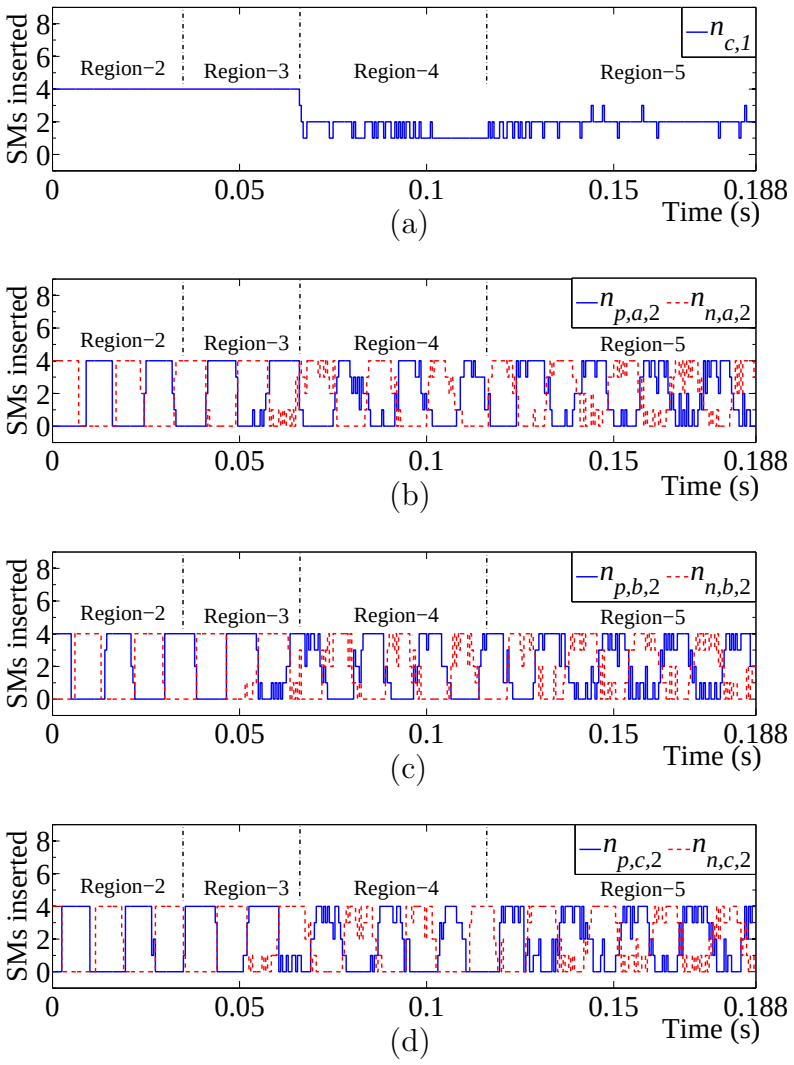

Fig. 8.8. MMC startup optimization results: (a) number of inserted SMs in each arm of MMC-1, (b), (c) and (d) number of inserted SMs in phase-a, b, and c of MMC-2.

sults of the system during the WECS startup process are shown in Fig. 8.11. The turbine and PMSG electromagnetic torques are shown in Fig. 8.11(a). As shown, the electromagnetic torque is controlled at 80% its rated value, i.e., $T_e = 2.58 \times 10^6$ Nm, to assist in building the rotor speed, shown in Fig. 8.11(b). The finite rise and fall times of the electromagnetic torque help avoid over-voltage stress on the devices. The positive value of the torque indicates the motor action of the PMSG. The generator- and grid-side qd currents are shown in Figs. 8.11(c)-(d), respectively. As depicted

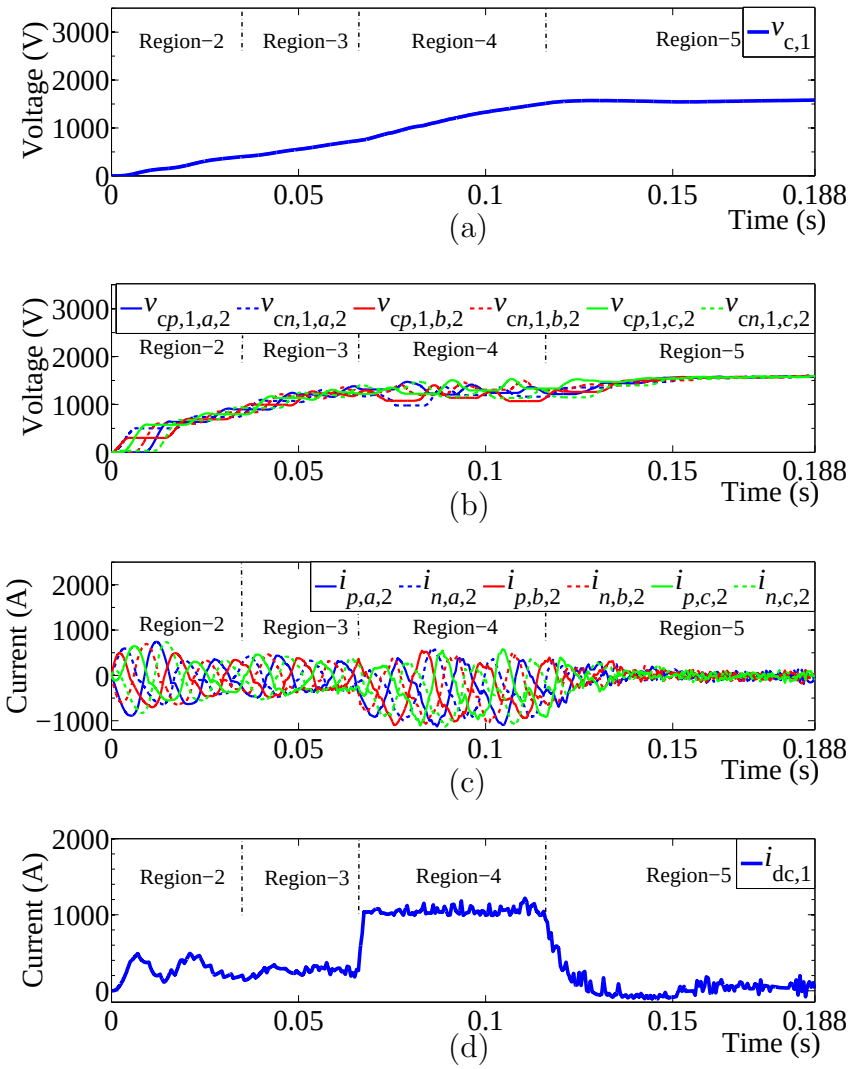

Fig. 8.9. The theoretical MMC waveforms during MMC startup: (a) SM capacitor voltages of MMC-1, (b) SM capacitor voltages of MMC-2, (c) arm currents of MMC-2, and (d) dc-link current into MMC-1.

in Figs. 8.11(b)-(c), the MMC-1 is under constant-current low-frequency operation, which places significant voltage ripple stress on the SM capacitors of MMC-1. However, the proposed Strategy I is able to reduce the SM capacitor voltage ripple as highlighted by the waveforms in Fig. 8.11(e). As shown in Fig. 8.11(e), the ripple voltage magnitude of the SM capacitor voltages of MMC-1 phase-a is controlled below 425 V. The corresponding arm currents and circulating currents of MMC-1 phase-a

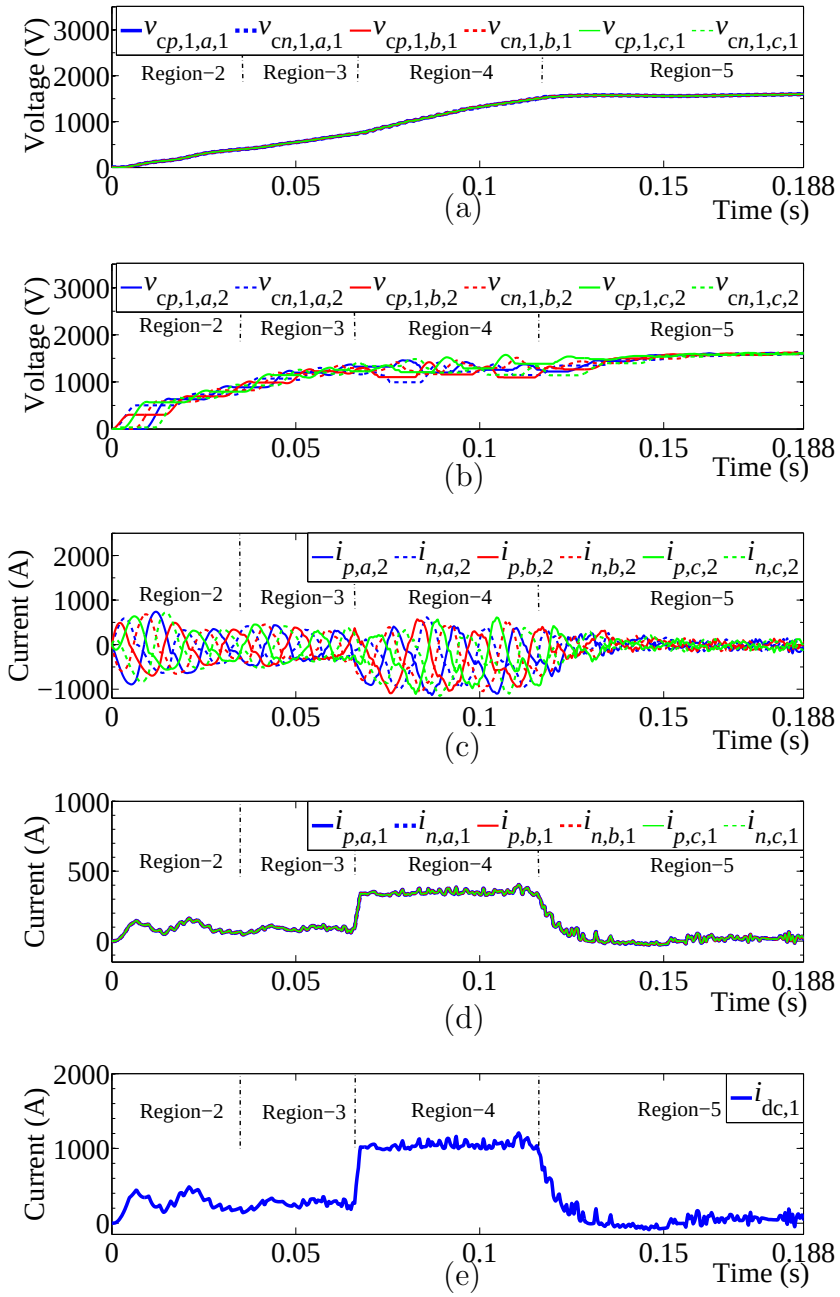

Fig. 8.10. Simulated MMC waveforms during MMC startup: (a) SM capacitor voltages of MMC-1, (b) SM capacitor voltages of MMC-2, (c) arm currents of MMC-2, (d) arm currents of MMC-1, and (e) dc-link current into MMC-1.

during the WECS startup are shown in Figs. 8.11(f)-(g), respectively. The phase-a SM capacitor voltages, arm currents, and circulating current of MMC-2 are shown

in Figs. 8.11(h)-(j), respectively. As shown in Figs. 8.11(e) and (h), the average SM capacitor voltages are maintained at 1600 V, thereby, validating the performance of the energy controller. Moreover, as shown in Fig. 8.11(j), the $\alpha\beta$ components of the circulating current are controlled to zero and do not contain any ac components. However, the phase-a circulating current contains some ac components due to the zero component of the circulating current containing the same. The presence of the ac component in the zero component of the circulating current is due to the ripple in the dc-link current that arises with the control of generator-side circulating currents during WECS startup.

8.5.3 Simulation: Normal WECS Operation Under Constant Wind Speed and Wind Gusts

Once the WECS startup is complete, normal WECS operation resumes. During normal WECS operation, the response of the WECS under a constant average wind speed of 8.5 m/s and thereafter, with two step changes in wind, i.e., -2.5 m/s at $t = 10$ s and 5.5 m/s at $t = 18$ s, respectively, are shown in Fig. 8.12. As shown in Fig. 8.12(a), with the change in wind speed at $t = 10$ s and $t = 18$ s, both the turbine and PMSG electromagnetic torques change. While the turbine torque changes almost abruptly, the electromagnetic torque, which is maintained proportional to the square of rotor speed, changes slowly. This can be attributed to the high inertia of the PMSG that results in a slow change of the rotor speed, as shown in Fig. 8.12(b). The sound operation of the generator- and grid-side current controllers and the MMC-1 and MMC-2 internal controllers under constant average wind speed as well as under wind gusts are shown in Figs. 8.12(c)-(e), 8.12(g)-(h), 8.12(j), respectively. While the generator- and grid-side currents track their references well, the SM capacitor voltages of MMC-1 and MMC-2 maintain an average voltage of 1600 V. The circulating currents of MMC-1 and MMC-2 do not contain any prominent ac components, as

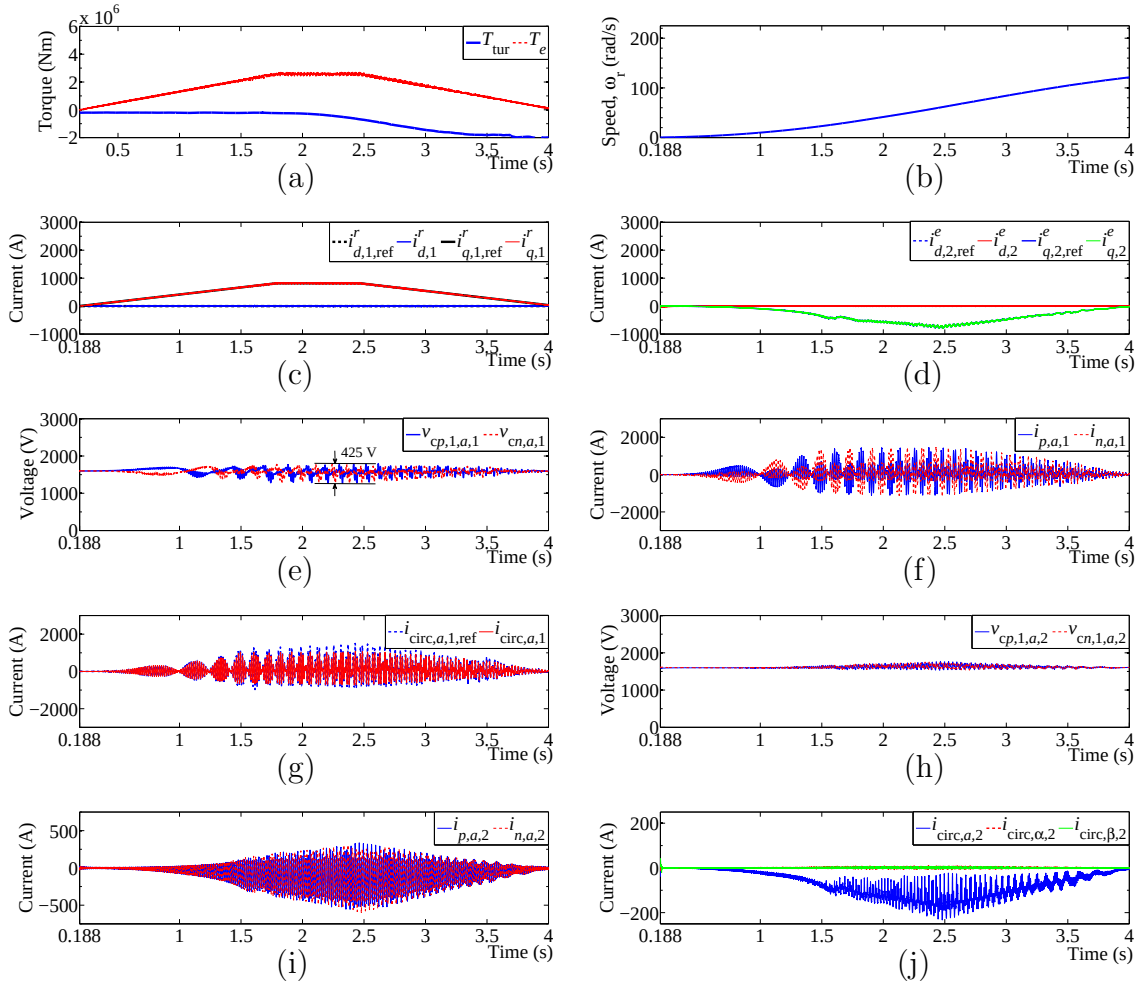

Fig. 8.11. Simulated waveforms of the WECS system during WECS startup: (a) turbine and PMSG electromagnetic torques, (b) rotor speed, (c) generator-side qd-axis currents, (d) grid-side qd-axis currents, (e) SM capacitor voltages of MMC-1 phase-a, (f) arm currents of MMC-1 phase-a, (g) reference and actual value of the circulating current of MMC-1 phase-a, (h) SM capacitor voltages of MMC-2 phase-a, (i) arm currents of MMC-2 phase-a, and (j) $\alpha\beta$ and phase-a circulating currents of MMC-2.

shown in Figs. 8.12(g) and (j), respectively. The arm currents of MMC-1 and MMC-2 are shown in Figs. 8.12(f) and (i), respectively.

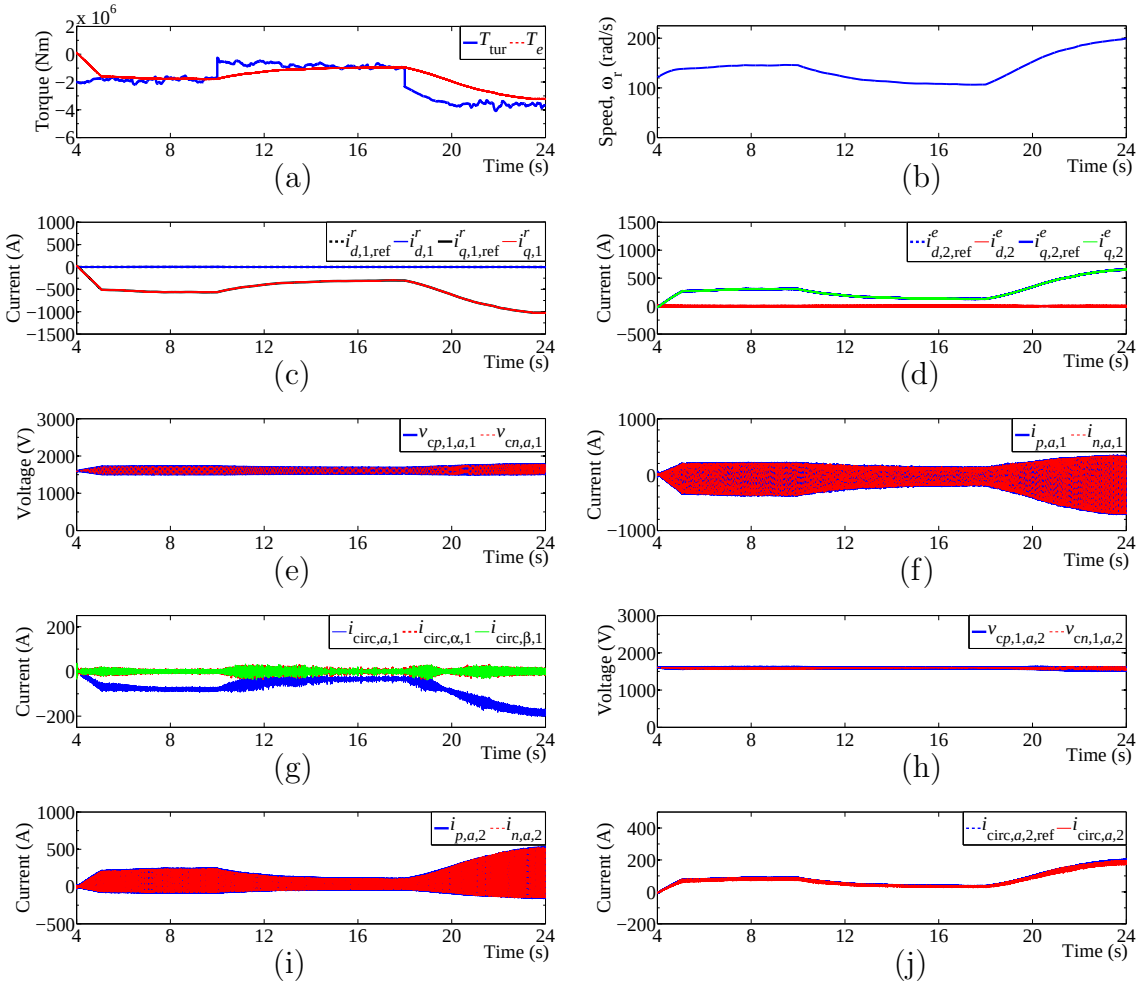

Fig. 8.12. WECS operation under constant wind speed and wind gusts: (a) turbine and PMSG electromagnetic torques, (b) rotor speed, (c) generator-side qd-axis currents, (d) grid-side qd-axis currents, (e) SM capacitor voltages of MMC-1 phase-a, (f) arm currents of MMC-1 phase-a, (g) $\alpha\beta$ and phase-a circulating currents of MMC-1, (h) SM capacitor voltages of MMC-2 phase-a, (i) arm currents of MMC-2 phase-a, (j) reference and actual value of the circulating current of MMC-2 phase-a.

8.5.4 Normal WECS Operation Under Single Phase-to-Ground Fault

The objective of this study is to investigate the performance of the proposed controllers under a temporary single phase-to-ground fault. Prior to the fault occurrence, the system of Fig. 8.1 is in a steady-state operating condition, transferring approximately 5 MW power. At $t = 25$ s, a line-to-ground fault is imposed on phase-c at the

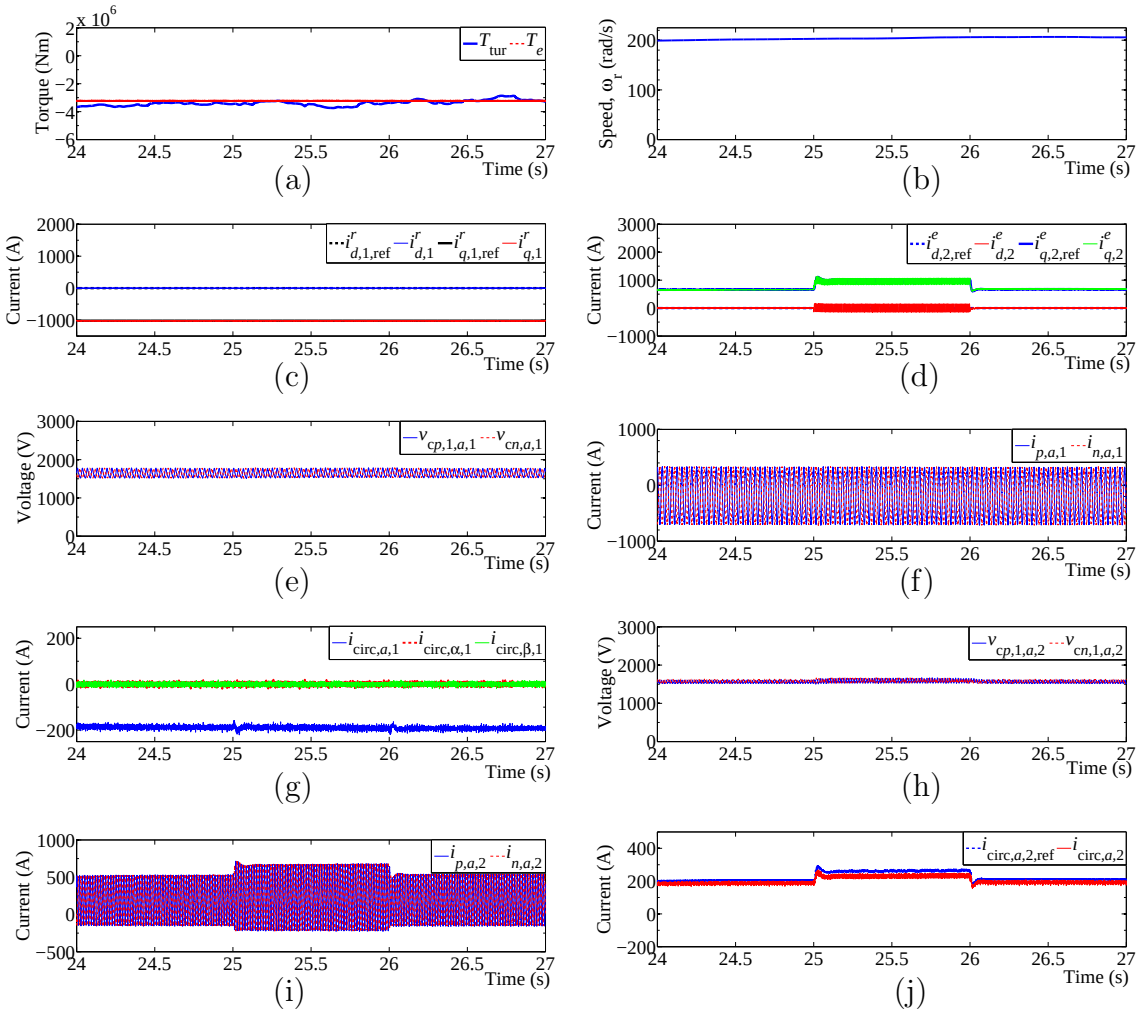

Fig. 8.13. WECS operation under single phase-to-ground fault: (a) turbine and PMSG electromagnetic torques, (b) rotor speed, (c) generator-side qd-axis currents, (d) grid-side qd-axis currents, (e) SM capacitor voltages of MMC-1 phase-a, (f) arm currents of MMC-1 phase-a, (g) $\alpha\beta$ and phase-a circulating currents of MMC-1, (h) SM capacitor voltages of MMC-2 phase-a, (i) arm currents of MMC-2 phase-a, (j) reference and actual value of the circulating current of MMC-2 phase-a.

PCC, which lasts for 1 s. The transient behavior of the system before and subsequent to the fault is shown in Fig. 8.13.

The turbine and PMSG electromagnetic torques and the rotor speed are shown in Figs. 8.13(a)-(b). As shown in the figures, there is no impact of the fault on the operation of the generator. This is due to the decoupling between the grid and

generator sides, which prevents the propagation of fault transients of the grid to the generator. Due to the aforementioned reason, the fault has no impact on the currents in the generator-side as shown in Fig. 8.13(c). The grid-side q-axis current, which shows a rise during the fault due to the sag in the ac-side phase voltages, is shown in Fig. 8.13(d). The ripple noticed in the grid-side q- and d-axis currents is due to the unbalanced grid-side currents.

The SM capacitor voltages, arm currents, and the circulating currents of MMC-1 and MMC-2 are shown in Figs. 8.13(e)-(j), respectively. While the average value of the SM capacitor voltages is maintained at 1600 V, the circulating currents show no ac components. However, the dc component of the circulating currents in MMC-2 are not the same during the fault due to the imbalance in the grid-side. The same may be noticed through the change in the reference value and the actual value of the phase-a circulating current of MMC-2 as shown in Fig. 8.13(j). Sound operation of the unbalance controller in the circulating current controller under grid-side fault is shown through this case study.

9. CONCLUSIONS AND FUTURE WORK

In this chapter, the conclusions of this research and the proposed future work are discussed.

9.1 Contributions and Conclusions

The scope of this thesis has been to research on control aspects of the MMC-based full-scale WECS. Towards the same, the following tasks have been accomplished:

- Advanced MMC models have been developed and validated through experimental results.
- A modulation strategy to generate the switching signals of the MMC has been proposed that minimizes the number of simultaneous and unnecessary changes in the state of the switches and reduces the computational burden. Satisfactory operation of the proposed modulation strategy has been verified through experimental case-studies on an MMC system with RL load.
- A new circulating current controller, based on proportional resonant controllers, has been proposed to maximize the efficiency and minimize the cost of the system. The aforementioned controller can be implemented to control the generator-side MMC during quadrature-torque operation or constant-torque high-speed operation and to control the grid-side MMC. The performance of the controller has been validated through experimental case-studies on MMC-based drive system and through time-domain simulation studies on a back-to-back MMC-based full-scale direct-drive WECS.
- Special strategies have been proposed to control the MMC under constant-current low-frequency operation. The aforementioned scenario arises during

WECS startup when the generator is controlled with constant torque so that the turbine may build its speed from standstill or low speed to a particular fixed speed. The proposed strategies aim to remove the low-frequency components of the SM capacitor voltage ripple through introduction of two additional degrees of freedom: common-mode voltage and circulating currents. The form of the common-mode voltage and circulating current has been optimized to minimize the losses and the SM capacitor voltage ripple. A controller design methodology to design the gains of the corresponding control system for constant-current low-frequency operation of the MMC has been proposed and the method has been shown to produce gains that provide local exponential stability. Satisfactory operation of the proposed strategies has been verified through various experimental case-studies on an MMC-based drive system and through time-domain simulation studies on a back-to-back MMC-based full-scale direct-drive WECS.

- An optimization algorithm that optimizes the gains of the control systems of a class of non-linear non-autonomous hybrid system has been proposed. The application of the aforementioned algorithm to the control systems of the MMC has also been explained. Experimental case-studies have shown encouraging results for the performance of the control systems with the gains determined from the proposed algorithm.

- A startup charging strategy has been proposed to minimize the charging time of the SM capacitors in the back-to-back MMC-based WECS and maintain the currents within their pre-defined limits. The proposed charging process is based on an offline model-based predictive control algorithm. It has been validated through time-domain simulations on back-to-back MMC-based full-scale direct-drive WECS.

9.2 Future Works

In this thesis, the control of MMC-based full-scale direct-drive WECS has been developed and validated. The direction of research in this thesis has been towards development of the system model, optimization of the state trajectory references under various operating conditions, selection of an appropriate form of the controller to control the state trajectories for the different operating conditions, development of initial guess for the gains of the proposed controllers such that the system is stable, optimization of the controller gains based on a developed algorithm, and optimization of the modulation strategy that generates the switching signals of the MMC and balances the SM capacitor voltages. The various operating conditions that have been considered are low-frequency constant-current, low-frequency quadrature-current, and high-frequency operations. Extreme conditions have also been considered to verify the robustness of the developed control systems that include wind gusts, fault in ac-side, and step changes in torque. However, the submodule fault conditions have not been considered. The aforementioned situation will require the development of fault detection algorithms and post-fault control systems. Furthermore, the control of the MMCs with redundant SMs under normal operation as well as under SM faults will need to be considered.

Another interesting area of research will be to explore the use of model-based predictive control (MBPC) to optimize the performance of MMCs under various operating conditions. The application of offline MBPC has been explored in this thesis for the startup charging problem. However, the online MBPC to control the MMC over all operating conditions is yet to be explored. The MBPC problem for an MMC is expected to be an NP problem and may be difficult to implement in real-time. Although some finite-set MBPC algorithms have been explored, either their algorithm is of non-polynomial order or there have been a lot of approximations assumed. An MBPC based on evolutionary algorithms or a combination of gradient-based and evolutionary algorithms and with certain approximations or artificial constraints to

convert the algorithm to one of polynomial order, may simplify the problem and elicits further exploration. Moreover, the performance of such an algorithm will need to be compared with the proposed control system in terms of the dynamic performance, steady-state performance, and imposed computational burden.

Finally, the design of the MMC-based full-scale direct-drive WECS needs to be optimized. The optimization algorithm may need to consider the type of SM, the number of SMs, the number of redundant SMs, the size and design of inductor, the size and type of capacitor, the type of switching devices, among others. The algorithm may consider optimizing the reliability, efficiency, and power quality with constraints imposed from the required circuit conditions.

REFERENCES

REFERENCES

[1] F. Deng and Z. Chen, "An offshore wind farm with DC grid connection and its performance under power system transients," in *IEEE Power and Energy Society General Meeting*, July 2011, pp. 1 – 8.

[2] A. Yazdani and R. Iravani, "A neutral-point clamped converter system for direct-drive variable-speed wind power unit," *IEEE Trans. Energy Convers.*, vol. 21, no. 2, pp. 596 – 607, June 2006.

[3] Z. Chen, J. Guerrero, and F. Blaabjerg, "A review of the state of the art of power electronics for wind turbines," *IEEE Trans. Power Electron.*, vol. 24, no. 8, pp. 1859 – 1875, Aug. 2009.

[4] H. Chandler, "Technology roadmap: Wind energy," OECD/IEA, Tech. Rep., 2009.

[5] P. Carlin, A. Laxson, and E. Muljadi, "The history and state of the art of variable-speed wind turbine technology," NREL, Tech. Rep., 2001.

[6] R. Teodorescu, M. Liserre, and P. Rodrigues, *Grid Converters for Photovoltaic and Wind Power Systems.* John Wiley & Sons, Ltd, 2011.

[7] L. H. Hansen, P. H. Madsen, F. Blaabjerg, H. C. Christensen, U. Lindhard, and K. Eskildsen, "Generators and power electronics technology for wind turbines," in *27th Annu. Conf. IEEE Industrial Electronics Society (IECON)*, vol. 3, 2001, pp. 2000–2005.

[8] L. H. Hansen, L. Helle, F. Blaabjerg, E. Ritchie, S. Munk-Nielsen, H. Bindner, P. Srensen, and B. Bak-Jensen, "Conceptual survey of generators and power electronics for wind turbines," Ris National Laboratory, Roskilde, Denmark, Tech. Rep., 2001.

[9] T. Sun, Z. Chen, and F. Blaabjerg, "Voltage recovery of grid-connected wind turbines after a short-circuit fault," in *29th Annu. Conf. IEEE Industrial Electronics Society (IECON)*, vol. 3, 2003, pp. 2723–2728 Vol.3.

[10] R. Pena, J. Clare, and G. Asher, "Doubly fed induction generator using back-to-back PWM converters and its application to variable-speed wind-energy generation," *IEE Proc. Electric Power Applications*, vol. 143, no. 3, pp. 231–241, 1996.

[11] R. Shukla and R. Tripathi, "Low voltage ride through (LVRT) ability of dfig based wind energy conversion system-i," in *Students Conf. Engineering and Systems (SCES)*, 2012, pp. 1–6.

[12] F. Blaabjerg, M. Liserre, and K. Ma, "Power electronics converters for wind turbine systems," *IEEE Trans. Ind. Appl.*, vol. 48, no. 2, pp. 708–719, 2012.

[13] X. Yuan, J. Chai, and Y. Li, "A transformer-less high-power converter for large permanent magnet wind generator systems," *IEEE Trans. Sustainable Energy*, vol. 3, no. 3, pp. 318 – 329, July 2012.

[14] C. Xia, X. Gu, T. Shi, and Y. Yan, "Neutral-point potential balancing of three-level inverters in direct-driven wind energy conversion system," *IEEE Trans. Energy Convers.*, vol. 26, no. 1, pp. 18 – 29, March 2011.

[15] J. Rodriguez, S. Bernet, B. Wu, J. Pontt, and S. Kouro, "Multilevel voltage-source-converter topologies for industrial medium-voltage drives," *IEEE Trans. Ind. Electron.*, vol. 54, no. 6, pp. 2930–2945, 2007.

[16] S. Kouro, M. Malinowski, K. Gopakumar, J. Pou, L. Franquelo, B. Wu, J. Rodriguez, M. Perez, and J. Leon, "Recent advances and industrial applications of multilevel converters," *IEEE Trans. Ind. Electron.*, vol. 57, no. 8, pp. 2553–2580, 2010.

[17] P. Samuel, R. Gupta, and D. Chandra, "Grid interface of wind power with large split-winding alternator using cascaded multilevel inverter," *IEEE Trans. Energy Convers.*, vol. 26, no. 1, pp. 299 – 309, March 2011.

[18] H. Sepahvand, M. Khazraei, M. Ferdowsi, and K. Corzine, "A hybrid multilevel inverter with both staircase and PWM switching schemes," in *IEEE Energy Conversion Congr. and Expo. (ECCE)*, Sept. 2010, pp. 4364 – 4367.

[19] M. Saeedifard, P. Barbosa, and P. Steimer, "Operation and control of a hybrid seven-level converter," *IEEE Trans. Power Electron.*, vol. 27, no. 2, pp. 652 –660, Feb. 2012.

[20] S. Pulikanti and V. Agelidis, "Hybrid flying-capacitor-based active-neutral-point-clamped five-level converter operated with SHE-PWM," *IEEE Trans. Ind. Electron.*, vol. 58, no. 10, pp. 4643 – 4653, Oct. 2011.

[21] T. Bruckner and S. Bernet, "The active NPC converter for medium-voltage applications," in *Industry Applications Conf. (IAS)*, vol. 1, 2005, pp. 84–91.

[22] J. Li, S. Bhattacharya, and A. Huang, "A new nine-level active NPC (ANPC) converter for grid connection of large wind turbines for distributed generation," *IEEE Trans. Power Electron.*, vol. 26, no. 3, pp. 961 – 972, March 2011.

[23] M. Winkelnkemper, F. Wildner, and P. Steimer, "Control of a 6MVA hybrid converter for a permanent magnet synchronous generator for windpower," in *18th Int. Conf. Electrical Machines*, Sept. 2008, pp. 1 –6.

[24] K. Ma and F. Blaabjerg, "Multilevel converters for 10 MW wind turbines," in *Proc. 2011-14th European Conf. Power Electronics and Applications (EPE)*, 2011, pp. 1–10.

[25] R. Teichmann and S. Bernet, "A comparison of three-level converters versus two-level converters for low-voltage drives, traction, and utility applications," *IEEE Trans. Ind. Appl.*, vol. 41, no. 3, pp. 855–865, 2005.

[26] T. Bruckner, S. Bernet, and H. Guldner, "The active NPC converter and its loss-balancing control," *IEEE Trans. Ind. Electron.*, vol. 52, no. 3, pp. 855–868, 2005.

[27] K. Ma, F. Blaabjerg, and D. Xu, "Power devices loading in multilevel converters for 10 MW wind turbines," in *IEEE Int. Symp. Industrial Electronics (ISIE)*, 2011, pp. 340–346.

[28] O. Senturk, L. Helle, S. Munk-Nielsen, P. Rodriguez, and R. Teodorescu, "Medium voltage three-level converters for the grid connection of a multi-MW wind turbine," in *13th European Conf. Power Electronics and Applications (EPE)*, 2009, pp. 1–8.

[29] H. Hosoda and S. Peak, "Multi-level converters for large capacity motor drive," in *Int. Power Electronics Conference (IPEC)*, 2010, pp. 516–522.

[30] A. Faulstich, J. Stinke, and F. Wittwer, "Medium voltage converter for permanent magnet wind power generators up to 5 MW," in *European Conf. Power Electronics and Applications (EPE)*, 2005, pp. 9 pp.–P.9.

[31] R. Guedouani, B. Fiala, E. M. Berkouk, and M. S. Boucherit, "Control of capacitor voltage of three phase five-level NPC voltage source inverter. application to inductor motor drive." in *Int. Aegean Conf. Electrical Machines and Power Electronics*, Sept. 2007, pp. 794 –799.

[32] H. Gheraia, E. Berkouk, and G. Manesse, "Feedback control of the input DC voltage sources of the seven levels NPC voltage source inverter," in *IEEE Africon*, vol. 2, 1999, pp. 691 –696.

[33] M. Hagiwara and H. Akagi, "Control and experiment of pulsewidth-modulated modular multilevel converters," *IEEE Trans. Power Electron.*, vol. 24, no. 7, pp. 1737 –1746, July 2009.

[34] J. Qin and M. Saeedifard, "Predictive control of a modular multilevel converter for a back-to-back HVDC system," *IEEE Trans. Power Del.*, vol. 27, no. 3, pp. 1538 – 1547, July 2012.

[35] Q. Tu, Z. Xu, and L. Xu, "Reduced switching-frequency modulation and circulating current suppression for modular multilevel converters," *IEEE Trans. Power Del.*, vol. 26, no. 3, pp. 2009–2017, July 2011.

[36] L. Angquist, A. Antonopoulos, D. Siemaszko, K. Ilves, M. Vasiladiotis, and H.-P. Nee, "Open-loop control of modular multilevel converters using estimation of stored energy," *IEEE Trans. Ind. Appl.*, vol. 47, no. 6, pp. 2516 – 2524, Nov.-Dec. 2011.

[37] R. Teodorescu and F. Blaabjerg, "Flexible control of small wind turbines with grid failure detection operating in stand-alone and grid-connected mode," *IEEE Trans. Power Electron.*, vol. 19, no. 5, pp. 1323–1332, 2004.

[38] M. Saeedifard and R. Iravani, "Dynamic performance of a modular multilevel back-to-back HVDC system," *IEEE Trans. Power Del.*, vol. 25, no. 4, pp. 2903 – 2912, Oct. 2010.

[39] S. Fan, K. Zhang, J. Xiong, and Y. Xue, "An improved control system for modular multilevel converters with new modulation strategy and voltage balancing control," *IEEE Trans. Power Electron.*, vol. 30, no. 1, pp. 358–371, Jan 2015.

[40] J. Mei, K. Shen, B. Xiao, L. Tolbert, and J. Zheng, "A New Selective Loop Bias Mapping Phase Disposition PWM With Dynamic Voltage Balance Capability for Modular Multilevel Converter," *IEEE Trans. Ind. Electron.*, vol. 61, no. 2, pp. 798–807, 2014.

[41] M. Hagiwara and H. Akagi, "Control and Experiment of Pulsewidth-Modulated Modular Multilevel Converters," *IEEE Trans. Power Electron.*, vol. 24, no. 7, pp. 1737 –1746, July 2009.

[42] M. Hagiwara, K. Nishimura, and H. Akagi, "A medium-voltage motor drive with a modular multilevel PWM inverter," *IEEE Trans. on Power Electron.*, vol. 25, no. 7, pp. 1786–1799, Jul. 2010.

[43] F. Deng and Z. Chen, "A control method for voltage balancing in modular multilevel converters," *IEEE Trans. Power Electron.*, vol. 29, no. 1, pp. 66–76, 2014.

[44] K. Ilves, L. Harnefors, S. Norrga, and H.-P. Nee, "Predictive sorting algorithm for modular multilevel converters minimizing the spread in the submodule capacitor voltages," *IEEE Trans. Power Electron.*, vol. 30, no. 1, pp. 440–449, Jan 2015.

[45] A. Hassanpoor, L. Angquist, S. Norrga, K. Ilves, and H.-P. Nee, "Tolerance band modulation methods for modular multilevel converters," *IEEE Trans. Power Electron.*, vol. 30, no. 1, pp. 311–326, Jan 2015.

[46] J. Qin and M. Saeedifard, "Reduced switching-frequency voltage-balancing strategies for modular multilevel hvdc converters," *IEEE Trans. Power Del.*, vol. 28, no. 4, pp. 2403–2410, Oct 2013.

[47] M. Hagiwara, R. Maeda, and H. Akagi, "Control and Analysis of the Modular Multilevel Cascade Converter Based on Double-Star Chopper-Cells (MMCC-DSCC)," *IEEE Trans. Power Electron.*, vol. 26, no. 6, pp. 1649–1658, 2011.

[48] X. Yang, J. Li, X. Wang, W. Fan, and T. Zheng, "Circulating current model of modular multilevel converter," in *Asia-Pacific Power and Energy Engineering Conf. (APPEEC)*, March 2011, pp. 1 – 6.

[49] M. Perez and J. Rodriguez, "Generalized modeling and simulation of a modular multilevel converter," in *IEEE Int. Symp. Industrial Electronics (ISIE)*, June 2011, pp. 1863 – 1868.

[50] K. Ilves, A. Antonopoulos, S. Norrga, and H.-P. Nee, "Steady-state analysis of interaction between harmonic components of arm and line quantities of modular multilevel converters," *IEEE Trans. Power Electron.*, vol. 27, no. 1, pp. 57 – 68, Jan. 2012.

[51] A. Korn, M. Winkelnkemper, and P. Steimer, "Low output frequency operation of the modular multi-level converter," in *IEEE Energy Conversion Congr. and Expo. (ECCE)*, Sept. 2010, pp. 3993 – 3997.

[52] A. Antonopoulos, L. Angquist, S. Norrga, K. Ilves, and H.-P. Nee, "Modular multilevel converter AC motor drives with constant torque form zero to nominal speed," in *IEEE Energy Conversion Congr. and Expo. (ECCE)*, Sept. 2012, pp. 739–746.

[53] J. Kolb, F. Kammerer, M. Gommeringer, and M. Braun, "Cascaded control system of the modular multilevel converter for feeding variable-speed drives," *IEEE Trans. Power Electron.*, vol. 30, no. 1, pp. 349–357, Jan 2015.

[54] M. Spichartz, V. Staudt, and A. Steimel, "Analysis of the module-voltage fluctuations of the modular multilevel converter at variable speed drive applications," in *12th Int. Conf. Optimization of Electrical and Electronic Equipment (OPTIM)*, May 2012, pp. 751 –758.

[55] M. Hagiwara, I. Hasegawa, and H. Akagi, "Startup and low-speed operation of an adjustable-speed motor driven by a modular multilevel cascade inverter (MMCI)," in *IEEE Energy Conversion Congr. and Expo. (ECCE)*, Sept. 2012, pp. 718–725.

[56] J. Reed, G. Venkataramanan, and F. Martinez, "Complex phasor modeling and control of modular multilevel inverters," in *IEEE Energy Conversion Congr. and Expo. (ECCE)*, Sept 2011, pp. 4013–4020.

[57] S. Deore, P. Darji, and A. Kulkarni, "Dynamic phasor modeling of modular multilevel converters," in *7th IEEE Int. Conf. Industrial and Information Systems (ICIIS)*, Aug 2012, pp. 1–6.

[58] Z. Li, P. Wang, Z. Chu, H. Zhu, Y. Luo, and Y. Li, "An inner current suppressing method for modular multilevel converters," *IEEE Trans. Power Electron.*, vol. 28, no. 11, pp. 4873–4879, Nov 2013.

[59] X. She, A. Huang, X. Ni, and R. Burgos, "AC circulating currents suppression in modular multilevel converter," in *38th Annu. Conf. IEEE Industrial Electronics Society (IECON)*, Oct 2012, pp. 191–196.

[60] G. Adam and B. Williams, "Half- and full-bridge modular multilevel converter models for simulations of full-scale HVDC links and multiterminal DC grids," *IEEE Journal of Emerging and Selected Topics in Power Electronics*, vol. 2, no. 4, pp. 1089–1108, Dec 2014.

[61] A. Das, H. Nademi, and L. Norum, "A method for charging and discharging capacitors in modular multilevel converter," in *37th Annu. Conf. IEEE Industrial Electronics Society (IECON)*, 2011, pp. 1058–1062.

[62] K. Shi, F. Shen, D. Lv, P. Lin, M. Chen, and D. Xu, "A novel start-up scheme for modular multilevel converter," in *IEEE Energy Conversion Congr. and Expo. (ECCE)*, 2012, pp. 4180–4187.

[63] J. Xu, C. Zhao, B. Zhang, and L. Lu, "New precharge and submodule capacitor voltage balancing topologies of modular multilevel converter for VSC-HVDC application," in *Asia-Pacific Power and Energy Engineering Conf. (APPEEC)*, 2011, pp. 1–4.

[64] K. Li and C. Zhao, "New technologies of modular multilevel converter for vsc-hvdc application," in *Asia-Pacific Power and Energy Engineering Conf. (APPEEC)*, March 2010, pp. 1–4.

[65] Y. Yang, Q. Ge, M. Lei, X. Wang, X. Yang, and R. Gou, "Pre-charging control strategies of modular multilevel converter," in *Int. Conf. Electrical Machines and Systems (ICEMS)*, Oct 2013, pp. 1842–1845.

[66] B. Li, D. Xu, Y. Zhang, R. Yang, G. Wang, W. Wang, and D. Xu, "Closed-loop precharge control of modular multilevel converters during start-up processes," *IEEE Trans. Power Electron.*, vol. 30, no. 2, pp. 524–531, Feb 2015.

[67] F. Gao, Z. Li, F. Xu, Z. Chu, P. Wang, and Y. Li, "Startup strategy of vsc-hvdc system based on modular multilevel converter," in *IEEE Energy Conversion Congr. and Expo. (ECCE)*, Sept 2014, pp. 1946–1952.

[68] E. Veilleux, "Interconnection of direct-drive wind turbines using a series connected DC grid," Master's thesis, University of Toronto, 2009.

[69] S. Heier, *Grid Integration of Wind Energy Conversion Systems*, 2nd ed. John Wiley & Sons, Ltd, 2006.

[70] M. P. Kazmierkowski, R. Krishnan, and F. Blaabjerg, *Control in Power Electronics, Selected Problems*. New York: Academic, 2002.

[71] R. Erickson, S. Angkititrakul, and K. Almazeedi, "A new family of multilevel matrix converters for wind power applications: Final report," University of Colorado Boulder, Colorado, and NREL, Tech. Rep., December 2006.

[72] P. C. Krause, O. Wasynczuk, and S. D. Sudhoff, *Analysis of Electric Machinery and Drive Systems*, 2nd ed. John Wiley & Sons, Ltd, 2004.

[73] X. Yang, J. Li, X. Wang, W. Fan, and T. Zheng, "Harmonic analysis of the DC capacitor voltage in modular multilevel converter based STATCOM," in *6th IEEE Conf. Industrial Electronics and Applications (ICIEA)*, June 2011, pp. 2575 – 2579.

[74] M. Guan, Z. Xu, and H. Li, "Analysis of DC voltage ripples in modular multilevel converters," in *Int. Conf. Power System Technology (POWERCON)*, Oct. 2010, pp. 1 – 6.

[75] A. Lesnicar and R. Marquardt, "An innovative modular multilevel converter topology suitable for a wide power range," in *IEEE Bologna Power Tech Conf. Proc.*, vol. 3, June 2003.

[76] H. Khalil, *Nonlinear Systems*. Prentice Hall PTR, 2002.

[77] S. H. Z. Edwin K. P. Chong, *An Introduction to Optimization*, 2nd ed. John Wiley & Sons, Inc., 2004. [Online]. Available: http://www.wiley.com/WileyCDA/WileyTitle/productCd-0471654000.html

[78] J. Kolb, F. Kammerer, and M. Braun, "Dimensioning and design of a modular multilevel converter for drive applications," in *15th Int. Power Electronics and Motion Control Conference (EPE/PEMC)*, Sept 2012, pp. LS1a–1.1–1–LS1a–1.1–8.

APPENDICES

A. CALCULATION OF THE SM CAPACITOR VOLTAGE RIPPLE

In this section, the magnitude of the SM capacitor voltage ripple of the MMC under fixed-frequency operation is mathematically derived. In the derivations, the common-mode voltage reference is assumed to be absent, i.e., $m_{\mathrm{cm}} = 0$.

- Case 1: The MMC operates without the circulating current controller. In this case

$$m_{\mathrm{circ},j} = 0, \tag{A.1a}$$

$$m_a = m \sin \omega t. \tag{A.1b}$$

Substituting for $m_{\mathrm{circ},j}$ and m_a from (A.1) in (3.37b), (3.37c), and (3.37d) and neglecting R_o and R_p, the magnitude of the fundamental and second-order harmonic components of the SM capacitor voltage ripple of each phase are given by

$$\delta v_{\mathrm{c1}} = \frac{P_g}{\omega C_{\mathrm{SM}} V_{\mathrm{dc}}} \left[\left(\frac{1}{3m\cos\phi} + \frac{m}{16\omega C_{\mathrm{SM}} Z} \left(\frac{1}{\cos\phi} - \frac{m^2}{3} \right) - \frac{m}{6} \right)^2 + \frac{1}{9} \left(1 + \frac{3m^2}{16\omega C_{\mathrm{SM}} Z} \right) \left(1 + \frac{m^2}{8\omega C_{\mathrm{SM}} Z} \right) \left(\frac{1}{\cos\phi} - 1 \right) \right]^{0.5}, \tag{A.2a}$$

$$\delta v_{\mathrm{c2}} = \frac{P_g}{12\omega C_{\mathrm{SM}} V_{\mathrm{dc}} \cos\phi} \left[\left(1 + \frac{3}{4\omega C_{\mathrm{SM}} Z} - \frac{m^2 \cos\phi}{4\omega C_{\mathrm{SM}} Z} \right)^2 + \frac{m^2 \cos\phi}{2\omega C_{\mathrm{SM}} Z} \left(1 + \frac{3}{4\omega C_{\mathrm{SM}} Z} \right) (1 - \cos\phi) \right]^{0.5}, \tag{A.2b}$$

where

$$Z = \frac{4\omega L_o}{N} - \frac{1}{4\omega C_{\mathrm{SM}}}(1 + \frac{m^2}{2}),$$

ϕ is the power factor angle. Design of the system is such that $Z > 0$. Consequently, the capacitor voltage ripple of the SMs in the upper and lower arms of phase-a become

$$\delta v_{cp,a} = \delta v_{\mathrm{c1}} \sin(\omega t + \psi_1) + \delta v_{\mathrm{c2}} \sin(2\omega t + \psi_2), \tag{A.3a}$$

$$\delta v_{cn,a} = -\delta v_{\mathrm{c1}} \sin(\omega t + \psi_1) + \delta v_{\mathrm{c2}} \sin(2\omega t + \psi_2), \tag{A.3b}$$

where

$$\psi_1 = \tan^{-1}\left(\frac{8m^2\omega C_{\mathrm{SM}} Z + m^4 - 3m^2 - 16\omega C_{\mathrm{SM}} Z}{\tan\phi\,(3m^2 + 16\omega C_{\mathrm{SM}} Z)}\right),$$
$$\psi_2 = \tan^{-1}\left(\frac{(4\omega C_{\mathrm{SM}} Z + 3)\tan\phi}{4\omega C_{\mathrm{SM}} Z + 3 - m^2}\right).$$

Defining $\theta_1 = (\omega t + \psi_1)$ and $\phi_1 = (\psi_2 - 2\psi_1)$, (A.3) can be re-written as,

$$\delta v_{cp,a} = \delta v_{\mathrm{c1}} \sin\theta_1 + \delta v_{\mathrm{c2}} \sin(2\theta_1 + \phi_1), \tag{A.4a}$$

$$\delta v_{cn,a} = -\delta v_{\mathrm{c1}} \sin\theta_1 + \delta v_{\mathrm{c2}} \sin(2\theta_1 + \phi_1). \tag{A.4b}$$

Similar expressions can be derived for phases b and c as well.

- Case 2: The MMC operates with the circulating current controller proposed in Section 4.3 of Chapter 4. In this case, $i_{\mathrm{circ},j} = \dfrac{i_{\mathrm{dc}}}{3}$ (assuming balanced conditions)

and the magnitude of the fundamental and second-order harmonic components of the SM capacitor voltage ripple become

$$\delta v_{\mathrm{c1}}^{\mathrm{CC}} = \frac{P_g}{\omega C_{\mathrm{SM}} V_{\mathrm{dc}}} \left[\left(\frac{1}{3m\cos\phi} - \frac{m}{6} \right)^2 + \frac{1}{9} \left(\frac{1}{\cos\phi} - 1 \right) \right]^{0.5}, \tag{A.5a}$$

$$\delta v_{\mathrm{c2}}^{\mathrm{CC}} = \frac{P_g}{12\omega C_{\mathrm{SM}} V_{\mathrm{dc}} \cos\phi}. \tag{A.5b}$$

Consequently, the capacitor voltage ripple of the SMs in the upper and lower arms of phase-a become

$$\delta v_{cp,a}^{\mathrm{CC}} = \delta v_{\mathrm{c1}}^{\mathrm{CC}} \sin\left(\omega t + \psi_{1,\mathrm{CC}}\right) + \delta v_{\mathrm{c2}}^{\mathrm{CC}} \sin\left(2\omega t + \phi\right), \tag{A.6a}$$

$$\delta v_{cn,a}^{\mathrm{CC}} = -\delta v_{\mathrm{c1}}^{\mathrm{CC}} \sin\left(\omega t + \psi_{1,\mathrm{CC}}\right) + \delta v_{\mathrm{c2}}^{\mathrm{CC}} \sin\left(2\omega t + \phi\right), \tag{A.6b}$$

where

$$\psi_{1,\mathrm{CC}} = \tan^{-1}\left(\frac{m^2 - 2}{2\tan\phi} \right). \tag{A.7}$$

Equation (A.6) can be re-written as

$$\delta v_{cp,a}^{\mathrm{CC}} = \delta v_{\mathrm{c1}}^{\mathrm{CC}} \sin\theta_2 + \delta v_{\mathrm{c2}}^{\mathrm{CC}} \sin\left(2\theta_2 + \phi_2\right), \tag{A.8a}$$

$$\delta v_{cn,a}^{\mathrm{CC}} = -\delta v_{\mathrm{c1}}^{\mathrm{CC}} \sin\theta_2 + \delta v_{\mathrm{c2}}^{\mathrm{CC}} \sin\left(2\theta_2 + \phi_2\right), \tag{A.8b}$$

where $\theta_2 = (\omega t + \psi_{1,\mathrm{CC}})$ and $\phi_2 = (\phi - 2\psi_{1,\mathrm{CC}})$.

Based on (A.2) and (A.5),

$$\delta v_{\mathrm{c1}} > \delta v_{\mathrm{c1}}^{\mathrm{CC}}, \tag{A.9a}$$

$$\delta v_{\mathrm{c2}} > \delta v_{\mathrm{c2}}^{\mathrm{CC}}. \tag{A.9b}$$

Therefore, the harmonics of the SM capacitor voltage ripple, when the circulating current controller is enabled, is definitely lesser than the case where it is disabled.

B. STABILITY ANALYSIS OF THE MMC UNDER VARIABLE-FREQUENCY OPERATION

B.1 Closed-loop System

The closed-loop dynamics of the system, comprising the MMC-based adjustable-speed drive with the control system described in Sections 5.3 and 5.4, is provided in this section. The closed-loop dynamics of the aforementioned system neglects the filter dynamics and assumes $K_{\mathrm{pv}} = 0$. The stability of this closed-loop system is proven in this section.

B.1.1 Closed-loop System Dynamics

From the motor qd current controller block diagram in Fig. 5.2, the fundamental frequency component of the reference waveforms of the ac-side phase voltages are given by

$$\begin{aligned}\boldsymbol{m}_{abc} &= \boldsymbol{T}(\theta_r)^{-1}\boldsymbol{m}^{r}_{qd0} \\ &= \frac{2K_{\mathrm{p}}}{V_{\mathrm{dc}}}\left(\boldsymbol{i}_{abc,\mathrm{ref}} - \boldsymbol{i}_{abc}\right) + \frac{2K_{\mathrm{i}}}{V_{\mathrm{dc}}}\boldsymbol{T}^{-1}\int \boldsymbol{T}\left(\boldsymbol{i}_{abc,\mathrm{ref}} - \boldsymbol{i}_{abc}\right)\mathrm{d}t + \frac{2\omega_r L_{\mathrm{eq}}}{\sqrt{3}V_{\mathrm{dc}}}\boldsymbol{X}\,\boldsymbol{i}_{abc} \\ &\quad + \frac{2}{V_{\mathrm{dc}}}\boldsymbol{e}_{abc}, \end{aligned} \tag{B.1}$$

where $\boldsymbol{i}_{abc} \approx \hat{\boldsymbol{i}}_{abc}$ is assumed.

Expanding the dynamic model of the MMC from (3.40) in Chapter 4 to all the phases results in

$$\frac{\mathrm{d}\boldsymbol{i}_{abc}}{\mathrm{d}t} = -\frac{R_{\mathrm{eq}}}{L_{\mathrm{eq}}}\boldsymbol{i}_{abc} + \frac{N}{4L_{\mathrm{eq}}}\left(\boldsymbol{m}_{abc} + m_{\mathrm{cm}}\boldsymbol{1}\right) \odot \boldsymbol{v}^{\Sigma}_{\mathrm{c},abc} - \frac{N}{4L_{\mathrm{eq}}}\left(\boldsymbol{1} - 2\boldsymbol{m}_{\mathrm{circ},abc}\right) \odot \boldsymbol{v}^{\Delta}_{\mathrm{c},abc} - \frac{1}{L_{\mathrm{eq}}}\left(\boldsymbol{e}_{abc} + \tilde{v}_{n,\mathrm{new}}\boldsymbol{1}\right), \tag{B.2a}$$

$$\frac{\mathrm{d}\boldsymbol{i}_{\mathrm{circ},abc}}{\mathrm{d}t} = -\frac{R_o}{L_o}\boldsymbol{i}_{\mathrm{circ},abc} - \frac{N}{4L_o}\left(\boldsymbol{1} - 2\boldsymbol{m}_{\mathrm{circ},abc}\right) \odot \boldsymbol{v}^{\Sigma}_{\mathrm{c},abc} + \frac{N}{4L_o}\left(\boldsymbol{m}_{abc} + m_{\mathrm{cm}}\boldsymbol{1}\right) \odot \boldsymbol{v}^{\Delta}_{\mathrm{c},abc} + \frac{V_{\mathrm{dc}}}{2L_o}\boldsymbol{1}, \tag{B.2b}$$

$$\frac{\mathrm{d}\boldsymbol{v}^{\Sigma}_{\mathrm{c},abc}}{\mathrm{d}t} = -\frac{1}{2C_{\mathrm{SM}}}\left(\boldsymbol{m}_{abc} + m_{\mathrm{cm}}\boldsymbol{1}\right) \odot \boldsymbol{i}_{abc} + \frac{1}{C_{\mathrm{SM}}}\left(\boldsymbol{1} - 2\boldsymbol{m}_{\mathrm{circ},abc}\right) \odot \boldsymbol{i}_{\mathrm{circ},abc} - \frac{1}{R_pC_{\mathrm{SM}}}\boldsymbol{v}^{\Sigma}_{\mathrm{c},abc}, \tag{B.2c}$$

$$\frac{\mathrm{d}\boldsymbol{v}^{\Delta}_{\mathrm{c},abc}}{\mathrm{d}t} = \frac{1}{2C_{\mathrm{SM}}}\left(\boldsymbol{1} - 2\boldsymbol{m}_{\mathrm{circ},abc}\right) \odot \boldsymbol{i}_{abc} - \frac{1}{C_{\mathrm{SM}}}\left(\boldsymbol{m}_{abc} + m_{\mathrm{cm}}\boldsymbol{1}\right) \odot \boldsymbol{i}_{\mathrm{circ},abc} - \frac{1}{R_pC_{\mathrm{SM}}}\boldsymbol{v}^{\Delta}_{\mathrm{c},abc}. \tag{B.2d}$$

Substituting for $\boldsymbol{m}_{abc}$ from (B.1) and $\boldsymbol{m}_{\mathrm{circ},abc}$ from (5.31) in (B.2), and linearizing the resulting system about its operating/reference point ($\boldsymbol{i}_{abc,\mathrm{ref}}$, $\boldsymbol{i}_{\mathrm{circ},abc,\mathrm{ref,meth}}$, $\boldsymbol{v}^{\Sigma}_{\mathrm{c},abc,\mathrm{ref}} = \dfrac{2V_{\mathrm{dc}}}{N}$, $\boldsymbol{v}^{\Delta}_{\mathrm{c},abc,\mathrm{op}} = \boldsymbol{0}$) by neglecting the higher-order terms in the Taylor series expansion results in

$$\frac{\mathrm{d}\boldsymbol{x}}{\mathrm{d}t} = \boldsymbol{A}(t)\boldsymbol{x}(t) + \boldsymbol{d}(t,\boldsymbol{x}), \tag{B.3a}$$

$$\boldsymbol{A}(t) = \begin{pmatrix} \boldsymbol{A}_3 & \boldsymbol{0} & \boldsymbol{A}_4 & \boldsymbol{A}_5 \\ \boldsymbol{0} & \boldsymbol{A}_6 & \boldsymbol{A}_7 & \boldsymbol{A}_8 \\ \boldsymbol{A}_{10} & \boldsymbol{A}_{11} & \boldsymbol{A}_{12} & \boldsymbol{0} \\ \boldsymbol{A}_{14} & \boldsymbol{A}_{15} & \boldsymbol{0} & \boldsymbol{A}_{16} \end{pmatrix}, \tag{B.3b}$$

$$\boldsymbol{d}(t,\boldsymbol{x}) = \begin{pmatrix} \boldsymbol{A}_2^{\mathrm{T}} & \boldsymbol{0} & \boldsymbol{A}_9^{\mathrm{T}} & \boldsymbol{A}_{13}^{\mathrm{T}} \end{pmatrix}^{\mathrm{T}} \int \boldsymbol{T}\delta\boldsymbol{i}_{abc}\mathrm{d}t, \tag{B.3c}$$

where

$$\delta \boldsymbol{i}_{abc} = \boldsymbol{i}_{abc} - \boldsymbol{i}_{abc,\mathrm{ref}}, \tag{B.4a}$$

$$\delta \boldsymbol{i}_{\mathrm{circ},abc} = \boldsymbol{i}_{\mathrm{circ},abc} - \boldsymbol{i}_{\mathrm{circ},abc,\mathrm{ref}}, \tag{B.4b}$$

$$\delta \boldsymbol{v}^{\Sigma}_{\mathrm{c},abc} = \boldsymbol{v}^{\Sigma}_{\mathrm{c},abc} - \frac{2V_{\mathrm{dc}}}{N}\boldsymbol{1}, \tag{B.4c}$$

$$\delta \boldsymbol{v}^{\Delta}_{\mathrm{c},abc} = \boldsymbol{v}^{\Delta}_{\mathrm{c},abc}, \tag{B.4d}$$

$$\boldsymbol{x} = \begin{pmatrix} \delta \boldsymbol{i}^{\mathrm{T}}_{abc} & \delta \boldsymbol{i}^{\mathrm{T}}_{\mathrm{circ},abc} & \delta \boldsymbol{v}^{\Sigma\mathrm{T}}_{\mathrm{c},abc} & \delta \boldsymbol{v}^{\Delta\mathrm{T}}_{\mathrm{c},abc} \end{pmatrix}^{\mathrm{T}}, \tag{B.4e}$$

$$\boldsymbol{A}_2 = \boldsymbol{T}^{-1}\frac{K_{\mathrm{i}}}{L_{\mathrm{eq}}}, \tag{B.4f}$$

$$\boldsymbol{A}_3 = -\frac{(K_{\mathrm{p}} + R_{\mathrm{eq}})}{L_{\mathrm{eq}}}\boldsymbol{I}_3 + \frac{\omega_r}{\sqrt{3}}\boldsymbol{X}, \tag{B.4g}$$

$$\boldsymbol{A}_4 = \frac{N\omega_r}{2\sqrt{3}V_{\mathrm{dc}}}\mathrm{diag}\Big(\big(\boldsymbol{X}\,\boldsymbol{i}_{abc,\mathrm{ref}}\big)^{\mathrm{T}}\Big) + \frac{Nm_{\mathrm{cm}}}{4L_{\mathrm{eq}}}\boldsymbol{I}_3 + \frac{N}{2V_{\mathrm{dc}}L_{\mathrm{eq}}}\mathrm{diag}\big(\boldsymbol{e}^{\mathrm{T}}_{abc}\big), \tag{B.4h}$$

$$\boldsymbol{A}_5 = -\frac{N}{4L_{\mathrm{eq}}}\boldsymbol{I}_3,\ \boldsymbol{A}_6 = -\frac{K_{\mathrm{p1}} + R_o}{L_o}\boldsymbol{I}_3,\ \boldsymbol{A}_7 = -\frac{N}{4L_o}\boldsymbol{I}_3,\ \boldsymbol{A}_8 = \boldsymbol{A}_4\frac{L_{\mathrm{eq}}}{L_o}, \tag{B.4i}$$

$$\boldsymbol{A}_9 = \frac{K_{\mathrm{i}}}{V_{\mathrm{dc}}C_{\mathrm{SM}}}\mathrm{diag}\big(\boldsymbol{i}^{\mathrm{T}}_{abc,\mathrm{ref}}\big)\,\boldsymbol{T}^{-1}, \tag{B.4j}$$

$$\begin{aligned}\boldsymbol{A}_{10} = {} & \frac{1}{V_{\mathrm{dc}}C_{\mathrm{SM}}}\left(K_{\mathrm{p}}\mathrm{diag}\big(\boldsymbol{i}^{\mathrm{T}}_{abc,\mathrm{ref}}\big) - \mathrm{diag}\big(\boldsymbol{e}^{\mathrm{T}}_{abc}\big)\right) - \frac{m_{\mathrm{cm}}}{2C_{\mathrm{SM}}}\boldsymbol{I}_3 \\ & - \frac{\omega_r L_{\mathrm{eq}}}{\sqrt{3}V_{\mathrm{dc}}C_{\mathrm{SM}}}\left(\mathrm{diag}\Big(\big(\boldsymbol{X}\,\boldsymbol{i}_{abc,\mathrm{ref}}\big)^{\mathrm{T}}\Big) + \mathrm{diag}\big(\boldsymbol{i}^{\mathrm{T}}_{abc,\mathrm{ref}}\big)\boldsymbol{X}\right),\end{aligned} \tag{B.4k}$$

$$\boldsymbol{A}_{11} = \frac{1}{C_{\mathrm{SM}}}\boldsymbol{I}_3 + \frac{2K_{\mathrm{p1}}}{V_{\mathrm{dc}}C_{\mathrm{SM}}}\mathrm{diag}\big(\boldsymbol{i}^{\mathrm{T}}_{\mathrm{circ},abc,\mathrm{ref}}\big),\ \boldsymbol{A}_{12} = \boldsymbol{A}_{16} = -\frac{1}{R_p C_{\mathrm{SM}}}\boldsymbol{I}_3, \tag{B.4l}$$

$$\boldsymbol{A}_{13} = \frac{2K_{\mathrm{i}}}{V_{\mathrm{dc}}C_{\mathrm{SM}}}\mathrm{diag}\big(\boldsymbol{i}^{\mathrm{T}}_{\mathrm{circ},abc,\mathrm{ref}}\big)\,\boldsymbol{T}^{-1}, \tag{B.4m}$$

$$\boldsymbol{A}_{14} = \frac{1}{2C_{\mathrm{SM}}}\boldsymbol{I}_3 + \frac{2K_{\mathrm{p}}}{V_{\mathrm{dc}}C_{\mathrm{SM}}}\mathrm{diag}\big(\boldsymbol{i}^{\mathrm{T}}_{\mathrm{circ},abc,\mathrm{ref}}\big) - \frac{2\omega_r L_{\mathrm{eq}}}{\sqrt{3}V_{\mathrm{dc}}C_{\mathrm{SM}}}\mathrm{diag}\big(\boldsymbol{i}^{\mathrm{T}}_{\mathrm{circ},abc,\mathrm{ref}}\big)\boldsymbol{X}, \tag{B.4n}$$

$$\begin{aligned}\boldsymbol{A}_{15} = {} & \frac{K_{\mathrm{p1}}}{V_{\mathrm{dc}}C_{\mathrm{SM}}}\mathrm{diag}\big(\boldsymbol{i}^{\mathrm{T}}_{abc,\mathrm{ref}}\big) - \frac{2}{V_{\mathrm{dc}}C_{\mathrm{SM}}}\mathrm{diag}\big(\boldsymbol{e}^{\mathrm{T}}_{abc}\big) - \frac{m_{\mathrm{cm}}}{C_{\mathrm{SM}}}\boldsymbol{I}_3 \\ & - \frac{2\omega_r L_{\mathrm{eq}}}{\sqrt{3}V_{\mathrm{dc}}C_{\mathrm{SM}}}\mathrm{diag}\Big(\big(\boldsymbol{X}\,\boldsymbol{i}_{abc,\mathrm{ref}}\big)^{\mathrm{T}}\Big),\end{aligned} \tag{B.4o}$$

and $K_{\mathrm{pv}} = 0$ is assumed. Equations (B.3) and (B.4) represent the linearized closed-loop dynamics of the MMC-based adjustable-speed drive system with the control

system described in Sections 5.3 and 5.4. The system described in (B.3) and (B.4) is a non-autonomous system and its stability, based on Lyapunov analysis of singularly perturbed non-linear non-autonomous systems [76], is proven in the next section.

B.1.2 Stability Analysis of the Closed-loop System

The system described by (B.3) and (B.4) is re-written as

$$\frac{\mathrm{d}\boldsymbol{x}_1}{\mathrm{d}t} = \boldsymbol{A}_{\mathrm{r}}(t)\boldsymbol{x}_1 + \boldsymbol{d}_1(t, \boldsymbol{x}_1, \boldsymbol{x}_2), \tag{B.5a}$$

$$\mu\frac{\mathrm{d}\boldsymbol{x}_2}{\mathrm{d}t} = \boldsymbol{A}_{\mathrm{b}}\boldsymbol{x}_2 + \boldsymbol{d}_2(t, \boldsymbol{x}_1, \mu), \tag{B.5b}$$

where

$$\mu = \frac{K_{\mathrm{p}}}{R_p C_{\mathrm{SM}}}\frac{1}{K_{\mathrm{p1}} + R_o}, \tag{B.6a}$$

$$\boldsymbol{x}_1 = \begin{pmatrix} \delta\boldsymbol{i}_{abc}^{\mathrm{T}} & \delta\boldsymbol{v}_{\mathrm{c},abc}^{\Sigma\mathrm{T}} & \delta\boldsymbol{v}_{\mathrm{c},abc}^{\Delta\mathrm{T}} \end{pmatrix}^{\mathrm{T}}, \tag{B.6b}$$

$$\boldsymbol{x}_2 = \delta\boldsymbol{i}_{\mathrm{circ},abc}, \tag{B.6c}$$

$$\boldsymbol{A}_{\mathrm{b}} = -\frac{K_{\mathrm{p}}}{R_p C_{\mathrm{SM}} L_o}, \tag{B.6d}$$

$$\boldsymbol{A}_{\mathrm{r}}(t) = \begin{pmatrix} \boldsymbol{A}_3 & \boldsymbol{A}_4 & \boldsymbol{A}_5 \\ \boldsymbol{A}_{10} & \boldsymbol{A}_{12} & \boldsymbol{0} \\ \boldsymbol{A}_{14} & \boldsymbol{0} & \boldsymbol{A}_{16} \end{pmatrix}, \tag{B.6e}$$

$$\boldsymbol{d}_2(t, \boldsymbol{x}_1, \mu) = \begin{pmatrix} 0 & \mu\boldsymbol{A}_7 & \mu\boldsymbol{A}_8 \end{pmatrix}\boldsymbol{x}_1, \tag{B.6f}$$

$$\boldsymbol{d}_1(t, \boldsymbol{x}_1, \boldsymbol{x}_2) = \begin{pmatrix} 0 & \boldsymbol{A}_{11}^{\mathrm{T}} & \boldsymbol{A}_{15}^{\mathrm{T}} \end{pmatrix}^{\mathrm{T}}\boldsymbol{x}_2 + \begin{pmatrix} \boldsymbol{A}_2^{\mathrm{T}} & \boldsymbol{A}_9^{\mathrm{T}} & \boldsymbol{A}_{13}^{\mathrm{T}} \end{pmatrix}^{\mathrm{T}}\int \boldsymbol{T}\delta\boldsymbol{i}_{abc}\mathrm{d}t. \tag{B.6g}$$

Based on (5.28a), (5.40a), and (5.43), $\dfrac{K_{\mathrm{p1}} + R_o}{K_{\mathrm{p}}}$ is large. Additionally, $R_p C_{\mathrm{SM}}$ is very large due to the large resistor R_p typically used in the voltage sensing circuit. Consequently, based on (B.6a), $\mu \to 0$. That is, the system in (B.5) and (B.6) can be

considered as a combination of a reduced-order system and a boundary-layer system as $\mu \to 0$.

Substituting $\mu = 0$ in (B.5b) results in

$$\boldsymbol{A}_{\mathrm{b}}\boldsymbol{x}_2 = 0 \Rightarrow \boldsymbol{x}_2 = 0. \tag{B.7}$$

The solution of $\boldsymbol{x}_2$ in (B.5b) with $\mu = 0$ is given by (B.7). Substituting $\boldsymbol{x}_2$ from (B.7) in (B.5a) results in a reduced-order system for the system described by (B.5) and (B.6), which is given by

$$\frac{\mathrm{d}\boldsymbol{x}_1}{\mathrm{d}t} = \boldsymbol{A}_r(t)\boldsymbol{x}_1 + \boldsymbol{d}_{1,n}(t, \boldsymbol{x}_1), \tag{B.8a}$$

$$\boldsymbol{d}_{1,n}(t, \boldsymbol{x}_1) = \begin{pmatrix} \boldsymbol{A}_2^{\mathrm{T}} & \boldsymbol{A}_9^{\mathrm{T}} & \boldsymbol{A}_{13}^{\mathrm{T}} \end{pmatrix}^{\mathrm{T}} \int \boldsymbol{T}\delta\boldsymbol{i}_{abc}\mathrm{d}t \tag{B.8b}$$

A "fast time" $\tau = \dfrac{t}{\mu}$ and a boundary-layer state $\boldsymbol{x}_{\mathrm{b}}(\tau) = \boldsymbol{x}_2(\mu\tau) = \boldsymbol{x}_2(t)$ are defined. Then, the boundary-layer system for the system described by (B.5) and (B.6) is given by

$$\begin{aligned} \frac{\mathrm{d}\boldsymbol{x}_{\mathrm{b}}}{\mathrm{d}\tau} &= \boldsymbol{A}_{\mathrm{b}}\boldsymbol{x}_{\mathrm{b}} + \boldsymbol{d}_2(t, \mathbf{x}_1, 0) \\ &= -\frac{K_{\mathrm{p}}}{R_p C_{\mathrm{SM}} L_o}\boldsymbol{x}_{\mathrm{b}}. \end{aligned} \tag{B.9}$$

The boundary-layer system given by (B.9) is exponentially stable, uniformly for any (t,$\boldsymbol{x}_1$), with the eigen-value of $-\dfrac{K_{\mathrm{p}}}{R_p C_{\mathrm{SM}} L_o}$ of algebraic multiplicity 3.

The reduced-order system described by (B.8) can be re-written as

$$\frac{\mathrm{d}\boldsymbol{x}_{1,1}}{\mathrm{d}t} = \boldsymbol{A}_{\mathrm{r,r}}\boldsymbol{x}_{1,1} + \boldsymbol{d}_{1,1}(t, \boldsymbol{x}_{1,2}), \tag{B.10a}$$

$$\mu_1\frac{\mathrm{d}\boldsymbol{x}_{1,2}}{\mathrm{d}t} = \boldsymbol{A}_{r,b}(t, \mu_1)\boldsymbol{x}_{1,2} + \boldsymbol{d}_{1,2}(t, \boldsymbol{x}_{1,1}, \boldsymbol{x}_{1,2}, \mu_1), \tag{B.10b}$$

where

$$\mu_1 = \frac{1}{R_p C_{\mathrm{SM}} K_{\mathrm{p}}}, \tag{B.11a}$$

$$\boldsymbol{x}_{1,1} = \begin{pmatrix} \delta \boldsymbol{v}_{c,abc}^{\Sigma\,\mathrm{T}} & \delta \boldsymbol{v}_{c,abc}^{\Delta\,\mathrm{T}} \end{pmatrix}^{\mathrm{T}}, \tag{B.11b}$$

$$\boldsymbol{x}_{1,2} = \delta \boldsymbol{i}_{abc}, \tag{B.11c}$$

$$\boldsymbol{A}_{\mathrm{r,r}} = \begin{pmatrix} -\dfrac{1}{R_p C_{\mathrm{SM}}} \boldsymbol{I}_3 & \boldsymbol{0} \\ \boldsymbol{0} & -\dfrac{1}{R_p C_{\mathrm{SM}}} \boldsymbol{I}_3 \end{pmatrix}, \tag{B.11d}$$

$$\boldsymbol{A}_{\mathrm{r,b}}(t, \mu_1) = -\frac{\left(\dfrac{1}{R_p C_{\mathrm{SM}}} + \mu_1 R_{\mathrm{eq}} \right)}{L_{\mathrm{eq}}} \boldsymbol{I}_3 + \mu_1 \frac{\omega_r}{\sqrt{3}} \boldsymbol{X}, \tag{B.11e}$$

$$\boldsymbol{d}_{1,1}(t, \boldsymbol{x}_{1,2}) = \begin{pmatrix} \boldsymbol{A}_{10}^{\mathrm{T}} & \boldsymbol{A}_{14}^{\mathrm{T}} \end{pmatrix}^{\mathrm{T}} \boldsymbol{x}_{1,2} + \begin{pmatrix} A_9^{\mathrm{T}} & \boldsymbol{A}_{13}^{\mathrm{T}} \end{pmatrix}^{\mathrm{T}} \int \boldsymbol{T} \boldsymbol{x}_{1,2} \mathrm{d}t, \tag{B.11f}$$

$$\boldsymbol{d}_{1,2}(t, \boldsymbol{x}_{1,1}, \boldsymbol{x}_{1,2}, \mu_1) = \begin{pmatrix} \mu_1 \boldsymbol{A}_4 & \mu_1 \boldsymbol{A}_5 \end{pmatrix} \boldsymbol{x}_{1,1} + \mu_1 \boldsymbol{A}_2 \int \boldsymbol{T} \boldsymbol{x}_{1,2} \mathrm{d}t. \tag{B.11g}$$

Since $K_{\mathrm{p}} R_p C_{\mathrm{SM}}$ is large due to the large R_p as explained earlier, $\mu_1 \to 0$. As $\mu_1 \to 0$, the system described by (B.10) and (B.11) can be considered as a combination of a reduced-order system and a boundary-layer system.

Substituting $\mu_1 = 0$ in (B.10b) results in

$$\boldsymbol{A}_{\mathrm{r,b}}(t, 0) \boldsymbol{x}_{1,2} = 0 \Rightarrow \boldsymbol{x}_{1,2} = 0 \tag{B.12}$$

The solution of $\boldsymbol{x}_{1,2}$ in (B.10b) with $\mu_1 = 0$ is given by (B.12). Substituting $\boldsymbol{x}_{1,2}$ from (B.12) in (B.10a) results in a reduced-order system for the system described by (B.10) and (B.11) and is given by

$$\frac{\mathrm{d}\boldsymbol{x}_{1,1}}{\mathrm{d}t} = \boldsymbol{A}_{\mathrm{r,r}} \boldsymbol{x}_{1,1}. \tag{B.13}$$

The reduced-order system given by (B.13), (B.11b), and (B.11d), is exponentially stable with the eigen-value of $-\dfrac{1}{R_p C_{\mathrm{SM}}}$ of algebraic multiplicity 6.

Furthermore, define another "fast time" $\tau_1 = \dfrac{t}{\mu_1}$ and let $\boldsymbol{x}_{1,\mathrm{b}}(\tau_1) = \boldsymbol{x}_{1,2}(\mu_1\tau_1) = \boldsymbol{x}_{1,2}(t)$. Then, the boundary-layer system for the system described by (B.10) and (B.11) is given by

$$\begin{aligned}\frac{\mathrm{d}\boldsymbol{x}_{1,\mathrm{b}}}{\mathrm{d}\tau_1} &= \boldsymbol{A}_{\mathrm{r,b}}(t,0)\boldsymbol{x}_{1,\mathrm{b}} + \boldsymbol{d}_{1,2}(t,\boldsymbol{x}_{1,1},\boldsymbol{x}_{1,\mathrm{b}},0)\\ &= -\frac{1}{R_p C_{\mathrm{SM}} L_{\mathrm{eq}}}\boldsymbol{x}_{1,\mathrm{b}}. \end{aligned} \tag{B.14}$$

The system described by (B.14) is exponentially stable, uniformly for any $(t,\boldsymbol{x}_{1,1})$, with the eigen-value of $-\dfrac{1}{R_p C_{\mathrm{SM}} L_{\mathrm{eq}}}$ of algebraic multiplicity 3.

Based on the aforementioned results, the following statements are true for the system described by (B.10) and (B.11):

1. The origin of the reduced-order system given by (B.13), (B.11b), and (B.11d) is exponentially stable.
2. The origin of the boundary-layer system given by (B.14) is exponentially stable, uniformly for any $(\mathrm{t},\boldsymbol{x}_{1,1})$.

Then, by Theorem 11.4 in [76] for singularly perturbed systems, the origin of the system described by (B.10) and (B.11) is exponentially stable, for small μ_1. That is, the origin of the reduced-order system for the system described by (B.5) and (B.6) is exponentially stable, for small μ_1.

Summarizing the results for the system described by (B.5) and (B.6), the following statements can be concluded:

1. The origin of the reduced-order system given by (B.10) and (B.11) is exponentially stable.
2. The origin of the boundary-layer system given by (B.9) is exponentially stable, uniformly for any $(\mathrm{t},\boldsymbol{x}_1)$.

Therefore, by Theorem 11.4 in [76] for singularly perturbed systems, the origin of the system described by (B.5) and (B.6) is exponentially stable, for small μ and μ_1. Consequently, the proof of stability of the closed-loop system comprising the MMC-based adjustable-speed drive with the control system described in Section 5.3 and 5.4, is concluded.

VITA

VITA

Suman Debnath was born in Thiruvananthapuram, India, in 1988. He received his bachelors and masters degrees in electrical engineering from Indian Institute of Technology Madras, TN, India, in 2010. Since 2010, he has been working towards his Ph.D. degree in power electronics and control at Purdue University, West Lafayette, IN, USA. His main research interests include modeling, simulation, analysis, and optimal control of power electronics in various applications that include grid integration of renewable energy sources (PV, wind), HVDC transmission, LED lighting, electric drives, among others.